ÉCOLE POLYTECHNIQUE DE BRUXELLES

UNIVERSITÉ LIBRE DE BRUXELLES

Image-based modelling of complex heterogeneous microstructures

Application to deformation-induced permeability alterations in rocks

Thesis presented by Karim EHAB MOUSTAFA KAMEL

in fulfilment of the requirements of the PhD Degree in Engineering Sciences and Technology ("Docteur en Sciences de l'Ingénieur et Technologie")

Academic Year 2020-2021

Supervisor: Prof. Thierry J. Massart

Co-supervisor: Prof. Pierre Gerard

Thesis jury :

Prof. Alessandro PARENTE (Université libre de Bruxelles, Chair)
Prof. Bertrand FRANÇOIS (Université libre de Bruxelles, Secretary)
Prof. Jean-Baptiste COLLIAT (Université de Lille)
Prof. Patrick SELVADURAI (McGill University)
Prof. Gioacchino VIGGIANI (Université Grenoble Alpes)

fnrs LA LIBERTÉ DE CHERCHER

To my beloved family...
My parents, my brother, my wife and my lovely son...

Acknowledgements

La thèse est un long chemin qui ne pourrait aboutir sans le soutien continu de personnes précieuses à qui je ne peux qu'adresser mes sincères remerciements.

Il me tient tout particulièrement à coeur de consacrer mes premiers remerciements à mon directeur de thèse, Monsieur le Professeur Thierry Massart. Si j'ai pu réaliser cette thèse, c'est certainement grâce à ces étoiles qui se sont alignées cette soirée à l'Athénée Léon Lepage, soirée durant laquelle j'ai mobilisé plus de 2h de son temps pour lui poser moult questions quant à mes choix d'études supérieures. Les réponses qu'il m'avait apportées à l'époque m'avaient convaincu d'entamer des études à l'Ecole Polytechnique de Bruxelles. C'est également par son soutien que j'ai pu obtenir le financement qui m'a permis la réalisation de cette thèse.

Je tiens également à remercier Pierre Gerard pour son encadrement et sa disponibilité. Cette thèse n'aurait pas pu voir le jour sans son aide et ses conseils éclairés. Je garde tout particulièrement en mémoire ces voyages à Assise et à Delft.

J'ai retiré beaucoup d'enseignements dans les collaborations scientifiques qui ont agrémenté ce travail. Je pense tout particulièrement à Monsieur le Professeur Jean-Baptiste Colliat qui a eu l'amabilité de m'accueillir dans son laboratoire de l'Université de Lille.

Je remercie également Messieurs les Professeurs Patrick Selvadurai, Cino Viggiani, Alessandro Parente et Bertrand François d'avoir accepté de me faire l'honneur d'être membres du jury de cette thèse.

Au-delà du corps académique, plusieurs personnes ont contribué à faire du Laboratoire SMC un cadre de travail exceptionnel. Je pense à Monsieur le Professeur Peter Berke qui a toujours réussi à me motiver et à maintenir une belle cohésion de groupe, mais également à Guy Paulus pour toute l'aide apportée sur le plan informatique et pour ces discussions enrichissantes au détour d'un couloir. Merci au Docteur Bernard Sonon pour m'avoir mis le pied à l'étrier en début de thèse. Une pensée à tous mes collègues pour les moments partagés ensemble : Alexis, Arash G., Roland, Batoma, Rohith, Liesbeth, Chaimae, Li, Anqi, Guerrit, Dominique, Varun, Ygee, Arash M. Ce fut un plaisir de partager tous ces bons moments en votre compagnie.

Un remerciement particulier à la « team Galère » pour son aide précieuse dans ce dernier sprint.

Ma famille, mes parents, mon frère, mes soutiens sans faille. Une pensée pour mon père qui ne peut assister à cet aboutissement...

Mon épouse et mon petit bout Adam.

Abstract

The permeability of rocks has a critical influence on their fluid transport response in critical geo-environmental applications, such as pollutant transport or underground storage of hazardous nuclear waste. In such processes, the materials microstructure may be altered as a result of various stimuli, thereby impacting the fluid transfer properties. Stress or strain state modifications are one of the main causes for such evolutions. To numerically address this concern, an integrated and automated numerical tool was developed and illustrated on subsets of microCT scans of a Vosges sandstone (i) to explore the links between the pore space properties and the corresponding macroscopic transfer properties, with (ii) an incorporation of the microstructural alterations associated with stress state variations by using a realistic image-based representation of the microstructural morphology.

The ductile mechanical deformation behavior under high confining pressures at the scale of the microstructure, inducing pore closures by local plastifications, was modelled using finite elements simulations with a non-linear elastoplastic law, allowing to take into account the redistribution of local stresses. These simulations require robust discretization tools to capture the complex geometry of the porous network and the corresponding solid boundaries of the heterogeneous microstructural geometries. To achieve this, an integrated approach for the conformal discretization of complex implicit geometries based on signed distance fields was developed, producing high quality meshes from both imaging techniques and computational RVE generation methodologies. This conforming discretization approach was compared with an incompatible mode-based framework using a non conforming approach. This comparison highlighted the complementarity of both methods, the former capturing the effect of more detailed geometrical features, while the latter is more flexible as it allows using the same (non conforming) mesh for potentially variable geometries.

The evolution of permeability was evaluated at different confining pressure levels using the Lattice-Bolzmann method. This uncoupled solid-fluid interaction made it possible to study the combined influence on the permeability, porosity and the pores size distribution of the pore space morphology and the solid skeleton constitutive law parameters during loading and unloading conditions. The results highlight the need to consider elastoplastic laws and heterogeneities in the rock

model to simulate the ductile behavior of rocks at high confining pressures leading to significant permeability alterations under loading, and irreversible alterations under loading/unloading cycles induced by progressive pore closures.

The proposed methodology is designed to be flexible thanks to the interfacing with 'classical' discretization approaches and can be easily readapted to other contexts given the block approach.

Contents

List of Figures

List of Tables

1 Introduction

Contents

1.1 Context

Experts from many fields such as petrochemistry, geology or hydrogeology are interested in understanding the link between the microstructural morphology of geomaterials and their transfer properties for many applications, including critical situations such as the transfer of pollutants or the storage of radioactive hazardous waste (Rutqvist et al., 2009), gas storage (Katz and Tek, 1981; Teatini et al., 2011; de Jong, 2015) or the sequestration of CO_2 (Delshad et al., 2013). The rock material is used in such cases as a natural protective barrier limiting fluid migration to the outside environment. These applications have to consider physical phenomena such as mechanical, a thermal loading as well as chemical degradation at the pore scale, leading to changes in the deformability, the strength or the transfer properties. At this pore scale, a geomaterial is composed by a solid skeleton and a pore space

allowing fluids to flow as illustrated in Figure 1.1[1]. As an example, the construction of DGRs (Deep Geologic Repositories) requires excavations at significant depths for building underground infrastructures, that induce stress redistributions. Another example is the storage of natural gas in underground installations (Katz and Tek, 1981). The gas is stored in the pores of rock materials such as sandstones. On demand, the gas is injected or extracted, which will induce stress redistribution around the storage wells (Hu et al., 2018). These stress redistributions can have a significant impact on the morphology of the solid skeleton and the pore space. Such a modification of the microstructure can impact the hydraulic transfer properties of the rock, such as the intrinsic permeability induced by clogging, re-closures, reopenings, of cracks or pores (Hu et al., 2020b). In this context, it has been shown in (Bérend et al., 1995) that the intrinsic permeability, a concept introduced by Darcy (Darcy, 1857) measuring the ability of a porous medium to allow fluids to pass through it, is mainly controlled by the spatial structure of the geomaterial, the porous network and the solid/fluid interaction, making it a key parameter in rock engineering. Historically, a central hypothesis of Biot's theory (Biot, 1941) is that the permeability or deformability characteristics remain unchanged during the coupled interaction of the fluid and the solid skeleton. However, in environmental geomechanical problems, the microstructure of the considered materials may evolve as a result of stresses on various scales.

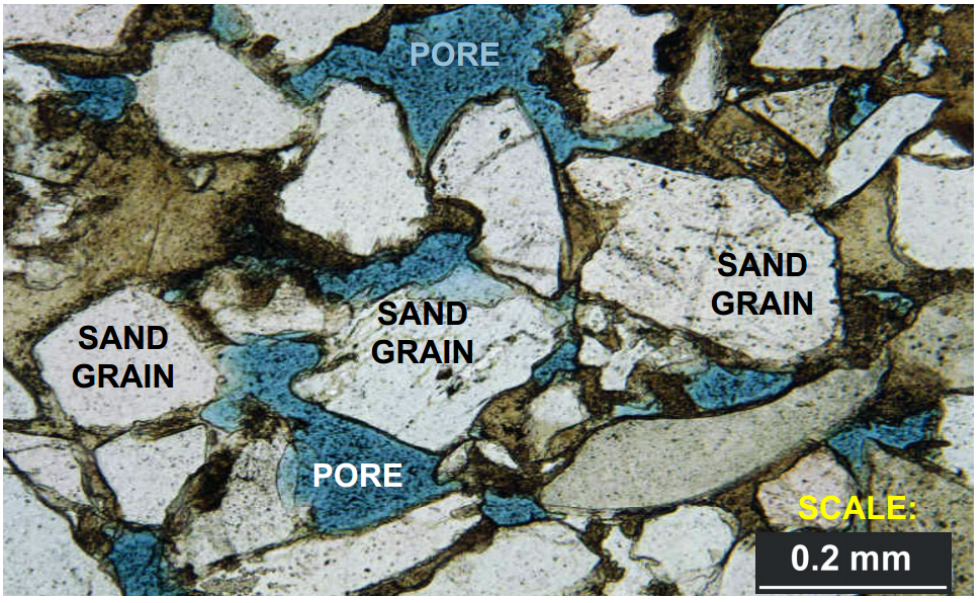

Figure 1.1: Highly magnified thin section of a piece of porous sandstone embedded in a blue epoxy to show the pore space - taken from [1]

[1] https://www.dartmouth.edu/~iispacs/Education/EARS18/Energy_2012/naturalGas/form/NaturalGas-formation.html

1.2 Experimental approaches of rocks mechanical behavior and its influence on the transfer properties

Over the years, numerous experimental investigations such as in (Kilmer et al., 1987; Farquhar et al., 1993; Morrow et al., 1984; Kwon et al., 2004; Meng and Li, 2013; Chalmers et al., 2012; Ghanizadeh et al., 2014; Gensterblum et al., 2015; Selvadurai, 2015; Selvadurai and Głowacki, 2017) have been carried out on different types of natural rocks and under different mechanical loadings in order to investigate the influence of the variation of the state of stress on the intrinsic permeability. Such research efforts have included (but were not limited to) deviatoric loading states in granites (Souley et al., 2001; Zoback and Byerlee, 1975) or basalts (Jiang et al., 2010), and isotropic compressive loadings in limestone (Selvadurai and Głowacki, 2008). A decrease of up to 40% of the permeability of a sandstone submitted to a confining pressure of 20 MPa was also noted by Fatt (Fatt and Davis, 1952). In the same way, a Vosges sandstone was shown to exhibit a decrease in permeability of about 50 % (Hu et al., 2018, 2020a) when an isotropic compressive stress state from 5 MPa to 40 MPa is applied.

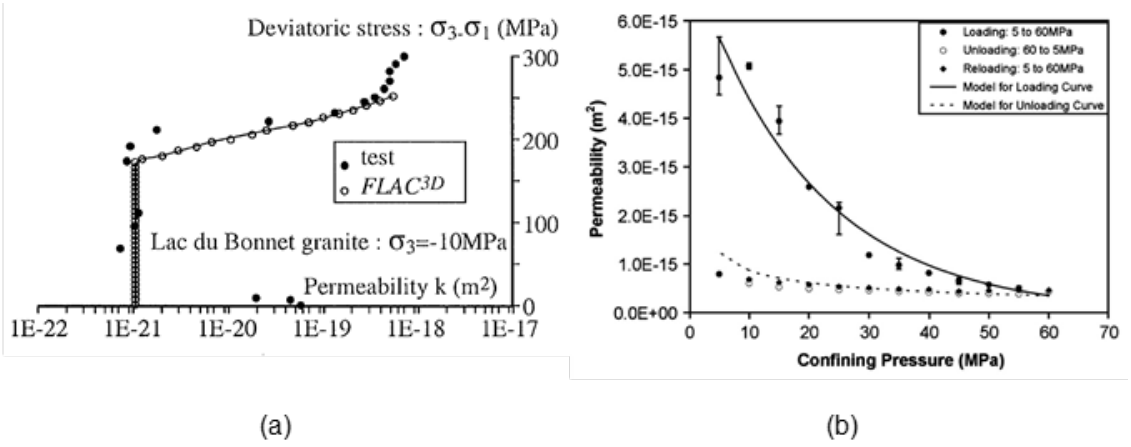

Figure 1.2: Permeability evolution induce by a stress state variation : (a) Permeability increase of granite from Lac du Bonnet induced by the application of a deviatoric stress - reproduced from (Souley et al., 2001), (b) Irreversible permeability decrease of Indiana limestone induced by the application of a triaxial compression - reproduced from (Selvadurai and Głowacki, 2008)

To single out two examples of such contributions within the vast body of literature on this topic, permeability variations related to cracking under deviatoric loadings states were obtained by (Souley et al., 2001) are illustrated in Figure 1.2a for a granite, with an initial decrease (initial crack closure) followed by an increase of the

permeability by several orders of magnitude. An irreversible decrease in permeability of a limestone caused by a triaxial isotropic compression was observed without significant macroscopic permanent deformation by (Selvadurai and Głowacki, 2008), see Figure 1.2b. Under such stress state variations, such effects can be conjectured to be associated with a modification of the pore space, potentially linked to local plastic deformations altering critical fluid flow pathways. In fact, the failure behavior of geological materials depends heavily on confining pressure and strain rate. Some rocks can break in the form of localized fractures and loose their cohesion leading to a quasi-brittle type of failure rupture under a relatively low confining pressure. Under certain temperature or pressure conditions, the response of rocks can evolve towards a more ductile behaviour, where the material will permanently deform. This mode of deformation is adopted in particular in the deep rock layers where the confining pressure is high (Choo and Sun, 2018). Figure 1.3 illustrates the transition between failure modes as a function of the confining pressure illustrating a Hamatsuda sandstone rock changing from a brittle to a ductile failure mode showing no macroscopic fracture at 49 MPa of confining pressure.

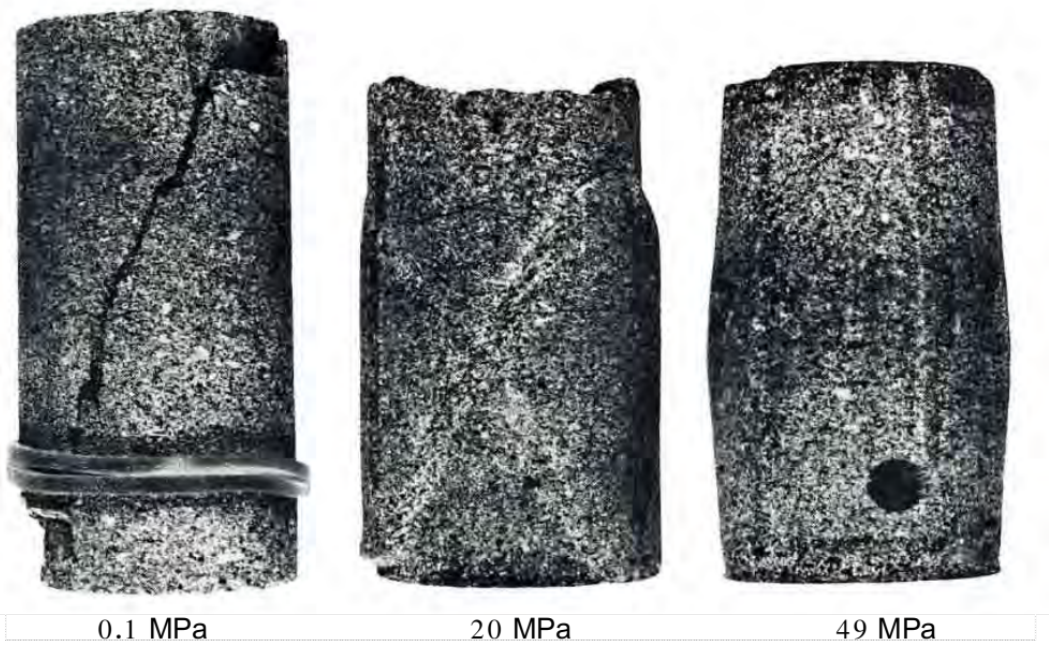

Figure 1.3: Laboratory samples of a Hamatsuda sandstone rock subjected to different confining pressures showing progressively the brittle–ductile transition : (Left) 0.1 MPa (Shear fracture), (Center) 20 MPa (Conjugate deformation band), (Right) 49 MPa (No macroscopic fracture - Bulging failure) repoduced from (Hoshino et al., 1972)

In general, most experimental approaches lead to semi-empirical relationships fitting the results of the tests such as Kozeny-Carman's law (Kozeny, 1927; Carman, 1937) linking the porosity to the permeability, or power laws linking permeability

and porosity to stress sensitivity such as the natural logarithm model (Walsh, 1981),or other phenomenological models as the power law model (Shi and Wang, 1986; Kwon et al., 2004), the exponential function model (Katsube et al., 1991), or the Two-Part Hooke's model (Zheng et al., 2015). However, these types of approaches do not allow a detailed investigation of the phenomena operating on the fine scale in order to gain insight on how a variation of the stress state way affect the rock microstructure, leading to a modification of the flow in porous network.

1.3 Numerical approaches of rocks micromechanical behaviors

To complement experimental approaches, the numerical models allowing accounting for permeability evolutions in connection with the micromechanical aspects have been developped progressively over the years (Sun et al., 2011). The uncoupled transfer properties were investigated in relation with the microstructure in several contributions. These studies have attempted to link the permeability properties to statistical and global characteristics of the pore space, such as the variance of the pore size distribution or their connectivity through their coordination number (Bernabé et al., 2010). Investigations have been conducted out on the basis of the explicit knowledge of the porous space by experimental methods. The non-evolving permeability properties were then analyzed on the basis of the characterization of porosity and tortuosity by tomography, in connection with Lattice-Boltzman methods (Sun et al., 2011). The relationship between microstructural evolutions (plastic compaction, dilatancy, thermal microcracking) and the macroscopic porosity and permeability has also been investigated experimentally by various authors (Bernabé et al., 2003). Numerical methods allowing to account for the variations of permeability associated with the variations of stresses were developed progressively. The evolution of the permeability due to microcracking was represented by macroscopic models with micromechanical motivation, in order to reproduce the effect of the anisotropy associated with cracking (Jiang et al., 2010; Levasseur et al., 2013). Despite the computational performances of these models, which allow their use in practical applications, their consideration of the connectivity and percolation aspects remains phenomenological. This has motivated the development of multi-scale numerical techniques based on the concepts of homogenization of fluid transport equations (Massart and Selvadurai, 2014; Narsilio et al., 2009). However, the microstructural geometries in these efforts remain simplified at this stage relative to the actual microstructures. Numerical homogenization methods based on explicit representations of microstructures have recently been developed for multiphysics in materials, for thermal processes and fluid

transfer couplings with mechanical behavior (Larsson et al., 2010; van den Eijnden et al., 2016). They are based on the definition of a heterogeneous Representative Volume Element (RVE), containing the microstructural description of the phase arrangement; and on the knowledge of their properties. Average theorems are then used to construct scale transitions, linking the average properties of the RVE to the microstructural fields.

1.4 Microstructural complexity

A description of the geometry of the phases and their behavior is required to use the mentionned homogenization approaches. Most of the existing approaches are based on simplifying hypotheses in terms of the microstructural geometry (Massart and Selvadurai, 2014; Larsson et al., 2010), or on the restriction to a given type of microstructural evolution like for instance cracking (Massart and Selvadurai, 2014; van den Eijnden et al., 2016). However, they are among the few to explicitly take into account in the upscaling the aspects related to the connectivity in microstructures. To consider the intricate geometries of complex disordered heterogeneous materials in finite elements simulations, realistic RVEs incorporating the specific features of their microstructures need to be obtained or produced. This can be achieved by exploiting experimental data from modern imaging techniques, such as tomography, to characterize the spatial organization of the various phases and pore space in porous/heterogeneous materials ; or by using generation techniques reproducing available experimental features such as the size distributions of inclusions/voids, their volume fraction or the tortuosity or the connectivity in the pore space (Sonon et al., 2012; Roubin et al., 2015). Considering complex heterogeneous microstructures for mechanical purposes leads to the bottleneck of discretization which might be a challenging task. Different approaches can be selected depending on the degree of the geometrical complexity of the microstructures. Techniques based on extended finite element (XFEM) with level sets enrichment functions (Moës et al., 1999; Moes et al., 2003; Sukumar et al., 2001), embedded finite elements (Simo et al., 1993), or embedded discontinuities (Benkemoun et al., 2010) avoid the constraint associated with complex geometry to have conform meshing. However, they can become difficult to extend, especially for problems incorporating aspects of finite deformations. Conforming mesh generation techniques, besides the fact that the generation processes can be tedious, have the advantage that they allow the use of any commercial software that incorporates the required constitutive laws. However, their implementation on complex microstructures remains a challenge.

1.5 Objectives

Experiments on various rocks have shown a measurable decrease in permeability potentially related to a modification of the pore space as a result of the deformation of the solid skeleton. However, an integrated computational tool allowing the analysis of permeability alterations of rocks induced by a variation of stress states by taking into account explicitly the geometrical complexity is still lacking. This motivates the development of a methodology to achieve this. In general, there is an interest in developing a numerical tool enabling (i) the exploration of the links between the properties of a porous network and the macroscopic transfer properties of the corresponding porous material and to (ii) the incorporation of microstructure evolutions related to variations in stress states.

An adapted answer to this general objective will require the development of an automated tool integrating, combining and interfacing specific technical approaches from different fields. Thus, the present work proposes to address the following necessary ingredients resulting into an image-based modelling methodology:

- a realistic and detailed description of the microstructural morphology (solid skeleton and porous network)
- the implementation of image processing tools allowing the generation of a geometrical model suitable for use in an efficient and cost-effective manner in a discretization process
- an effective and optimized discretization tool for complex microstructures, efficiently taking into account the interfaces between the different phases, in order to conduct finite element simulations including geometrical and material non-linearities in view of multi-scale analysis
- an assessment of advanced discretization methods handling complex microstructural geometries
- interfacing into FEM approaches able to simulate the non-linear mechanical behaviour of rocks
- an efficient image-based evaluation of the macroscopic permeability on the initial microstructure as well as the deformed geometries

The existing approaches available for each of the above-mentioned ingredients are discussed in more detail in the Computational modelling Section, identifying the choices and developments needed to set up a complete image-based simulation procedure. By complete, it is meant on the one hand that it should have the capacity to analyse the alterations in permeability reported experimentally in the

literature by explicitly taking into account the microstructural morphology, and on the other hand that it should be sufficiently flexible to allow testing a series of hypotheses linking the microstructure to permeability. This would pave the way to a better understanding of the microscopic scale physical mechanisms that have a significant impact on the macroscopic transfer properties. To highlight the relevance of process with an illustrative material, μCT scans of a Vosges sandstone were provided by the University of Lille from (Hu et al., 2018). The thesis will focus on the ductile behaviour of highly confined rock generating local plasticity. Therefore, the brittle behaviour of the rock will not be considered in the modelling as well as questions related to strain localization phenomena. It should be mentionned that the long-term goal of the tools developed in the scope of this thesis is to provide ingredients that would contribute to engineering problems in the build-up of closed form stress-permeability relationships or in nested multiscale approaches to be used at the regional scale, such as FE^2 methods (Feyel, 2003).

1.6 Outline

In order to address the objectives presented in the previous section, the present manuscript is structured as follows :

Chapter 2 presents a brief review of the state of the art related to the set of existing computational models able to capture the mechanical behaviour of rocks and the influence that a stress state variation can have on macroscopic transfer properties as well as a justification of the choices of the approaches developed in the next chapters to answer the three research questions derived from the global objective of the thesis.

Chapter 3 is devoted to description of the fundamental notions of geometry representation and numerical tools for geometry processing, and that will be needed for the developments presented in the following chapters.

Chapter 4 presents an integrated approach for the conformal discretization of complex inclusion-based RVE geometries described implicitly, based on experimental techniques or through computational RVE generation methodologies to deal with complex periodic heterogeneous RVEs.

Chapter 5 presents an assessment of computational techniques enabling automated simulations of complex porous rocks microstructures based on 3D imaging techniques. A treated subset of a CT-scanned sandstone sample is used to compare

the results obtained by two advanced discretization frameworks namely the conformal meshing tools presented in Chapter 4 and a non-conforming method that uses a kinematic enrichment by incompatible modes to represent the heterogeneous geometry. Mechanical simulations are conducted on a subset of a scanned sample of a sandstone under triaxial loading conditions for isotropic compressive loading and for loading conditions involving a stress deviator.

Chapter 6 presents an integrated approach to investigate the critical mechanical deformations of the microstructure that generate permeability alterations of a Vosges sandstone when a stress state variation is applied based on the developments presented in Chapters 4 and 5. The method developed addresses an automated computational procedure starting from the processing of representative microstructures obtained by CT-Scan, and combining the use of finite element simulations to describe the mechanical deformation and Lattice-Boltzmann simulations for the evaluation of the changes in permeability under isotropic triaxial loading conditions.

Chapter 7 concludes the work and discusses the perspectives related to the developments presented in the previous three chapters.

2

Computational modelling

Contents

2.1 Introduction

This chapter provides an essential background for computational modelling of rocks in order to justify the modelling choices deployed and detailed in the following chapters. In order to implement an integrated approach able to capture permeability alterations in rocks induced by a stress state variation using an explicit representation

of the microstructural morphology, the modelling approaches are subdivided into the three following points:

- Geometrical modelling approaches of the rock microstructure
- Methods for simulating the mechanical behaviour of rock and their underlying discretizations
- Methods for evaluating the permeability from the microstructures

The literature for each point is clearly far too extensive to provide an exhaustive review of existing approaches.Therefore, for each of the above-mentioned points, only a part of these methods will be briefly presented in order to discuss and to select the most appropriate modelling tools.

2.2 Rock microstructure modelling

Obtaining a representative geometry of a rock microstructure for investigating the permeability alterations as a function of applied stress states can be done either by exploiting data from micro-tomographs (Mees et al., 2003; Cnudde and Boone, 2013) or by virtual reconstruction from fundamental morphological indicators such as porosity, pore connectivity, pores size distribution, specific surface area or tortuosity.

2.2.1 Exploitation of 3D imaging techniques

Advanced imaging techniques such as X-ray microtomography (Mees et al., 2003; Cnudde and Boone, 2013; Desrues et al., 2010), FIB-SEM (Song et al., 2015), TEM (Wiktor et al., 2012), synchrotron (Fusseis et al., 2014) have recently provided high-performance tools for analysing natural rocks with faster, more accurate and easier access to the 3D microstructure without being intrusive to the geomaterial (Robinet et al., 2012; Keller et al., 2013). Such imaging techniques characteristic scales range from the nanometer to the millimeter scale. This enabled more information to be extracted related to the morphology of the microstructure, either for the porous network or for the solid skeleton (Arns et al., 2005b; Andrä et al., 2013a,b; Andrew et al., 2013; Blunt et al., 2013). In fact, focusing on scanning techniques allowing to obtain the microstructural phase arrangement, computed tomography (CT) nowadays allows addressing a variety of scales (micro-tomography or at higher scales) and of geomaterials such as soils (Hashemi et al., 2014; Viggiani et al., 2004; Desrues et al., 2010; Andò et al., 2013), rocks (Chen et al., 2006; Andrä et al., 2013b; Blunt et al., 2013) or mixtures (Li et al., 2016). Such investigations addressed the mechanical behaviour of geomaterials (Chen et al., 2006; Li et al., 2016), their transport properties (White et al., 2006; Blunt et al., 2013); or their coupled

processes (Hashemi et al., 2015). The investigations on the effect of microstructural features on the overall behaviour fostered the emergence of image-based modelling in the multiscale modelling community. Such approaches basically consist of the exploitation of CT scan imaging techniques to obtain geometries for subsequent modelling efforts. A 3D image is reconstructed from absorption properties (for X-ray computed tomography for instance), leading to a voxelized representation of samples. Image processing such as segmentation techniques is then used to allow identifying the phases to which each voxel belongs as illustrated in Figure 2.1(a) for a subset of a Vosges sandstone scan (Hu et al., 2018). Image processing adapted to geomaterials constitutes a full domain of research when complex materials have to be processed, for instance when three phase materials have to be characterized (Hashemi et al., 2014). More details about segmentation processes applied in the scope of this work are provided in Chapter 3.

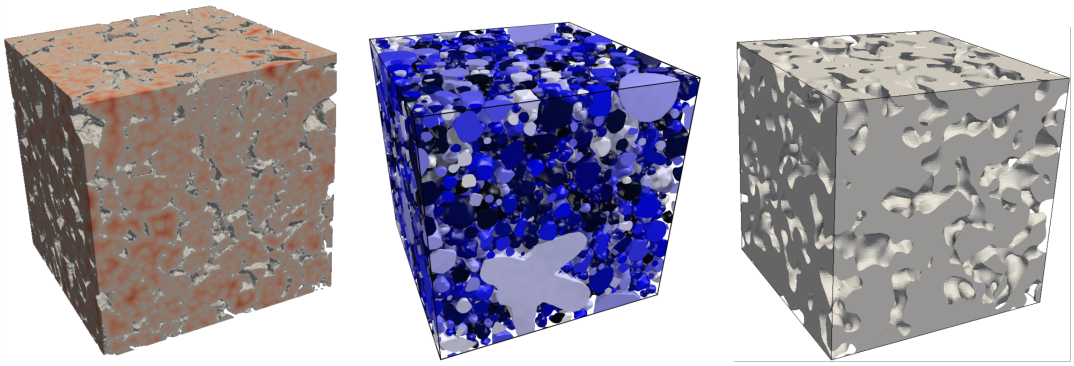

(a) (b) (c)

Figure 2.1: 3D different complex microstructural geometries : (a) Subset of a scan of a Vosges sandstone reproduced from (Hu et al., 2018), Representative Volume Elements (RVEs) virtually generated: (b) RSA controlled by neighboring distance functions - DN-RSA reproduced from (Sonon et al., 2012), (c) Excursion set of correlated random fields with morphological control of the porous medium reproduced from (Roubin et al., 2015)

2.2.2 Virtual geometry generation

Virtual generation approaches are methods that seek to reproduce as closely as possible virtually the real complexity of the morphology of microstructures. In the scope of rock microstructures, the idea is to be able to use physical parameters of the porous medium quantified experimentally, such as porosity, specific surface, grain size distribution or pore size distribution, to generate a geometry as close as possible to the real morphology. The most common approaches in the literature generate inclusion-based morphologies via molecular dynamics principles by using simple geometries such as spheres, ellipsoids or cylinders (Ghossein and Lévesque,

2012; Ghossein and Lévesque, 2013, 2014). Others use sequential addition (Cooper, 1988) for ease of implementation. Inclusions are placed one by one, and the positions of previously added inclusions are not influenced by subsequent ones. It consists of an iterative process that tries adding a new inclusion in the packing at each step. The position of the new inclusion to be added is randomly chosen, potentially leading to inter-penetrations with previously positioned inclusions. A process based on signed distance fields through the use of neighboring maps has significantly improved this addition process by a priori selecting remaining accessible areas. Furthermore, the use of implicit descriptions and their manipulations also greatly increases the morphological complexity of added inclusions leading to the generation of particularly complex geometries of different types such as inclusion-based media (see Figure 2.1(b)), porous media, open/closed foams or composite fibers (Sonon et al., 2012; Sonon and Massart, 2013; Sonon et al., 2015). Others focus on stochastic approaches allowing the generation of random geometries representing the complexity of a porous medium such as the generation and thresholding of correlated Gaussian fields giving them a spatial structure (Adler, 2008) as illustrated in Figure 2.1(c). In this spirit, the work of (Roubin et al., 2015) allowed the possibility to partially control the morphological generation by analytically determining correlations between statistical quantities such as threshold, mean, variance or correlation length of random fields to morphological properties such as volume, surface or Euler characteristic, giving a considerable improvement to morphological modelling.

These tools provide a significant degree of flexibility in terms of the possibility of testing a series of morphological hypotheses based on parametric studies, by isolating one by one the parameters of the model, whereas experimental methods struggle to achieve this. Despite the resulting complexity of the generated geometries, these methods may still suffer from a lack of representativeness of a porous network or the solid skeleton of rocks.

2.2.3 Selection of geometrical descriptions to consider

Once, the morphological paramaters captured by imaging techniques, the virtual reconstruction methods based on random sequential addition (Sonon et al., 2012), excursion sets (Roubin et al., 2015), or even stochastic generation methods (Liang et al., 2000; Keehm, 2004; Andrä et al., 2013a) have the advantage of overcoming the systematic and potentially costly use of imaging equipments such as microtomographs or synchrotrons. They also offer the possibility of extended parametric studies through the generation of a large number of virtual samples with equivalent properties. However, these methods do not provide yet a fully controllable generation of the precise and complex morphological configuration of the porous network of a natural rock that an imaging technique would allow. Geometrical descriptions

obtained by imaging techniques are, among other things, dependent on the type of material scanned and on the resolution of the extracted images. Thus, depending on the quality of the images, their resolution, and the intended application, specific image processing and segmentation techniques are required in order to efficiently identify the different phases of the material. Yet, whenever data are available, it should be preferred as it allows more information to be given to the physical interpretation of the results obtained.

2.3 Mechanical simulations on rocks

From computational viewpoint, the understanding of the mechanical behaviour of the rock microstructure under variation of stress states requires not only taking into account the geometrical complexity of the microstructure in the simulations but also constitutive laws allowing to simulate experimentally identified mechanical phenomena acting in the rock. Rocks are natural geological materials which are by nature potentially heterogeneous, discontinuous, brittle, inelastic, and contain numerous weak zones causing initiation of failures. Two classes of approaches exist for modelling their behavior, i.e. continuous and discontinuous approaches, each addressing specific modelling problems. The continuum-based approaches imply that the domain of interest cannot be separated. The continuity between neighbouring points must be preserved in order to use constitutive laws involving strains that are derivatives of the displacement field. On the other hand, the discontinuous approaches treat elements as separated discrete (potentially deformable) entities interacting through contact or cohesive laws. Generally, in the continuum-based approaches, modelling the deformation of the system is the main purpose, while in discontinuous methods, rigid body motions coming typically with large movements is the main point of interest. The choice of either class of methods is therfore mainly a question of physics to be reproduced (Nikolić et al., 2016).

The most widely used continuum-based approach in the computational mechanics field is the Finite Element Method (FEM) due to its ability of representing complex geometries with material heterogeneities, boundary conditions and non-linear behavior such as elastoplasticity (Zienkiewicz et al., 2005). On the other hand, with the growing need for modelling the discontinuous behavior of rocks, an alternative to continuum modeling, the discrete element method (DEM) has emerged. This method directly simulates the interactions between a large number of particles with parameters such as a particle size distribution and contact parameters such as stiffness and coefficient of friction (Cundall and Strack, 1979; Cundall, 1988; Nikolić et al., 2016) as illustrated in Figure 2.2(c). The method solves the equations of motion and allows de-bonding and detaching of elements, thus

representing real discontinuities. This makes it suitable for problems with large number of fractures which are dominant in failure process. More details on its application to geomechanical problems can be found in (Pande et al., 1990). Recent advances have allowed the use of more complex shapes, with level-set descriptions coupled to the DEM enabling the geometrical descriptions of particles based on μCT scans resulting in a more realistic behaviour of the macroscopic behaviour of sand (Kawamoto et al., 2018).

However, the choice to simulate the deformation of the rock microstructure and evaluate its impact on the modification of the porous network affecting its permeability naturally leads to the selection of a FEM approach especially for cohesive material as the sandstone considered in this work as illustrative material. This therefore implies the need for an efficient discretization framework to take into account the interfaces present in the microstructure discussed in the following.

2.3.1 Discretization methods

The literature on mesh generation is way too extensive to offer an exhaustive review here. The scope of interest within the framework of this work is to be able to generate high quality meshes able to take into account interfaces and heterogeneities of the material in an efficient way and be able to consider material and geometrical non-linearities of the material in simulations. Then, once a description of material interfaces is obtained, two main discretization approaches can be used, namely conforming and non conforming approaches.

Conforming methods

The classical approach to discretize geometries for FEM simulations is to build a mesh with element boundaries conforming with the material interfaces within the microstructure as illustrated in Figure 2.2(a). Very effective meshing methods exist (see (Baker, 2005; Shewchuk, 2012) for an introduction to this topic), the most popular ones being based on Delaunay refinement (Ruppert, 1995; Shewchuk, 2002; Frey and George, 2000) or advancing front methods (Lo, 1991; Schöberl, 1997). The former refers to a criterion leading to a specific connectivity associated with a given set of points that can also be used in the advancing front method. The latter consists in constructing the mesh by progressively adding elements starting from the interfaces, and leading to well controlled elements sizes. For both methods, the initial node placement strategy is critical to obtain a consistent mesh (George, 1997; George and Borouchaki, 1998; Shewchuk, 2012; Frey and George, 2000). However, the task of generating such meshes is repeatedly reported as cumbersome by the community. The reason invoked is twofold. The first one is the fact that some

particular cases with very intricate geometries are difficult to mesh, in particular for very close inclusions or sharp edges. The second one is that most efficient conforming mesh generator softwares like GMSH (Geuzaine and Remacle, 2009), TetGen (Si, 2015), GHS3D (TetMesh-GHS3D, 2010), Triangle or Netgen (Schöberl, 1997) as well as meshing tools in finite elements packages generally are available for explicit geometries but not for implicit descriptions on which the image-based models are based. Explicit formulations describe an interface based on points explicitly located in an Euclidean space. In implicit descriptions, an interface is described as a sub-space satisfying a given set of constraints written in terms of the spatial coordinates. Both these families of geometry descriptions will be shortly outlined in this section (More details are given in Section 3.2). Therefore a preprocessing must be developed to provide suitable triangulated surfaces and allow the generation of usable conforming FE meshes for implicit geometries. In fact, existing meshing softwares are generally time consuming to use and difficult to couple with an image-based geometry (whether derived from scans or from virtual geometry generators), and a finite element solver to yield an automated pipeline suited for wide parametric studies.

Geometries built from image information are difficult to discretize in computational models. As a result, a large proportion of contributions using experimental microstructural information uses the segmented voxel description as a finite element mesh (Boyd and Müller, 2006; Klaas et al., 2013; Potter et al., 2012). This produces structured hex-based meshes resulting in jagged phase boundaries with potential consequences when the non-linear behavior has to be taken into account. The poor representation of the material interfaces geometry by stair-case surfaces requires the use of smoothing methods (Boyd and Müller, 2006; Hormann, 2003; Potter et al., 2012), which leads to inacuracies of fields derived from post-processing of the computations. This is especially true for materially non linear computations in which spurious stress concentrations significantly alter the local behavior within the meshed geometry (Yang et al., 2019; Liu et al., 2017). Efficient meshing methods dealing with multiple materials were developed using octree-based isocontouring in the past few years by (Zhang et al., 2005, 2010) with applications in medical imaging to represent the different tissues (Klaas et al., 2013; Zhang et al., 2005, 2010). However, only few of them addressed finite elements simulations including periodicity, notably for multi-scale analysis purposes, a non trivial issue for complex geometries. Some methods presented in (Drach et al., 2014; Fritzen and Böhlke, 2011; Grail et al., 2013; Potter et al., 2012) are available but the presented results are generally either based on simplified geometries already described explicitly, or based on voxel meshing (Klaas et al., 2013). This triggered researchers to use non conforming discretization methods (Legrain et al., 2011a; Moës et al., 1999).

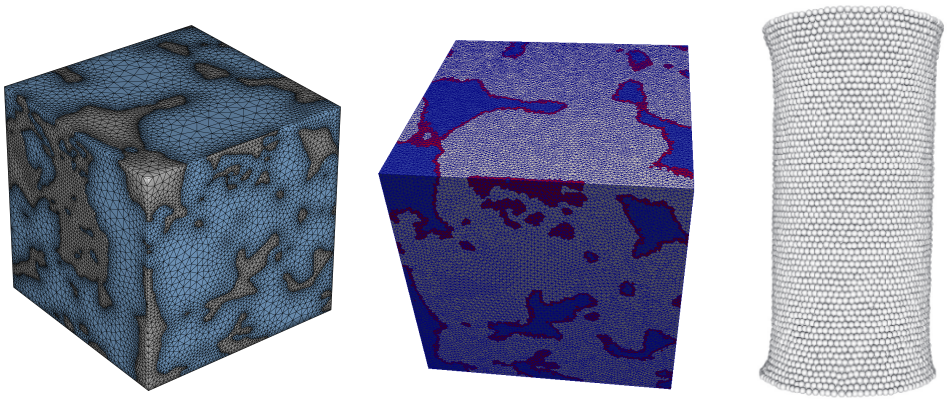

(a) (b) (c)

Figure 2.2: (a) Conforming FEM mesh and (b) non conforming mesh showing in red the elements crossing the interface of a subset of Vosges sandstone used for simulations in Chapter 5, (c) DEM model of sand represented by an assembly of sphere interacting between each other reproduced from (Kawamoto et al., 2018)

Non-conforming methods

Although being very efficient because they allow the use of well defined existing FEM packages, the production of conforming discretizations can be particularly intricate for complex heterogeneous geometries leading, to localized poor quality elements for intricate geometrical configurations. More importantly, it may be difficult to consider evolving morphologies resulting of the development of cracks. An alternative consists of building the approximation from non conforming approaches like the extended finite element (XFEM) or embedded finite elements (EFEM) (Legrain et al., 2011b; Moës et al., 1999; Sukumar et al., 2001; Simo et al., 1993; Benkemoun et al., 2010) as illustrated in Figure 2.2(b). The main difference then lies in the fact that the nodes are positioned independently of the material interfaces between the solid phase and the pore space, thus presenting the advantage of uncoupling the geometrical information from the mesh generation process. This thus avoids the need for relocating these nodes according to the heterogeneous geometry. As a result of the use of a non conforming mesh, many elements are, for a given geometry, cut in two parts by a physical interface between the solid and the pore phase. Each of the two sub-domains of these elements defined by such an interface is included in a material phase, the properties of which are assumed to be known and different from the neighboring one. In order to allow these elements to represent this contrast of properties, it is necessary to enrich their kinematics. The enrichment concept is used to introduce specific local features of the solution such as strong discontinuities in the displacement field and stress singularities linked with growing cracks (Moës et al., 1999; Dolbow et al., 2000, 2001; Béchet et al., 2005; Moës and Belytschko,

2002) or weak discontinuities (gradient discontinuities) in the displacement field linked with material interfaces in heterogeneous microstructures (Sukumar et al., 2001; Moes et al., 2003). An implicit representation of the input geometry is used to achieve this localization of enriched elements. It is also used to ensure the mesh independency using level set functions to identify elements that are cut by an interface, and to build the enrichment functions for those. The specific case of the discretization of image based or tomography based data has been also covered (Lian et al., 2013; Legrain et al., 2011b; Yuan et al., 2014).

2.3.2 Selection of the discretization approach to consider

Non conforming approaches present the advantage to uncouple the geometrical information from the mesh generation process which can be intricate for complex geometries. This allows an easier generation of periodic structured meshes, in particular for multi-scale analysis purposes. However, this is often associated with the need to re-implement complex constitutive models in inhouse non-conforming discretization packages added to the fact that these non-conforming methods are much more difficult to formulate in the case of finite strains. Conversely, in conforming meshes, the geometrical information is used in the discretization process making it potentially more complex and costly. The continued use of classical (commercial) finite element packages motivates the parallel development of procedures to produce classical conforming discretizations for complex geometries. This, in part, is also motivated by the wish to benefit from already implemented complex constitutive models in existing packages and their availability in conjonction with finite strain formulations. Currently, rather few contributions deal with the generation of conforming meshes on complex multi-body geometries. In view of this, it is of interest to develop methods able to easily and robustly mesh conformly arbitrary complex implicit geometries for various applications in the physics of materials. This work presents in Chapter 4 an integrated approach for the conformal discretization of complex heterogeneous RVEs suited for classical finite elements computations. A methodology using an extended version of the truss analogy proposed by Persson-Strang (Persson and Strang, 2004; Persson, 2005) in order to deal with complex (periodic) heterogeneous microstructures. The main advantage of this generator is the use of distance functions describing the microstructural geometry to be discretized for producing a conformal and periodic mesh of these complex geometries with high quality triangle and tetrahedral elements using a dynamic node repositioning. The information obtained through the distance functions (complex geometrical description, distance to neighbours, curvatures,etc) allows the process benefiting from sufficient details to handle particularly complex cases.

2.4 Permeability evaluation

Permeability measures the capacity of a fluid to flow through a porous medium. It is part of the proportionality constant in Darcy's law (see Equation 2.1), the relationship expressing the flow $\boldsymbol{v}$ in terms of the pressure gradient ∇p. This phenomenological law is considered valid at low Reynolds numbers when the flow is laminar without considering gravitational effect. Indeed, under this condition, permeability is independent of fluid properties such as the density and the viscosity; and of the pressure gradient (Eshghinejadfard et al., 2016). Darcy's law reads

$$\boldsymbol{v} = -\frac{\mathbf{K}}{\mu} \cdot \nabla p \tag{2.1}$$

where $\mathbf{K}$ represents the permeability tensor, p the pore fluid pressure, $\boldsymbol{v}$ the velocity vector and μ the dynamic viscosity.

This law is valid regardless of the fluid considered or the saturation conditions. In Equation (2.1), the permeability K is computed as the product between the intrinsic permeability K_{int} and the relative permeability k_{rel} (that depends on the degree of saturation). The intrinsic permeability K_{int} (expressed in m^2) does not depend on the fluid considered and is mainly controlled by the spatial structure and the porous network of the geomaterial, as well as the solid/fluid interaction (Bérend et al., 1995).

In this thesis, only water permeability under saturated conditions will be investigated. Under those conditions, the permeability K is thus similar to the intrinsic permeability K_{int}, and both terms will be used indistinctly in the thesis.

Generally, a pore network consists of a system of large chambers (body pores) interconnected with narrow pores (throat pores). Permeability is mainly controlled by the percolation into pore throats, while the pore chambers contribute essentially to the porosity. Thus, a small variation in the throats can induce large variations in permeability without significantly affecting the porosity (Zheng et al., 2015).

Different strategies exist to compute the permeability of porous media ranging from (semi)-empirical models to numerical models. Only selected strategies are presented in the following sections. For the sake of brevity, computational methods generally compute the permeability using Darcy's law, by subjecting the porous medium to a low enough pressure gradient to ensure a slow incompressible flow assuming small inertial forces between two opposite boundaries. This is done along the 3 main direction in order to reconstruct the permeability tensor K.

2.4.1 (Semi)-empirical models

One class of approaches aims at estimating different parameters such as grain/pore size distributions which are then used in empirical laws derived from experimental measurements. As an example, one can cite the (semi)-empirical laws linking porosity to permeability such as Kozeny-Carman's law (Kozeny, 1927), the power laws linking permeability and porosity to stress sensitivity such as the natural logarithm model (Walsh, 1981), the power law model (Shi and Wang, 1986; Kwon et al., 2004), the exponential function model (Katsube et al., 1991), or the Two-Part Hooke's model (Zheng et al., 2015). However, these methods do not provide indications on how the fluid behaves within the complex porous space.

2.4.2 Traditional Computational Fluid Dynamics

This class of approaches, implementing a direct pore scale modelling, aims at numerically solving the Navier-Stokes equations for low Reynolds number fluid flows in the pore space with traditional computational fluid dynamics (CFD). Among the methods, finite elements (Narsilio et al., 2009; Borujeni et al., 2013; Narváez et al., 2013), finite volumes (Guibert et al., 2015; Petrasch et al., 2008) and finite differences schemes (Mostaghimi et al., 2012; Manwart et al., 2002) can be cited. These traditional mesh-based CFD approaches follow a top-down approach by discretizing the Stokes or Navier–Stokes equations on a (structured or unstructured) mesh (Icardi et al., 2014). Due to its naturally volume conserving behavior, the finite volume method is often preferred as traditional mesh-based CFD methods. These methods are numerically efficient and can simulate fluid flow with very large density and viscosity ratios (Meakin and Tartakovsky, 2009). More details about these methods can be found in (Thijssen, 2007).

2.4.3 Lattice-Boltzmann method

The Lattice-Botzmann method (Sun et al., 2011; Keehm, 2004; Boek and Venturoli, 2010; Ahrenholz et al., 2006; Hyväluoma et al., 2012; Manwart et al., 2002; Narváez et al., 2013), also belonging to the direct pore scale modelling, is a modern approach in Computational Fluid Dynamics often used to solve the incompressible, time-dependent Navier-Stokes equations, numerically in agreement with FEM solutions (Kandhai et al., 1998; Thijssen, 2007). The method finds its origin in a molecular description of a fluid. Based on cellular automata theory, it describes the fluid volume in a complex pore-geometry in terms of the interactions of a massive number of particles following simple local rules, namely, collision and propagation which can be understood as a discretization of the behavior of an ideal gas. The Lattice Boltzmann method solves a discretized Boltzmann equation of fluid-particle

distributions that move and interact on a regular lattice with very few degrees of freedom (Ramstad et al., 2010). A particle distribution for each possible particle velocity vector is defined at each node on a regular lattice. The voxel grid of the 3D image obtained from a micro-CT scan or a virtually generated geometry can directly be used as lattice, thus the method does not require a complex meshing procedure. More in-depth details about the Lattice-Boltzmann method applied to geomaterials can be found in (Sukop and Thorne, 2007).

2.4.4 Pore network modelling

The idea behind pore network modelling (Bultreys et al., 2015, 2016; De Boever et al., 2016; Dong and Blunt, 2009) is to reduce the complexity of the pore network by splitting it into a discrete network. The virtual representation of the continuous pore network is thus reduced to an assembly of pore bodies connected by pore throats (constrictions) of different sizes as illustrated in Figure 2.3. This way of modelling a pore space was seen to better correlate experimental properties of porous media than a bundle of capillary tubes model (Bultreys et al., 2016).

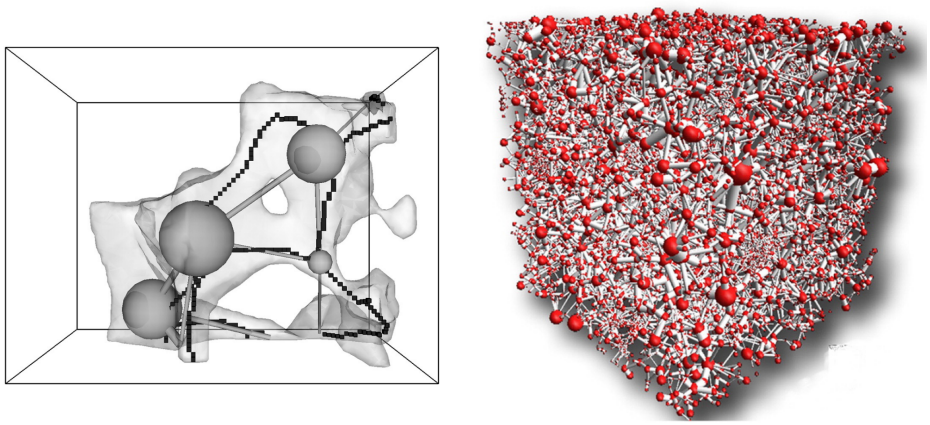

(a) (b)

Figure 2.3: (a) Representation of the simplified pore space with pore bodies as spheres and pore throats as cylinders from Sheppard et al. (2005) while the black lines represents the medial axis (b) Pore network model extracted from a micro-CT scan of a sandstone reproduced from (Bultreys et al., 2015)

2.4.5 Selection of the permeability evaluation approach to consider

According to the objective of the thesis, strategies taking into account the complexity of the flow inside the porous network are preferred. Traditional CFD methods

such as Finite Elements Methods (Borujeni et al., 2013; Narváez et al., 2013) or Finite Volume Methods (Guibert et al., 2015; Petrasch et al., 2008) require mesh refinement levels stronger than the image resolution to ensure mesh convergence and simulation stability. Consequently, obtaining a accurate permeability estimate leads to significant computational costs (Guibert et al., 2015; Succi, 2001), in addition to the complexity of generating a mesh adapted to this type of geometry. Conversely, the Lattice-Boltzmann method is prone to parallelization (McClure et al., 2014). Due to their highly parallelizable potential and the possibility to directly perform simulations on voxellized images, Lattice-Boltzmann simulations are often a preferred choice to simulate the fluid behaviour in geological materials for which a geometry can be obtained via X-Ray microtomography (Martys and Chen, 1996; Cancelliere et al., 1990; Keehm, 2004; Andrä et al., 2013b). In fact, the voxel grid of the 3D image obtained from a micro-CT scan or a virtually generated geometry can directly be used as lattice. Consequently, no complicated meshing procedure is required, making this approach very flexible. Yet, one of the main disadvantages of the method is its computational inefficiency, even with a massively parallel implementation. The runtime scales approximately inversely with the real flow rate (Blunt et al., 2013), which motivated some researchers to use simplifying methods such as pore network modelling (Bultreys et al., 2015; De Boever et al., 2016; Dong and Blunt, 2009). However, the need to implement an integrated and automated methodology tracking the evolution of permeability according to the mechanical deformation of the solid skeleton motivates here the choice of the Lattice-Boltzmann method to simulate flows within the complex microstructures.

2.5 Conclusion and methodology adopted

In this chapter, a brief review of the state of the art was carried out, addressing the different modelling approaches allowing the development of an integrated and automated approach that reproduces numerically the permeability alterations of the rock under stress state variations.

Until now, investigations related to this field have been essentially conducted on the experimental field, mostly without considering the microstructure morphology. The advances in the field of numerical modelling do not yet seem to consider microstructures with complex geometries in the simultaneous framework of deformability of the solid skeleton and its impact on the permeability induced by an evolution of its percolating porous network.

Imaging techniques such as μCT scans are increasingly used to provide an access to the internal morphology of the solid skeleton and the porous network of the geomaterials' microstructure. Their exploitation makes it possible to acquire much

more realistic morphologies than those obtained by virtual generation, even though the subsequent geometries become morphologically increasingly complex. This realistic approach makes it possible to get closer to the behaviour of the considered rock. However, contributions in geomechanics simulating the deformability of complex microstructures via conventional FEM simulations by considering on the one hand non-linear constitutive laws and on the other hand a well-defined interface between the different phases of the material are uncommon. This is mainly due to a lack of efficient conformal mesh generation tools able to handle implicitly defined geometries in a fully automated manner and to produce an optimized mesh of sufficient quality to ensure the convergence of simulations at an affordable computation costs.

Finally, concerning permeability evaluation, given the technical limitations encountered by direct methods such as FEM and FVM when addressing morphologically complex microstructures and the possibility of simulating flows directly on pore space geometries coming from μCT scans using Lattice-Boltmzann simulations, the latter method remains a preferred choice for flow simulations in geological materials.

In order to respond to the need to develop a simulation tool linking the macroscopic permeability to the evolution of the morphology of a porous space, this thesis will be subdivided into three main contributions:

Contribution 1 The development of an automated conformal mesh generator capable of addressing heterogeneous microstructures with implicitly defined complex geometries in order to mesh them in an approach taking into account interfaces in a accurate manner. The process is based on an extension of the truss analogy methodology proposed by Persson-Strang (Persson and Strang, 2004; Persson, 2005). The optimization is aimed at both the quality of the mesh and the number of degrees of freedom obtained by selective refinement in the zones of interest without altering the geometric representation. The integration of periodicity is envisioned for multi-scale simulations if periodic geometries are available. The developments are intended to be general and are equally suited to image-based models as to models obtained virtually. This contribution will be the scope of Chapter 4.

Contribution 2 Is the conformal approach presented in contribution 1 necessarily advantageous when simulating the mechanical behaviour of geometrically complex microstructures compared to a non-conformal approach such as EFEM? An assessment of both methods is necessary in order to highlight the advantages and disadvantages of each method. Tools allowing to segment cleanly and process

the μCT scans to make them suitable for simulation need to be set up upstream. This contribution will be the scope of Chapter 5.

Contribution 3 The development of an integrated and automated model to analyze the effect of changes of permeability under compressive stress states and its application on a model problem in which the connected pore size becomes sufficiently small to affect the fluid flow. This should enable to analyze the effects of the modification of the porous space morphology on the macroscopic properties of permeability. For this purpose, the simulation framework will combine the use of (non linear) mechanical simulations via the finite element method and fluid simulations via the Boltzmann lattice method. The scope of the contribution is limited to the ductile behaviour of the rock justifying the use of elastoplastic laws. The combined use of both approaches requires interfacing by revoxellisation of the deformed mesh obtained using the methodology presented in contribution 1. All these elements constitute the scope of Chapter 6.

The developments discussed in the following chapters are mainly aimed at setting up tools to better understand at the microstructural level the link between deformation and permeability alterations at the macroscopic level. The tools are designed to test fine scale assumptions based on mechanical and geometrical parameters. These include the effect on permeability of parameters such as porosity, pore size distribution, pore connectivity, Young modulus, cohesion, angle of friction, and the consideration of multiple constituents in the solid skeleton. In order to respond to this, the last two contributions will be based on the exploitation of a scan of a Vosges sandstone provided by the University of Lille (Hu et al., 2018).

This chapter is partly based on the "Geometry representation" section of the book chapter entitled "Advanced geometry representations and tools for microstructural and multiscale modelling" currently "In Press" for the 53th issue of Advances in Applied Mechanics (Sonon, Ehab Moustafa Kamel and Massart., 2021, Volume 53)

3

Computational tools for geometry representation

Contents

3.1 Introduction

This thesis makes an extensive use of implicit geometrical descriptions for complex rock microstrucural geometries. Therefore, a brief summary of the numerical methods used in this work for geometrical representations and image processing are provided in the following sections.

3.2 Geometry representation

In order to obtain an optimal representation of complex geometries for subsequent use in numerical simulations, it is important to realize that their representation strongly

impacts the way they can be manipulated. Methods for representing geometries are diverse, and it is crucial to properly select the representation and the corresponding methods depending on the targeted application. This requires a minimal account for practical aspects for a proper selection. Here, the case of boundary geometries is considered. This refers to curves bounding 2D planar domains, or surfaces bounding 3D volume domains. These terms will be referred to as interfaces to denote (sub)domain boundaries in arbitrary space dimensions. Closed, orientable, non branched and non self intersecting interfaces will be considered, except for the interfaces representing the boundaries of subdomains only partially contained in RVEs. Such interfaces are considered closed if periodicity is considered for the RVE. Two geometry descriptions can be considered for manipulations. Explicit descriptions describe an interface based on points explicitly located in an Euclidean space. In implicit descriptions, an interface is described as a sub-space satisfying a given set of constraints written in terms of the spatial coordinates. Both these families of geometry descriptions will be shortly outlined in this section.

3.2.1 Implicit geometries and level sets

The tools used in implicit representations allow using geometries in computational methods for physical modelling up to an arbitrary precision. An implicit description of interfaces can be built on level sets of continuous functions $LS(\mathbf{x}, \ldots)$, in which $\mathbf{x}$ denotes spatial coordinates. Level sets of 3D functions (respectively 2D functions) are surfaces (respectively curves) defined implicitly by expressions of the type

$$LS(\mathbf{x}, \ldots) = k \tag{3.1}$$

where k is an iso-value of the function representing the interface as illustrated in Figure 3.1(a)

Level-set functions used to define geometries can be of different natures and may depend on various parameters. A well-kown example of level set function is the gray-scale density map obtained by X-ray (Computed) Tomography (CT) scans in (many) research fields such as medecine, biology or mechanics. Such a diversity stems from the ability of this formalism to model and handle geometries with arbitrarily complex features. Such functions are defined in terms of spatial coordinates, but their argument can extend to other parameters depending on their use (e.g. time for evolving interface problems, morphological parameters for RVE geometry generation (Ghazi et al., 2019)). A particular choice for this function is the signed distance function. Interfaces represented by level sets are closed except when they cross the boundary of the domain where $LS(\mathbf{x}, \ldots)$ is defined. The smoothness of the geometry representation depends on the continuity

of $LS(\mathbf{x}, \ldots)$, leading to well-defined normals and curvatures (if C^2 continuity is enforced), curvature jumps (if C^1) or interfaces sharp features (if C^0 is considered). Since the domain of definition of $LS(\mathbf{x}, \ldots)$ can be partitioned into two distinct regions in which $LS(\mathbf{x}, \ldots)$ is respectively larger and lower than k, level sets-based geometries are always orientable. By convention in this work, the domain with values lower or equal to k is the included domain. In most examples, the value of k will be set to zero. Useful properties of the geometries can directly be deduced from the implicit description based on the spatial derivatives of the level set functions as the gradient, the second derivatives, the divergence and the Gausssian curvature. A crucial feature of implicit representations is that they allow handling arbitrarily complex geometries (Sethian, 1999; Osher and Fedkiw, 2003).

In a computational context, level set functions have to be evaluated and manipulated using finite sets of values. To this end, they are sampled on regular grids discretizing the domain under investigation, combined with an interpolation to recover continuous functions in order to define level sets. The discrete treatment of level set functions obviously affects the evaluation of its spatial derivatives.

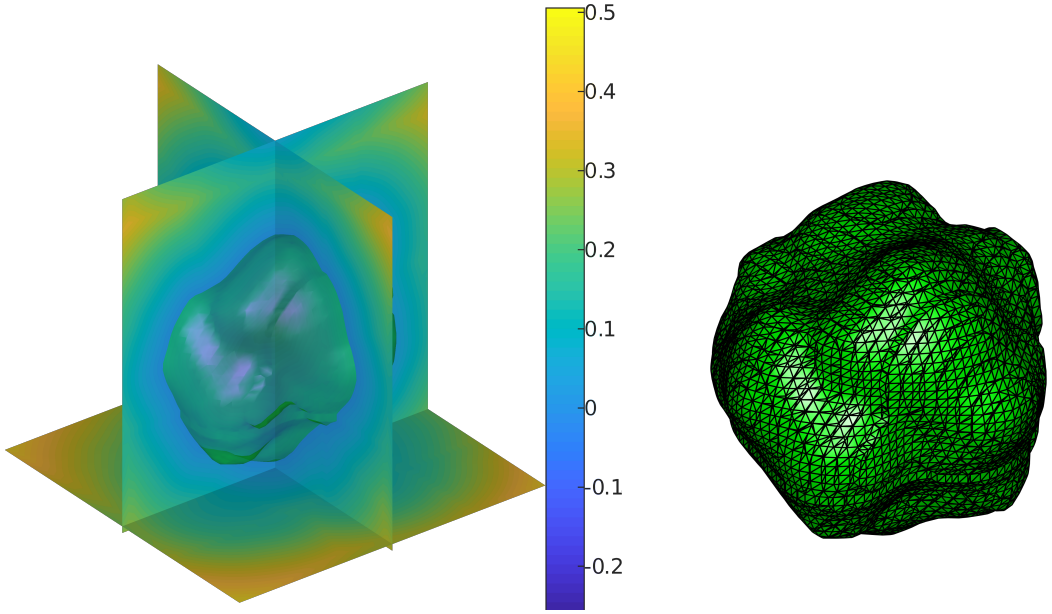

Figure 3.1: 3D illustration of (a) a signed distance field of a grain with three 2D cutted views and (b) its corresponding triangulated surface extracted with a marching cube algorithm

3.2.2 Explicit geometries

The simplest explicit geometry representations for interfaces consist of polygons in 2D and triangulated surfaces in 3D. Such representations will be denoted here as

discrete geometries. Given the objective of this thesis in terms of microstructural geometry representations, only such discrete geometries will be considered among explicit descriptions for their ease of use and their suitability for our needs. They will be used as a complement to implicit descriptions for tasks that are difficult or imprecise to perform with the latter.

In 2D, polygons are used to discretize interfaces, consisting of sequences of points or vertices linked by straight line segments or edges. A polygon is defined by the ordered list of the coordinates of its vertices. Edges are defined automatically as the straight segments linking two consecutive vertices. In 3D, discretized interfaces consist of triangulated surfaces, i.e. assemblies of triangular facets that approximate the geometry. The minimal set of data to define a triangulated surface is the (unordered) list of the coordinates of its vertices together with a connectivity table determining its facets. For triangulated surfaces, the face normals are used to determine the interface orientation. The faces, edges and vertices of polygons and triangulated surfaces are called the primitives of a discretized geometry.

While many CAD and advanced drawing softwares nicely handle complex representations such as NURBSs, simpler tools for scientific data visualization generally offer polygons and triangulated surfaces rendering. If implicit geometries are used for the definition of the interfaces, their discretization into polygons and triangulated surfaces should be addressed. An intensive use of Euclidean distances and signed distance fields will be made in this work. This can be achieved based on implicitly or explicitly described geometries. The latter will be used here when distance fields need to be computed for a matter of convenience. Note however that Euclidean distance computations are not restricted to explicit geometries. Several methods, called distance transforms, can be used to approximate the signed distance field of an implicit geometry through the transformation of its level set function. Here, an exact evaluation is targeted to allow ruling out any potential issue related to small uncontrolled errors.

3.2.3 Conversion between implicit and explicit geometries

If level set functions are used as the primary definition of interfaces, complemented by specific operations applied on discrete geometries, discretized representations of the geometries should be extracted from the associated level set functions. This operation is called contouring.

Contouring

The process of contouring a level set function consists of finding sampling points on a given level set of this function, and using them as control points of a parametric formulation or to build polygons in 2D and triangulated surfaces in 3D. For advanced uses, as Euclidean distance computations, specifically developed tools are available. The most established contouring technique is the marching cube method (marching square in 2D) for grid sampled data and extends to the marching tetrahedron (and triangle in 2D) for mesh based data (Lorensen and Cline, 1987; Cline et al., 1988) as illustrated in Figure 3.1(b). This algorithm generates a straight segment by grid square in 2D and up to four triangular faces by grid cube in 3D. Vertices of those segments and faces are located on grid cell edges and lie exactly on the considered level set according to a linear interpolation scheme of the level set function. The algorithm visits each cell of the grid, searching for cells intersected by the interface, checking how many cell nodes have a negative value of the level set function. Alternatively, dual contouring methods can be used (Ju et al., 2002). Their principle is similar to that of the marching cube, except that they use a vertex inside each intersected cell rather than on each intersected edge. Their main advantage is to produce higher quality triangulations. However, generally, the triangulated surface produced by these methods tends to be of poor quality requiring further processing to make it suitable for use in the finite element meshing process proposed in Chapter 4. Both marching cube and dual contouring methods fail at extracting sharp features on loci where the contoured level set function is only C^0. This can be addressed by adding more information, storing the exact derivatives of the level set. Normals to the level set are then available and sharp features can be detected and reconstructed approximately (Kobbelt et al., 2001; Ju et al., 2002). However, in most applications, level set function derivatives are accessible only approximately on discrete grids and are inaccurately evaluated near sharp features. Exact derivatives can be accessed using derivatives of a high order polynomial basis that interpolates level set functions on the grid, but this obviously destroys the sharp features.

Euclidean distance computations

The tools for geometry representations classically make intensive use of distance fields. The signed distance field of an orientable interface will be denoted here $DS(\mathbf{x})$ and is defined such that $|DS(\mathbf{x})|$ gives for each position $\mathbf{x}$ the distance from $\mathbf{x}$ to the closest point of the interface. By convention in this work, the $sign(DS(\mathbf{x}))$ will be negative inside the domain enclosed by the interface and positive elsewhere, see Figure 3.2. This function is a particular level set function defining the interface by its zero level set. As a result, the conversion of an explicit representation into

an implicit one can be based on the evaluation of the signed distance field of the considered geometry. As a natural level set function of the interface to which it gives the distance, the gradient of a distance field is normal its interface, while its second derivatives reflect the curvature of the interface. Moreover, the norm of the gradient of a signed distance fields is equal to 1 everywhere, which is not true for an arbitrary level set function. This property is reflected by the fact that distance fields are solutions of the Eikonal equation,

$$|\nabla DS(\mathbf{x})| = V(\mathbf{x}) \tag{3.2}$$

With $V(\mathbf{x}) = 1$ everywhere and with the boundary condition $F(\mathbf{x}) = 0$ on the interface.

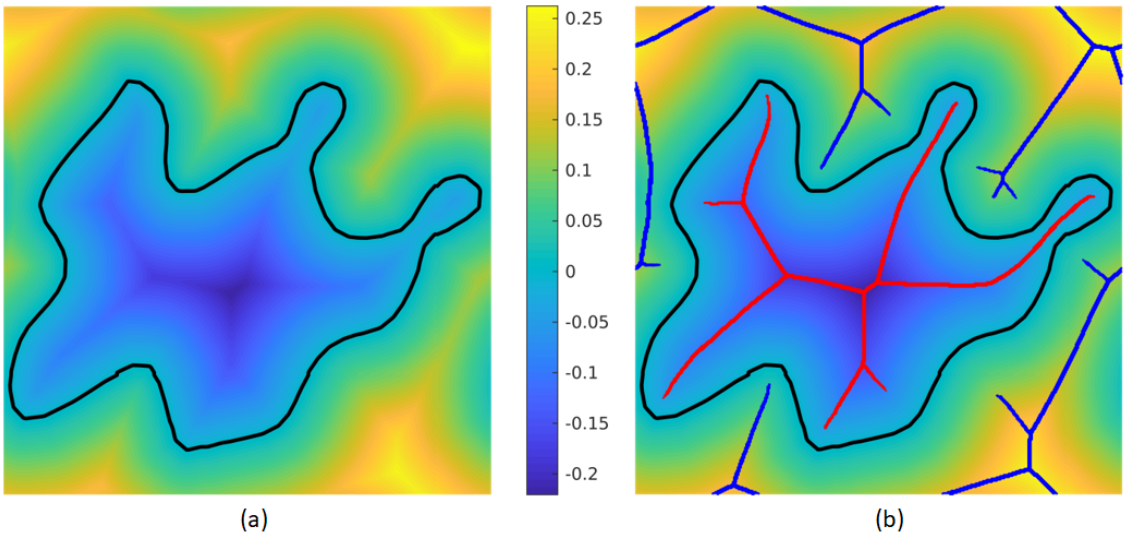

Figure 3.2: (a) Signed distance fields for a 2D arbitrary shaped inclusion (the interface is represented in black), (b) representation for this inclusion of the medial axis (the red curves are the inner medial axis while the blue curves are the outer medial axis representing respectively the local minima and maxima of the signed distance field)

For a proper accuracy matter during the underlying meshing process discussed in Chapter 4, an exact distance field in 3D needs to be computed. The distance from a point to a triangulated surface is the minimum of distances between this point and all the primitives of the geometry. The Euclidean distance from a point $\mathbf{p}$ to a triangle can either be the distance to the plane containing the face, the distance to a line containing one of the edges or the distance to a vertex. One can discriminate between those cases by localizing the projection $\mathbf{p}'$ of the point on the face plane. If $\mathbf{p}'$ lies in the triangle, the distance to the plane must be chosen. If $\mathbf{p}'$ is outside the triangle but projects orthogonally on an edge, the distance from this edge must be chosen. In other cases, the distance from a vertex is the

solution. To compute the distance one can thus first compute the distance to the plane, and localize the projected point $\mathbf{p}'$ in this plane. Then, the distances to edges or vertices are computed in the plane, the total distance being computed as the combination of $|\mathbf{p}' - \mathbf{p}|$ and the in plane distance.

The distance field from a triangulated surface requires the distance to all M triangles and the choice of the minimal value for all N sampled points. A brute force method to compute such a field is obviously inefficient as a fraction $(M-1)/M$ of the computation is useless. Several optimization aspects can be implemented to decrease the associated computation cost. The most efficient one is to construct a Voronoï cell for each primitive. If a complete distance field is required this can be difficult in 3D, but if a maximum distance is set, simple polyhedral characteristics that contain the corresponding Voronoï cells can be defined.

When evaluating a signed distance field, in addition to the Euclidean distance values, one should also classify sampled points as being inside or outside the domain enclosed by the interface and set their sign values accordingly. This requires the interface to be orientable, which is always the case if its primary definition is a level set function. In this case, the attribution of a sign to computed distance values is direct since the sign of the original level set function may be simply copied on the distance field. On the contrary, if the input geometry is a triangulated surface, an additional post processing is required, and the nearest primitive to each point has to be stored. The sign of a distance field from a surface is trivially computed if one is able to evaluate an outward normal to the surface at the nearest primitive from each point.

3.3 Image processing

Subsequent developments presented, notably, in Chapters 5 and 6 use experimental 3D images, require tools to process these images efficiently in order to build a simulable model.

3.3.1 Morphological operators

Mathematical morphology is an image-analysis and processing technique using the algebra of non-linear operators. It is often applied to binary images and for applications where shape of objects and efficiency matter. The most common and basic operators are the erosion and dilation on the basis of which more complex operations are possible such as opening, closing and geodesic reconstruction. The section below explains briefly these operations based on details provided by (Sonka et al., 2007; Glasbey and Horgan, 1995; Ronse, 2008; Soille, 2003).

Dilation - Erosion

Set theory is the mathematical logic on which the morphology is based. It enables modelling any real image using point sets. Binary images can be modelled as a 2D point set. The pixels of interest of the image or the object would have a value equal to 1 (point set X) while the background is represented by pixels values equal to 0. For a given morphological operation, a small point set B, called structuring element, is applied on the points of interest of the image (point set X). The structuring element is usually defined by a relative pixel reference O which is a current point moving across the entire the image. Some typical shapes of structuring elements are shown in Figure 3.3. The results of the morphological operation can be 0 or 1, and is stored in the output image at the current pixel position.

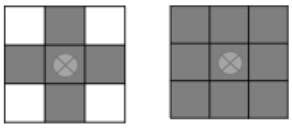

(a) (b)

Figure 3.3: Common shapes of structuring elements : (a) Octahedron (b) Cube

The dilation is one of the basic morphological operation. As shown in Figure 3.4, a binary image is defined in which the set X corresponds to the pixels of interest defined as grey in this example (pixel value equal to 1), while the background is white (pixel value equal to 0). A simple 3x3 set structuring element E is also considered. To apply dilation on the grey pixels set X, the reference point of the structuring element E is placed at any pixel of the object. If any pixels of E comes on the top a grey pixel of X, the output pixel at the current reference point position of E will be grey. The dilation thus consists of an operation of extension of the object set. This is mathematically denoted as follow (where $\mathcal{E}^2$ is the 2 dimensional Euclidian space):

$$X \oplus E = \left\{ p \in \mathcal{E}^2 : p = x + b, x \in X \text{ and } b \in E \right\} \tag{3.3}$$

The erosion is the dual operator of dilation and consists on the other hand to reduce the object set. Considering the same set X and structuring element E, Erosion is applied after placing the reference point of E at any pixels of the image. If all the pixels of E are placed on grey pixels of set X, then the output pixel at the current reference point position of E will be grey. The operation is denoted as follows (where E_p represents the set E translated by any vector p):

$$X \ominus E = \left\{ p \in \mathcal{E}^2 : E_p \subseteq X \right\} \tag{3.4}$$

The Figure 3.4 illustrates both the erosion and dilation processes using the 3x3 octahedric structuring element (see figure 3.3(a)) .

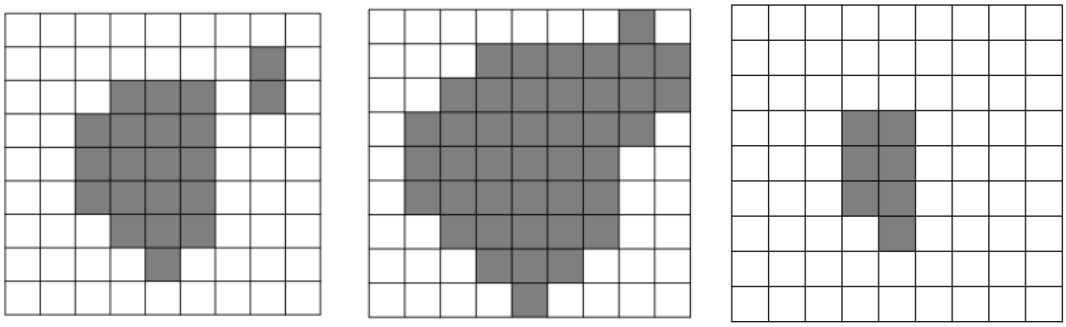

(a) (b) (c)

Figure 3.4: (a) Binary image where the set X is in grey (b) Output image after dilation (c) Output image after erosion

Opening - Closing

Opening and closing are morphological operations resulting of the combination of erosion and dilation. When erosion is followed by a dilation, the result is called opening.

$$X \circ E = (X \ominus E) \oplus E \tag{3.5}$$

On the other hand when dilation is followed by erosion the resulting operation is called closing.

$$X \bullet E = (X \oplus E) \ominus E \tag{3.6}$$

These operations can filter objects of the desired size in order, for example, to simplify a porous network, to isolate a certain pore size or to compute a pore size distribution. Figure 3.5 illustrates the results of both operations using the same set X and structuring element E than previously.

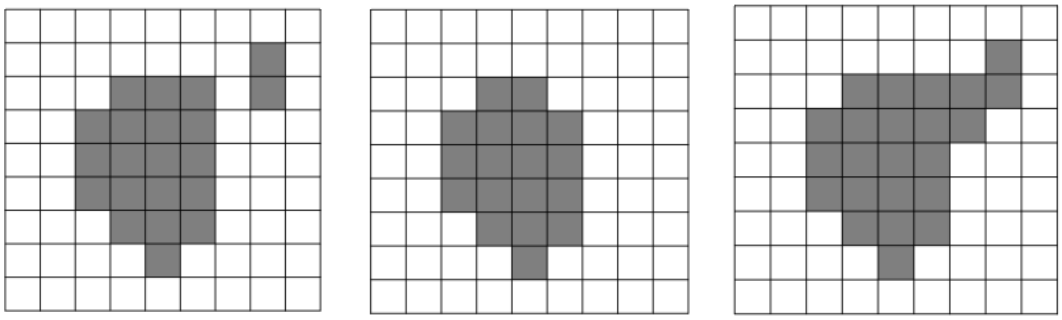

(a) (b) (c)

Figure 3.5: (a) Binary image where the set X is in grey (b) Output image after opening (c) Output image after closing using an octahedron as structuring element

Geodesic reconstruction

Other techniques of interest are the geodesic methods that consist in applying morphological operations in some part of the image. It uses the same concept of structuring element while adding a new set called mask and a subset called markers. The geodesic reconstruction consists in applying consecutive geodesic dilation on the marker inside the mask until stability of the operation is reached. The geodesic dilation is based on the conventional dilation as presented in the previous sections, except that it is applied on a mask, which is a part of the binary image, that limits the dilation process. Here is the mathematical formalism which defines geodesic dilation δ_E^r:

$$\delta_E^r = (\delta_E(\mathbf{J})) \cap \mathbf{Y} \tag{3.7}$$

where J is the marker, Y the mask image and δ_E the basic dilation with structuring element E.

Equation (3.7) allows defining the geodesic reconstruction R_E^r consisting in N iterations of geodesic dilation as follows:

$$R_E^r = \bigcup^{N \geq 0} \left\{ (\delta_E^r)^N \right\} \tag{3.8}$$

Figure 3.6 shows such an operation of geodesic reconstruction. When a specific object is meant to be determined in the binary image, it will be defined as the marker, while all the remaining objects of the domain are considered as a mask. Starting from this, the geodesic dilation occurs for several iterations until the desired object is reconstructed without the unwanted information.

An example of the application of geodesic reconstruction that will be used used in Chapter 5 and 6 is the identification of the different types of pores involved in a porous space in order to isolate them and in particular to remove occluded porosities. As shown in Figure 3.7, an occluded pore is a pore with no connection to the external boundaries, while a connected pore is a pore with at least one connection to an external boundary. An interconnected pore is a pore with an interconnection between two opposite sides of the porous medium. To isolate occluded proposities, the markers are chosen as the boundary pore pixels in 2D (respectively voxels in 3D) of the domain while the other pores pixel in 2D (respectively voxel in 3D) are used as a mask (see Figure 3.7). The basic notion that limits the iteration process of dilation is the geodesic distance. The latter is measured as the shortest distance between two points within a specific set. It defines the number of steps to conduct the geometric reconstruction since it represents the path to follow from the boundary of the domain to the center of it. The connected and interconnected pores are extracted from the binary image by taking respectively the union and the intersection of the geodesic R_E^r reconstruction result from each boundary mask.

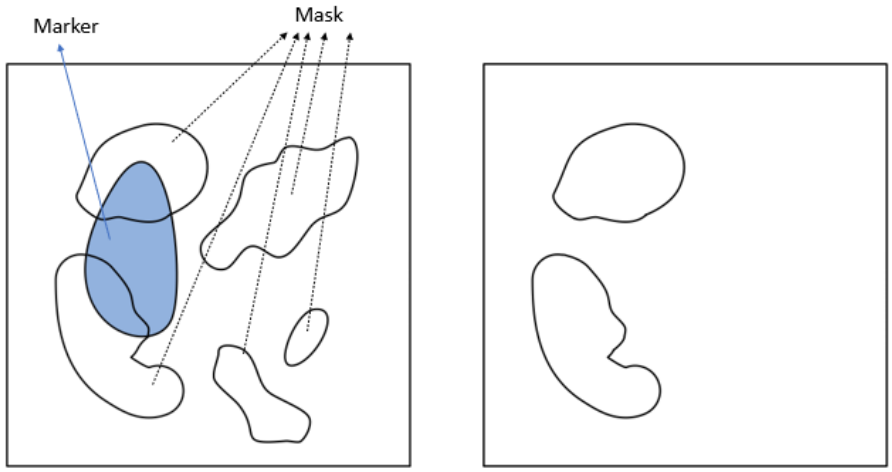

Figure 3.6: Geodesic reconstruction process using marker applied on a mask keeping only the regions of interest

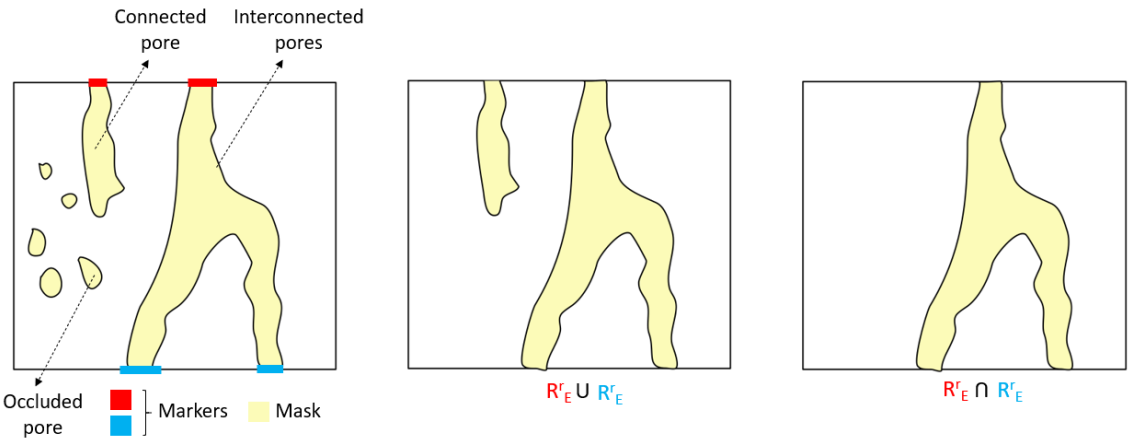

Figure 3.7: Application of geodesic reconstruction on a pore space to discriminate interconnected, connected or occluded pores

3.3.2 Filters

In the developments of the thesis, a median filter and a gaussian filter will be applied respectively to reduce the noise on original images and to smoothen the contours after applying morphological operations on binary images to remove, for example, occluded pores.

Median filter

The median filter is a non-linear filtering method also usually used for smoothing and noise reduction (Sonka et al., 2007). This technique provides an output image where each pixel value is defined by the median value of its original neighborhood. This is achieved by defining a structuring element that crosses the entire input image. For each relative pixel position of the structuring element, the neighborhood

pixel values are sorted in a list and the middle number is selected as the output pixel value. Compared to the Gaussian filter, the median filter performs better at preserving edges.

Gaussian filter

The Gaussian filter aims at smoothing the images on which it is applied by reducing noise. It is a linear filtering image processing technique, consisting in a convolution between the image function and a Gaussian mask or kernel. The latter is mathematically defined as follows :

$$G(x,y) = \frac{1}{\sqrt{2\pi}\sigma} e^{-\left(x^2+y^2\right)/2\sigma^2} \tag{3.9}$$

where x and y are the image co-ordinates and σ the standard deviation of the associated probability distribution (Sonka et al., 2007). Since the kernel has a Gaussian distribution it tends to give more importance to the center pixels of the neighborhood on which it is applied, leaving the most distant pixels with lower influence. Therefore, the standard deviation σ is the only parameter to adjust regarding the amplitude of smoothing desired.

3.3.3 Segmentation

Segmentation is an important step of image processing when it comes to discriminate regions of a given image regarding the correlation of objects of interest contained in the image. Many segmentation methods exist and can be based on regions, edges, or the global knowledge of the image. A review of these techniques can be found in (Sezgin and Sankur, 2004) with a more focused review on advanced segmentation methods adapted for X-ray micro-CT scans of porous materials in particular in (Iassonov et al., 2009). Depending on the image quality, segmentation can often be a bottleneck in the image analysis process, in particular for images with low contrast-to-noise ratio or which contain certain artifacts. This point requires particular consideration as it may generate sensitivity on the results of subsequent simulations which might not be negligible. A common way to perform segmentation is to use thresholding techniques including the Otsu method or the hysteresis thresholding. The latter methods allow discriminating objects from background, especially in gray-levels images. Besides that, the level set method is also used for segmentation purpose. These techniques used in the following Chapters are briefly described in the next sections.

Otsu's method

Finding a convenient threshold to perform a segmentation on a gray-levels given image is not an easy task. The a priori knowledge of some properties of the image such as the image histogram is required for this purpose. The Otsu's method (Otsu, 1979) is a segmentation technique that tries and tests several possible thresholds based on the histogram of the image and finds the optimal threshold that maximizes the inter-class variance and minimize the intra-class variance. In order to exploit this method efficiently, it is important to denoise the image to clearly reveal the potential multimodality of the histogram discriminating background and foreground and thereby facilitate the threshold computation.

Hysteresis thresholding

Hysteresis thresholding also referred to as dual thresholding is an edge-based segmentation technique (Canny, 1987). This approach is used after edge detection, knowing that edges are made of pixels where texture, gray-levels or brightness change abruptly, which allows reducing the sensitivity to residual image noise. In fact, an upper and a lower threshold for the edge magnitude are set. Then, an iteration process is used until the optimal threshold is found. Pixels with a gray value in the first interval are classified belonging to a certain material phase, while pixels in the second interval are only considered to belong to this phase if connected to pixels from the first interval.

Level-set-based segmentation

Level-sets-based methods correspond to a class of deformable models in which the desired shape is obtained by propagating an interface represented by iso-contours in 2D or iso-surfaces in 3D (Caselles et al., 1997; Chan and Vese, 2001; Shi and Karl, 2008; Bernard et al., 2009). It thereby allows obtaining smoothed contours. The basic principle is to define a prior arbitrary initial boundary shapes represented in a form of closed curves, i.e. contours. These contours will evolve iteratively according to shrink/expansion operations related to the constraints of the image and reach their final state when the desired boundaries minimizing a given energy functional are met. Level set approaches move contours implicitly as a particular level of a function (Osher and Fedkiw, 2003).

This chapter is based on the article titled "An integrated approach for the conformal discretization of complex inclusion-based microstructures" which was published in the March 2019 issue of Computational Mechanics (Ehab Moustafa Kamel et al., 2019, Volume 64, pp. 1049–1071)

4

An integrated approach for the conformal discretization of complex inclusion-based microstructures

Abstract

Computational homogenization techniques nowadays are extensively used to gain a better understanding of the links between complex microstructural features in materials and their corresponding (evolving) macroscopic properties. This requires robust tools to discretize complex microstructural geometries and enable simulations. To achieve this, the present contribution presents an integrated approach for the conformal discretization of complex inclusion-based RVE geometries defined implicitly based on experimental techniques or through computational RVE generation methodologies. The conforming mesh generator extends the Persson-Strang truss analogy in order to deal with complex periodic heterogeneous RVEs. Such an approach, based on signed distance fields, carries the advantage that the level set information maintained in previously presented RVE generation methodologies (Sonon et al., 2012) can seamlessly be used in the discretization procedure. This provides a natural link between the RVE geometry generation and the mesh generator to obtain high quality optimized FEM meshes exploitable in regular codes and softwares.

Keywords: Conforming Meshes, Implicit geometries, Heterogeneous materials, Multi-scale analysis, Mesh Optimization, FEM

Contents

4.1 Introduction

4.1.1 Context

Materials with various degrees of randomness at the microscale are met in many different engineering problems related for instance to rocks, bones, masonry, concrete or metallic foams. For instance, heterogeneities strongly affect the permeability of rocks, thereby influencing the transient fluid transport processes in critical geo-environmental applications. In such processes, mechanical loading may alter the material microstructure, thereby impacting the fluid transfer properties (Selvadurai and Głowacki, 2008; Hemes et al., 2015; Song et al., 2015).

Nowadays, multiscale analysis is used for identifying the microstructural processes responsible for a macroscopic effect, or for linking average macroscopic properties to the material properties of constituents (Kouznetsova et al., 2002; Massart and Selvadurai, 2014; Masson et al., 2000; Sanchez-Palencia, 1980; Sun et al.,

2011). Computational homogenization defines a general framework to model the physics of a microstructural representative volume element (RVE) and to derive the macroscopic behavior of an heterogeneous material using scale transition rules (der Sluis et al., 1999; Kouznetsova et al., 2002; Stroeven et al., 2004; Terada et al., 2000). Many computational contributions based on homogenization with periodic boundary conditions use simplified geometric microstructural representations, which can induce strong approximations for the considered materials averaged properties (Kouznetsova et al., 2001, 2002).

To consider complex geometries in finite elements simulations, two main ingredients are required. First, for complex disordered heterogeneous materials, realistic RVEs incorporating the specific features of their microstructures need to be obtained or produced. This can be achieved by exploiting experimental data from modern experimental techniques, such as tomography, to characterize the spatial organization of the various phases and pore space in porous/heterogeneous materials ; or by using generation techniques reproducing available experimental features such as the size distributions of inclusions/voids, their volume fraction or the tortuosity or the connectivity in the pore space.

Secondly, these complex microstructural geometries have to be discretized by advanced techniques, able to conform to the internal material boundaries in an efficient manner. Mesh generation is a critical step in a modelling process, linking the definition of the geometry to the solution of discretized partial differential equations. Unlike for models representing the geometry of industrial parts via CAD tools, a model that aims at representing the physics of heterogeneous materials at the microscale requires incorporating complex geometries that are often defined implicitly. Such real geometries are represented by means of simple grids of points sampling the material density. Over time, idealized (virtually generated) microstructures have become more and more complex as well, with the enhancement of generation techniques and can be represented similarly to data obtained with Computed Tomography scans (Roubin et al., 2015; Sonon et al., 2012). Finally, a seamless transition between the generation and discretization steps is desirable to obtain a fully automated computational approach that does require any intervention of the analyst.

The present contribution focuses on the problematic of mesh generation in the context of multi-scale analysis of heterogeneous materials with complex microstructures.

4.1.2 Related work

The literature on mesh generation is way too extensive to offer an exhaustive review here. Once a description of material interfaces is obtained, two main discretization approaches can be used. Non conforming approaches, like XFEM (Legrain et al., 2011b; Moës et al., 1999; Sukumar et al., 2001) present the advantage to uncouple the geometrical information from the mesh generation process which can be difficult for complex geometries. This allows an easier generation of periodic structured meshes. However, this is often associated with the need to re-implement complex constitutive models in inhouse non-conforming discretization packages. Conversely, in conforming meshes, the geometry information is used in the discretization process. This makes it more complex and costly, but carries the advantage of using standard FE packages with available constitutive laws.

Most efficient conforming mesh generator softwares like GMSH (Geuzaine and Remacle, 2009), TetGen (Si, 2015), GHS3D (TetMesh-GHS3D, 2010), Triangle or Netgen (Schöberl, 1997); as well as meshing tools in finite elements packages generally are available for explicit geometries but not for implicit descriptions. Therefore an interface must be developed to provide suitable triangulated surfaces and allow the generation of usable conforming FE meshes for implicit geometries. In most of softwares, triangulation is achieved by Delaunay triangulation or by front advancing methods. The former refers to a criterion leading to a specific connectivity associated with a given set of points that can also be used in the advancing front method. The latter consists in constructing the mesh by progressively adding elements starting from the interfaces, and leading to well controlled elements sizes. For both methods, the initial node placement strategy is critical to obtain a consistent mesh (George, 1997; George and Borouchaki, 1998; Shewchuk, 2012; Frey and George, 2000).

Realistic geometries are difficult to discretize in computational models. As a result, a large proportion of contributions using experimental microstructural information uses voxel-based discretization methods (Boyd and Müller, 2006; Klaas et al., 2013; Potter et al., 2012). This leads to a poor representation of the material interfaces geometry by stair-case surfaces that requires the use of smoothing methods (Boyd and Müller, 2006; Hormann, 2003; Potter et al., 2012), or to inacuracies of fields derived from post-processing of the computations. This is especially true for materially non linear computations in which spurious stress concentrations significantly alter the local behavior within the RVE.

Efficient meshing methods dealing with multiple materials were developed using octree-based isocontouring in the past few years by (Zhang et al., 2005, 2010) with applications in medical imaging to represent the different tissues (Klaas et al., 2013; Zhang et al., 2005, 2010). However, only few of them addressed finite elements simulations with periodicity, a non trivial issue for complex geometries. Some

methods presented in (Drach et al., 2014; Fritzen and Böhlke, 2011; Grail et al., 2013; Potter et al., 2012) are available but the presented results are generally either based on simplified geometries already described explicitly, or based on voxel meshing (Klaas et al., 2013). This triggered researchers to use non conforming mesh (Legrain et al., 2011a; Moës et al., 1999).

In view of this, it is of interest to develop methods able to easily and robustly mesh arbitrary implicit geometries for various applications in the physics of materials.

4.1.3 Outline

Currently, rather few articles deal with the generation of conforming meshes on complex multi-body geometries. The present contribution proposes an integrated approach for the conformal discretization of complex heterogeneous RVEs suited for classical finite elements computations. It mainly focuses on the discretization step for geometries provided by RVE geometry generators already developed in (Roubin et al., 2015; Sonon et al., 2012, 2015; Sonon and Massart, 2013) for particulate granular media, porous media, foams or woven composites. The meshing methodology extends the truss analogy of Persson-Strang (Persson and Strang, 2004) in order to deal with complex (periodic) heterogeneous microstructures. The main advantage of this generator is the use of distance functions describing the microstructural geometry to be discretized for producing a conformal and periodic mesh of these complex geometries. The information obtained through the distance functions (complex geometrical description, distance to neighbours, curvatures,...) allows the process benefiting from sufficient details to handle particularly complex cases. The surfaces of the inclusions are meshed and optimized independently, simplifying the problem before producing a volume triangulation via 3D constrained Delaunay triangulation after boundary faces meshing. To this end, the mesh optimization using the extended Persson method makes it possible to generate a final result that allows to preserve the conformity and ensure periodicity while producing high-quality elements that open the way for FEM simulation on complex geometries. The approach, based on signed distance fields, carries also the advantage that the level set information used during the generation of the microstructural geometry (Sonon et al., 2012) can seamlessly be used in the discretization procedure, providing a natural link between RVEs generation and the mesh generation.

The present contribution is structured as follows. Section 4.2 provides an overview on implicit geometries and on the specific ingredients required to implicitly define RVEs. The resulting implicit RVE geometry constitutes the input for the new developed mesh generator. Section 4.3 recalls the truss analogy process presented by P.O. Persson (Persson and Strang, 2004) to optimally mesh single body implicit geometries and its adaptation for heterogeneous geometries. It presents how

boundary conformity at material interfaces can be ensured by forcing nodes to move only tangentially to these surfaces, and how an optimization algorithm can be built on the truss analogy based on a repulsive force field, to obtain high quality element shapes. Section 4.4 presents the extended meshing algorithm by first enlighting the difficulties related to the conforming meshing of complex periodic heterogeneous RVEs. Secondly, the meshing and optimization procedures are adressed, focusing on the issues related to the conformal meshing of materials internal boundaries. Section 4.5 illustrates some meshing results of complex RVEs. Finally, Section 4.6 discusses the results and potential further improvements of the procedure. The discretization procedure is available for both 2D and 3D discretizations. Since 3D meshing requires more specific treatments, the present contribution will focus more particularly on the 3D implementation, even though some parts are illustrated for the 2D for the sake of clarity.

4.2 Input Geometries

4.2.1 Implicit Geometries

In a microstructural heterogeneous geometry, interfaces separating phases can be described either explicitly by means of triangular facets in 3D or implicitly. A curve or a surface ϕ can be represented implicitly by means of the level sets of functions $LS(\mathbf{x}, ...)$:

$$\phi \equiv LS(\mathbf{x}, ...) = k \tag{4.1}$$

where $\mathbf{x}$ represents the spatial coordinates and k the iso-value of the function.

In a computational context, level set functions $LS(\mathbf{x}, ...)$ are evaluated on finite regular grids defining the domain of the geometry. The complete definition of continuous functions from those requires the association of an interpolating scheme. Due to the discrete nature of LS evaluations, the actual positions of material interfaces depend on the grid resolution and on the interpolation scheme used to define the LS function, making them not uniquely defined. Typically, the use of a linear interpolation requires the grid resolution to be fine enough with respect to the represented geometry. The same consequences hold for the computation of the spatial derivatives, the approximation of which can be obtained by finite differences.

The level-set function used to define geometries can be of different nature and may depend on various parameters. A well-kown example of level set functions is the gray-scale density map obtained by X-ray (Computed) Tomography (CT) scans in (many) research fields such as medecine, biology, mechanics or environmental applications; highlighting their ability to model and handle geometries with arbitrarily complex

features. $LS(\mathbf{x})$ also gives access to some of their intrinsic properties such as the direction or curvature of the curve (resp. surface). The gradient of $LS(\mathbf{x})$ is indeed related to the normal to the level sets of $LS(\mathbf{x})$ as level sets of a function are perpendicular to its gradient. Moreover, their second derivatives give access to the local curvatures of the interface, as the divergence of the normalized gradient of LS furnishes the local mean curvature (Goldman, 2005; Sethian, 1999).

A particular choice for this function is the signed distance function to ϕ (Osher and Fedkiw, 2006; Sethian, 1999).

$$\phi \equiv DS\left(\mathbf{x}\right) = 0 \; with \; |grad(DS(\mathbf{x}))| = 1 \tag{4.2}$$

Given an interface ϕ dividing the RVE domain Ω in two sub-domains Ω^+ and Ω^-, the signed distance function of ϕ is a function $DS_\phi(\mathbf{x})$ with the value of the signed euclidian distance from $\mathbf{x}$ to ϕ, with by convention a negative value attributed to points included in the domain Ω^-. These functions can be easily computed from any level set function using the Fast Marching Method (Osher and Fedkiw, 2006).

4.2.2 Implicitly defined RVEs

In the context of microstructural RVE geometry generation, a combination of level set functions can be used to represent complex and/or multi-body geometries. In addition to DS functions defining inclusions, in multi-body situation, such as in RVE illustrated in Figure 4.1, *global distance functions* $DN_k(\mathbf{x})$ can be used as global descriptors of the microstructural geometry. The notation DN_k denotes the distance to the k_{th} nearest neighbour. To evaluate properly these functions, a distance function DS_{ϕ_i} is required to each inclusion i. As a consequence, the CTX scan of a heterogeneous geometry, grouping the representation of all inclusions in a single LS function, cannot directly be used to evaluate DN_k functions without specific processes. Conversely, it is possible to reconstruct any DS_{ϕ_i} based on DN_k functions. $DN_1(\mathbf{x})$ represents the first nearest neighbor distance function and can be used strictly as a distance function defining implicitly every inclusion boundary inside the RVE with a single function.

$$DN_1(\mathbf{x}) = \min_i \left[DS_{\phi_i}\left(\mathbf{x}\right)\right] \tag{4.3}$$

Further morphological information about the RVE can be obtained from $DN_2(\mathbf{x})$, the second nearest neighbor. More generally, DN_k functions partly describe the morphology of a set of inclusions. These functions will be used in the present contribution to detect some local configurations requiring a finer mesh.

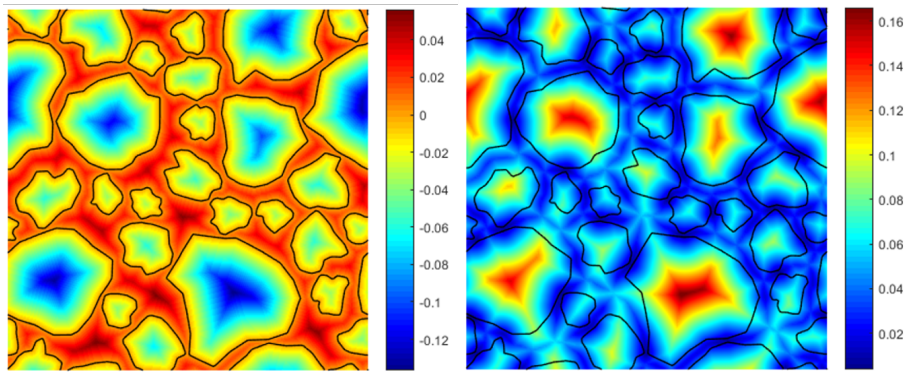

Figure 4.1: *Left* : Global signed distance function $DN_1(\mathbf{x})$ for a given RVE - *Right* : $DN_2(\mathbf{x})$ function, the second nearest neighbor, for the same RVE

4.3 Mesh generation for implicit geometry of homogeneous structures

A meshing tool called *distmesh* was developed in MATLAB by P.O. Persson (Persson, 2005; Persson and Strang, 2004). It starts from a non-conformal initial discretization transformed into a conformal mesh by using an auxiliary structural computation on a truss network in which the bars correspond to the edges of the mesh elements. This auxiliary computation makes use of a repulsive force field moving the nodes located inside the geometry domain towards the interfaces, while being constrained to remain in the domain based on the level set function that describes the implicit geometry. The code developed by P.O. Persson (Persson, 2005; Persson and Strang, 2004) for homogeneous geometries has the aim to remain simple and public. Its central concept is explained now to allow its extension towards periodic heterogeneous complex structures in Section 4.4.

4.3.1 Global discretization process

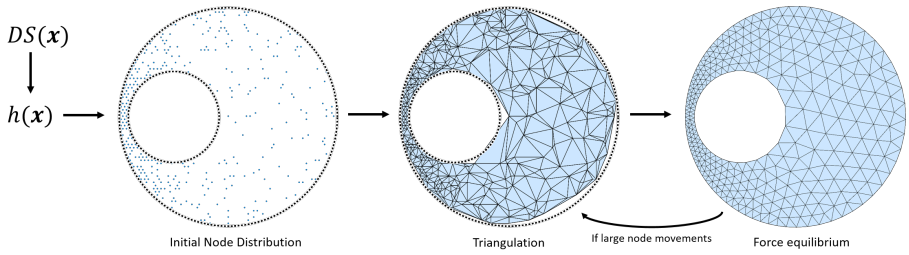

Figure 4.2: Global meshing process of (Persson and Strang, 2004) divided in four main stages taking as input an implicit geometry. (reproduced from (Persson and Strang, 2004))

The meshing procedure for homogeneous structures is essentially divided in four stages as shown in Figure 4.2. The first stage consists in defining a size function $h(\mathbf{x})$ to be used as a space-dependent target for elements sizes, depending on geometrical or physical features. More details on this stage can be found in (Persson, 2005) and further in this paper. The second stage generates an initial node distribution on which a triangulation is subsequently produced. Persson proposed in (Persson and Strang, 2004) an efficient generation procedure for the initial node distribution, based on a probabilistic distribution called rejection method. The last stage optimizes the nodes positions according to a force equilibrium process using an auxiliary truss analogy explained in the next section to achieve optimal element shapes.

In finite element simulations, the error upper bounds depend only on the smallest angle of the mesh elements (Lo, 2015; Persson and Strang, 2004). Accurate numerical results are therefore obtained if 2D triangles tend to be equilateral (Field, 2000; Lo, 2015). A commonly used measure to evaluate the quality of tetrahedra is therefore the ratio based on their largest inscribed and smallest circumscribed spheres. This ratio tends to a value 1/3 for a regular tetrahedron. An element quality factor q is then defined by :

$$q = 3\,\frac{r_{insc}}{r_{circ}} \tag{4.4}$$

Other quantification methods also exist and are addressed in more details in (Field, 2000; Freitag and Ollivier-Gooch, 1997; Gargallo-Peiró et al., 2015; Klingner and Shewchuk, 2008).

4.3.2 Mesh quality optimization

The mesh quality optimization is based on an iterative technique that uses a simple mechanical analogy between the edges of a simplex mesh and the bars of a truss, or equivalently a structure made of springs (Persson and Strang, 2004). In this analogy, the edges of tetrahedral elements and the mesh nodes correspond respectively to the bars and joints of a truss system. By assuming an appropriate force-displacement relationships for the bars, the final nodes position (p) for a set of forces (F) can be found iteratively by solving for static equilibrium according to

$$\mathbf{F}(\mathbf{p}) = \textstyle\sum_i \mathbf{F}_{int,i}(\mathbf{p}) + \mathbf{F}_{ext,i}(\mathbf{p}) = 0 \tag{4.5}$$

where $\mathbf{F}_{int}$ and $\mathbf{F}_{ext}$ are respectively the internal forces present in the bars and the external forces stemming from boundary constraints (supports). These latter are introduced by means of the signed distance function to ensure the conformity of the mesh at an imposed boundary.

The force vector $\mathbf{F}(\mathbf{p})$ depends on the topology of the truss system. In the present case, $\mathbf{F}(\mathbf{p})$ is not continuous accross arbitrary $\mathbf{p}$ variations because Delaunay retriangulations are performed when large node movements occur, thereby inducing some difficulties to solve the system.

A simple approach was therefore proposed by Persson to solve the system, using an artificial time-dependence. The following system of ODEs is considered (in non physical units), with initial condition $\mathbf{p}(0) = \mathbf{p}_0$ being the initial node distribution :

$$\frac{d\mathbf{p}}{dt} = \mathbf{F}(\mathbf{p}), \qquad t \geq 0 \tag{4.6}$$

Indeed, $\mathbf{F}(\mathbf{p}) = 0$ is satisfied if a stationary solution is reached. The latter is found by integrating (4.6) in time using the forward Euler method.

$$\mathbf{p}(t_{n+1}) = \mathbf{p}(t_n) + \Delta t\, \mathbf{F}(\mathbf{p}(t_n)) \tag{4.7}$$

Internal forces $F_{int}(\mathbf{p})$ allow steering the equilibrium state toward a configuration matching the size function $h(\mathbf{x})$. To this end, as illustrated in Figure 4.3, a repulsive force field $f(l, l_0)$ is defined on each bar (i.e. each tetrahedral element edge) depending on its current length l and its prescribed length l_0 interpolated from the size function $h(\mathbf{x})$ according to :

$$f(l, l_0) = \begin{cases} k\,(l_0 - l) & \text{if } l < l_0 \\ 0 & \text{if } l > l_0 \end{cases} \tag{4.8}$$

$$\text{where } k = \frac{l + l_0}{2\,l_0} \approx 1 \tag{4.9}$$

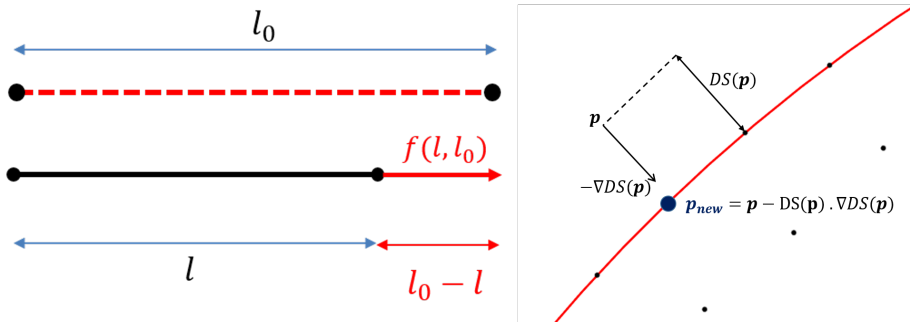

Figure 4.3: *Left :* Repulsive force field in bar smaller than the targeted length l_0 - *Right :* Boundary constraints of nodes moving outside the implicitly defined boundary reproduced from (Persson and Strang, 2004)

This repulsive force field tends to move internal nodes towards the boundaries of the domain. The nodal force vector $F(\mathbf{p})$ of the equivalent truss system thus contains both the internal forces from the bars ($\mathbf{F}_{int}$) ensuing from the $f(l, l_0)$ field

and the reactions at the boundary nodes ($\mathbf{F}_{ext}$). Boundary nodes are themselves prevented to exit the domain based on the level set function that describes the implicit geometry of the interface. The reactions are oriented along the normal to the boundary defined by the gradient of the distance field function to this boundary :

$$F_{ext}(\mathbf{p}(t_n)) = -DS(\mathbf{p}(t_n))\,\nabla DS(\mathbf{p}(t_n)) \tag{4.10}$$

$$\mathbf{p}(t_n) = \mathbf{p}(t_n) + \Delta t\ (F_{ext}(\mathbf{p}(t_n)) + F_{int}(\mathbf{p}(t_n))) \tag{4.11}$$

The solution is considered to be obtained when the value of the maximum node movement is below a certain tolerance.

In case node movements between two iterations are too large, a retriangulation is performed to modify the topology of the mesh and the optimization process is restarted until a stationnary solution is found (see Figure 4.2) producing very high quality meshes. There are essentially four stopping criteria in the optimization process:

- A maximum number of iterations
- A maximum number of retriangulations
- A retriangulation criterion implemented in case of significant node movements (see quantification below), and iterations number is reset to 0 after retriangulation
- A criterion also defined for stopping the optimization process when the configuration of the mesh is sufficiently stable

The criteria are left to the user discretion since they are modifiable parameters in the dashboard of the mesh generator. The quantitative input parameters values for these criteria used in the mesh generations illustrated in the manuscript are as follows: The maximum numbers of iterations and of retriangulations are set at 50 and 10 respectively. These numbers are selected in order to limit the computation time in case of non-convergence of the process. If the system does not converge, the process starts again with a five times smaller time step to make the movement of the nodes slower. If the system still does not converge, it means that the process has not found the optimal position of the nodes based on the size map set upstream, leading to areas where the elements are expected to be of poor quality. In this case, the process restarts from the beginning by modifying the initial parameters to reproduce a new more refined size map to better reflect the geometrical complexity. A retriangulation is applied when the most stressed bar undergoes a contraction or extension larger than 10% of its length. The optimization process itself is stopped

when the most stressed bar of the equivalent truss undergoes a contraction or extension of less than 0.1% of its length. Note that these are parameter values that the user may want to modify. They will essentially affect the computation time and the time for the process to converge to get high quality elements according to the defined stopping criterion.

4.4 Extension to complex heterogeneous RVEs mesh generation

The Persson-Strang truss analogy for mesh optimization presented in the previous section is robust and effective for small and medium sized meshes based on single body geometries. However, many challenges appear in 3D when meshes have to be produced for complex heterogeneous RVEs. Among them, the presence of internal boundaries separating the inclusions from the matrix to produce conforming meshes makes the problem more intricate. Furthermore, multi-scale analysis often requires the capability to produce periodic meshes, which in 3D configurations requires specific implementations.

In the following sections, an adapted approach extending the Persson-Strang truss analogy is outlined in order to deal with complex periodic heterogeneous microstructures based on signed distance fields.

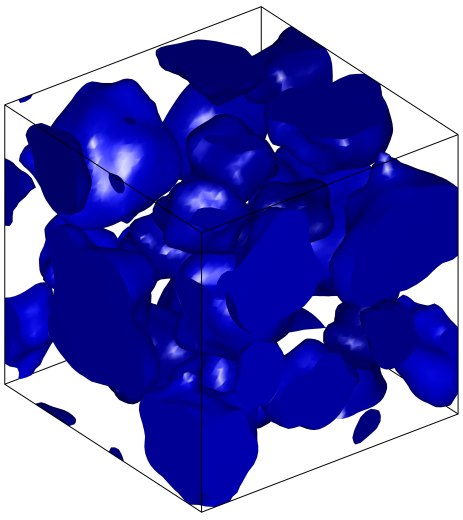

Figure 4.4: Reference RVE generated by the RVE generation procedure defined in (Sonon et al., 2012) to illustrate the meshing process of complex heterogeneous microstructures

4.4.1 Global meshing strategy

The mesh generation process for the RVE is subdivided in five steps as follows :

1. Definition of a size function $h(\mathbf{x})$ based on specific/particular geometrical features
2. Generation of an initial periodic node distribution based on an octree decomposition
3. Optimized surface meshing of the internal material interfaces, based on an initial triangulation obtained by contouring algorithms to enforce conformity
4. Optimized external boundaries meshing for periodicity
5. Optimized volume meshing of inclusions and matrix based on a Constrained Delaunay Tetrahedralization (CDT) starting from the surface meshes (produced in 3 and 4)

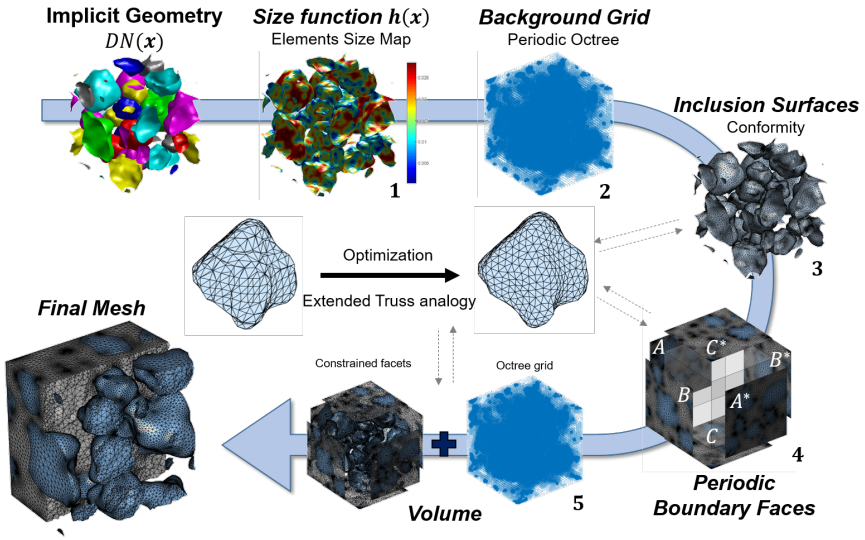

Figure 4.5: Global meshing strategy based on reference RVE

The procedure starts similarly to the original Person-Strang methodology, i.e. defining a size function $h(\mathbf{x})$ to control the elements sizes. The amount of nodes is increased where complex shapes of inclusions require taking into account local features such as high curvatures, small gaps or wide size distributions of inclusions. The size function is therefore used in the optimization process and the initial distribution of nodes detailed in sections 4.4.2 and 4.4.3, in order to refine the discretization only at the positions of interest.

A key difficulty with Delaunay-based mesh generators remains the enforcement of mesh conformity at material interfaces. This issue is even more complex in 3D, and still a challenging problem both in theory and practice (Si and Gärtner, 2010). When applying the original Persson-Strang methodology to homogeneous domains, no specific treatment for internal boundaries is required. Therefore,

the triangulation of an initial distribution of nodes and its optimization is only performed once. For heterogeneous structures, the conformity is more difficult to ensure due to the presence of nodes on both sides of the material interfaces before triangulation. Furthermore, it is not trivial to ensure periodicity of a 3D triangulation, even when starting from a periodic nodes configuration. A solution to ensure conformity and periodicity is to first mesh the inclusion interfaces and the RVE boundaries to avoid the presence of crossing tetrahedra. Once those surfaces are meshed, Boundary-conforming tetrahedral meshes are generated with a constrained Delaunay triangulation to preserve the inclusions surfaces. To do that, the Delaunay criterion is not strictly applied anymore in the neighbourhood of the constrained facets (Shewchuk, 2002; Si, 2010). This motivates the decomposition of the procedure into several steps. Each meshing stage (surface meshing, external boundary faces meshing and 3D bulk meshing) involves two steps, namely the triangulation and the optimization process using an extended version of the principle of the Persson-Strang truss analogy.

The inclusion surfaces are first meshed set by set after extracting their zero-isosurface from the $LS(\mathbf{x})$ defining them by contouring algorithms. Then, to ensure periodicity, the RVE external boundary faces are considered as 2D meshes in which the traces of inclusions cutting the RVE boundary are discretized first, making the RVE boundary meshing process easier. The periodic enclosing surface mesh is formed by extracting, meshing, copying, translating and merging the three non-opposite faces.

Then, the entire volume is meshed by providing the optimized boundary faces and internal surface meshes as input for the Constrained Delaunay Tetrahedralization (CDT) module of the well-known meshing software TetGen (Si, 2015), thereby ensuring periodicity and internal conformity of the final mesh.

Finally, a post-processing step provides mesh corrections if self-intersections of triangles in the interfaces still appear in the obtained mesh. It also attributes the elements to the inclusion and the matrix phase, and records information about external boundary nodes in order to ease the definition of finite elements boundary conditions.

The following subsections provide detailed information on how to implement each step of the procedure.

4.4.2 Size Function $h(\mathbf{x})$

Dealing with 3D complex geometries as sketched in Figure 4.4 with a uniform mesh size may induce a large numbers of elements, as stress gradient at sharp features and small gaps between inclusions then prescribe the overall mesh size. A size function defining spatially variable element sizes therefore becomes critical.

To take into account local geometrical or physical features in the meshing procedure, the narrowness between inclusions (*nar*), the curvature of interfaces (*curv*) and the initial interface size (*iis*) will be used in order to prescribe mesh refinements where needed, see Figure 4.6 and Figure 4.7. To this end, the size function $h(\mathbf{x})$ is constructed from the neighboring distance functions DN_k defined in Section 4.2 and readily available if the heterogeneous microstructure was computationally generated.

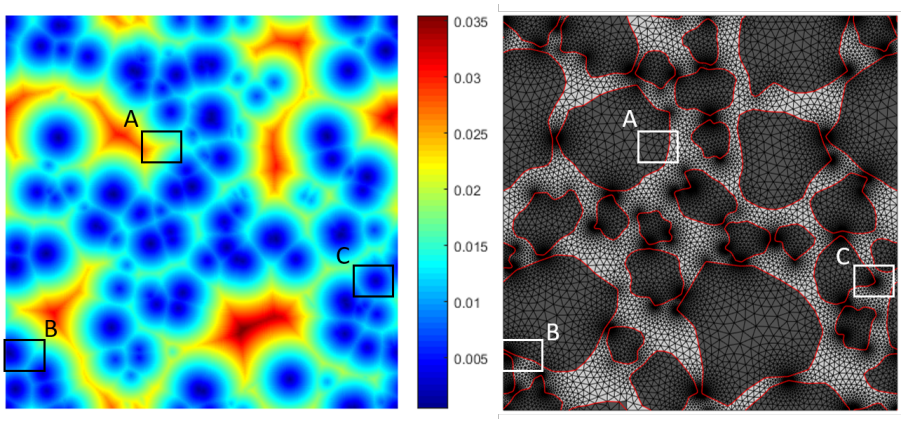

Figure 4.6: *Left:* Size function $h(\mathbf{x})$ - *Right:* Corresponding optimized 2D mesh taking into account local features (initial interface size, narrownes, curvature) from $h(\mathbf{x})$

The initial interface size (iis) is taken as the maximum element size allowed on the interfaces to have a sufficiently accurate representation of the geometry of the RVE. This value is taken constant on all the interfaces.

$$h_{iis}(\mathbf{x}) = iis \tag{4.12}$$

The narrowness representing the proximity between two interfaces, is computed by taking into account the distance to the closest second neighboring inclusion $DN_2(\mathbf{x})$ from interfaces. In an inclusion-based RVE, $DN_2(\mathbf{x})$ is always positive since each inclusion is completely separated from the others in the RVE. To better control the element size refinement accross the gap between two inclusions, a parameter nb_{EL} is defined as the number of elements from the considered source point to its respective second closest neighboring inclusion. A corresponding element size can be derived according to

$$h_{nar}(\mathbf{x}) = \frac{DN_2(\mathbf{x})}{nb_{EL}} \tag{4.13}$$

In 3D, the maximum principal curvature is used in order to evaluate the smallest radius of curvature of an interface (Persson, 2005). Methods based on triangulated surfaces are available to evaluate curvatures as presented in (Rusinkiewicz, 2004). However, for implicit geometries, the curvature can be directly obtained by finite

differences from the implicit function. Computing the curvature from the first neighboring distance of the whole RVE (global signed distance function) DN_1 is subject to the same limitations as extracting properly the inclusion surfaces at once. For accuracy reasons, the curvature computation is performed for each inclusion separately. In practice, the maximum principal curvature κ_1 is computed from the mean and gaussian curvatures K_M and K_G. K_M is computed according to relationship

$$K_M = -\nabla \cdot \nabla DN_1 \tag{4.14}$$

while the gaussian curvature is obtained by

$$K_G = \nabla DN_1 * H^* (DN_1) * \nabla DN_1^T \tag{4.15}$$

where H^* is the adjoint of the hessian matrix. This allows computing principal curvatures

$$\kappa_{1,2} = K_M \pm \sqrt{K_M^2 - K_G} \tag{4.16}$$

A curvature controlled element size $h_{curv}(\mathbf{x})$ is then obtained by equation (4.17) where κ is the maximum principal curvatures in absolute value while α is parameter allowing to adjust the sensitivity to the curvature in the size function.

$$h_{curv}(\mathbf{x}) = \frac{\alpha}{|\kappa(\mathbf{x})|} \tag{4.17}$$

To avoid significant element size variations over short distances in the definition of the size function that would lead to poor quality elements, the size function $h(\mathbf{x})$ is required to evolve smoothly by using a gradient limiting size variation (Persson, 2005):

$$\|\nabla h(\mathbf{x})\| = g \tag{4.18}$$

To meet this constraint, minimum initial imposed size values h_0 depending on the three geometrical parameters *iis*, *nar* and *curv* are first computed on source points $\mathbf{x}_{sp}$ by interpolation from $DN_1(\mathbf{x})$ and $DN_2(\mathbf{x})$.

$$h_0(\mathbf{x}_{sp}) = min(\{h_{iis}(\mathbf{x}_{sp}), h_{nar}(\mathbf{x}_{sp}), h_{curv}(\mathbf{x}_{sp})\}) \tag{4.19}$$

For accuracy, the source points $\mathbf{x}_{sp}$ are selected as nodes located on the interfaces that are extracted using a contouring algorithm at the precision of the initial regular grid $\mathbf{x}$.

The values are then propagated smoothly over the spatial coordinates $\mathbf{x}$. In the case of a bounded convex domain (Persson, 2005), the following equation can be used :

$$h(\mathbf{x}) = \min_{sp}(h_0(\mathbf{x}_{sp}) + g\,|\mathbf{x} - \mathbf{x}_{sp}|) \tag{4.20}$$

where $h(\mathbf{x})$ is the size function evaluated on the regular grid and g is the gradient limiting factor introduced in equation (4.18).

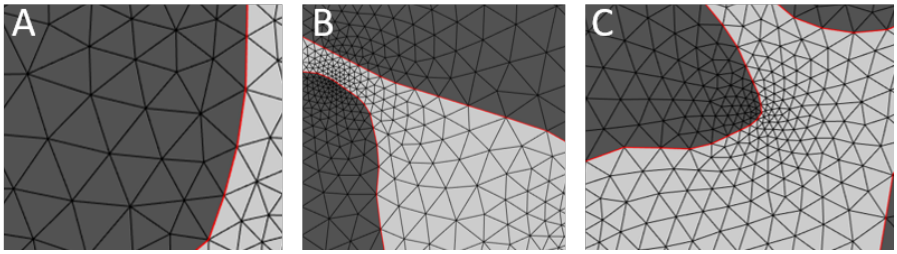

Figure 4.7: Zoom on frames of Figure 4.6 : Initial interface size (A), Narrowness (B), Curvature (C)

Figure 4.8 illustrates the resulting size function for the inclusion based microstructure depicted in Figure 4.4 interpolated on the inclusions surfaces from the regular grid.

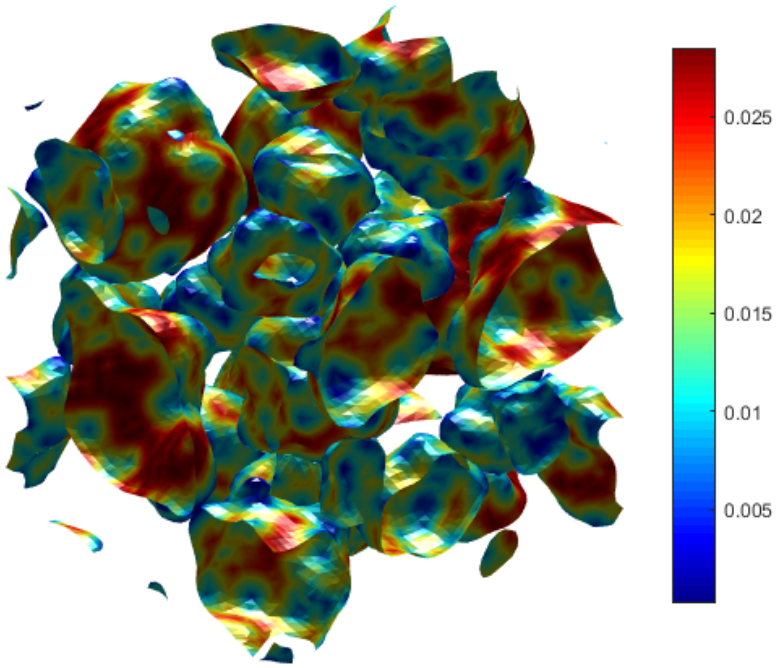

Figure 4.8: Interpolated size function $h(\mathbf{x})$ on interfaces

Following the same methodology, extending $h(\mathbf{x})$ to account for other geometrical or physical features can be achieved straightforwardly if required.

4.4.3 Initial nodes distribution

Several methods are available to distribute nodes inside a domain based on regularly spaced grids or on probabilistic distributions (Lo, 2015). Rejection methods (Persson, 2005) based on probabilistic node distributions as initially proposed by Persson (Persson and Strang, 2004) may be interesting in view of their efficiency. However, for periodic inclusion-based RVEs enclosed in a cube (or a parallellepiped), more adapted node distributions can be obtained based on octrees linked to the size function. A periodic octree (Legrain et al., 2011a; Macri and De, 2008; Paiva et al., 2006) distribution is therefore used here. The distribution starts from the 8 RVE corners and is refined recursively based on the size function $h(\mathbf{x})$ previously computed. At each recursion, the size function is interpolated at the cube mid-edges and at its geometrical center. If one of the interpolated values is smaller than the cube edges, the cube is divided into eight identical cubes. The new vertices are added to the node distribution and the process is repeated on the eight new smaller cubes. The process continues until all cubes have a satisfactory size with respect to $h(\mathbf{x})$.

This defines in a simple way a nodes distribution corresponding at best to the mesh size function $h(\mathbf{x})$, i.e. providing a higher nodes density near the interfaces and larger elements further from it, as illustrated for a 2D configuration in Figure 4.9. In fact, Persson,s method is effective when the auxiliary truss bars are close to their equilibrium positions, i.e. the length of the initial bars from the Delaunay triangulation undergoing extension or contraction are close to the length defined by the size function. Otherwise, the resolution of the truss by the forward Euler method may introduce strong oscillations if the initial length of the bars is far from the desired length, and therefore it may not converge.

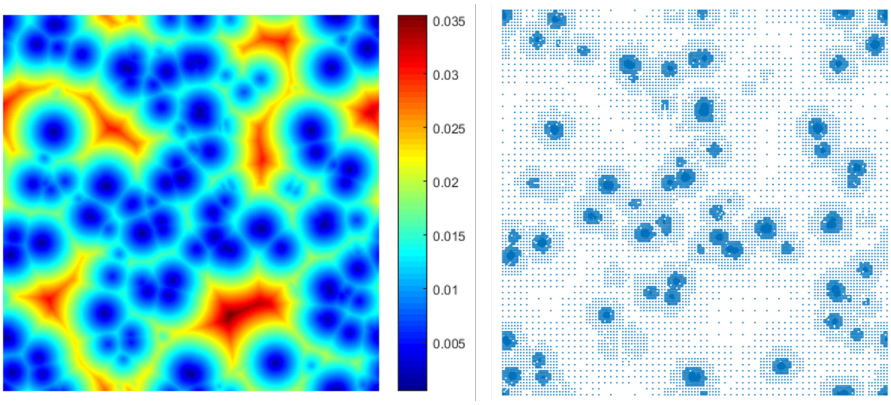

Figure 4.9: *Left:* 2D size function $h(\mathbf{x})$ - *Right:* Corresponding 2D quadtree node distribution

Generally, a consequence is then the poor quality of elements generated near the interfaces by a constrained Delaunay triangulation. However, thanks to the

distance function, it is possible first to remove nodes too close to the interfaces. After nodes are moved by the optimization procedure driven by the truss analogy (see Section 4.4.7), well shaped elements are obtained.

Using Periodic Octree distributions has some additional practical advantages making it possible to meet three objectives in the proposed generator:

- Obtaining an initial distribution of nodes between which the interdistance is close to that requested in the size function,
- Obtaining an initial triangulation with good elements quality due to the strategic positioning of nodes to feed the optimization procedure with a proper 'initial guess',
- Enforcing the same spatial node distribution on opposite external boundaries to allow periodic meshes generation

These objectives allow minimizing the number of operations required in the optimization process since the nodes are not very far from their equilibrium positions.

4.4.4 Inclusion boundaries meshing

The main meshing steps for the interfaces are illustrated in Figure 4.10 for the microstructure presented in Figure 4.4. In order to satisfy the size parameters given in input, the level-set grid $LS(\mathbf{x})$ that geometrically describes the RVE is reinterpolated on an initial 3D regular grid of points according to the iis parameter (initial interface size). This reinterpolation allows an adapted (to iis) individual or set extraction of the zero isosurfaces defining the inclusions boundaries by the Marching Cubes algorithm (Lorensen and Cline, 1987). Then, these surfaces are selectively refined according to narrowness and curvatures. This allows conforming the surfaces mesh size to the size map generated upstream.

In spite of the simplicity, robustness and efficiency of this procedure, the resulting surface triangulation is of poor quality leading to poor 3D elements (almost-flat tetrahedra) (Shewchuk, 2012), as illustrated in Figure 4.10.2. This initial surface triangulation is therefore optimized in surface using the truss analogy and used subsequently as input for the 3D constrained Delaunay triangulation.

Another issue linked to the use of the marching cube algorithm for the construction of interfaces is the existence of ambiguous cases when the background regular grid is not refined enough. For inclusion-based RVEs with small gaps between inclusions, critical issues arise quickly, as very close inclusions tend to merge spuriously. The refinement of the background regular grid is possible but is a costly solution as it induces a cubically growing memory consumption for 3D configurations, and does not strongly solve the problem.

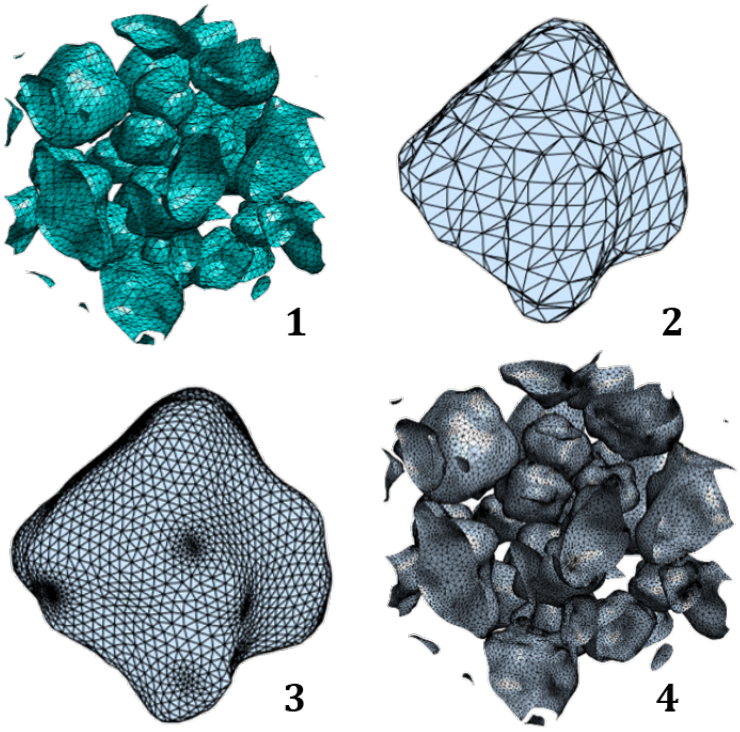

Figure 4.10: Inclusions surface meshing main steps : (1) Isosurface extraction via Marching Cubes algorithm; (2) Boundary constraints; (3) Optimization via truss analogy, edge flipping, local mesh refinement; (4) Adding to the set of meshed inclusions

A solution is therefore to perform an individual extraction of each of the inclusion surfaces. This is possible if independent signed distance functions are available or can be built for each inclusion. This allows decreasing memory needs and computation time by using coarser grids for extraction and increase cache efficiency as memory chunks that are accessed are smaller.

The surface mesh optimization is analogous to a 2D problem constrained to the interfaces of inclusions. During the optimization process, the extracted triangulation is subjected to normal constraints making the movement possible only along the surfaces (see Figure 4.3). This is achieved using the distance function from which the interface is extracted. Based on the distance to the surface and computing its normal at each iteration, nodes moving away from the surface are pushed back to the surface, thereby allowing only tangential movements by means of Equation 4.10.

The low quality initial triangulation obtained from the marching cube extraction involves a significant variation in size of the elements edges. The triangulated surface mesh of inclusions boundaries (material interfaces) is therefore further simultaneously improved by three different processes consisting of local mesh refinement, local connectivity update and node relocation by truss analogy.

Local mesh refinement is applied according to the size function $h(\mathbf{x})$. Wherever necessary with respect to $h(\mathbf{x})$, triangles are divided into four triangles keeping

the same aspect ratio as shown in Figure 4.11 to avoid increasing the distortion of newly created triangles. Particular attention is paid to the edges intersecting the RVE boundaries to keep a periodic mesh upon refinement.

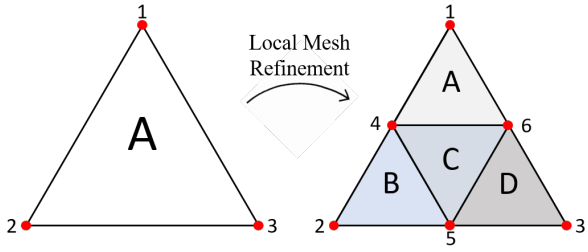

Figure 4.11: Local mesh refinement : Regular division of a triangular element as a function of $h(\mathbf{x})$

Starting with bars of very different lengths from the ones desired according to the size function $h(\mathbf{x})$ in the auxiliary truss computation leads to large displacements. Therefore, it is possible to improve the topology by modifying the local connectivity via edge flipping. Considering two adjacent triangles, the edge connectivity is flipped in order to increase their quality and leave the rest of the triangulation unaffected (see Figure 4.12). It speeds up the optimization process significantly as it acts locally. External RVE boundary edges are however not affected to preserve periodicity.

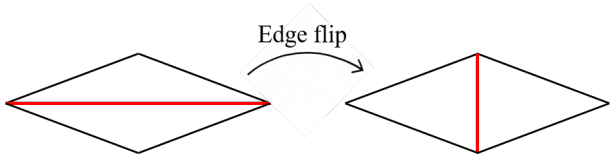

Figure 4.12: Local triangular element update : Edge Flip

Node relocation allows displacing nodes by imposing internal forces in the bars based on the truss analogy (Persson and Strang, 2004). This method works very well when the initial length of bars is close to the length targeted by the size function. If the initial triangulation starts far from the truss equilibrium state and involves topology changes, movement instabilities can occur leading to self-intersections. When the implicit geometry of an inclusion described by a distance field is extracted into an explicit one using the Marching Cube algorithm to produce a facetted description of the surface of an inclusion, the initial mesh contains not only elements of poor quality (see Figure 4.13(a)), but also highly variable element sizes that can induce significant movement during the optimization process. It is clear that the artificial time parameter used in the resolution of the truss by the forward Euler method is important and should not be too high to avoid oscillations. On the other hand, it is possible to find areas where the elements are much too large. This can

be attenuated by selective refinement illustrated in Figure 4.13(b). They can also be too small according to the desired size. To avoid these self-intersections, or at least to reduce them drastically, a coefficient α is introduced to control the weight of the desired length (l_0) in the internal force field.

$$f(l, l_0) = k\ (\alpha\, l_0 - l) \tag{4.21}$$

This force field acts similarly to a Laplacian smoothing function (Field, 1988) if $\alpha\, l_0$ is taken close to zero in the first iterations unlike in (Persson and Strang, 2004) where a purely repulsive force field is used. It induces mainly attractive forces in the bars according to (4.21). The forces applied in the bars are proportional to their own current length, inducing tension in small bars and compression in longer bars in such a way that displacement variations are smoothen out. Combined with the flip edge, this will induce contraction in the long bars and extension in the small bars, thus reducing the potential risks of self-intersection while increasing the quality of the elements. Even if not entirely robust, the progressive increase of the targeted length result in an increase of the initial element shape quality without inducing self-intersections.

Progressively, as the α parameter is exponentially increased towards 1, the effective targeted length l_0 takes a larger influence in the expression of the force fields. The choice of the exponential function according to iterations is an arbitrary choice motivated by the fact that the first movement variations must be the least influenced by the desired length given by the size map until the bars reach a length close to the one defined in the size function to avoid strong movements. The force field thus evolves smoothly from a purely attractive field based only on the current length of the bars to an attractive/repulsive one based on the size function $h(\mathbf{x})$ until reaching equilibrium. Figure 4.13 shows on one side (c) the result of the optimization without using the α parameter and on the other side (d) with using the α parameter for the same time step ($\Delta t = 0.1$). Of course, decreasing the time step will also reduce the self-intersections shown in Figure 4.13(c) at the expense of computation time.

To enforce periodicity, there is a need to know which nodes are linked to each other on the opposite faces. Note that the isosurface extraction of periodic RVEs gives a periodic node distribution on opposite faces. Then, surface contours and nodes on the RVE external boundary faces are extracted from the initial surface triangulation as illustrated in Figure 4.14. These nodes are reordered for each inclusion in order to easily find them together with their corresponding ones on opposite faces. This step aims at providing the necessary information for node movement coordination of periodic nodes to enforce periodicity at each iteration

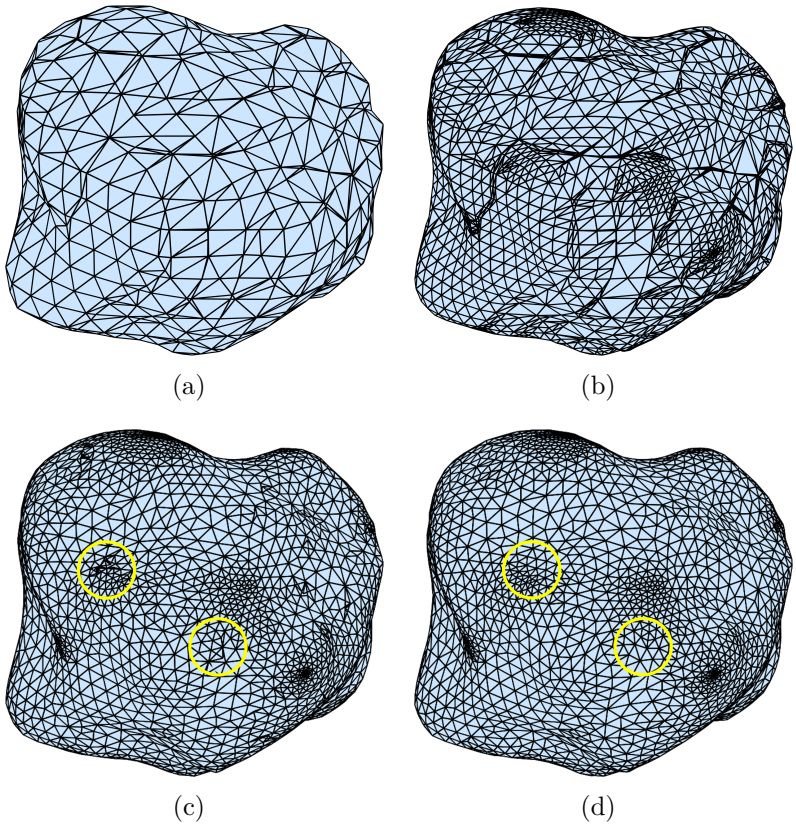

Figure 4.13: (a) Extracted inclusion with Marching Cubes algorithm, (b) Selective refinement of inclusion according to size function, (c) Optimization process with α parameter equals to 1 with yellow circles showing self-intersections, (d) Optimization process with a smooth increase of parameter α from 0 to 1. Yellow circles showing clean meshes compared to (c).

of the optimization, and for using it as a starting point to mesh the external boundaries in the next step (cf. Section 4.4.5).

In the truss analogy process, forces are applied to move nodes. To ensure that RVE boundary nodes remain on the external faces, the displacement normal to the direction of the face is prevented. Due to the interactions with adjacent nodes, the forces applied on a node and its periodic equivalent are not necessarily the same. The movement coordination ensuring periodicity is enforced by applying identical forces on both nodes of opposite faces as the average of forces determined on them separately.

Particular attention is paid on nodes located on the corners and edges of the RVE for which the displacements are constrained respectively in 3 and 2 directions.

At the end of the inclusions surface optimization process, the nodes and triangular facets are fixed on the interfaces and are not modified during the rest of the meshing procedure.

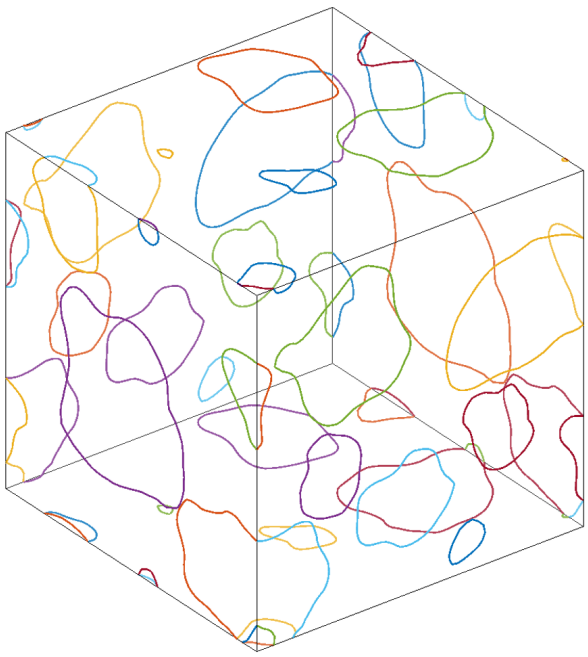

Figure 4.14: External boundary edge nodes extraction and movement coordination to ensure periodicity

4.4.5 RVE Boundaries meshing

Three non opposite faces from the parallelepipedic RVE faces are extracted, meshed and optimized by the truss analogy process.

The three master boundary faces A, B and C are defined respectively in planes $x = 0,\ y = 0,\ z = 0$. External boundary edges and nodes are extracted from the optimized surface mesh with octree nodes lying at the external boundaries of the RVE. The problem is simplified by transforming the 3D boundary nodes on the three planes to deal with 2D problems as illustrated in Figure 4.15.

Then, the extracted surface contours (intersections of inclusions with the RVE face) and nodes are constrained together with corner nodes to generate an initial triangulation using a 2D constrained Delaunay triangulation (see Figure 4.16). The optimization of this triangulation includes in this case two steps. Iteratively, the Persson-Strang truss analogy is applied in the three planes ($x = 0,\ y = 0,\ z = 0$) separately to optimize the surface meshing of the boundary faces until the mean quality starts stagnating. Then, a retriangulation of the face is performed to update the topology in order to reach a targeted element quality (see Figure 4.16).

Finally, as illustrated in Figure 4.17, the opposite slave RVE boundary faces are created by copying the master boundary faces and translating them to their position. The end of this sub-process merges the 6 RVE boundary faces with the internal inclusions surfaces meshes. The merged surfaces (internal and external) constitute the constrained facets to ensure the internal mesh conformity and the

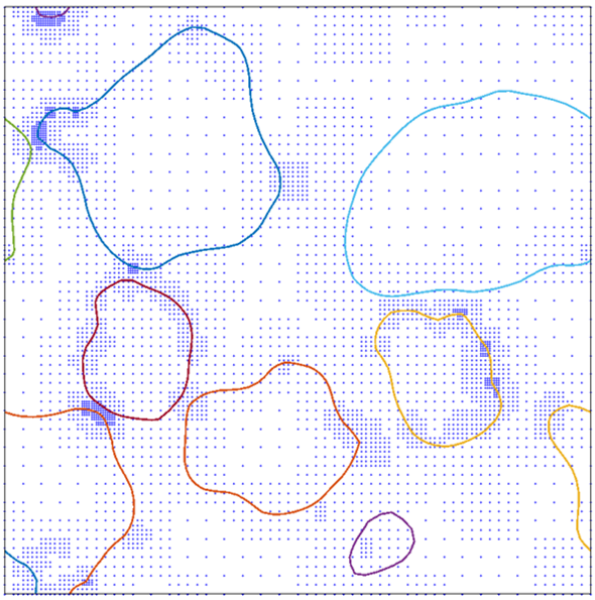

Figure 4.15: 2D simplification - External boundary faces meshing : Extraction of external boundary surface edges and nodes and octree nodes lying to the considered face

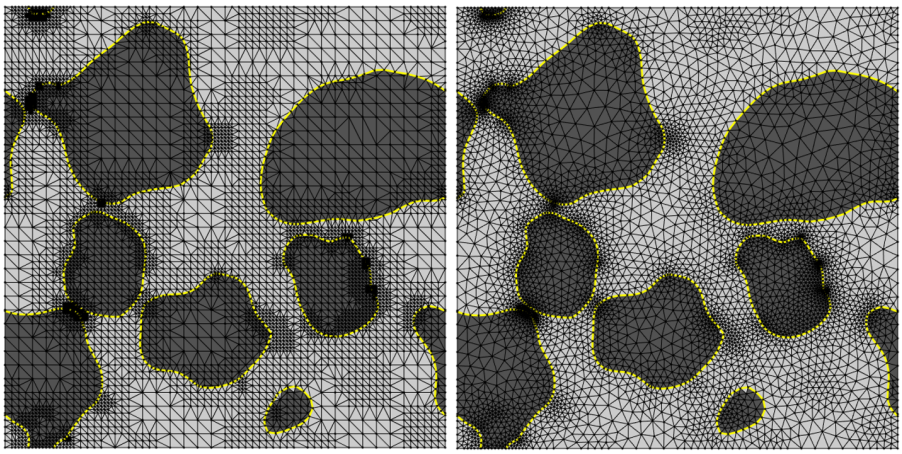

Figure 4.16: 2D simplification : *Left* Initial constrained delaunay triangulation - *Right* Optimized external boundary face mesh using Persson-Strang truss analogy (Persson and Strang, 2004)

periodicity of the mesh, by providing a closed surface mesh to the constrained Delaunay tetrahedralization (CDT) in the next step of volume meshing.

4.4.6 Volume Meshing

The final step in the meshing process consists in the generation of the volume mesh. Optimized boundary faces and internal surface meshes are used as input to the constrained Delaunay tetrahedralization while the background grid on which the CDT is performed originates from the octree nodes distribution. The CDT module of

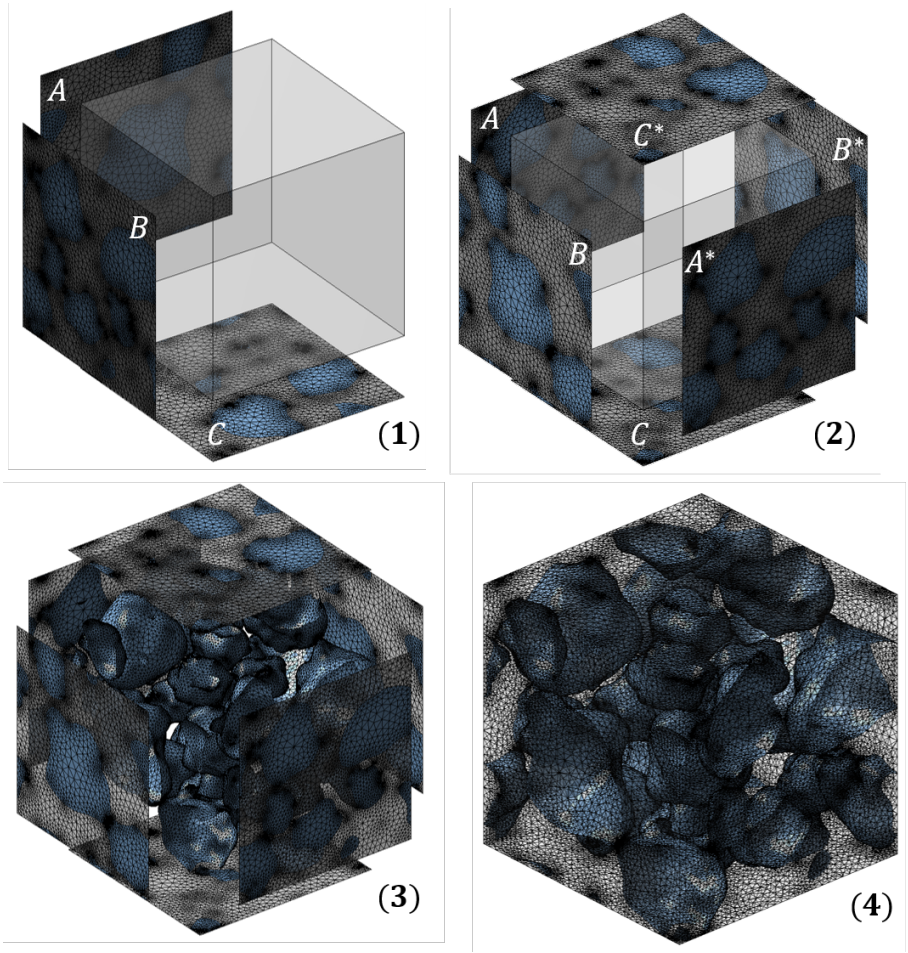

Figure 4.17: 3D periodicity : (1) 2D meshing of non-opposite master faces in plan ($x = 0$,$y = 0$,$z = 0$, (2) Copy and translation of the slave faces, denoted with * to their corresponding positions, (3) Addition of the internal inclusion surfaces meshes, (4) Merge of the external boundary faces with the internal inclusions surfaces meshes and removing duplicated nodes

the well-known and robust mesh generator TetGen (Si, 2015) is used for this purpose. Due to the complexity of the geometries and the imposed constraints (conformity and periodicity), the resulting mesh contains low quality elements, especially close to the interfaces. The truss analogy process is therefore used in order to increase the volume elements quality. As mentioned in the previous section, this optimization includes several steps. In addition to the force equilibrium smoothing function and the retriangulations already explained, a specific treatment to get rid from very specific bad shaped elements, also called slivers or flat tetrahedra (Lo, 2015) is performed, as outlined in the next section.

4.4.7 Extended Persson-Strang truss analogy

To ensure better stability on the node displacements during the mesh optimization and to get rid from slivers which may cause finite element computation to fail (Frey and George, 2000; Persson, 2005), the original truss analogy methodology is modified with an adapted ball-vertex spring method (Bottasso et al., 2005; Lin et al., 2014). This is achieved by introducing additional (linear) springs on bad-shaped elements (with quality lower than a certain threshold) as illustrated in Figure 4.18. The role of these additional springs is to resist the motion of a node towards its opposite faces. In a given tetrahedron, node a is selected as the node located closest to its opposite triangular face and is computed as the normal projection e of the node a on the face bcd. The method is then combined with the size function to apply repulsive forces on a in the normal direction to get it far enough from bcd. A consequence is a drastic reduction of bad-shaped elements and avoidance of nodes crossing triangles during the smoothing process.

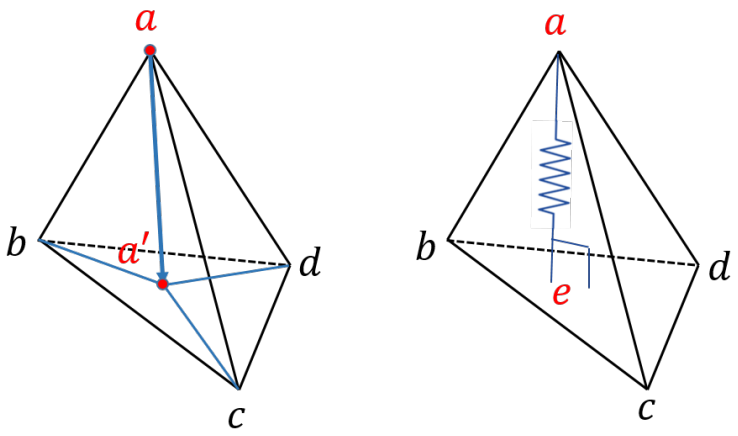

Figure 4.18: *Left:* Tetrahedron collapse mechanism with the edge spring method generating slivers - *Right:* Ball-vertex spring method by connecting the closest point a with its opposite triangular face bcd to ensure stability and get rid from slivers.

Also, faster convergence can be obtained by combining attractive and repulsive force fields (J. Bossen and Heckbert, 1996; Koko, 2015). Globally, the principle remains the same as in (Persson and Strang, 2004) except the expression of the force field in the bars f_{bars} used. While the initial algorithm used exclusively repulsive forces to push nodes accross the interfaces, in this heterogeneous case, extracted nodes already lie on the triangulated internal surfaces from the beginning of the 3D constrained meshing process making the optimization process more stable.

4.4.8 Summary

The mesh generation times and the parameters on which the subprocesses depend are summarized in Table 4.1. An initial fine mesh is used for the explanation of the process (Mesh fine : #366536 nodes,#2178896 elements). A coarser one is also illustrated in Figure 4.19 (Mesh coarse : #50839 nodes, #305892 elements). In addition, this Figure shows the effect of iis, respectively 0.05 and 0.03 for coarse and fine mesh for a cube box of length 1, on the final mesh. The computing times mentioned here are obtained for mesh generations done on a ThinkPad P50 i7 6700HQ, 32 GB RAM coded in MATLAB.

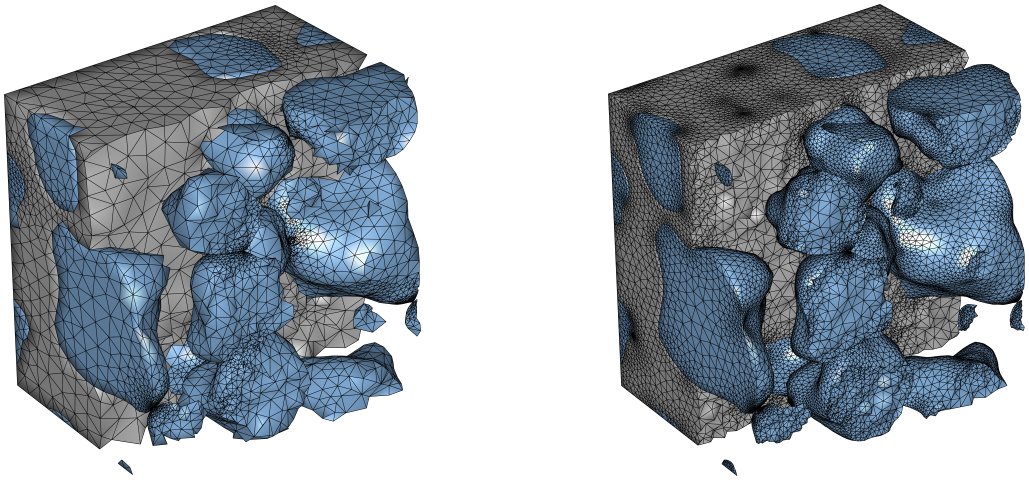

Figure 4.19: Left - Cut view of coarser Mesh 1 (#50839 nodes, #305892 elements), Right : Cut view of finer Mesh 2 (#366536 nodes,#2178896 elements)

Considering that the generator was coded in an interpreted language, the evolution of the computation times should be analysed as a function of the mesh refinement and among the process relative to each other, rather than according to their absolute value. It would be easy to obtain much lower computation time by recoding the critical routines a compiled language. In addition, the surfaces are meshed and optimized one by one or set by set, which leaves the door open for easy parallelization of the process and therefore significant time savings. The routines have been designed to be vectorized and therefore optimized even if it is an interpreted language. However, optimization processes require looping on the elements leading to higher computation times.

4.5 Applications

In order to study more realistically the influence of small scale heterogeneities on the macroscopic behavior of heterogeneous materials, complex microstructural geometries have to be obtained.

	Mesh coarse	Mesh fine	
Step	**Time (s)**	**Time (s)**	**Parameters**
Size function	13.71	31.77	Initial interface size Narrowness Curvature Gradient limiting factor
Surface Meshing	17.25	53.07	# Inclusions Marching Cube extraction at initial interface size Selective refinement (due to narrowness and curvature) Self-intersections check Periodicity constraints Optimization process
Octree node distribution	1.26	6.19	Size function (iis,curv,nar) Density parameter
Boundaries meshing	5.89	16.06	#Extracted boundary surface constrained edges # Boundary nodes Optimization process
Volume meshing	47.56	266.52	# Constrained facets # Nodes Optimization process
Total	85.67	373.61	

Table 4.1: The mesh generation times and the parameters on which the subprocesses depend. The computing times mentioned here are obtained for mesh generations done on a ThinkPad P50 i7 6700HQ, 32 GB RAM coded in MATLAB. Considering that the generator was coded in an interpreted language, the evolution of the computation times should be analysed as a function of the mesh refinement and among the process relative to each other, rather than according to their absolute value.

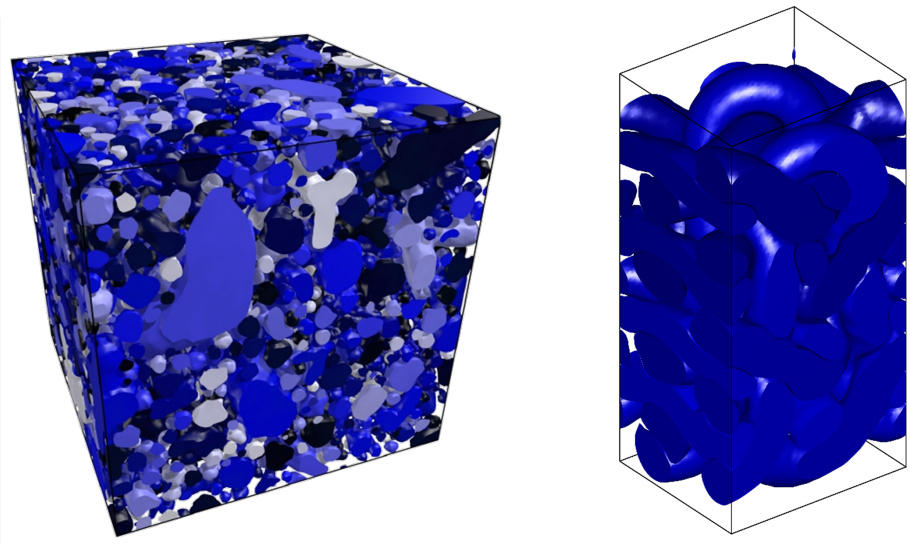

Figure 4.20: Examples of different types of RVEs generated by (Sonon et al., 2012, 2015; Sonon and Massart, 2013) : inclusion-based microstructure (left) and a woven composite (right)

Some of these RVEs are discretized in this section in order to show the capabilities of the new mesh generator. Three types of RVEs are shown for illustration, (i) inclusion-based media (Sonon et al., 2012), (ii) woven composite (Sonon and Massart, 2013; Wintiba et al., 2017), and (iii) random geometry obtained with excursion sets of random fields.

The first example is an RVE generated by DN-RSA developed by (Sonon et al., 2012). This tool is based on a distance-controlled random sequential addition algorithm. It has the capability to generate inclusion-based microstructures with large size distributions and arbitrary shapes with precise control on neighboring distances. This example illustrates a periodic inclusion-based material composed by 222 inclusions of various shapes and sizes with an inclusion volume fraction of 50,87%. The size distribution of inclusions varies between 0.05 and 0.35 for a cubic RVE of size 1. The resulting mesh shows a high quality distribution of elements with less than 1.5% of elements with quality lower than 30% (cf. Equation (4.4)). No slivers affecting FEM simulations are found.

The second example is an RVE of a complex periodic three dimensional textile reinforced composite RVE with very small gaps between yarns as illustrated in Figure 4.22. By using level set functions, the generation tool has the ability to control the gap thickness and to remove automatically any residual interpenetration, while controlling the volume fraction of each familily of yarns in the RVE, that traditionnally other methods fail. More details about the generation of the geometry for this application can be found in (Sonon and Massart, 2013) and (Wintiba et al., 2017).

The meshing methodology developed here can be naturally extended to discretize geometries obtained from RVEs generated by other techniques or from image-based CT scans (Hashemi et al., 2014). Recently, RVE generation methods based on excursion sets of correlated Random Fields (RFs) with morphological control were developed in (Roubin et al., 2015), producing complex randomly shaped heterogeneous material at different scales. These excursion sets, or thresholding of an RF, can be statistically controlled both geometrically (volume and surface area) and topologically (Euler characteristic) by linking analytically these to the statistical parameters of an RF, see (Adler, 2008) for more details. This tool leads to the generation of geometries such as matrix/inclusion morphologies or porous materials, involving opened or closed porosity as well as representing grain or pore size distributions. Figure 4.23 illustrates a conforming mesh of a RVE generated by excursion sets of Random Fields.

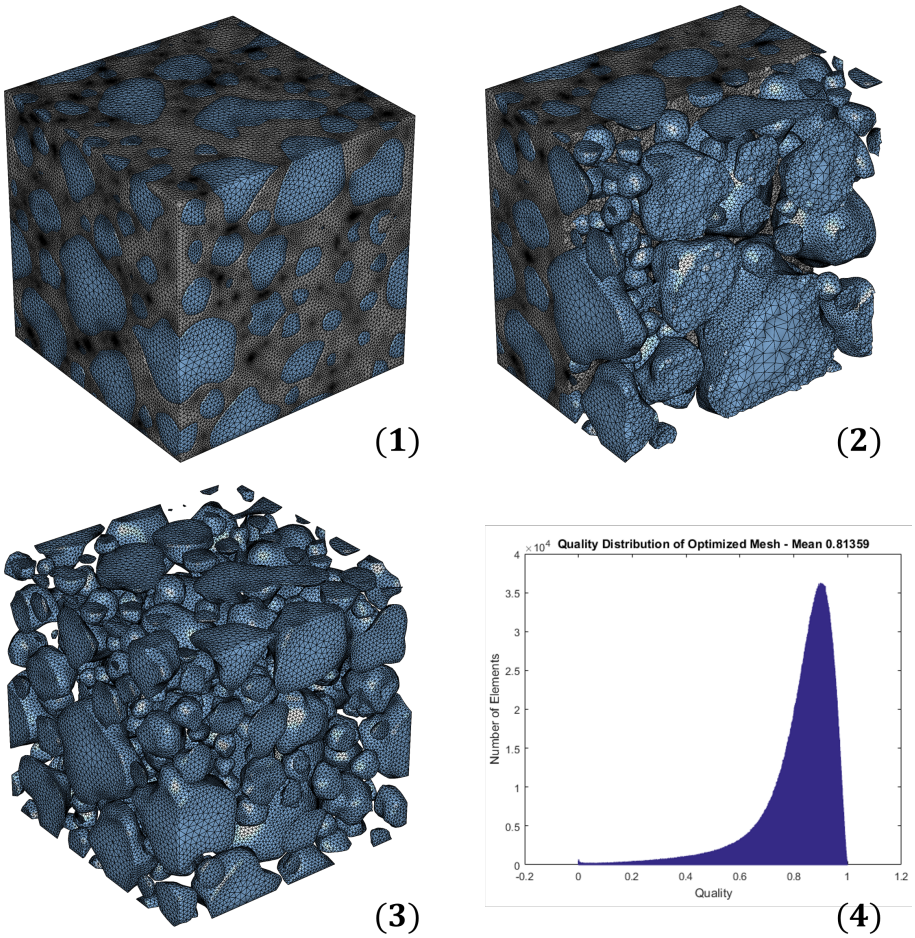

Figure 4.21: Final periodic and conform mesh of the RVE (#Nodes=1 236 685/#Elements=7 501 711) : (1) Global view of the optimized mesh for both phases (inclusions/matrix), (2) Cut view of the inclusion-based RVE, (3) Inclusions meshes only, (4) Quality distribution - Mean quality : 81.36%

4.6 Discussion

The examples shown in the Applications section show the generator's ability of the generator to mesh complex geometries of very different shapes. The use of distance fields provides the necessary information to refine the areas of interest to take into account the geometrical complexity associated to rather high curvatures or narrow matrix zones between neighbouring inclusions. However, inaccuracies may appear in the evaluation of the orientation of the normal to interfaces and therefore on the nodal reaction forces on the inclusions surfaces. This may lead to self-intersections in the resulting mesh. It is a known issue addressed already by several contributions, see (Attene, 2014; Lo, 2015). For this case, these irregularities comes from the grid resolution of the input geometry compared with its curvature. In fact, refining locally the mesh would not solve the problem as the gradient quality can not be better than the initial grid resolution. A solution is to smoothen

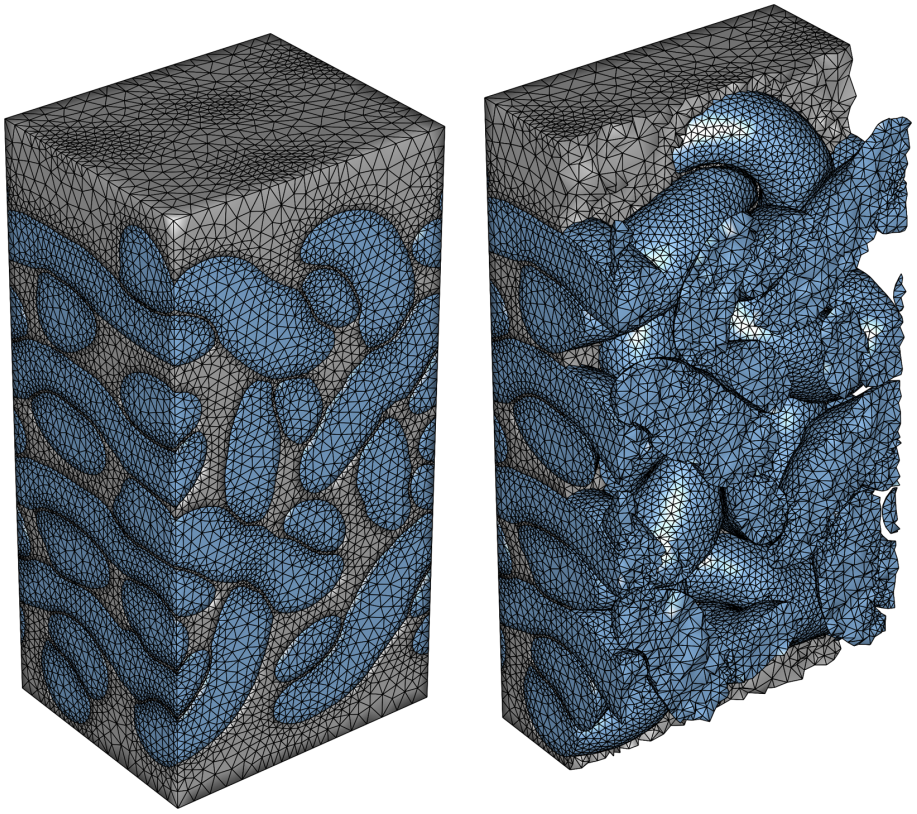

Figure 4.22: Final periodic and conform mesh of the RVE (#Nodes=119 096/#Elements=729 350) - *Left* : Global view of the optimized mesh for both phases (inclusions/matrix) - *Right* Cut view of the woven composite RVE

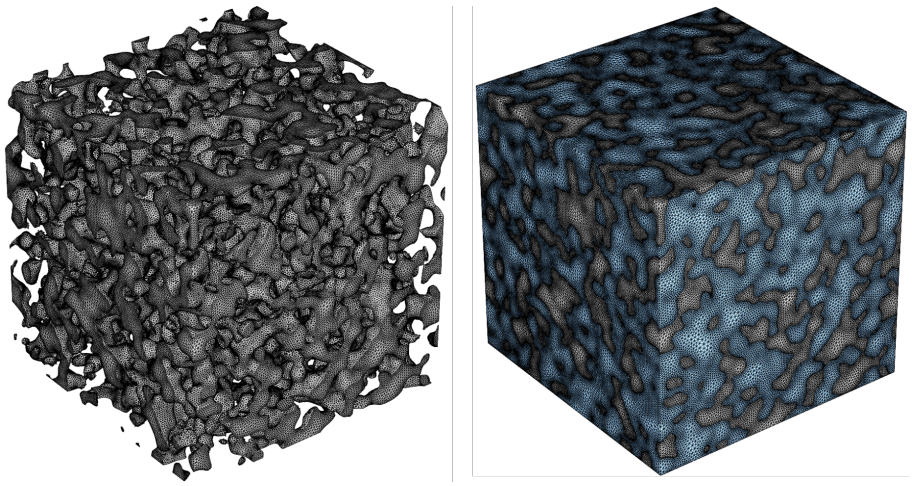

Figure 4.23: Final conform mesh of the RVE based on excursion sets with a cube of size $a = 1$, $\sigma^2 = 1$, $l_c = 0.04$ (#Nodes=2 398 675/#Elements=14 601 647). The threshold is taken at 0.45 leading to a porosity of 33%. : *Left* : Matrix - *Right* Matrix/Inclusions

locally the level set function if the problem appears loosing in return locally some of the details. Another solution is to implement a predictor-corrector process to stabilize the forward euler resolution scheme.

In relative terms, with the procedure implemented here, the presence of self-intersections in particularly complex shapes is lower than 0.01 % of the total number of surface elements. A simple solution proposed here is to remove them from the surface triangulation, which results in the opening of surfaces initially closed. When the volumic CDT is applied, some parts of the surface are therefore not constrained anymore. During, the optimization process moving the nodes to reach the targeted length size defined by $h(\mathbf{x})$, it is possible to satisfy the empty circumsphere criterion of a Delaunay triangulation and to preserve the conformity of the very small missing part by avoiding crossing elements even if CDT is not applied there.

As presented in Section 4.4.4, the constraint of using global level-sets functions is that they do not preserve the sharp features when an explicit facetted geometry is extracted by a Marching cubes algorithm (Lorensen and Cline, 1987). In the context of this article, the case of sharp edges has therefore not been addressed because it requires a dedicated development. An implicit geometrical description that preserves sharp edges, as present for instance in open cell metallic foams, was proposed in (Sonon et al., 2015). It is based on the slicing of distance fields or level sets by ad hoc functions to describe sharp edges. The mesh generator proposed here could perfectly be extended to account for such features. It would consist in resorting to the methodology proposed in (Sonon et al., 2015) to extract the sharp edges.

Also, the use of an improved marching cubes for the extraction of isosurfaces from scattered datas or an octree-based dual contouring method (Zhang et al., 2005, 2010) could be used in future developments to produce a better initial adapted surface triangulation allowing a faster convergence of the optimization and potentially allowing preventing non-manifold triangulations.

The subsequent attribution of elements to proper material phases is done thanks to TetGen in most general cases. For inclusions with removed self-intersections, the detection of closed surfaces is no longer possible. For these particular inclusions, the attribution of elements to the material phases is done by interpolating the level set function value at the centroid of the tetrahedra.

As seen in Section 4.5, due to the complexity of the shapes, a few bad-shaped tetrahedra may still be present after the optimization process. Those elements are mainly located in areas with strong curvatures (requiring greater refinement) as well as at the neighborhood of the intersection between the external boundary faces of the RVE and surfaces of the inclusions. For the latter, the boundaries may exhibit sharp edges that give rise to very flat elements. Taking into account the proximity to the boundary faces through selective refinement without breaking

the periodicity of the mesh would drastically reduce the number of poor quality elements. The example of inclusion based medium shows that less than 1.5% of elements have a quality lower than 30%. Even if the ratio of bad-shaped elements remains very low, this issue could become critical in simulations involving finite deformations or strong anisotropy. A solution of tetrahedral mesh improvement method presented by (Klingner and Shewchuk, 2008) that uses a broader set of operations such as topological transformation could be a good option for further improvements to get rid from these few low quality elements.

4.7 Conclusion

The present contribution presents a new conforming mesh generation methodology for 2D and 3D periodic (or not) complex heterogeneous RVEs. The implementation is adapted and optimized for the RVEs generation tools developed by (Sonon et al., 2012) in order to propose an integrated approach. However, a natural extension can be built for general implicit geometries obtained from other geometry generation or from experimental techniques such as CT scans.

The newly developed approach is an iterative Delaunay mesh generator based on an extended Persson-Strang truss analogy optimization process. Such an approach, based on signed distance fields, carries the advantage that the level set information used during the generation of the geometry of the microstructure by (Sonon et al., 2012) can seamlessly be used in the subsequent discretization procedure.

The meshing process is hierarchical and aims at generating a triangulation, optimizing and constraining progressively interfaces, boundary faces and the volume. It offers a specific control on the inherent specificities of each part and leads to the generation of high quality FEM meshes.

On the internal surfaces, nodes are preventing from moving outside by systematically constraining their normal movement acting like boundary reactions while tension/compression forces act in the bars to reach the desired lengths defined by the size function. The latter allows optimizing the node distribution as a function of geometrical features such as curvature, nearness and narrowness. The distorsion of the elements is reduced by using a gradient limiting factor to better control the growing elements size. Periodicity is ensured by meshing independently non opposite master RVE faces before copying, translating and merging them to form the periodic enclosing box while conformity is ensured by using the Constrained Delaunay Tetrahedralization.

This chapter is based on the article titled "Advanced discretization techniques for image-based modelling of porous rocks" which was published in the January 2020 issue of Acta Geotechnica (Ehab Moustafa Kamel et al., 2020, Volume 15, pp. 57–77)

5

Comparison of advanced discretization techniques for image-based modelling of heterogeneous porous rocks

Abstract

This contribution presents an assessment of computational techniques enabling automated simulations of complex porous rocks microstructures based on 3D imaging techniques. A subset of a CT-scanned sandstone sample is used to compare the results obtained by two advanced discretization frameworks. Raw scan results are processed by a level set-based segmentation technique to produce smooth geometries prone to finite element discretizations. A recently developed technique is outlined for conforming mesh generation for complex porous geometries described implicitly by functions. This allows generating high quality tetrahedral meshes with selective refinement. Next to this, a technique that uses a kinematic enrichment by incompatible modes to represent the heterogeneous geometry is explained. Both techniques use the same implicit geometry as main input for the simulations. Mechanical simulations are conducted on a subset of a scanned sample of a sandstone under triaxial loading conditions for isotropic compressive loading and for loading conditions involving a stress deviator. The results are compared and discussed based on local stress distributions and on a Mohr-Coulomb criterion with tensile cut-off. The results show that both discretization strategies yield complementary tools and allow envisioning automated simulations based on raw CT scan data for porous rocks exhibiting complex pore space morphologies.

Keywords: Rock Mechanics, Porous Rocks, Automated Meshing, Finite Elements, Embedded Discontinuities, CT scan, Image-based Modelling

Contents

5.1 Context

The mechanical and fluid transport behaviour of porous geomaterials is strongly dependent on their microstructure, and in particular on the morphological properties of their pore or fracture networks. Furthermore, these microstructural features may evolve as a result of mechanical loading, which induces further couplings between the mechanical response and the transport properties.

As a result, many research efforts have been devoted in the past to investigate the link between the microstructure of geomaterials (in the broad sense) and their overall properties. Initially, many of these contributions dealt with the effect of degradation and cracking evolution on the mechanical response of geomaterials. This was achieved using various techniques such as micromechanically-inspired models (Shao et al., 1999), discrete element modelling (Li et al., 2017) or RVE computations (Li et al., 2015). Fluid transport properties and their link to cracking evolution were also scrutinized using micromechanically-inspired models (Shao et al., 1999) and multiscale techniques (Massart and Selvadurai, 2012, 2014).

With the development of experimental imaging techniques at different scales, the investigations on the effect of microstructural features on the overall behaviour received even more attention.

Focusing on scanning techniques allowing to obtain the microstructural phase arrangement, computed tomography (CT) nowadays allows addressing a variety of scales (micro-tomography or at higher scales) and of geomaterials such as soils (Hashemi et al., 2014), rocks (Chen et al., 2006) or mixtures (Li et al., 2016). Such investigations are devoted to their mechanical behaviour (Chen et al., 2006;

Li et al., 2016), to their transport properties (White et al., 2006); or to coupled processes (Hashemi et al., 2015).

Early efforts in the use of 3D images for analysis and modelling of rocks behaviour started with an effort reconstructing a 3D granite mesostructure (at the scale of a full lab specimen), based on an iterative milling and scanning system presented in (Chen et al., 2006). The procedure was used to conduct 3D Brazilian test simulations on a real mesostructural geometry by means of a finite difference scheme. Subsequent efforts at similar (large) scales were devoted to jointed rocks (sandstone) (Yu et al., 2016), in which computed tomography was used to analyse and model the effect of joints shape on the mechanical behaviour; and to feed soil-rock mixture 2D simulations (Li et al., 2016).

Experimental efforts in the field of rock mechanics to capture microstructural features used micro-tomography (μCT) to investigate the microstructural changes in the pore space during unconfined compression tests in Gosford sandstone (Sufian and Russell, 2013). This was achieved by scanning samples at different loading levels prior to failure in order to link the pore structure evolution to the macroscopic energy dissipation. In situ μCT observations of porosity evolutions under triaxial tests were also investigated for calcarenite in (Raynaud et al., 2012). The relationship between specific surface and porosity in ten different types of sandstone was scrutinized in (Rabbani and Jamshidi, 2014) by μCT in order to build modified Carman-Kozeny equations for sandstones; and real time (in situ) μCT triaxial experiments were performed in sandstone to assess the effect of chemical corrosion in (Feng et al., 2004).

With the availability of the detailed 3D microstructural geometry, μCT also allowed feeding microstructural mechanical computations making direct use of the image information. Such observations were mostly used to feed 3D DEM simulations on sandstones at the RVE and at the sample scales (Li et al., 2015). Strength anisotropy was scrutinized in Berea sandstone together with an μCT assessment of the porosity levels to feed 2D DEM simulations (Kim et al., 2016). Additional efforts addressed the upscaling of transport properties by using multiscale approaches using finite element macroscopic computations fed by a lattice Boltzmann framework based on 3D μCT images (White et al., 2006; Sun and fong Wong, 2018).

Next to the direct use of 3D images, μCT observations were also exploited to reconstruct equivalent geometrical models which can subsequently be used in finite element simulations. Such a reconstruction strategy was proposed in (Zhou and Xiao, 2017) for porous rocks (sandstone). It was next extended in (Zhou and Xiao, 2018a) using simulated annealing, leading to models that do not consist of the scanned geometry itself, but rather of equivalent geometries reproducing the essential features identified in the scans. These techniques were also applied in (Zhou and Xiao, 2018b) to triaxial tests with comparisons to experiments.

These previous contributions in the literature show that there is an interest in addressing the simulation of microstructural processes in porous rocks using directly the 3D images obtained by μCT. However, the discretization of such geometries may quickly become extremely complex. The purpose of the present contribution is to compare two novel discretization strategies that allow building models in an automated way based on a raw 3D μCT image. The first of these discretization strategies consists of a recent extension of the meshing tool relying on the Persson-Strang analogy (Persson and Strang, 2004; Ehab Moustafa Kamel et al., 2019) to build a high quality conforming tetrahedral mesh. It relies on an implicit description of the geometry of the solid phase and of the pore space of a porous rock. The second strategy is based on the projection of such an implicit geometry on an unstructured tetrahedral mesh, with an incompatible kinematic enrichment defined at the element level to account for the heterogeneity of phases. The comparison will here be performed through mechanical simulation on a subset of the CT-scanned image of a sandstone (Hu et al., 2018).

To build this comparison, this contribution will be structured as follows. Section 5.2 will outline the pre-processing required from the raw μCT scan data (segmentation and smoothing) to provide the implicit geometrical information for the discretization tools. Section 5.3 will next detail the procedures followed by each strategy to construct the discretization based on the implicit geometry devised in Section 2 from the raw μCT scan data. Section 5.4 will compare the results obtained by both strategies for a sandstone μCT scan sample subjected both to a pure isotropic triaxial stress state and to a triaxial stress state involving a stress deviator. Finally the results will be discussed in Section 5.5, before conclusions are drawn in Section 5.6.

5.2 Problem statement and segmentation

In the context of image-based modelling of heterogeneous porous rocks, the porous microstructure can be obtained either by reconstruction of equivalent geometrical models from the exploitation of 3D images or by virtual generation according to morphological quantitative features (Sonon et al., 2012; Roubin et al., 2015). When dealing with image-based models, the interfaces separating the pore space from the solid phase can be described either explicitly by means of triangulated surfaces in 3D, or implicitly by means of level-set functions and/or distance fields. The latter approach offers the ability to model and handle geometries with arbitrarily complex features. When using level sets, a curve Φ in 2D, respectively a surface

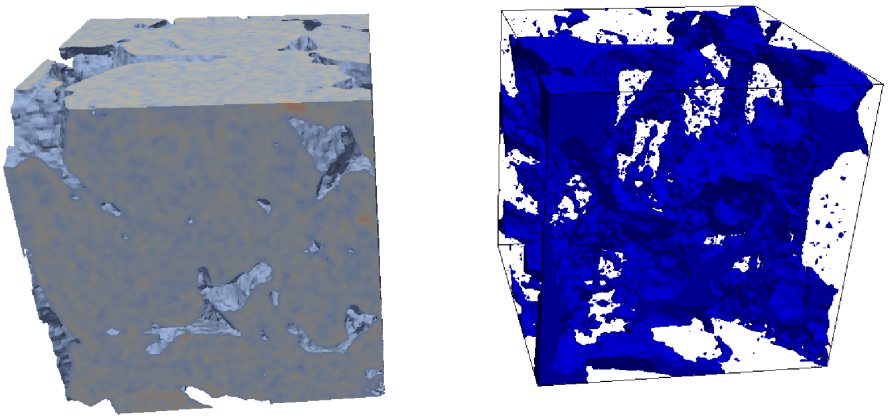

Figure 5.1: Subset of Vosges sandstone sample obtained by X-ray tomography from Cong Hu's thesis (Hu et al., 2018) : solid part (left) and pore space (right) of the sandstone

in 3D, can be represented implicitly by means of the level sets of functions of spatial coordinates $\mathbf{x}$ denoted $LS(\mathbf{x}, ...)$:

$$\Phi \equiv LS(\mathbf{x}, ...) = k \tag{5.1}$$

where k represents the iso-value of the function.

A well-known example of level set function consists of the gray-scale density map obtained by X-ray CT scans increasingly used in the context of rock mechanics. To exploit properly imaging techniques, the segmentation process is however a crucial step. Indeed, it must accurately reflect the complexity of the geometry at hand, be able to identify the different phases of the material, and make the results usable in the subsequent processes. The sample used in this paper to illustrate the comparison between the two selected discretization methods is a subset of the CT scan of a dry Vosges sandstone obtained by X-ray tomography as part of Cong Hu's PhD thesis (Hu et al., 2018). The scan resolution is 5 microns per voxel for a geometry size of 100x100x100 voxels (see Figure 5.1).

Since the pore space (18.04% of total porosity) of the studied sandstone sample is very strongly connected (about 99%), the occluded porosities represent only very small cavities. These may require a high level of refinement in the discretization step if they are still taken into account in the segmentation process. Therefore, assuming that their impact on the simulation results discussed in this paper will be negligible, they will be removed from the voxel grid before segmentation in order to reduce computation times. To achieve this, a geodesic reconstruction (Beucher, 2001) is applied to the given grayscale image using as a mask the 6 boundaries of the scan sample, so that only the connected porosities remain.

For the image segmentation, an automated thresholding by Otsu's method (Otsu, 1979) is suitable when the histogram of the grayscale of the images shows two distinct

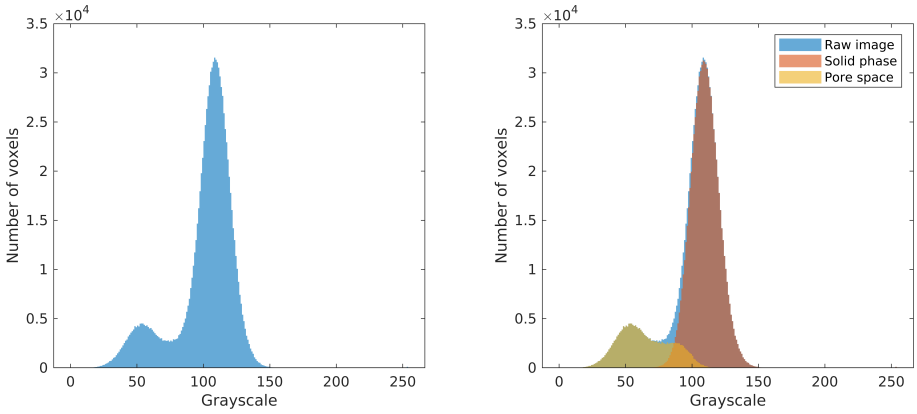

Figure 5.2: (a) Histogram of the geometry, (b) Decomposition of the histogram in two phases taking into account the overlapping with the level-set segmentation method

Figure 5.3: Comparison between : (a) a slice of the micro-CT scan, (b) thresholding process obtained by Otsu's method at 76 grayscale value, (c) level-set segmentation

normal distributions. Otherwise, overlapping will induce thresholding management that may atrophy part of the information. In addition, this method often requires the application of a Gaussian filter to smoothen the interfaces, a required step to obtain a mesh-prone resulting geometry. Among the other available segmentation techniques, the level-sets-based methods correspond to a class of deformable models in which the desired shape is obtained by propagating an interface represented by 2D iso-contours (3D iso-surfaces) (Caselles et al., 1997; Chan and Vese, 2001; Shi and Karl, 2008) giving thereby smoothed contours.

Even if in this case two peaks can be distinguished relatively clearly, a level-set segmentation method based on Bernard's work (Bernard et al., 2009) will be used as illustrated in Figure 5.2. In this chosen method, the implicit function is modeled as a continuous parametric function expressed on a B-spline basis, that allows obtaining a smooth level-set function and a satisfactory segmentation result of the image given in input; even if it is noisy. Figure 5.3 illustrates a comparison between an image built from the raw micro-CT scan data, using the thresholding by the Otsu method, and using the level-set segmentation for a 2D slice.

The segmentation process was applied here for each of the slices of a raw 3D CT scan, before being stacked to form the whole result in 3D as illustrated in Figure 5.4.

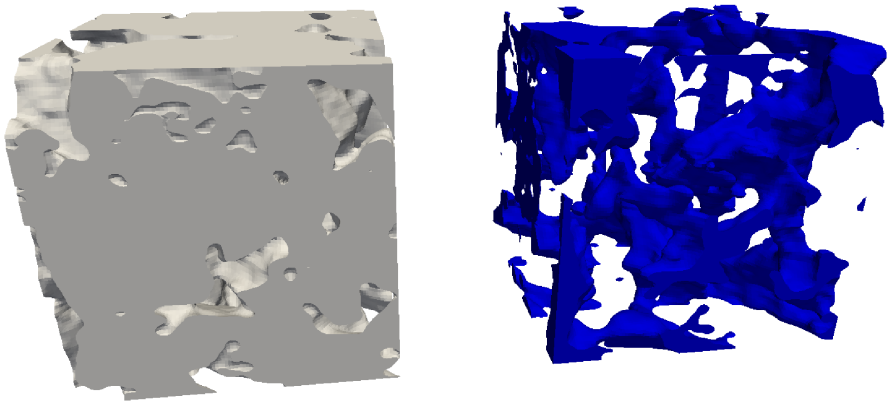

Figure 5.4: Resulting segmentation of the solid part (left) and pore space (right) of the subset of sandstone micro-CT scan

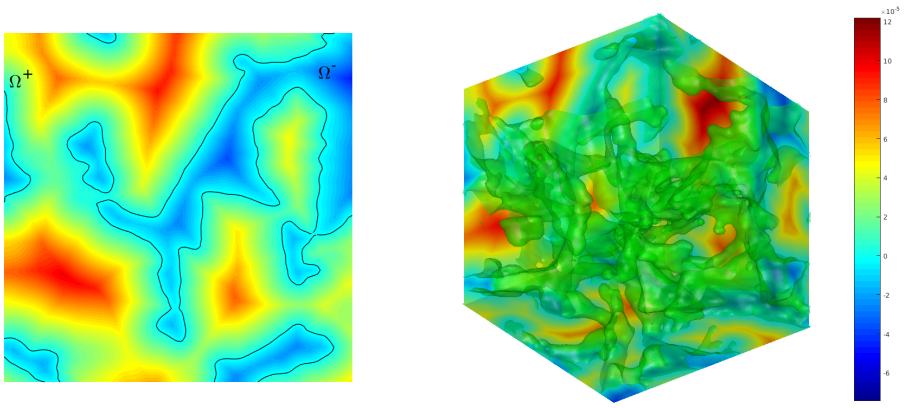

Figure 5.5: Signed distance field of the sandstone sample where Ω^+ is the positive part corresponding to the solid part and Ω^- the negative part corresponding to the porous space

The discretization methods presented in the following sections require the use of signed distance functions which is a particular choice for level-set functions (Osher and Fedkiw, 2003; Sethian, 1999). The signed distance function of Φ is a function $DS(\Phi(\mathbf{x}))$ with the value of the signed euclidian distance from $\mathbf{x}$ to Φ. Here, the RVE domain Ω is divided into two sub-domains Ω^+ and Ω^- representing respectively the solid phase and the pore space, and Φ representing their interface. A negative value of the distance function is attributed by convention to the domain Ω^- as illustrated in Figure 5.5. Practically, this distance function is evaluated on a discrete grid of points regularly placed on the spatial domain of interest of the scanned sample.

In order to maintain a sufficient accuracy without requiring excessive refinement of the background grid, the signed distance function is computed from an exact Euclidean signed distance field evaluation from discretized geometries (Sonon et al., 2012) extracted with a Marching Cube process (Lorensen and Cline, 1987). Other methods exist such as for instance the fast marching method (Osher and Fedkiw,

2003) that features interesting execution times. However, it generally only yields an approximation of the signed distance, while the discretization processes require an accurate definition of the euclidean distance. Figure 5.5 right illustrates the signed distance field of the segmented micro-CT of the sandstone geometry obtained using an exact distance computation. This distance function will be used as a basis for the discretization procedures used in the next section.

5.3 Image-based modelling for heterogeneous geomaterials

5.3.1 Conforming discretization of implicit geometries

The discretization approach explained here is based on the generation of conforming meshes for complex heterogeneous geometries, based on their implicit description by signed distance functions. The methodology was originally proposed by (Persson and Strang, 2004) for homogeneous structures and extended to heterogeneous structures by (Ehab Moustafa Kamel et al., 2019).

The conforming mesh generation strategy is subdivided into four main steps as follows :

1. Definition of a size function $h(\mathbf{x})$ based on specific geometrical characteristics
2. Generation of a nodes distribution based on an octree decomposition using this size function
3. Optimized surface meshing of the internal pore space surface and of the external structure boundaries (i.e. the external faces of the scan sample)
4. Optimized volume meshing based on a Constrained Delaunay Tetrahedralization (CDT) starting from the enclosed surface mesh generated during step 3.

Size function definition

The procedure starts by defining a size function $h(\mathbf{x})$, where $\mathbf{x}$ represents the spatial coordinates, that is used to control the elements sizes. Dealing with complex microstructures can quickly lead to a large number of degrees of freedom in the simulation process due to important mesh refinements. In fact, complex shapes of the microstructure motivate taking into account local features such as narrow gaps (nar), high curvatures ($curv$) or initial interface sizes (iis), thereby requiring a local increase of the nodes density. The size function is constructed based on the distance function to generate such non-uniform meshes refined only locally where

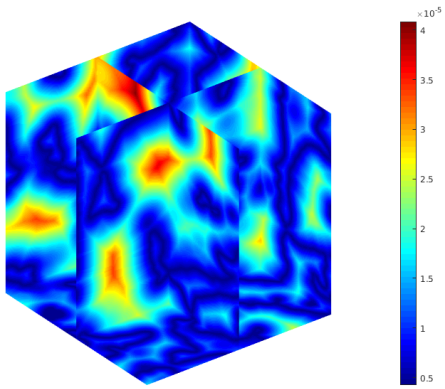

Figure 5.6: 2D slices of size function $h(\mathbf{x})$ based on the segmented sandstone

it is necessary. The size function is thus the starting point of the optimization process and of the initial nodes generation. The minimum initial imposed size values h_0 depending on the three geometrical parameters iis, $curv$ and iis are first computed as expressed in Equation (5.2). In the present context, a low sensitivity to curvature is used to avoid too large differences in the element sizes that can cause a conditioning problem of the stiffness matrix in FEM simulations.

$$h_0(\mathbf{x}) = min(\{h_{iis}(\mathbf{x}), h_{nar}(\mathbf{x}), h_{curv}(\mathbf{x})\}) \tag{5.2}$$

To avoid poor quality elements due to significant element size variations on small distances, a smooth evolution of the size function is enforced using a gradient limiting factor g (Persson, 2005) expressed as

$$\|\nabla h(\mathbf{x})\| = g \tag{5.3}$$

Figure 5.6 illustrates the size function $h(\mathbf{x})$ of the segmented sandstone sample.

Optimization by means of extended Persson-Strang truss analogy

Dealing with complex geometries makes it difficult to reach an ideal mesh in which only quasi-regular tetrahedra are present. The objective of the optimization process is to minimize the magnitude of the difference between the lengths of the edges in an element, and this over the entire mesh, in order to reach an optimal element quality for a given triangulation. This is achieved by finding an optimal configuration of the nodes positions for a given connectivity. The mesh quality optimization is based on an iterative technique that uses a simple mechanical analogy between the optimal mesh for a given connectivity and the equilibrium configuration of a 3D truss of elastic bars of stress-free lengths, or equivalently a structure made of springs (Persson, 2005). In this analogy, the edges of tetrahedral elements and the mesh nodes correspond respectively to the bars and joints of a

truss system. To this end, an attractive/repulsive force field $f(l, l_0)$ is defined on each bar, depending on its current length l and its desired length l_0 set by the size function $h(\mathbf{x})$. This force field steers the nodes positions towards optimal elements shapes. By assuming an appropriate force-elongation relationship for the bars, the final nodes positions ($\mathbf{x}$) for a set of fictitious forces ($\mathbf{F}$) can be found iteratively by solving for static equilibrium according to

$$\mathbf{F}(\mathbf{x}) = \sum_i \mathbf{F}_{int,i}(\mathbf{x}) + \mathbf{F}_{ext,i}(\mathbf{x}) = 0 \tag{5.4}$$

where $\mathbf{F}_{int}$ and $\mathbf{F}_{ext}$ are respectively the internal forces present in the bars and the external forces coming from boundary constraints defined by fixing nodes on the boundary of the domain to be meshed (enclosing surface for a 3D mesh, enclosing contour for a surface mesh).

The fictitious force vector $\mathbf{F}(\mathbf{x})$ acting on each node depends on a changing topology of the truss system (i.e. if a new triangulation is produced during the node relocation process). This renders $\mathbf{F}(\mathbf{x})$ not continuous accross arbitrary $\mathbf{x}$ variations, thereby inducing difficulties to solve the system. When large node movements arise, such Delaunay retriangulations are indeed performed to improve the truss topology. The non-linear equations system can be simply resolved asymptotically by introducing an artificial time dependency (5.5) and using a forward first order Euler time integration scheme (5.6) starting from an initial Delaunay triangulation. Such a scheme is used until a stationary state is reached according to a pre-defined tolerance. The resulting fictitious mechanical equilibrium is achieved when the nodes movements tend to vanish.

The following system of ordinary differential equations (ODEs) is considered (in non physical units), with the initial condition $\mathbf{x}(0) = \mathbf{x}_0$ being the initial node distribution :

$$\frac{d\mathbf{x}}{dt} = \mathbf{F}(\mathbf{x}), \qquad t \geq 0 \tag{5.5}$$

$$\mathbf{x}(t_{n+1}) = \mathbf{x}(t_n) + \Delta t\, \mathbf{F}(\mathbf{x}(t_n)) \tag{5.6}$$

Practically, the expression (5.7) is used for the internal repulsive/attractive forces field, allowing internal forces $\mathbf{F}_{int}(\mathbf{x})$ to reach the equilibrium state in a configuration matching the size function $h(\mathbf{x})$

$$f(l, l_0) = k\,(l_0 - l) \quad \text{where } k = \frac{l + l_0}{2\,l_0} \approx 1 \tag{5.7}$$

To accelerate the convergence and get rid of slivers (zero volume elements) which may cause finite element computations to fail (Frey and George, 2000; Lo, 2015; Persson, 2005), an adapted ball-vertex spring method (Bottasso et al., 2005;

Lin et al., 2014) is used during the optimization process by introducing additional (linear) springs on badly-shaped elements resisting the movements of a node of an element towards its opposite face in the element.

Each meshing step, namely the pore space surface meshing, the external structure boundary faces meshing and the 3D bulk meshing (of the solid phase and the pore space) implies an optimization process of the initial triangulation using this extended version of the principle of the described Persson-Strang truss analogy.

Initial node distribution

The mesh generation process starts with the initialization of an unconnected nodes distribution. A recursive refining process starting from the 8 corners of the structure is applied, in such a way that the local nodes density is related to the defined size function giving an octree decomposition (Legrain et al., 2011b; Macri and De, 2008; Paiva et al., 2006). The advantage of such a method is to obtain a smoothly distributed initial nodes set controlled by $h(\mathbf{x})$, placing nodes close to their equilibrium position in the optimization process, and thereby reducing the number of retriangulations needed to get high quality FEM meshes.

Surface Meshing

The main difficulty with Delaunay-based mesh generators remains the enforcement of mesh conformity at material boundaries for heterogeneous materials, especially in 3D. In the present case this arises at the interface between the solid phase and the pore phase. Ensuring the conformity when nodes are present on both sides of the material boundaries before triangulation is a tricky task and is still a challenging problem both in theory and practice (Si, 2010, 2015). This is the reason that motivates the decomposition of the meshing process by meshing first the internal pore space surface and the external structure boundaries, in order to form the enclosed discretized surface that can be given as an input to 3D constrained Delaunay triangulation (CDT). As illustrated in Figure 5.7, a Marching Cube algorithm (Lorensen and Cline, 1987) is applied to extract the iso-surface corresponding to the internal pore space surface, giving an initial uniform ill-shaped surface triangulation (bad quality elements). This surface triangulation is then optimized by extended Persson truss analogy and refined locally according to the size function, generating a discretization appropriate for finite elements simulations.

Then, the 6 boundary faces of the sample microstructure are extracted, meshed and optimized with the extended Persson truss analogy, simplifying the problem by transforming the 3D boundary nodes on the six planes to deal with 2D problems. The external contours of material boundaries and the boundary nodes coming from

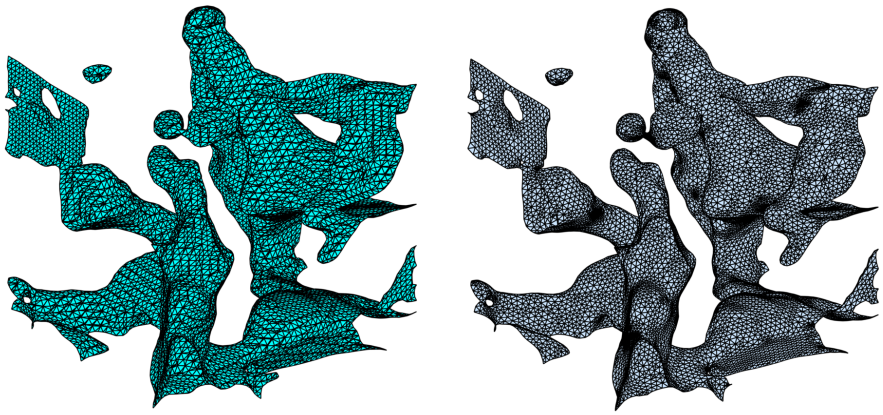

Figure 5.7: Subset of the whole surface mesh - Left : Initial non optimized surface triangulation obtained by the Marching Cube algorithm (Lorensen and Cline, 1987), Right : Optimized mesh based on extended Persson-Strang truss analogy

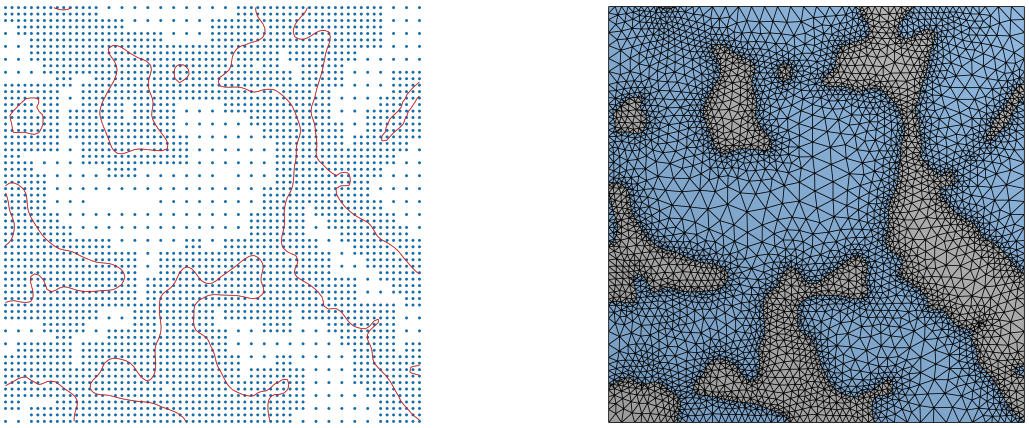

Figure 5.8: Left : Extraction of external contours of sandstone sample and octree nodes belonging to the choosen face, Right : Optimized external structure boundary face mesh using extended Persson-Strang truss analogy

the octree decomposition are extracted to mesh independently the 6 boundary faces as a 2D problem as illustrated in Figure 5.8.

The process ends by merging the 6 optimized structure boundary faces meshes with the optimized internal pore space surface meshes; that will constitute the constrained facets providing a closed surface mesh to the CDT to ensure the mesh conformity as illustrated in Figure 5.9.

Volume meshing

The last step aims at generating the volume mesh for the solid phase volume and for the pore space volume, applying an efficient method that can generate boundary-conforming tetrahedral meshes such as CDT (Shewchuk, 2002). The constrained facets are given as input to the CDT module of the well-known and

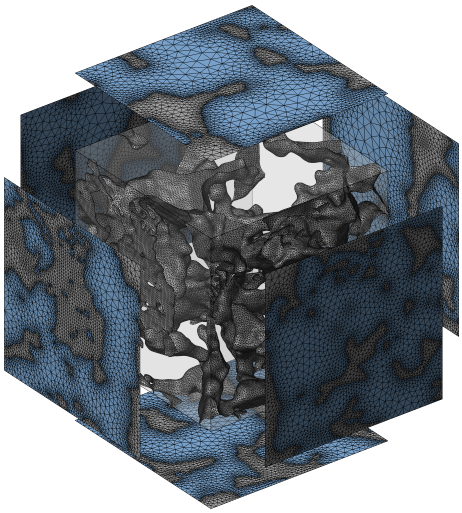

Figure 5.9: Exploded view of merged internal material boundaries and external structure boundaries constituting the enclosed constrained facets taken as input in CDT

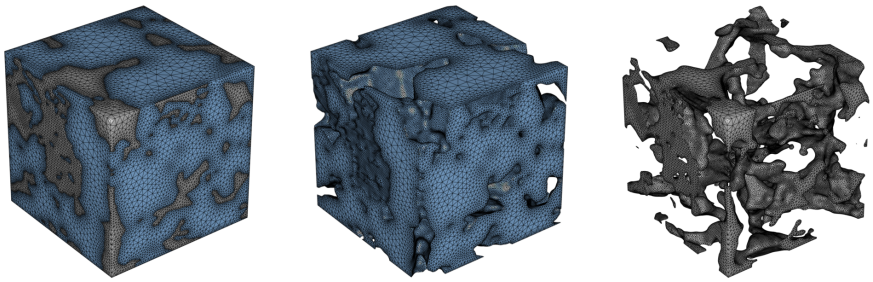

Figure 5.10: Final optimized conform mesh of the RVE (# Nodes=256 303/# Elements=1 525 220) - Left : Global view of the optimized mesh for both phases (Solid phase/Pore space), Center : Solid phase meshed only, Right : Pore space meshed only

robust mesh generator TetGen (Si, 2015), while the octree nodes distribution constitutes the background grid on which the CDT is applied. Finally, the extended Persson truss analogy process is applied to improve low quality elements appearing near the constrained facets due to the geometrical complexity and the imposed conformity. Figure 5.10 illustrates the optimized conforming mesh generated for the segmented sandstone sample.

5.3.2 Embedded weak discontinuity models

Regarding the problem of heterogeneous medium meshing, the most natural approach is to turn to conforming meshes as presented previously. Although being very efficient, the whole process may still suffer from poor quality elements

for intricate geometrical configurations. More importantly, it may be difficult to consider evolving morphologies resulting of the development of cracks.

An alternative consists of building the approximation from non-adapted meshes. The main difference then lies in the fact that the nodes are positioned independently of the interfaces between the solid phase and the pore space. This avoids the need for relocating these nodes according to the heterogeneous geometry. This aspect is a major advantage towards some applications, such as probabilistic numerical studies with materials with a fine scale geometry that is not controlled. As a result of the use of a non conforming mesh, many elements - potentially all of them - are, for a given geometry, cut in two parts by a physical interface between the solid and the pore phase. Each of the two sub-domains of these elements defined by such an interface is included in a material phase, the properties of which are assumed to be known and different from the neighboring one. In order to allow these elements to represent this contrast of properties, it is necessary to enrich their kinematics by adding discontinuities in the interpolation of the strain field - so-called "weak" discontinuities. Figure 5.11 shows a typical 4 noded element with such a discontinuity.

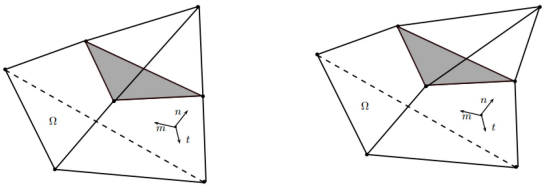

Figure 5.11: Four noded element enriched by a strain discontinuity: left undeformed; right deformed.

Hence the kinematic enrichments constitute the keystone of this methodology. Originally developed to assess the problems posed by cracking in Finite Element models, such an enrichment is also advantageous in the context of the explicit consideration of heterogeneity. The methods of practical implementation of kinematic enhancements within a Finite Element model can be classified into two broad categories. Global approaches, on the one hand, are essentially based on the Partition of Unity. The enrichment then consists of the addition of interpolation functions and thus consists of adding global unknowns and global equations. The XFEM - eXtended Finite Element Method (Moës et al., 1999) - belongs to this first category and has been used, for example, to describe three-dimensional arrangements of non-overlapping spheres (Moes et al., 2003). An enrichment can be also be built, on the other hand, from a purely local point of view, leading to the family of methods called EFEM - Embedded Finite Element Method (Simo et al., 1993). Also originally developed to tackle the problem of cracking - in particular the numerical

localization induced by the use of softening laws - these approaches lead to an enrichment by means of local functions at the element level. Each of these added functions leads to an additional unknown and an additional scalar equation. The local character of those equations however makes it possible to condense them at the element level, thus preserving the size of the assembled discrete problem. Within this second family of methods of enrichment, the Method of Incompatible Modes is chosen here (Ibrahimbegovic and Wilson, 1991).

The theoretical framework of the Incompatible Modes Method is based on the three fields variational form from Hu-Washizu (Washizu, 1982). In this form, the potential energy writes:

$$\Pi_{HW}(u,\varepsilon,\sigma) = \int_\Omega \Psi(\varepsilon)\,\mathrm{d}\Omega - \int_\Omega \sigma\cdot(\varepsilon-\nabla^s u)\;\mathrm{d}\Omega - \int_{\partial\Omega_{vN}} u\cdot\bar{t}\,\mathrm{d}S \tag{5.8}$$

According to the basic principle of EFEM methods (Simo and Rifai, 1990), the strain field ε can be enriched according to the form $\varepsilon = \nabla^s u + \tilde{\varepsilon}$. This gives an expression depending on the displacement field u, the enrichment $\tilde{\varepsilon}$ and the stress field σ:

$$\Pi_{HW}(u,\tilde{\varepsilon},\sigma) = \int_\Omega \Psi(\nabla^s u+\tilde{\varepsilon})\,\mathrm{d}\Omega - \int_\Omega \sigma\cdot\tilde{\varepsilon}\,\mathrm{d}\Omega - \int_{\partial\Omega_{vN}} u\cdot\bar{t}\,\mathrm{d}S \tag{5.9}$$

The stationary character of Π_{HW} leads to the three-field formulation of the enriched mechanical problem:

Knowing: $\bar{t} : \partial\Omega_{vN} \to \mathbb{R}$
For all: $u \in \mathbb{U}_0$, $\tilde{\varepsilon} \in L_2(\Omega)$ and $\sigma \in L_2(\Omega)$
Find: $u \in \mathbb{U}$, $\tilde{\varepsilon} \in L_2(\Omega)$ and $\sigma \in L_2(\Omega)$
Such that:

$$\int_\Omega \nabla^s u\cdot\frac{\partial\Psi}{\partial\varepsilon}\mathrm{d}\Omega - \int_{\partial\Omega_{vN}} u\cdot\bar{t}\;\mathrm{d}S \quad + \int_\Omega \tilde{\varepsilon}\cdot\left(\frac{\partial\Psi}{\partial\varepsilon}-\sigma\right)\mathrm{d}\Omega - \int_\Omega \sigma\cdot\tilde{\varepsilon}\mathrm{d}\Omega = 0 \tag{5.10}$$

A compact spatial discretization for each of these fields can be defined. The Incompatible Modes Method - from which its name derives - provides, for the enriched deformation field, a base of orthogonal functions in $L_2(\Omega)$ to the ones chosen for the interpolation of the stress field.

$$\nabla^s u^h = B^T\cdot U \tag{5.11}$$

$$\tilde{\varepsilon}^h = G^T\cdot\upsilon \tag{5.12}$$

$$\sigma^h = P^T\cdot s \tag{5.13}$$

This type of interpolation leads to two sets of - potentially nonlinear - equations to solve that can be grouped as a vector of residual equations $\mathbf{r}$. On the one hand, a

set of global coupled equations $\mathbf{r}_{FE}$ is stemming from the FEM assembly operation; while on the other hand, a set of decoupled local equations r_e associated with each of the new parameters of incompatible modes is introduced. These parameters are the additional unknowns associated with the enrichment of the kinematics.

$$\mathbf{r} = \begin{bmatrix} \mathbf{r}_{\mathrm{FE}} \\ [r_{\mathrm{e}}]_{\mathrm{e}} \end{bmatrix} = \begin{bmatrix} \int_{\Omega} B \cdot \frac{\partial \Psi}{\partial \varepsilon} \mathrm{d}\Omega - \int_{\partial \Omega_{v_N}} N \cdot \bar{t} \, \mathrm{d}S \\ \left[\int_{\Omega} G^e \cdot \frac{\partial \Psi}{\partial \varepsilon^e} \, \mathrm{d}\Omega \right]_{\mathrm{e}} \end{bmatrix} \tag{5.14}$$

The key point of the Incompatible Modes Method lies in its local character, and thus in the r_e decoupled equations. Even in a nonlinear case, their solving is very fast and the incompatible mode parameters can be easily condensed at the local level (Wilson, 1974).

Using the Incompatible Modes Method, in order to construct the enrichments, the CT scan sample 3D image is projected on a tetrahedral unstructured mesh generated using the GMSH software (Geuzaine and Remacle, 2009). This projection is a feature offered by the python library SPAM (Andó et al., 2019; Furrer and Sain, 2010; Gerber and Furrer, 2015; Gerber et al., 2017). This allows identifying tetrahedra from each phase (solid phase and pore space) and the tetrahedra crossed by the interface that are enriched kinematically. For the considered scan, this results the model illustrated in Figure 5.12.

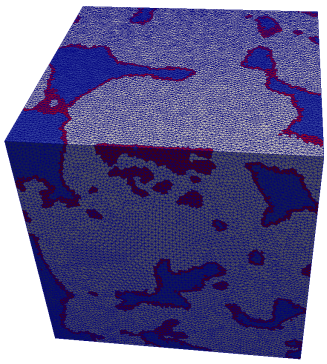

Figure 5.12: Embedded weak discontinuity models (# Nodes=234 996/# Elements=1 329 159) obtained from the CT scan with solid elements (grey), pore space elements (blue), enriched elements (red)

5.4 Comparison of FEM and EFEM methods based on a segmented sandstone sample

To illustrate the ability of the models to conduct image-based finite element simulations, and to build the comparison between their results, the models derived from the CT scans are now subjected to two triaxial mechanical loading conditions

as illustrated in Figure 5.13. First, a purely isotropic triaxial compression. The considered sample being isotropic (because of its limited size, unlike the overall material (Hu et al., 2018)), this matches an almost isotropic triaxial macroscopic strain state. Second, the sample is subjected to a deviatoric state to assess the magnitude of the local stress concentrations obtained in typical scenarii of triaxial testing.

Unlike in conforming finite element simulations, the Embedded Finite Element method requires considering a second phase in the pore space, described by solid-like constitutive laws. To comply with this requirement, the simulations use a second phase in the pore space with properties close to water (Poisson coefficient and the shear modulus tend towards 0.5 and 0 respectively). Preferring to avoid any consideration of fluid flow, the test is assumed undrained in the simulation.

The simulations are conducted with linear elastic materials. The model consists of a solid phase with properties $E = 10$ GPa and $\nu = 0.2$. The pore space is filled with a medium with properties $E = 0.13$ GPa and $\nu = 0.49$ to simulate the presence of an interstitial fluid (water). It is obvious that the values of the parameters used in simulations are somewhat arbitrary in the sense that they are values of macroscopic parameters used in a microscopic context. As a matter of facts, microscopic parameters in rock mechancis are difficult to identify and require advanced methods such as micro-indentation tests (Randall et al., 2009; Mahabadi et al., 2012) or micro-scratch tests (Akono et al., 2011) to determine them. Even with such tests, microstructural simulations are useful to derive values of actual model parameters and for interpretations, which motivates investigating the effect of their variation as performed in the sequel.

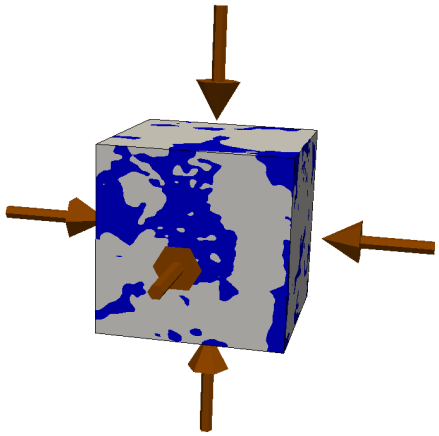

Figure 5.13: Sandstone sample of size $[500\,\mu m, 500\,\mu m, 500\,\mu m]$ subjected to a purely isotropic compression

For the interpretation of the numerical results, a classical Mohr-Coulomb failure criterion is considered, associated with a cut-off criterion for the tensile strength.

In this composite criterion, the tensile cut-off aims at representing conditions giving rise to local cracking, while the Mohr-Coulomb part represents local conditions for the onset of local plasticity. It writes in $\sigma_3 - \sigma_1$ plane:

$$\begin{cases} \text{compression } \sigma_1 = K_p\,\sigma_3 + \sigma_c \\ \text{tension } \ \sigma_3 = -\sigma_t \end{cases} \tag{5.15}$$

in which σ_c is the uniaxial compressive strength, σ_t is the tensile strength and

$$K_p = \frac{1 + sin\phi}{1 - sin\phi} \tag{5.16}$$

where ϕ is the friction angle. With a Mohr-Coulomb failure criterion, the uniaxial compressive strength can be expressed in terms of the cohesion c and friction angle as:

$$\sigma_c = \frac{2\,c\,cos\phi}{1 - sin\phi} \tag{5.17}$$

The macroscopic cohesion c and friction angles ϕ of the Vosges sandstone are deduced from shear strength data obtained from triaxial tests and reported in (Besuelle et al., 2000). They are equal to 10 MPa and 37°respectively. Those values are also consistent with the ones reported by Hu (Hu et al., 2018). A uniaxial compressive strength σ_c of 60 MPa is therefore considered. No direct experimental data are available on the tensile strength of the Vosges sandstone. Recent efforts showed that the tensile strength values obtained by different techniques can differ significantly (Perras and Diederichs, 2014). Practical estimates for the tensile strength of different sandstones were reported in (Cai, 2010), with a link to the uniaxial compressive strength given by

$$\sigma_t = \frac{\sigma_c}{R} \tag{5.18}$$

The value of the ratio R was found to range from 8 to 26 (with exceptionally even larger values). As a result, there is an interest to consider different values for the post-processing of computational results in the sequel, and tensile strengths considered from 2 to 6 MPa will be considered.

For the interpretation of the failure mechanisms, a plastic state parameter (PP) is computed locally based on the local stress state. It represents in a way the normalized distance to the nearest failure line of the composite criterion (Mohr-Coulom or cutoff). It writes:

$$\text{PP} = \begin{cases} \max\left(\underbrace{\left|\dfrac{\sigma_1}{K_p\,\sigma_3 + \sigma_c}\right|}_{\text{MC}}; \underbrace{\dfrac{-\sigma_3}{\sigma_t}}_{\text{Tension}}\right) & \text{if } \sigma_3 > -\sigma_t \\ \underbrace{\dfrac{-\sigma_3}{\sigma_t}}_{\text{Tension}} & \text{if } \sigma_3 \leq -\sigma_t \end{cases} \tag{5.19}$$

A local value above one of this ratio indicates that the onset of material nonlinearity is reached. A parametric variations of the plastic parameters (PP) is equivalent to changing the properties of the material.

Only the solid phase of interest is reported on the figures of the next sections. For the embedded discontinuity model, the solid phase value of the enriched elements is plotted for the entire element for simplicity, hence the jagged aspect of the boundary.

Finally, the choice was made here to compare the methods based on models generating a comparable simulation cost. In other words, the assembly and system solving is made similar by using meshes containing comparable numbers of nodes (256300 and 235000 for FEM and EFEM respectively) and elements (1525000 and 1329000 for FEM and EFEM respectively).

5.4.1 Conforming model

The application of a triaxial isotropic compression of 50 MPa is first considered. This stress level matches the ones of classical tests (Selvadurai and Głowacki, 2008). This stress state is imposed by means of imposed deformations through applied kinematically uniform boundary conditions on the sample (uniform displacement of the model boundaries). The subset of the CT scan considered shows a isotropic behaviour, leading to a triaxial isotropic compression. Note that the base material is not fully isotropic (Hu et al., 2018), and the isotropy of the considered sample is caused by its limited size (lack of representativity).

A first analysis of the effect of heterogeneity induced by the presence of the pores can be performed by extracting the locations in the sample where tensile stresses are present (tensile stresses are considered here negative according to the usual convention in rock mechanics). Such stress states are represented in Figure 5.14. The left part of Figure 5.14 depicts the histogram of the most negative local principal stresses σ_3 in the mesh (lowest principal stress value when considering tensions as negative). The right part of Figure 5.14 represents the negative part of this histogram. It can be seen here that the presence of the pore space has a negligible effect on the presence of local tensions in the microstructure when considering a macroscopically isotropic stress state.

The composite criterion (5.15) for the detection of the onset of cracking and plasticity can be further exploited to examine the local conditions for the presence of local material nonlinear response. Figure 5.15 left depicts the local stress states in the sample together with the assumed composite criterion for $R = 15$ ($\sigma_t = 4$ MPa). All points located outside the criterion are indicating that the cracking/plasticity onset is reached inside the microstructure. It can be seen that the macroscopic isotropic compression state (no macroscopic deviatoric stress) is translated into a set of stress states that significantly deviates from a isotropic stress state locally.

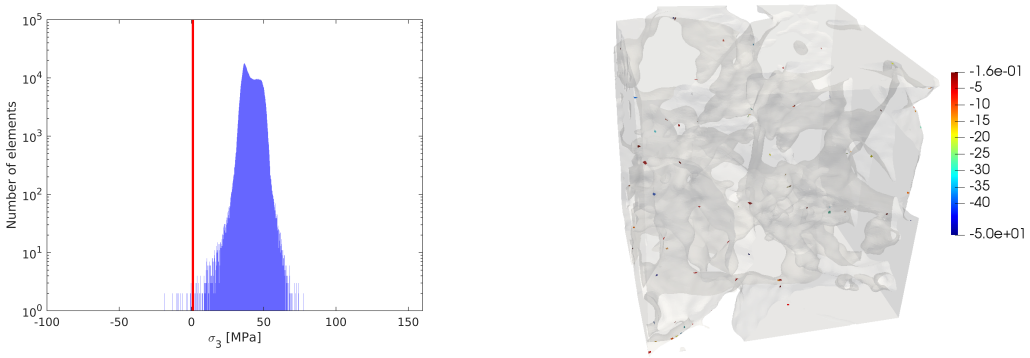

Figure 5.14: Finite elements - Isotropic loading - Left : Histogram of σ_3 values obtained by FEM (red line isolates the tensile values), Right : Elements undergoing tension in the 3D volume predicted by FEM

For most of the points representing the stress states in this figure, the largest compressive principal stress exceeds the lowest compressive stress by a factor that ranges from 1 to 3. Yet, the number of points exceeding the criterion remains rather limited. Most of the points located outside the criterion activate mainly the Mohr-Coulomb part of the criterion. Note that this assessment is purely based on the assumption that the fine scale material parameters values are comparable to the ones identified macroscopically. Figure 5.15 left also allows assessing to what extent a change of fine scale material strength parameters with respect to the macroscopic ones would affect the development of local plasticity. It can be seen from Figure 5.15 left that only a decrease of the angle of friction would significantly affect the number of stress state points exceeding the criterion. This is also reflected in Figure 5.15 right that represents the value of the local plastic state parameter (PP) according to the minor principal stress. The horizontal dashed line represents the threshold above which local failure/plasticity would be activated. From this figure, it can be seen that an important number of points are located above PP = 0.5.

Further illustrations of the results can be given in order to understand the link between the microstructural geometry and the presence of stress states for which the failure criterion is reached. To this end, the PP defined above is depicted on cuts in the sample in Figure 5.17, where a PP value of 1 is attributed to the points exceeding the composite failure criterion. Note that such higher values are also located in positions closer to the external faces of the sample as a result of the stiff boundary conditions applied.

As a second illustration, a triaxial loading with an important deviator is applied on the sample. Based on the data reported in (Besuelle et al., 2000), the loading considered is determined such that it matches a stress state at which the macroscopic failure is not yet reached, but for which an increase of the deviator would reach the macroscopic shear strength criterion in its linear part. This loading is taken as

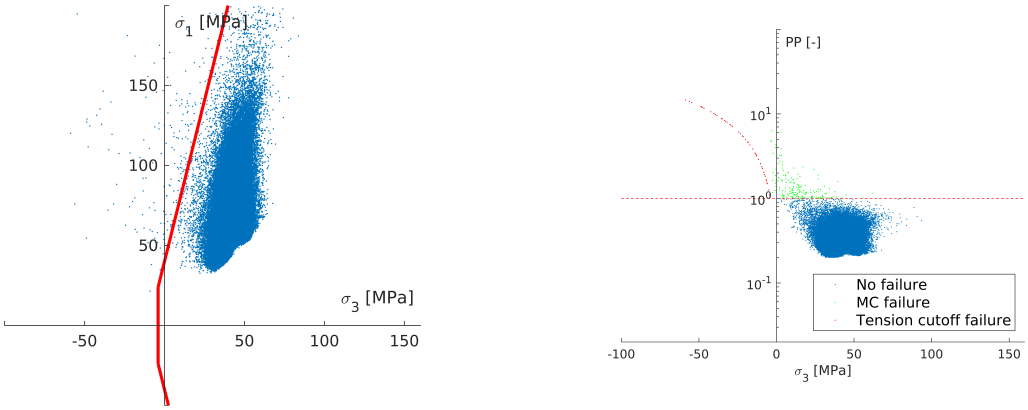

Figure 5.15: Finite elements - Isotropic loading - Left: Stress state representative points in $\sigma_3 - \sigma_1$ plane. In red, failure line expressed with a Mohr-Coulomb criterion with the parameters defined above ($c = 10$ MPa, ϕ =37°) and with tensile cut-off at $\sigma_t = 4$ MPa, Right: Plasticity state parameter (PP) with points exceeding the tensile part of the criterion in green and the Mohr-Coulomb criterion in red

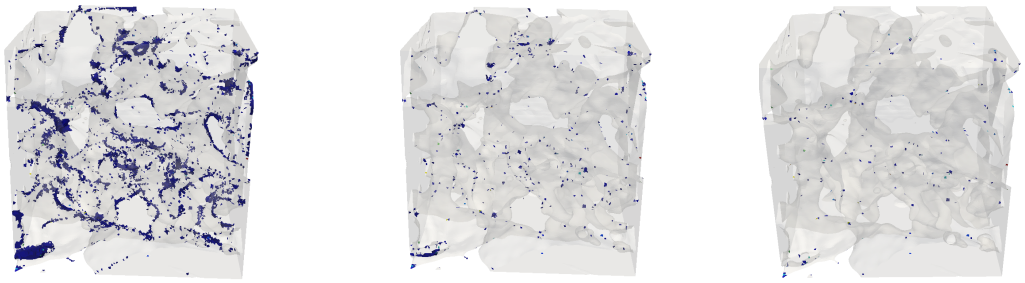

Figure 5.16: Finite elements - Isotropic loading - Plasticity state parameter : PP ≥ 0.5 (Left), PP ≥ 0.7 (Center), PP ≥ 1 (Right)

σ_1 =50 MPa, $\sigma_2 = \sigma_3$ =20 MPa. To apply those boundary conditions, the principal (compressive) stress values are translated into principal (contraction) strain values, using the homogenized stiffness of the material. The homogenized stiffness of the material was obtained from simulations, and was assumed isotropic for the sample used here (homogenized values from computations showed a deviation of less than 2.3% with respect to isotropy for the stiffness components).This of course may have an impact on the isotropic or anisotropic nature of a real sandstone. But, as mentionned in Section 2, this subset was taken as such essentially for numerical considerations (i.e. computational cost), and not to assess the degree of isotropy of the material.

Figure 5.18 represents the local stress states in the sample for the above deviatoric macroscopic loading. Clearly, the deviatoric loading further expands the range of the local major principal stress. A significant number of representative points exceed the criterion, showing that plasticity and failure are locally extended within the sample. Note of course that the simulation remains elastic, and that stress redistributions

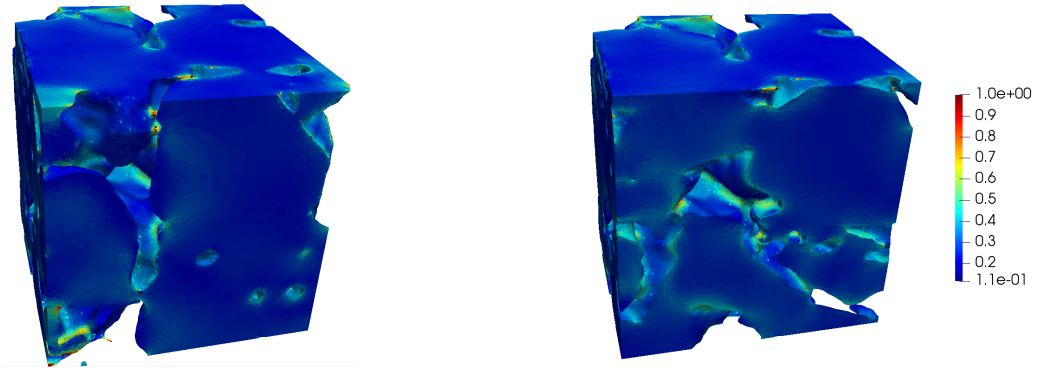

Figure 5.17: Finite elements - Isotropic loading - Plasticity indicator PP in the 3D volume, for two cuts ($x = 0$ on the left and $x = 82$ on the right) in the sample. Elements exceeding composite failure criterion match (in red) are characterised by a PP of 1.

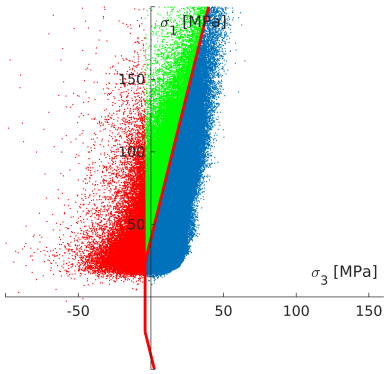

Figure 5.18: Finite elements - Deviatoric loading - Stress state representative points in $\sigma_3 - \sigma_1$ plane of the deviatoric case with elements activated by the tensile parts in red and MC parts in green. In red, failure line expressed with a Mohr-Coulomb criterion with the parameters defined above ($c = 10$ MPa, ϕ =37°) and with tensile cut-off at $\sigma_t = 4$ MPa

.

have to be expected as from the first plastification. The corresponding spatial distribution of points having exceeded the criterion in the sample is given in Figure 5.19. It is clear from this figure that the local material nonlinearity is reached through both parts of the criterion. It also illustrates that the tension part of the criterion is increasingly reached for decreasing tensile strength as expected.

5.4.2 Embedded discontinuity model

Like for the finite element model, the embedded discontinuity approach is first tested using the the triaxial compression case. This is achieved using the mesh presented in Figure 5.12.

For the isotropic compression, the histogram of the lowest principal stress values in the model is depicted in Figure 5.20. Unlike for the finite element case, no element in the mesh is found to be subjected to local tensile stresses. This difference may

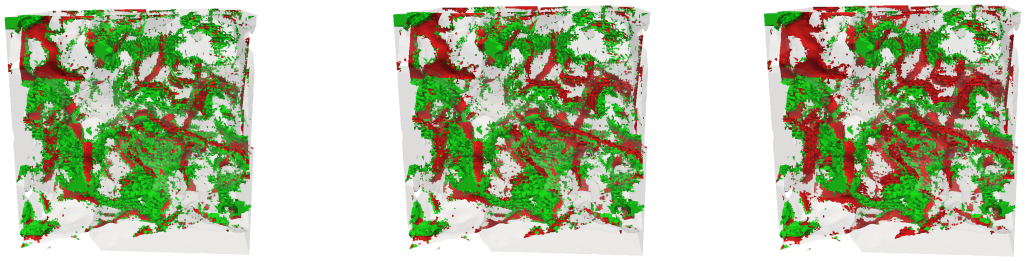

Figure 5.19: Finite elements - Deviatoric loading - Elements where the PP is above 1 depending on whether the tensile (red) or MC parts (green) are activated for different value of σ_t : 6 MPa (Left), 4 MPa (Center), 2 MPa (Right)

be related to the local level of discretization. The embedded discontinuity model makes use of a uniform element size, while the classical finite element model uses selective refinement/unrefinement depending on the local features of the geometry. In view of the limited amount of tensile stressed elements found based on the finite element model, this is however not a problematic difference.

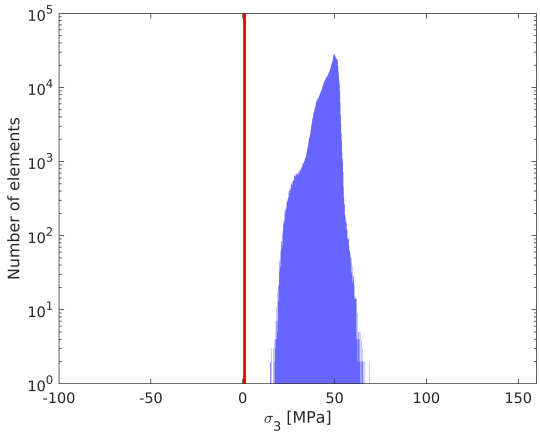

Figure 5.20: Embedded discontinuity model - Isotropic loading - Histogram of σ_3 values obtained by the embedded discontinuity model

Points representing the stress states with respect to the assumed criterion are represented in Figure 5.21 left. This distribution of points in the $\sigma_3 - \sigma_1$ space is quite different from the similar graph obtained by classical finite elements (Figure 5.15). With the embedded discontinuity model, the translation of the macroscopic isotropic compression state into local stress states exhibits a significantly lower deviation from a isotropic stress state. For most of the points representing the stress states in Figure 5.21, the largest compressive principal stress exceeds the lowest one by a factor that ranges from 1 to 2 (rather than 3 for the conforming finite element simulation). Like deduced from the finite element model, only a decrease of the angle of friction would significantly affect the number of stress state points exceeding

the criterion, but in lower proportions than with the conforming finite element simulation. This is also reflected in Figure 5.21 right. The horizontal dashed line represents the threshold above which plasticity would be activated. From this figure, it can be seen that much lower values of PP should be considered to embed points representing stress states inside the sample. As a consequence, Figure 5.16 remains quite different from the equivalent figure for finite elements. Much less points are found in the range of PP above 0.7, even though the figure corresponding to PP=0.5 is rather similar to the classical finite element case.

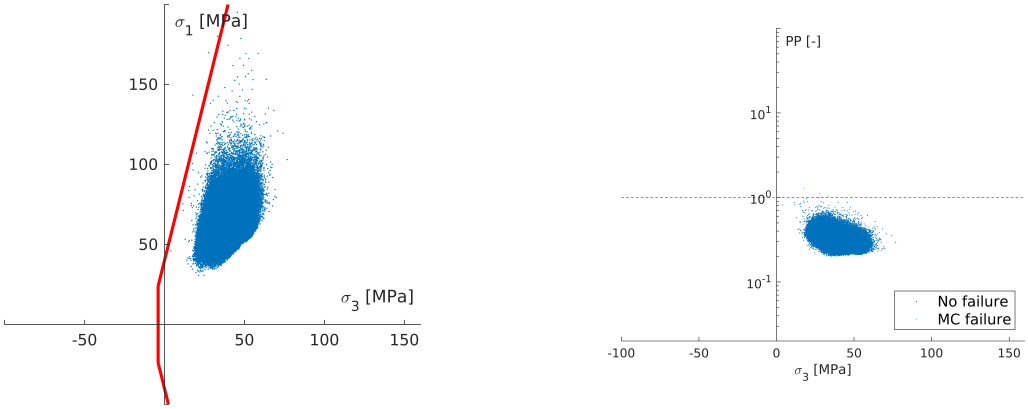

Figure 5.21: Embedded discontinuity model - Isotropic loading - Left: Stress state representative points in $\sigma_3 - \sigma_1$ plane. In red, failure line expressed with a Mohr-Coulomb criterion with cut-off in tension $\sigma_t = 4MPa$, Right: Plasticity state parameter (PP) with points exceeding the tensile part of the criterion in green and the Mohr-Coulomb criterion in red

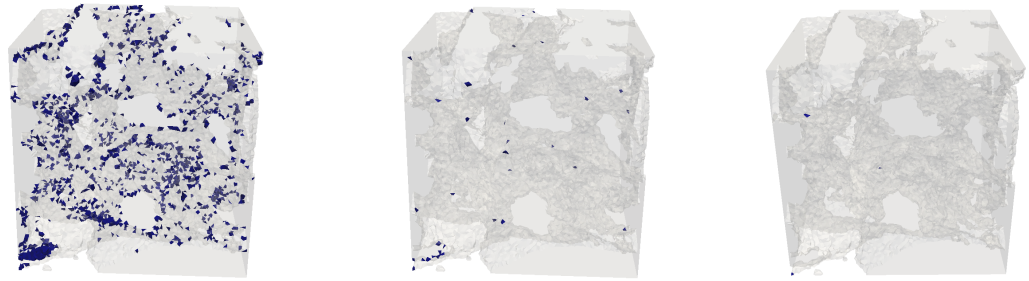

Figure 5.22: Embedded discontinuity model - Isotropic loading - Plasticity state parameter : PP ≥ 0.5 (Left), PP ≥ 0.7 (Center), PP ≥ 1 (Right)

These examples show that the model results differ due to their essential features. The classical finite element model is defined such that local geometrical features are captured by selective refinement. Small pores are strongly refined, while large solid components are discretized by coarser elements. Conversely, the embedded model has the objective to allow discretizing any microstructures (here any subset of a full CT scan) with the same uniform mesh. The small features are thus

less well captured in the latter, while it shows a much improved flexibility for studying many configurations with the same mesh. This is further illustrated when comparing the cuts given in Figure 5.23 with their conforming finite element counterpart in Figure 5.17.

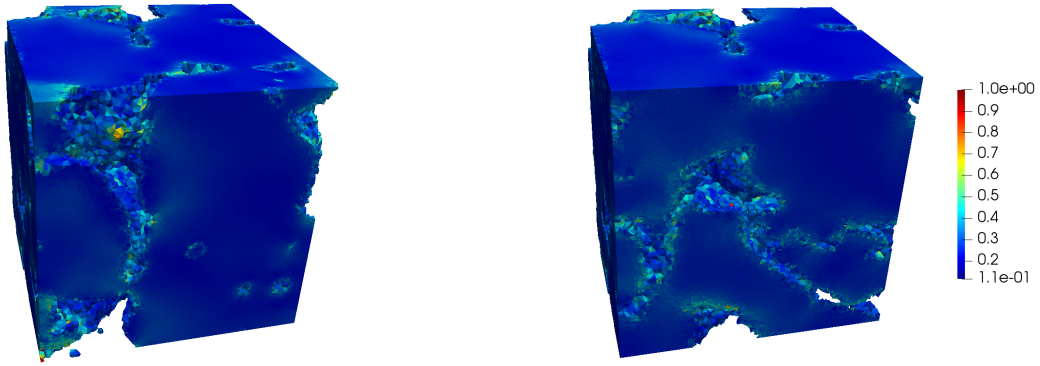

Figure 5.23: Embedded discontinuity model - Isotropic loading - Plasticity indicator in the 3D volume, for two cuts ($x = 0$ on the left and $x = 82$ on the right) in the sample. Points undergoing plasticity match (in red) are characterised by a PP of 1

When subjected to the same deviatoric loading as the classical finite element model, the identified trends are confirmed. Figure 5.24 represents the local stress states in the $\sigma_1 - \sigma_3$ plane. Like for the isotropic compression case, the range of variation of the most compressive principal stress remains more restricted in the embedded discontinuity model than for classical finite elements, as can be appreciated by comparing Figure 5.24 with Figure 5.18. The number of points having exceeded the tensile part of the criterion is also much lower. This translates directly in the spatial distribution of points having exceeded the criterion represented in Figure 5.25. When comparing Figure 5.25 with Figure 5.19, it can be noticed that the tensile failure is much less detected in the embedded discontinuity model, irrespective of the level of tensile strength considered. Some detailed zones having reached the Mohr-Coulomb part of the criterion are also less detected (see for instance the top-left-back part of the sample in Figures 5.25 and 5.19). These latter differences seem to be concentrated in the smallest pores, a fact that points again to the local refinement levels as explained above.

5.4.3 Comparison of FEM and EFEM results

To have a clearer comparison between the results of both models on detailed views, a cut of the 3D results is provided here for the lowest compressive stress and for the value of PP.

For the isotropic loading case, Figure 5.26 compares the values of the lowest principal stress in a slice at $x = 82$ for both methods, while Figure 5.27 compares

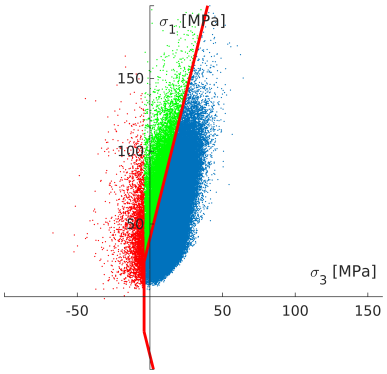

Figure 5.24: Embedded discontinuity model - Deviatoric loading - Stress state representative points in $\sigma_3 - \sigma_1$ plane of the deviatoric case with elements activated by the tensile parts in red and MC parts in green. In red, failure line expressed with a Mohr-Coulomb criterion with the parameters defined above ($c = 10$ MPa, ϕ =37°) and with tensile cut-off at $\sigma_t = 4$ MPa

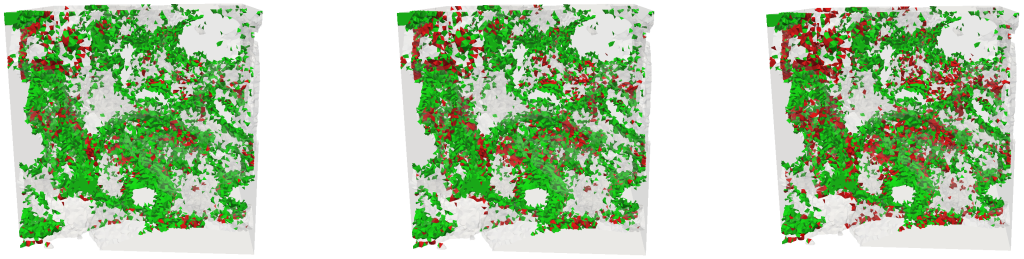

Figure 5.25: Embedded discontinuity model - Deviatoric loading - Elements where the PP is above 1 depending on whether the tensile (red) or MC parts (green) are activated for different value of σ_t : 6 MPa (Left), 4 MPa (Center), 2 MPa (Right)

the plasticity indicator PP. Some boundary effects appear at the surface of the solid phase in the embedded discontinuity model. They may be related to the use of strongly differing properties between the solid phase and the pore fluid-like phase. Yet, the stress distribution plot illustrates that the overall stress distribution is similar for both models, with only a more accurate estimation of the stress concentrations as a result of the selective mesh refinement in the classical finite element model. It can also be seen that the smallest pores (or the position at which the pore throats are smallest) are better reproduced by the classical finite elements for the same reason. An identical conclusion can be drawn from the map of the PP parameter. Note that as presented above, the levels of stress in this cut induced by the triaxial isotropic compression do not trigger plasticity/failure as indicated by the level of PP reached.

A similar set of figures are produced below for the deviatoric loading tested. For the isotropic loading case, Figure 5.28 compares the values of the most tensile principal stress in a slice at $x = 82$ for both methods, while Figure 5.29 compares the plasticity indicator PP. Here also, the overall distributions of the stress field

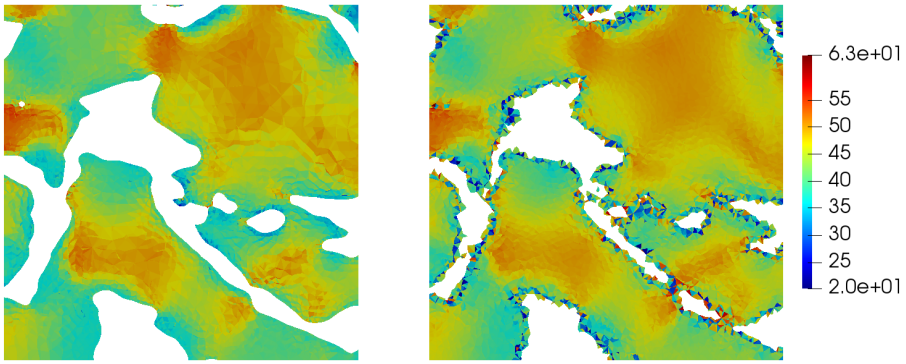

Figure 5.26: FEM (left) and EFEM (right) results of σ_3 values on a slice in plane $x = 82$ for the isotropic loading case. Only the solid phase is represented for the sake of clarity

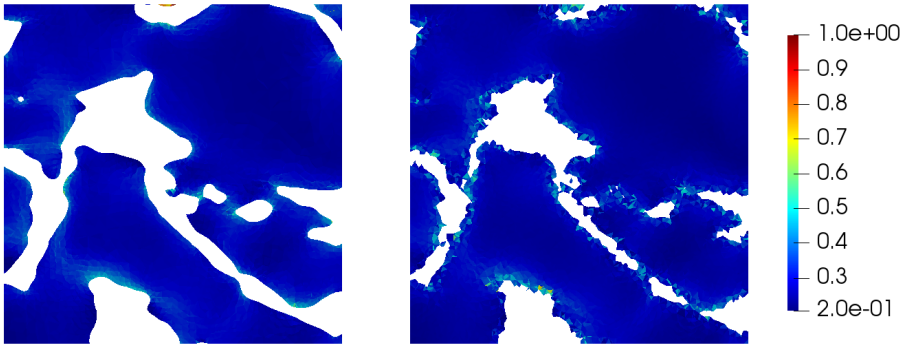

Figure 5.27: FEM (left) and EFEM (right) results of PP values on a slice in plane $x = 82$ for the isotropic loading case. Only the solid phase is represented for the sake of clarity

and the PP values are globally matching, with only deviations related to the selective refinement present in the finite element model, but not in the embedded discontinuity model. Note that the PP value color bar was capped to a unit value. Dark red values therefore include elements in which PP is larger than unity, and in which local failure/plasticity is indeed triggered. In these zones, the refined elements of the conforming finite element model have a clear impact on their extent with respect to the embedded discontinuity model.

5.5 Discussion

The computations performed in this contribution based on a 3D image of a sandstone show that automated computational models can be set up to exploit raw CT scan data. The detailed comparison of two discretization schemes able to process such raw data showed that both approaches are consistent with each other delivering complementary features. The finite element mesh generation

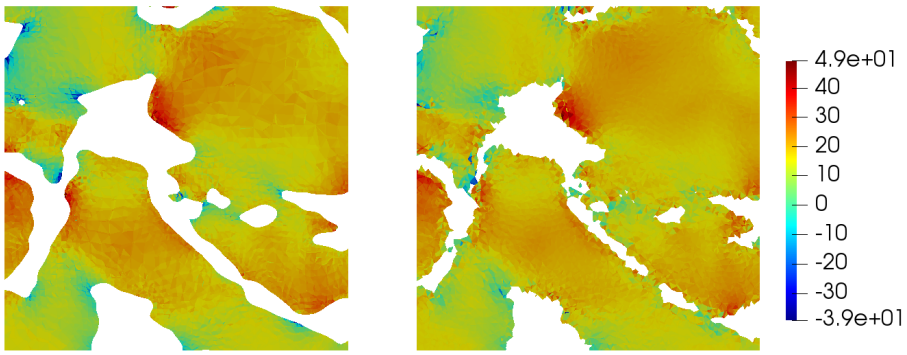

Figure 5.28: FEM (left) and EFEM (right) results of σ_3 values on a slice in plane $x = 82$ for the deviatoric loading case. Only the solid phase is represented for the sake of clarity

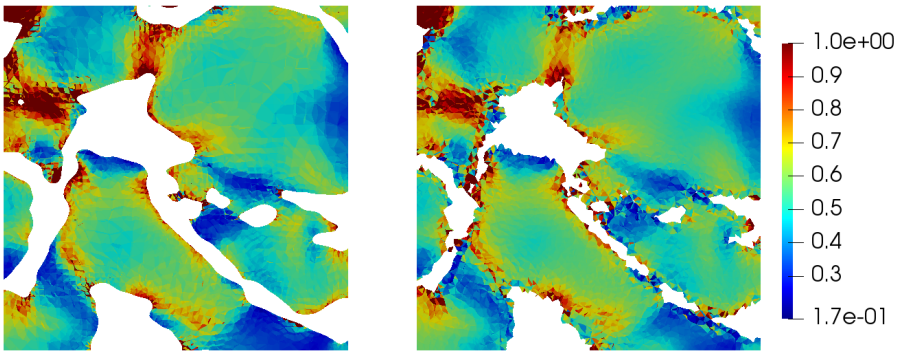

Figure 5.29: FEM (left) and EFEM (right) results of PP values on a slice in plane $x = 82$ for the deviatoric loading case. Only the solid phase is represented for the sake of clarity

with selective refinement allows capturing detailed geometrical features of the microstructure. However, it requires a pre-processing stage to produce tetrahedral meshes with high quality elements. The embedded discontinuity-based models reproduce the overall mechanical effects. Being based on uniform size meshes, they are not designed to capture all the geometrical details, but present the advantage that their non conforming mesh can be projected on any microstructural geometry without change. The macroscopic homogenized response of both methods yields the same homogenized elastic properties (since the volume fractions of the phases are reproduced), but this agreement should of course be questioned when considering plasticity.

Next to these direct comparisons of results reached by both methods, some additional comments can be given, related to the selection of the methodology to use depending on the objectives targeted.

The first comment relates to the computational cost of the methods. The representation of the heterogeneous geometry by means of embedded weak discontinuities induces a marginal computational preprocessing cost that consists of the

detection of elements cut by the boundary surface of the pore network. A simple unstructured mesh can be used, which allows efficient simulations pre-processing. The kinematic enrichment is computed at the element level, and can be condensed before assembly, which does not cause any additional cost in terms of the generated system of discretized equations. Post-processing would however require an additional implementation of tetrahedra cutting for vizualization purposes (not implemented here). With respect to these features, the generation of a conforming mesh incurs the pre-processing cost associated with the generation of the target size function, and with the mesh optimization step for surface meshes and 3D meshes. These operations can however be optimized to reach a situation in which the set-up of model could be reached in a few minutes. Secondly, the use of a conforming mesh with element sizes constrained by local features leads to rather fine discretizations with the associated assembly and solving cost. This should be balanced with respect to the intended accuracy, but more importantly requires a careful understanding of the effects of the size functions parameters (dependency of element sizes to curvatures, to narrowness of pore channels, etc.). Finally, postprocessing of the results is fully standard as a result of the use of regular finite element meshes. Existing standard or dedicated FE packages with existing dedicated constitutive laws and formulations can also be used.

Other features remain different between both methodologies as a result of the construction of the approximation. The embedded discontinuity methodology has the benefit of being extendable towards strong discontinuities for representing cracking. This is not the case for regular finite elements that require additional ingredients for the modelling of cracks (XFEM, embedded strong discontinuities, gradient regularization ...). Conversely, the consideration of an empty pore space (drained tests) can be more directly addressed by the conforming approach (no elements generated in the pore space) than by the embedded discontinuity approach that assumes the presence of a second phase in the definition of the discretization. A voided material therefore has to be approximated by a low stiffness material in the latter case, which may cause conditioning problems in the limit of a vanishing stiffness of the pore phase. Also, the extension to a quadratic interpolation of the displacement field is immediate for the conforming mesh generation (even though costly in terms of solving), while this is not straightforward in the case of embedded discontinuities.

From a physical viewpoint, the material properties of the solid phase were taken equivalent to the macroscopic material parameters as determined by (Hu et al., 2018) and by data from literature (Besuelle et al., 2000). This choice can of course be debated, and as illustrated in Section 5.4, the resulting locations affected by tensile stresses can affect results. Any decrease of the tensile strength may have a

considerable effect on the regions affected locally. The same reasoning holds to a lower extent for the Mohr-Coulomb part of the criterion. These facts bear significance for estimations of stress-induced permeability variations. As described in (Selvadurai and Głowacki, 2008; Massart and Selvadurai, 2014), isotropic and deviatoric triaxial loading on rocks can lead to permanent alterations of the permeability, potentially as a result of local material nonlinearities induced by the heterogeneity associated with the pore space structure. The results illustrated here show that 3D image-based models would allow investigating such potential microstructural effects.

5.6 Conclusion

This contribution presented the assessment of computational discretization strategies allowing to conduct automated simulations based on raw CT scan data for porous rocks with complex pore space morphologies. Both methods rely on pore and solid phase geometrical descriptions based on implicit functions and distance fields. Such a description can be obtained by level set-based segmentation techniques that were used here. Based on such implicitly described heterogeneous geometries, two discretization schemes were outlined. The first one makes use of the implicit description of the geometry to produce a conforming finite element discretization of the solid and pore phases. Based on the geometrical information, it allows generating selectively refined tetrahedral meshes to capture the complex geometry of the porous network and the corresponding solid boundaries. Complementarily, a second strategy based on a kinematic enrichment by incompatible modes is used to account for material boundaries based on a non-conforming mesh with uniform element sizes.

Mechanical simulations conducted on the CT scan pre-processed geometry show that both methods are consistent with each other. The conformal finite element procedure allows capturing the effect of more detailed geometrical features, while the incompatible mode-based framework is more flexible as it allows using the same (non conforming) mesh for potentially variable geometries. It is again emphasized that the simulations remain elastic, and that stress redistributions that have to be expected as from the first plastification cannot be captured by such simulations.

Future works are envisioned to exploit the benefit of both approaches. Some local geometrical information of the microstructure (translated as the target element size function defined in Section 3.1) could be used to produce tailored non conforming meshes with selective refinement by octree meshing at a marginal pre-processing cost. Finally all the tools that have been developed in this paper are adapted for simulations with a non linear mechanical behaviour of the solid phase (plasticity and tension cutoff), which allow considering the stress redistribution within the microstructure.

This chapter is based on the article titled "Image-based computational modelling of stress induced permeability alterations in sandstones" which is under preparation to be submitted in "International Journal of Rock Mechanics and Mining Sciences"

6

Image-based modelling of stress induced permeability alterations in sandstones

Abstract

This contribution presents an integrated and automated methodology for the computational analysis of permeability alterations in natural rocks under varying stress states, taking explicitly into account the complexity of the rock microstructure. The capacity of the methodology is highlighted on a subset of the microCT scans of a Vosges sandstone. After the generation of a high quality conformal mesh of the subset, isotropic compression at the scale of the microstructure is applied through FEM simulations. The adoption of non linear elastoplastic constitutive laws allows considering the local stress redistributions within the specimen. The mechanical loading of the subset highlights pore closures by local plastification. Permeability is evaluated at different confining pressures using the Lattice-Bolzmann method. Such a procedure allows analysing the impact of the pore space morphology (i.e. total porosity, pore size distribution, connectivity of the pore space, etc.) as well as the mechanical properties (i.e. stiffness and shear strength) on the evolution of the permeability under loading.

Keywords: Rock Mechanics, CT scan, Porous Rocks, Permeability alteration, Image-based Modelling, Automated Meshing, Finite Elements, Lattice-Boltzmann

Contents

6.1 Context

Experts from many fields such as petrochemistry, geology or hydrology are interested in understanding the link between the microstructural morphology of geomaterials and their transfer properties for a multitude of industrial applications, including critical applications such as radioactive waste storage (Rutqvist et al., 2009), gas storage (de Jong, 2015) or the sequestration of CO_2 (Delshad et al., 2013). The rock is used in those cases as a natural protective barrier limiting fluid migration to the outside environment. These applications have to consider physical phenomena such as mechanical, thermal and chemical loadings at the scale of the pore space that can potentially have a significant impact on the macroscopic properties of the rock. An example is the storage of natural gas in underground installations (Katz and Tek, 1981). The gas is stored in the pores of rock materials such as sandstones. On demand, the gas is injected or extracted, which will induce stress redistribution around the storage wells (Hu et al., 2018). These stress redistributions can have a significant impact on the morphology of the solid skeleton and the pore space. Such a modification of the microstructure can impact the hydraulic transfer properties of the rock, such as the intrinsic permeability induced by clogging, re-closures, reopenings, of cracks or pores (Hu et al., 2020b). In this context, it has been shown in (Bérend et al., 1995) that the permeability, a concept introduced by Darcy (Darcy, 1857) measuring the ability of a porous medium to allow fluids to pass through it,

is mainly controlled by the spatial structure of the geomaterial, the porous network and the solid/fluid interaction, making it a key parameter in rock engineering. In this aspect, numerous experimental investigations have been carried out in the past on natural rocks in order to investigate the influence variations of the state of stress on permeability such as in (Kilmer et al., 1987; Farquhar et al., 1993; Morrow et al., 1984; Kwon et al., 2004; Meng and Li, 2013; Chalmers et al., 2012; Ghanizadeh et al., 2014; Gensterblum et al., 2015; Selvadurai and Głowacki, 2008; Selvadurai, 2015; Selvadurai and Głowacki, 2017). A decrease of up to 40% of the permeability of a sandstone submitted to a confining pressure of 20 MPa has been noted by Fatt (Fatt and Davis, 1952). In the same way, a Vosges sandstone undergoes a decrease in air permeability of about 50 % (Hu et al., 2018, 2020a) when an isotropic compressive stress state from 5 MPa to 40 MPa is applied. Permeability variations related to cracking under deviatoric loadings states were obtained by (Souley et al., 2001) for a granite, with an initial decrease (initial crack closure) followed by an increase of the permeability by several orders of magnitude. An irreversible decrease in permeability of a limestone caused by a triaxial isotropic compression was observed without significant macroscopic permanent deformation by (Selvadurai and Głowacki, 2008). This implies that under loading/unloading conditions, the irreversible decreases observed in permeability are assumed to be probably linked to the presence of local plastic deformations inducing a modification of the pore space potentially characterised by an alteration of the critical fluid flow paths.

In general, the modelling of rock physics is based either on theoretical models based on idealized microstructures and calibrated on experimental measurements, or on empirical laws derived from experimental measurements. As an example, one can cite the (semi)-empirical laws linking porosity to permeability such as Kozeny-Carman's law (Kozeny, 1927; Carman, 1937), the power laws linking permeability and porosity to stress sensitivity such as the natural logarithm model (Walsh, 1981), the power law model (Shi and Wang, 1986; Kwon et al., 2004), the exponential function model (Katsube et al., 1991), or the Two-Part Hooke's model (Zheng et al., 2015). However, these types of approaches do not allow a detailed investigation of the phenomena operating on the microscopic scale in order to gain insight on how a variation of the stress state way affect the rock microstructure leading to a modification of the flow in the porous network.

More recently, advanced imaging techniques such as X-ray microtomography (Mees et al., 2003; Cnudde and Boone, 2013; Desrues et al., 2010), FIB-SEM (Song et al., 2015), TEM (Wiktor et al., 2012) or synchrotron (Fusseis et al., 2014) have provided high-performance tools for analysing natural rocks with faster, more accurate and easier access to the 3D microstructure. This enabled more information to be extracted about the structure of the porous network (Arns et al., 2005b; Andrä

et al., 2013a,b; Andrew et al., 2013; Blunt et al., 2013). As a result, in addition to permeability, porosity or pore size distribution obtained by experimental methods, other parameters such as pore connectivity, tortuosity, percolation networks can be identified without being intrusive to the geomaterial (Robinet et al., 2012; Keller et al., 2013). Obviously, the evaluation of these additional properties remains dependent on the resolution and the volume of data available. Combined with high performance computing, these methods started paving the way towards multiple possibilities in terms of numerical analysis.

From a numerical point of view, various strategies have been used for the simulation of fluid flow within porous microstructures, from Lattice-Botzmann methods in experimentally obtained topologies (Sun et al., 2011; Keehm, 2004; Boek and Venturoli, 2010; Ahrenholz et al., 2006; Hyväluoma et al., 2012; Manwart et al., 2002; Narváez et al., 2013) to methods that identify the equivalent Darcy's properties. Such approaches are based on the Parallel Plates Model in the case of a fault flow (Massart and Selvadurai, 2012, 2014), use the Random Walk Model (Hu et al., 2013), or solve the Navier-Stokes equations based on finite elements (Narsilio et al., 2009; Borujeni et al., 2013; Narváez et al., 2013), finite volumes (Guibert et al., 2015; Petrasch et al., 2008), or finite differences schemes (Mostaghimi et al., 2012; Manwart et al., 2002). Through approaches such as pore network modelling (Bultreys et al., 2015, 2016; De Boever et al., 2016; Dong and Blunt, 2009), the complexity of the pore network is reduced to an assembly of pore bodies and pore throats of different sizes connected to each other through a virtual representation of the pore network as an assembly of pore bodies and pore throats of different sizes connected to each other. Due to their highly parallelizable potential and the possibility to directly perform simulations on voxellized images, Lattice-boltzmann methods are often a preferred choice to simulate the fluid behaviour on complex microstructures obtained via X-Ray microtomography (Andrä et al., 2013a). In contrast, few numerical studies have addressed the influence of stress state variations on the detailed local geometrical alterations of the porous network generated at the microstructural level, and in turn its impact on the transfer properties. Indeed, mechanical simulations on microstructures with complex geometries require tailored efficient discretization schemes. Different approaches can be selected for this purpose, depending on the degree of the geometrical complexity of the microstructures. Techniques based on extended finite element approaches (XFEM) (Legrain et al., 2011b; Moës et al., 1999; Sukumar et al., 2001) with level sets enrichment functions, CutFEM approaches (Csati et al., 2020) or embedded finite elements (Simo et al., 1993; Benkemoun et al., 2010) allow the use of non-conform meshing, which can be adapted for complex geometries. However, they may become cumbersome, especially for problems incorporating 3D aspects or finite deformations. Conversely, conformal

meshing generation methods give the possibility to be used in well-established FE simulation softwares, but the discretization generation on complex geometries can quickly become expensive and fastidious. Also, the cost of mechanical simulations on such complex porous geometries requires an optimization of the mesh element sizes according to morphological characteristicss refining in an automated way the zones of interest. To address these challenges, conformal mesh generation techniques adapted to complex geometries have been developed in (Ehab Moustafa Kamel et al., 2019), and compared with non-conformal mesh generation methods in (Ehab Moustafa Kamel et al., 2020), respectively the scope of Chapter 4 and 5 of this thesis.

These developments of 3D imaging techniques and of robust meshing tools for image-based modelling motivate the development of an integrated numerical methodology able to extract realistic microstructural geometrical data of rocks obtained for example from X-ray microtomographies. After their processing and meshing in a conforming approach, non linear mechanical FE simulations can be used to analyse the deformability of the microstructural solid skeleton. A fluid flow analysis with a Lattice Boltzmann approach can be performed on the undeformed and the deformed microstructures in order to investigate the influence of the (plastic) mechanical deformation on the transfer properties. The objective is thus to be able to model explicitly pore scale deformations that have a significant impact on the macroscopic permeability alterations. Such numerical results can provide arguments to the assumption of local pores closure (proposed amongst others by (Selvadurai and Głowacki, 2008)) to explain the experimental irreversible change in permeability under loading-unloading of rock specimens while no significant irreversible macroscopic deformations are observed. In addition, the proposed automated integrated computational procedure thereby allows testing a number of relevant and interesting pore scale assumptions in order to better understand the fine scale mechanical phenomena significantly affecting the fluid flow within the microstructure and altering the macroscopic permeability.

In order to highlight the changes in permeability obtained on a rock sample subjected to a series of stress state variations based on numerical modelling, this contribution will be structured as follows. Section 6.2 will outline the problem statement linked to the choice of a representative material sample, motivating the choice of using μCT scans to feed the integrated process of this contribution. Section 6.3 will detail the integrated strategy for determining the permeability at different levels of macroscopic deformation, addressing respectively the image processing, the discretization of the processed geometry, the nonlinear elasto-plastic FEM simulations and the permeability computation by means of Lattice-Boltzmann simulations. Section 6.4 will present the results of possible applications with the new integrated strategy presented in Section 6.3 illustrating the influence of fine

mechanical parameters on the decrease in permeability under isotropic compression. Finally, Section 6.5 will be devoted to the discussion of the methodology and to the application results, before establishing the conclusions and perspectives in the last Section. The test material used in this contribution is a Vosges sandstone made available by the University of Lille(Hu et al., 2018), but the methodology is intended to be modular, flexible in its block approach and applicable to other types of geomaterials.

6.2 Problem statement

Obtaining a representative geometry of a rock microstructure for investigating the permeability alterations as a function of applied stress states can be done either by exploiting data from micro-tomographs (Mees et al., 2003; Cnudde and Boone, 2013) or by virtual reconstruction from fundamental morphological indicators such as porosity, pore connectivity, pores size distribution, specific surface area or tortuosity. The virtual reconstruction methods based on random sequential addition (Sonon et al., 2012), excursion sets (Roubin et al., 2015), or even stochastic generation methods (Liang et al., 2000; Keehm, 2004; Andrä et al., 2013a) have the advantage of overcoming the systematic and potentially costly use of imaging equipments such as microtomographs, synchrotrons. They also offer the possibility of extended parametric studies through the generation of a large number of virtual samples with equivalent properties. However, these methods do not provide a controlled generation of the precise and complex morphological configuration of the porous network of a natural rock that an imaging technique would allow. Micro-CTs are widely used to characterize the 3D microstructure of geomaterials with a resolution ranging from millimeters to micrometres (Cnudde and Boone, 2013; Desrues et al., 2010; Viggiani et al., 2004; Andò et al., 2013). Geometrical descriptions obtained by imaging techniques are, among other things, dependent on the type of material scanned and on the resolution of the extracted images. Thus, depending on the quality of the images, their resolution, and the intended application, specific image processing and segmentation techniques are required in order to efficiently identify the different phases of the material. A realistic representation of the microstructure of a Vosges sandstone obtained from a μCT scan provided by the University of Lille (Hu et al., 2018), will be used to illustrate the construction of a geometrical model and its exploitation for permeability evaluations. The integrated process of modelling the permeability alterations induced by a variation of stress states presented in this contribution will have as a starting point a model derived from μCT. It is emphasized that the procedure due to its flexible and general nature, also makes it possible to process virtually generated geometries. For the sake of

simplification, only two phases with an explicit boundary will be considered: the solid phase and the pores. In order to make the process manageable within reasonable computation times, the model must be based on a volume smaller than the sample, yet representative of the complete sample in terms of porosity, permeability and pores size distribution. Generally speaking, in a rock, the permeability tends to converge towards its macroscopic value when the selected subset is roughly 10 times larger than the diameter of the largest pore size (Gniewek and Hallatschek, 2019; De Boever et al., 2016; Arns et al., 2005a), or when the sample size is on the order of the millimeter (Guibert et al., 2015; Mostaghimi et al., 2012). The specific choices and treatments related to the case of Vosges sandstone as well as the results obtained are detailed in the Applications section after having established the modelling strategy discussed in the following section.

6.3 Numerical modelling of deformation-induced permeability alterations

The integrated process of modelling permeability alterations in rocks under varying stress states is subdivided into 3 main stages as illustrated in Figure 6.1, namely the pre-processing, the simulation and the post-processing stages. The first one aims at progressively constructing the numerical model in order to feed the mechanical simulations. It consists first in processing the obtained 3D μCT scans to generate a geometry the boundaries of which, separating the solid skeleton from the pore space, are defined so as to be usable in a discretization process. This means a suppression of small object such as small occluded porosities, an efficient identification of the voxel phases and a smoothing process to reduce the roughness or the sharpness of the boundaries. The second part of the pre-processing stage aims at generating an optimized conforming mesh based on the methodology proposed in (Ehab Moustafa Kamel et al., 2019) and serving as an input to the mechanical simulations. The second stage involves, on the one hand, simulating the deformability of the rock via the use of finite element method (FEM) simulations and, on the other hand, simulating fluid flow inside the deformed pore space using a Lattice-Boltzmann framework after mesh revoxellisation (LBM). Finally, a post-processing stage further extracts the altered permeabilities, porosities and pore size distributions (PSD) of the deformed microstructure to provide a complete set of data to analyse the effects of the deformations on the mentioned parameters.

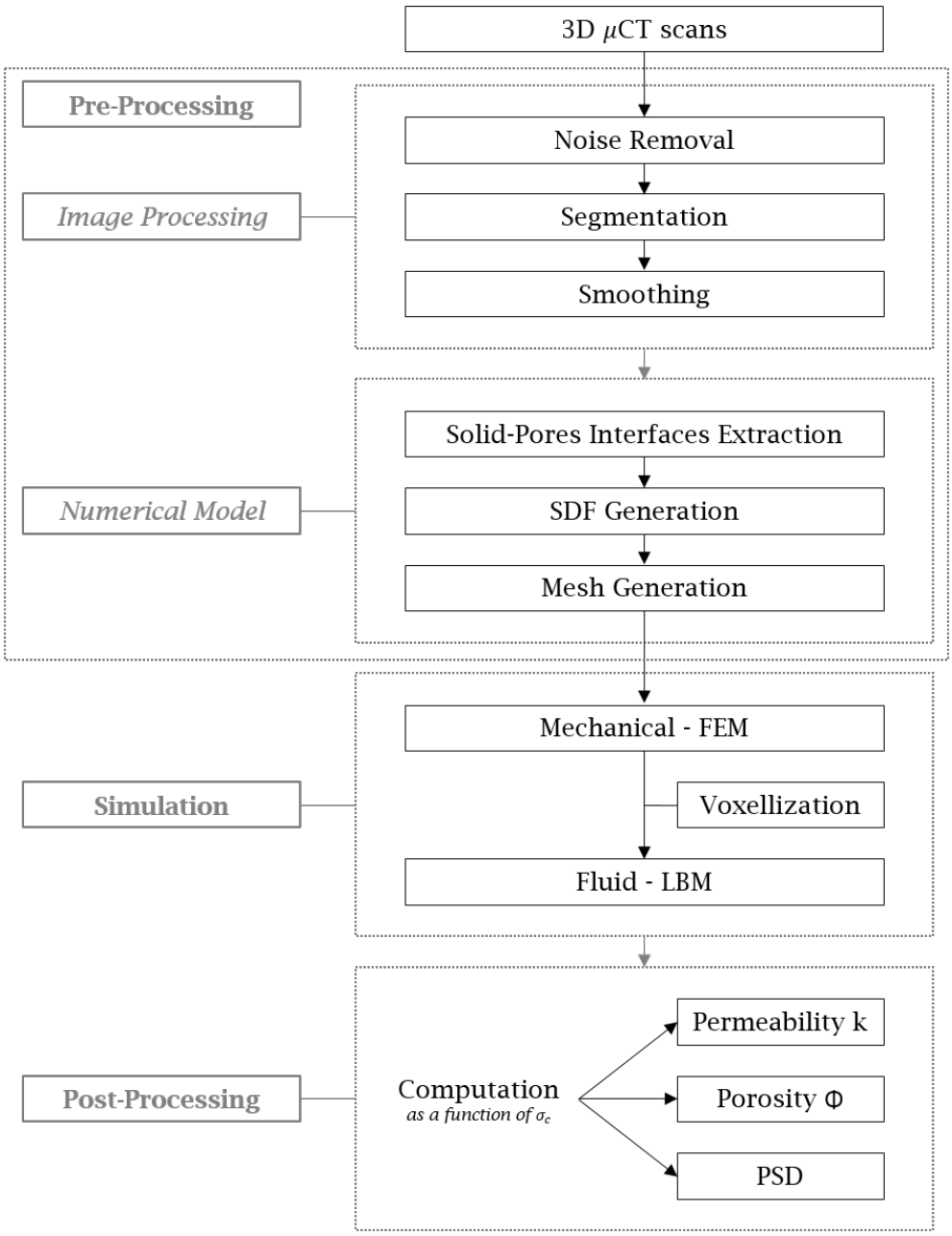

Figure 6.1: Process overview : The first step involves a pre-processing stage, treating first 3D μCT scans of a natural rock before generating a conforming mesh. The second stage involves mechanical and fluid simulations to simulate respectively the deformability of the solid skeleton and the flow in the deformed pore space with a voxellisation process of the deformed mesh at differents level of deformability. The last stage computes the resulting permeabilities, porosities and PSDs on the deformed configurations.

6.3.1 Image processing

The geometrical descriptions obtained by X-ray CT scans are given in the form of a gray-scale density map expressed on a voxel grid, and subsequently translated into level-set functions (Sethian, 1999) of the density of different constituents in the rock. The latter, called implicit functions, make it easier to describe particularly complex geometries where a curve Φ in 2D, respectively a surface in 3D, can be represented implicitly by means of the level sets of functions of spatial coordinates $\mathbf{x}$ denoted $LS(\mathbf{x}, ...)$:

$$\Phi \equiv LS(\mathbf{x}, ...) = l \tag{6.1}$$

where l[1] represents the iso-value of the function.

Each component of the 3-dimensional matrix describing the density map, called a voxel, has an intensity value associated to it, indicating a grey level where low attenuation corresponds to dark grey tones ranging from 0 (black) to a maximum value (white) depending on the color depth (i.e. 255 for unsigned 8 bits) with unique spatial coordinates describing the geometry. The isolation of voxels with a particular intensity to identify the differents constituents of the material is called segmentation, a key step to the analysis of tomographic data. Many segmentation techniques exist and their selection is highly dependent on the intended application (Fusseis et al., 2014; Kaestner et al., 2008; Iassonov et al., 2009; Wang et al., 2011a,b). In fact, depending on the number or density of the phases, the resolution of the scans, the quality of the images, the spatial arrangement and shapes of objects, the methods to be used can vary (Kaestner et al., 2008). Among the variety of them, methods based on thresholding (Canny, 1987; Otsu, 1979) or on active contours (Caselles et al., 1997; Chan and Vese, 2001; Shi and Karl, 2008; Bernard et al., 2009) can be cited. These latter methods, also known as level-sets-based active contour methods, correspond to a class of deformable models in which the desired shape is obtained by propagating an interface represented by 2D iso-contours (3D iso-surfaces) giving thereby smoothed contours. However, the active contours methods can quickly make the process expensive for large geometries, due to the extra dimension added by the levels-sets. Depending on the quality of the scanned images, the use of some filters may be necessary before the segmentation process in order to enhance the isolation of the phases during the segmentation (Kaestner et al., 2008). In this contribution, and for the sake of simplification, only two phases in the Vosges sandstone are considered with an explicit boundary: the solid phase composed of solid grains and cement, and the pores. Finally, to make the microstructure suitable for FEM

[1]The notation is different from the other chapters so as not to confuse the notations of the iso-value and of the permeability respectively

meshing and to optimize the computing time without excessively compromising the accuracy of the geometry, a simplifying process on the segmented 3D image may be necessary through the application of a smoothing process (Haddad and Akansu, 1991; Shapiro and Stockman, 2001; Nixon, 2012) to slightly reduce the roughness of the interfaces and the suppression of small features like occluded porosities. In fact, an excessive reduction of the roughness can significantly affect permeability.

6.3.2 Signed distance-based meshing process

In order to perform finite element simulations, the geometrical model obtained by means of the image processing must allows an efficient mesh generation. This is associated with contradicting constraints. On the one hand, in order for the model to be as close as possible to the real geometry, this crucial step must be able to handle the complexity of the morphology. On the other hand, the mesh must not be excessively dense so as to maintain a realistic computational cost. Thus, the mesh must be optimized so that refinement is only applied in the areas of interest, i.e. regions with high geometrical complexity or high stress gradients. Also, the mesh generator must be able to efficiently take into account solid/void interfaces and produce high quality meshes so that stability problems do not arise in the case of FEM simulations incorporating geometrical and material non-linearities. The discretization approach used in the scope of this contribution is based on the generation of conforming meshes for complex heterogeneous geometries, based on their implicit description by signed distance functions (Osher and Fedkiw, 2003; Sethian, 1999). The methodology was originally proposed by (Persson and Strang, 2004) for homogeneous structures and was recently extended to heterogeneous structures by (Ehab Moustafa Kamel et al., 2019) adressed in Chapter 4. These signed distance fields (SDF) allow flexible and efficient controls during the meshing process. Indeed, they can provide a series of useful informations for mesh generation such as the distance to the closest internal and external interfaces or the curvature. A particular choice for level-set functions describing the geometry is made here. A distance field devoted $DS(\phi(\mathbf{x}))$ is used, where at each point of a regular discrete grid of the domain of interest the signed Euclidean distance to the nearest ϕ interface is evaluated. The RVE domain Ω is subdivided into two sub-domains Ω_+ and Ω_- representing respectively the solid skeleton and the pore space of the model to which the computed Euclidean distances to the solid-pore interface are assigned a positive and negative value respectively. In order to preserve sufficient accuracy, avoid the appearance of sharp features and thus limiting numerical stability problems during the discretization process, this signed distance field is computed from an exact computation of the signed Euclidean distance using python toolbox MeshToSDF based on the implementation proposed in (Park et al., 2019). To achieve this, the field

is generated from the distances computed from the triangulated surfaces obtained by a Marching Cube process representing the Pores/Solid Skeleton interfaces (Lorensen and Cline, 1987). The method is indeed more expensive than the use of methods such as the Fast Marching Method (Sethian, 1999) but it carries the advantage of producing a accurate signed distance field, the basis of the discretization process. In fact, the Fast Marching Method, a priori a much less expensive approach, leads to an approximation of the distance values depending on the level of refinement of the grid on which it is evaluated this potentially leads to instability issues during the meshing process. Using the signed distance field, the conforming mesh generation strategy is composed by two main ingredients. The first one is the definition of an element size function $h(\mathbf{x})$ based on specific geometrical characteristics optimizing the initial spatial node distribution. The second one is based on an iterative technique that uses a simple mechanical analogy between the optimal mesh for a given connectivity and the equilibrium configuration of a 3D truss of elastic bars (or a network of springs) associated to the size of tetrahedral finite elements. In this analogy, an internal force field is applied in these bars that steers the bar lengths towards the targeted lengths defined by the element size function. The nodal force vector F of the equivalent truss system thus contains both these internal forces from the bars ($\mathbf{F}_{int}$) achieving an optimal element shapes and the reactions at the boundary nodes ($\mathbf{F}_{ext}$) constraining them on the solid-pore interface and ensuring the conformity of the mesh as shown in Equation (6.2)[2] and (6.3) and illustrated in Figure 6.2. More details about the methodology can be found in (Ehab Moustafa Kamel et al., 2019).

$$\mathbf{F}(\mathbf{x}) = \sum_i \mathbf{F}_{int,i}(\mathbf{x}) + \mathbf{F}_{ext,i}(\mathbf{x}) = 0 \tag{6.2}$$

$$F_{ext}(\mathbf{x}) = -DS(\mathbf{x})\,\nabla DS(\mathbf{x}) \tag{6.3}$$

6.3.3 FE simulations of rock mechanical loading

In order to simulate the deformability of a rock induced by a variation of stress state, the model obtained will be subjected to isotropic triaxial compressive stress states. The conforming mesh generation procedure gives the possibility to use robust conventional FEM softwares integrating the constitutive laws of interest. In this context, the present contribution makes the choice to use the FEM software ABAQUS (Simulia, 2014) given the availability of constitutive laws specific to geomechanics with finite strains. In order to investigate the impact of local plastifications within the microstructure under isotropic compression on the

[2]The notation is different from the other chapters so as not to confuse the notation of the spatial coordinates of nodes and the pressure which is denoted p here

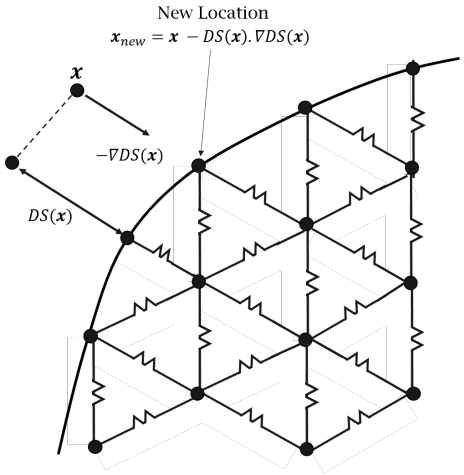

Figure 6.2: Schematic 2D view of the optimization process applying boundary constraints of nodes moving outside the implicitly defined boundary and the structure composed of a network of bars (or springs) steered toward the targeted length provided by the element size function $h(\mathbf{x})$

permeability, an elastoplastic constitutive law of the material is considered for the solid phase. Due to the geometrical complexity, other mechanical phenomena such as contact, further damage or cracking of the material will not be considered. To a certain extent, the behaviour of the rock under high isotropic confining pressures can be considered as rather ductile (Hu et al., 2018; Hoshino et al., 1972), which justifies the use of elastoplastic constitutive laws. In this contribution, an elastoplastic law with a Mohr Coulomb (MC) yield criterion is adopted. The MC criterion assumes that plastic yielding occurs when the shear stress in the material reaches a value that depends linearly on the normal stress in the same plane. The Mohr-Coulomb yield model is illustrated in Figure 6.3 and defined by the following equation

$$\tau = c - \sigma_n \tan\phi \tag{6.4}$$

where σ_n is the normal stress which is negative in compression in ABAQUS convention, τ the shear stress, c the cohesion and ϕ the angle of friction of the material.

To be more convenient, the Mohr-Coulomb yield-limit F can be expressed in terms of the stress invariants, see Equation (6.5), namely the hydrostatic pressure p, the von Mises equivalent deviatoric stress q and r the third invariant of the deviatoric stress respectively given by Equations (6.6), (6.7) and (6.8).

$$F \equiv \left(\frac{1}{\sqrt{3}\cos\phi}\sin\left(\Theta + \frac{\pi}{3}\right) + \frac{1}{3}\cos\left(\Theta + \frac{\pi}{3}\right)\tan\phi\right) q - p\tan\phi - c = 0 \tag{6.5}$$

$$p = -\frac{1}{3}\,\text{trace}\,(\boldsymbol{\sigma}) \tag{6.6}$$

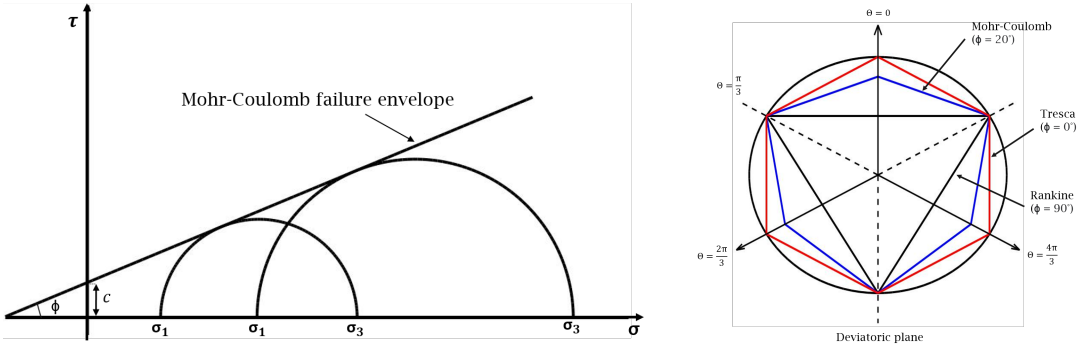

(a) (b)

Figure 6.3: Mohr-Coulomb yield model (a) and yield surface in deviatoric plane (b) reproduced from ABAQUS theory manual (Simulia, 2014)

$$q = \sqrt{\frac{3}{2}(\mathbf{S} : \mathbf{S})} \tag{6.7}$$

$$r = \left(\frac{9}{2}\mathbf{S} \cdot \mathbf{S} : \mathbf{S}\right)^{\frac{1}{3}} \tag{6.8}$$

where the deviatoric stress $\mathbf{S}$ is expressed as

$$\mathbf{S} = \boldsymbol{\sigma} + p\mathbf{I} \tag{6.9}$$

and the deviatoric polar angle as

$$\cos(3\Theta) = \left(\frac{r}{q}\right)^3 \tag{6.10}$$

The flow potential, G, used together with the Mohr-Coulomb yield surface in ABAQUS is a hyperbolic function in the meridional stress plane and a smooth elliptic function proposed by (Menétrey and Willam, 1995) in the deviatoric stress plane as illustrated respetively in Figures 6.4(a) and 6.4(b). The continuous and smooth nature of this flow rule ensures that the plastic flow direction is always uniquely defined (Menétrey and Willam, 1995), avoiding some issues in the finite elements simulations. The equation of the flow potential is given as

$$G = \sqrt{\left(\epsilon c|_0 \tan\psi\right)^2 + \left(R_{mw} q\right)^2} - p\tan\psi \tag{6.11}$$

$$R_{mw}(\Theta, e) = \frac{4\left(1-e^2\right)\cos^2\Theta + (2e-1)^2}{2\left(1-e^2\right)\cos\Theta + (2e-1)\sqrt{4\left(1-e^2\right)\cos^2\Theta + 5e^2 - 4e}} R_{mc}\left(\frac{\pi}{3}, \phi\right) \tag{6.12}$$

$$R_{mc}\left(\frac{\pi}{3},\phi\right) = \frac{3-\sin\phi}{6\cos\phi} \tag{6.13}$$

where ψ is the dilation angle measured in the $p - R_{mw}q$ plane (see Figure 6.4(a)), $c|_0$ is the initial cohesion yield stress, ϵ the meridional eccentricity defining the rate at which the hyperbolic function approaches and e the deviatoric eccentricity expressed as

$$e = \frac{3-\sin\phi}{3+\sin\phi} \tag{6.14}$$

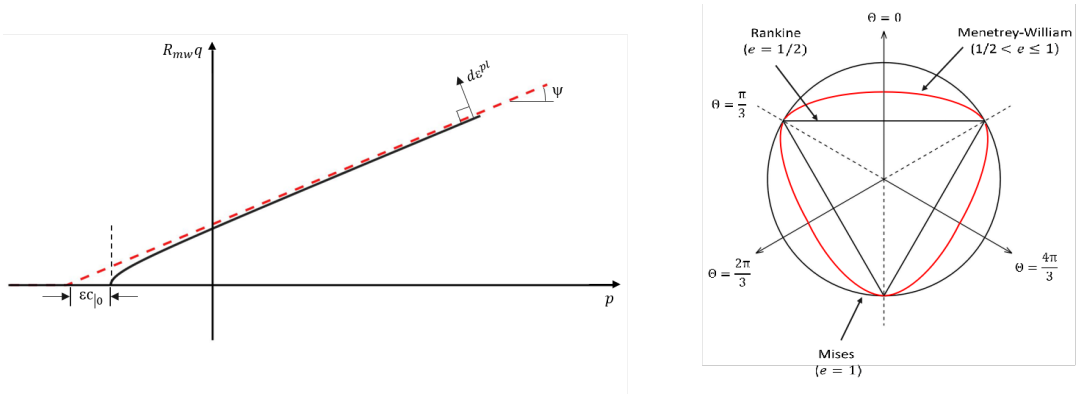

(a) (b)

Figure 6.4: (a) Hyperbolic flow potential in the meridional stress plane, (b) Menétrey-Willam flow potential in the deviatoric stress plane reproduced from Abaqus theory manual (Simulia, 2014)

Isotropic cohesion hardening is considered for the hardening behavior of the Mohr-Coulomb yield surface. The hardening curve given in Equation (6.15) describes the cohesion yield stress as a function of the plastic strain where $c|_0$ is the initial cohesion value, while $c|_f$ is the final cohesion value at a plastic strain value ε^p_{eq} of 1. The angle of friction is kept constant, thus no hardening or softening behavior is considered for the angle of friction keeping it constant.

$$c = c|_0 + \frac{(c|_f - c|_0)\,\varepsilon^p_{eq}}{B_c + \varepsilon^p_{eq}} \tag{6.15}$$

where B_c is a coefficient corresponding to the equivalent plastic strain to half the evolution of cohesion (Collin, 2003).

The equivalent plastic strain, a scalar value giving an indication on the intensity of the plastic strain is computed following Equation (6.16).

$$\bar{\varepsilon}^{pl} = \int \frac{1}{c}\boldsymbol{\sigma} : d\varepsilon^{pl} \tag{6.16}$$

In addition to the consideration of material non-linearities through the use of a Mohr-Coulomb constitutive law, geometrical non-linearities are also considered. These FEM simulations are performed for the solid phase using an implicit Newton-Raphson procedure. Furthermore, since the plastic flow is non-associated, an unsymmetric matrix storage is considered.

6.3.4 Permeability evaluation

The tools presented in the previous sub-sections provide the essential ingredients to perform the simulations to describe the deformation of the solid skeleton of the rock sample under mechanical loading. One then needs to evaluate the permeability of the porous network that has been modified following the deformation of the solid skeleton. Permeability measures the capacity of a fluid to flow through a porous medium. It is part of the proportionality constant in Darcy's law, the relationship expressing the flow $\boldsymbol{v}$ in terms of the pressure gradient ∇p. This phenomenological law is considered valid at low Reynolds numbers when the flow is laminar without considering gravitational effect. Indeed, under this condition, permeability is independent of fluid properties such as density, viscosity and pressure gradient (Eshghinejadfard et al., 2016). Darcy's law reads

$$\boldsymbol{v} = -\frac{\mathbf{K}}{\mu} \cdot \nabla p \tag{6.17}$$

where $\mathbf{K}$ represents the permeability tensor, p the pore fluid pressure, $\boldsymbol{v}$ the velocity vector and μ the dynamic viscosity.

This law is valid regardless of the fluid considered or the saturation conditions. In Equation (6.17), the permeability $\mathbf{K}$ is computed as the product between the intrinsic permeability $\mathbf{K_{int}}$ and the relative permeability k_{rel} (that depends on the degree of saturation). The intrinsic permeability $\mathbf{K_{int}}$ (expressed in m^2) does not depend on the fluid considered and is mainly controlled by the spatial structure and the porous network of the geomaterial, as well as the solid/fluid interaction (Bérend et al., 1995). In this contribution, only water permeability under saturated conditions will be investigated. Under those conditions, the permeability $\mathbf{K}$ can thus replaced by the intrinsic permeability $\mathbf{K_{int}}$.

Different strategies exist to simulate flows within complex geometries. For the type of geometries considered here with complex and irregular boundaries, traditional computational fluid dynamics (CFD) methods such as Finite Elements Methods (Borujeni et al., 2013; Narváez et al., 2013) or Finite Volume Methods (Guibert et al., 2015; Petrasch et al., 2008) require mesh refinement levels stronger than the image resolution to ensure mesh convergence and simulation stability. Consequently, obtaining an accurate permeability estimate leads to significant computational costs

(Guibert et al., 2015; Succi, 2001), in addition to the complexity of generating a mesh adapted to this type of geometry. Conversely, the Lattice-Boltzmann method is prone to parallelization (McClure et al., 2014). Due to the possibility of using it directly on complex pore space geometries of rocks (Martys and Chen, 1996; Cancelliere et al., 1990; Keehm, 2004; Andrä et al., 2013b), it remains a preferred choice for flow simulations in geological materials. In fact, the voxel grid of the 3D image obtained from a micro-CT scan or a virtually generated geometry can directly be used as lattice. Consequently, no complicated meshing procedure is required, making this approach very flexible. This method is a modern approach in Computational Fluid Dynamics often used to solve the incompressible steady-state, time-dependent Navier-Stokes equations (see Equations (6.18) and (6.19)) numerically in agreement with FEM solutions (Kandhai et al., 1998; Thijssen, 2007).

$$-\mu\nabla^2\boldsymbol{v} + \nabla p = \boldsymbol{f} \tag{6.18}$$

$$\nabla \cdot \boldsymbol{v} = 0 \tag{6.19}$$

Yet, one of the main disadvantages of the method is its computational inefficiency, even with a massively parallel implementation. The runtime scales approximately inversely with the real flow rate (Blunt et al., 2013), which motivated some researchers to use simplifying methods such as pore network modelling (Bultreys et al., 2015; De Boever et al., 2016; Dong and Blunt, 2009). However, the need to implement an integrated and automated methodology tracking the evolution of permeability according to the mechanical deformation of the solid skeleton motivates here the choice of the Lattice-Boltzmann method to simulate flows within the complex microstructures. The method finds its origin in a molecular description of a fluid. Based on cellular automata theory, it describes the fluid volume in a complex pore-geometry in terms of the interactions of a massive number of particles following simple local rules, namely, collision and propagation which can be understood as a discretization of the behavior of an ideal gas. These rules recover the Navier-Stokes equation at the macroscopic level (Rothman et al., 1998; Ladd, 1994).

The Lattice Boltzmann method describes the evolution of a discretized fluid-particle distribution function $f(\mathbf{x}, t, \zeta)$ that moves and interacts on a regular lattice with very few degrees of freedom (Ramstad et al., 2010). $f(\mathbf{x}, t, \zeta)$ represents the probability of finding a fictitious particle in a certain location of domain $\mathbf{x}$ with a certain velocity ζ at a certain time t (Eshghinejadfard et al., 2016). The discretized Boltzmann equation in time and space, and the conversion of the space of velocities ζ into a finite set of velocities c_i describing the degrees of freedom of the movement allowed in the lattice reads :

$$f_i\left(\mathbf{x}+\mathbf{c}_i\Delta t, t+\Delta t\right) - f_i(\mathbf{x},t) = -\frac{1}{\tau}\left[f_i(\mathbf{x},t) - f_i^{eq}(\mathbf{x},t)\right] \tag{6.20}$$

where f_i, f_i^{eq}, τ and Δt are respectively the distribution function of particles moving with speed c_i, an equilibrium distribution function, the dimensionless relaxation time related to the kinematic lattice viscosity ν (see Equation (6.21)) and the time step. The right-hand side of the discretized Boltzmann equation accounts for the Bhatnagher-Gross-Kook (BGK) collision model (Bhatnagar et al., 1954) describing a relaxation process towards equilibrium.

$$v = \left(\tau - \frac{1}{2}\right) c_s^2 \Delta t \tag{6.21}$$

where $c_s = 1/\sqrt{3}$ is the sound speed given in non-dimensional form.

A particle distribution for each possible particle velocity vector is defined at each node on a regular lattice as illustrated in Figure 6.5. The number of these vectors is constrained by exclusively enabling particles to jump to a neighboring node in one time step. Packets of particles are propagated according to their velocities during each time step of the simulation. The velocity populations are relaxed by a collision step (Meakin and Tartakovsky, 2009) following a collision rule. The simplest one is the single-relaxation time Bhatnagar–Gross–Krook (BGK) approximation. However, to ensure better numerical stability for simulations in the complex pore-geometry of the microstructure, multiple relaxation times (MRT) are often used (Gniewek and Hallatschek, 2019). More in-depth details about the Lattice-Boltzmann method applied to geomaterials can be found in (Sukop and Thorne, 2007; Eshghinejadfard et al., 2016).

The input required for the method is a discretisation in the form of a voxel grid. In our procedure, the deformed geometry is given by the deformed 3D mesh obtained as a result of the FEM simulations described in the previous sub-section. This mesh is converted into a voxellisation for each confining level using a ray intersection method based on the algorithm developed by (Patil and Ravi, 2005) from a MATLAB code (Adam, 2020).

The flow simulations are then carried out using the open source software PALABOS (PArallel LAttice BOltzmann Solver) (Latt et al., 2020), a framework for general-purpose computational fluid dynamics (CFD), with a kernel based on the lattice Boltzmann method (LBM) using the code provided by (Gniewek and Hallatschek, 2019). Velocity fields of the fluid flow are solved using the D3Q19 lattice as illustrated in Figure 6.5(b), and are achieved by imposing a pressure difference Δp small enough to ensure an incompressible flow in a laminar regime between two opposite faces of the subset constituting the inlet and the outlet for each of the directions $x-y-z$. No-slip boundary conditions are applied to the solid

material boundaries, i.e. to the pore walls. For this purpose, the solid boundaries are handled with a simple bounce-back condition, meaning that a packet of particles that hits a solid wall node at a certain time step is “bounced back” to the node in the pore space where it came from (Llewellin, 2010) as illustrated in Figure 6.5(a). Once the flows have been computed respectively in the 3 main directions, the permeability tensor is extracted using Darcy’s law. The "scalar" equivalent permeability is then calculated by geometrically averaging the permeabilities obtained for the 3 directions, an estimate considered more appropriate for sandstones (Selvadurai and Selvadurai, 2014). Note that the results obtained are given in lattice units and must be converted into physical units (Latt, 2008). For the permeabilities, this requires multiplying by the square of the voxel length.

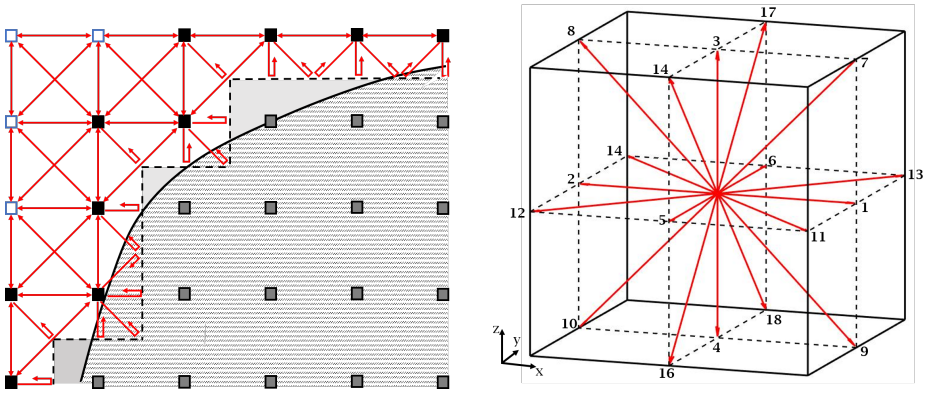

(a) (b)

Figure 6.5: (a) Bounce-back condition reproducing the no-slip boundary conditions adapted from (Llewellin, 2010), (b) Discrete velocities of the D3Q19 lattice

6.3.5 Pore size distribution

Pore size distributions provide relevant information on the distribution of pore volume fractions according to their radii. Their evolution throughout the loading process could potentially identify the pore radii where the deformation would be preferentially localized. Through the access to the porous network via imaging techniques, pore size distributions can be geometrically determined. The main idea is to determine the amount of volume for each pore radius potentially covered with spheres in 3D without overlapping with the solid skeleton leading to the definition of a continuous PSD. To do this, the algorithm provided by (Münch and Holzer, 2008) via the Beat (Münch and Holzer, 2008) plugin available in open-source image processing software Fiji (Schindelin et al., 2012) first calculates a distance field within the pore space giving the information of the closest Euclidean distance to the boundaries separating the pores from the solid skeleton. The algorithm then starts

with the widest area corresponding to the radius r of the largest sphere that can be placed without overlapping. The algorithm then progresses by covering the pores with spheres of gradually decreasing radius r until the entire pore volume is covered.

However, they do not provide more information on critical throats. Indeed, in sandstones, the porous geometry consists of a system of large chambers (body pores) interconnected with narrow pores (throat pores) restricting the fluid flow. Thus, permeability is mainly controlled by the percolation pore throats, while the pore chambers contribute essentially to the porosity. A small variation in the throats can induce large variations in permeability without significantly affecting the porosity (Zheng et al., 2015). Thus, the extraction from the overall pore size distribution of a reduced distribution around the radii of critical throats would allow investigating how pore throats and pore chambers are affected by variations in the stress state. In this perspective, in addition to the computation of continuous PSDs, the plugin can geometrically simulate PSDs obtained by mercury intrusion porosimetry (MIP). The ink-bottle effect generated by these simulations somehow provides a distribution of pore sizes reduced to their most critical throats along the percolation paths as shown in Figure 6.6. These PSDs obtained by geometrical MIP simulations are generated on the basis of a region growing algorithm (Chang and Li, 1995) with constraint. In fact, a new voxel can only join the region if it meets the growing criterion, together with all voxels of its spherical neighborhood with radius r_s in 3D (Münch and Holzer, 2008). The information of the smallest pore radius along the percolating path reduces the continuous PSD to the critical throats of the pore network. More details about the method are given in (Münch and Holzer, 2008). Note that the process is used in this contribution to obtain a geometrical information on the pore throats and is not intended to simulate a proper MIP experiment. In the following, the term PSD will refer to the continuous PSD while MIP will refer to the pore size distributions obtained via MIP simulations defined in this section. Both are generated by using the Beat plugin (Münch and Holzer, 2008) available in the Fiji software (Schindelin et al., 2012).

6.4 Applications

6.4.1 Materials

Based on the micro-CT scans of a Vosges sandstone obtained by (Hu et al., 2018), the applications presented in this section will make use of a subset of these μCT's. The Vosges sandstone is representative of the class of materials suitable as host rock for gas storage. This rock is characterized by cemented and strongly interpenetrated grains, resulting in a highly interconnected pore network with a very low fraction of occluded pores. The cylindrical sample that has been scanned has a height

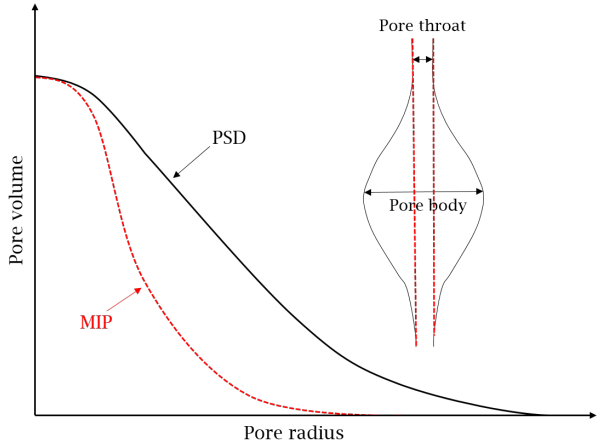

Figure 6.6: Schematic view of a continuous PSD and a PSD obtained by MIP simulation showing the impact on the pore size distribution when reducing the pore sizes to their smallest throat pores along the percolation pathways due to the ink-bottle effect

of 12.14 mm with a diameter of 5.31 mm. The porosity and the air permeability measured experimentally in lab conditions for a similar sample are respectively about 19 % and $6 \times 10^{-13} m^2$ (Hu et al., 2018). The voxel size of the sample studied is $5 \times 5 \times 5\,\mu m$. Figure 6.7 illustrates a 3D voxel-based view of a cubic subset of the Vosges sandstone μCT scans with an edge length of 1.5 mm on each side, highlighting the morphology of the porous space and the marginal presence of occluded porosity (less than 1% of the porosity).

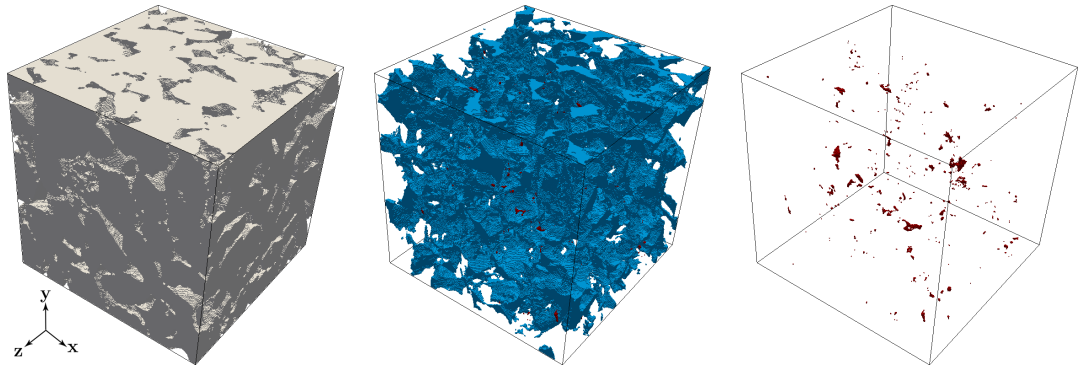

(a) (b) (c)

Figure 6.7: 3D voxel-based view of a segmented Vosges sandstone subset of 1.5 mm obtained by X-ray tomography from Cong Hu's thesis (Hu et al., 2018) : (a) solid skeleton, (b) pore space, (c) occluded pores

6.4.2 Assumptions/Questions

The capabilities of the integrated procedure proposed here to investigate the alteration of the permeability under isotropic triaxial compression explicitly considering

the microstructural morphology are now illustrated. To this end, and to demonstrate how the tool can be used to test assumptions about the microstructural (pore scale) behaviour, three assumptions/questions are here addressed for such a demonstration:

1. First, Vosges sandstone essentially has a brittle behaviour at low confinement. However, a transition to a more ductile behaviour takes place when the confining pressure applied to the sandstone approaches 40 MPa as mentioned in (Hu et al., 2018). For higher macroscopic confining pressures above 40 MPa, local plastic straining is likely to occur. There is an interest in assessing how the introduction of a microstructural plastic behavior and its parameters such as friction or cohesion influence permeability alterations due to loading.

2. Second, a rock is heterogeneous by nature and is composed of different constituents with different nature and properties. Sandstone is a rock in which different grains are interpenetrated and cemented together. This cement layer binding the grains has weaker properties than those of grains composed mainly of quartz. Cement is therefore the preferential site for the initiation of cracking or plastification phenomena with a potentially significant impact on the modification of the porous network. It is therefore of interest to investigate the effect of the presence of a thin cement layer with weaker material properties. Our computational procedure will therefore be used to assess the impact on permeability of considering a cement layer with weaker properties, made of 10% of the solid volume fraction and located closest to the pore network walls. The aim here is not to identify the cement via segmentation but rather to test a hypothesis by considering a constant thickness of cement around the solid phase by attributing weaker properties to the elements included in this thickness.

3. Third, as mentioned in the introduction, experimental studies on rocks such as (Selvadurai and Głowacki, 2008; Hu et al., 2018) have observed permeability hysteresis after unloading the samples from an applied isotropic compressive loading potentially linked to an irreversible modification of the pore network by local plastification of the solid skeleton during mechanical loading. The effect of unloading at different loading levels on the permeability alterations will therefore be assessed.

It is emphasized that this type of microstructural assumptions can only be tested computationally based on a model incorporating the detailed morphology of the porous network, as the one proposed here.

6.4.3 Pre-processing

Image processing

After applying a median filter (Stone, 1995) to reduce the image noise, an hysteresis thresholding (Canny, 1987) was applied as illustrated for a slice of the sample in Figure 6.8. In fact, this segmentation method allows a better local voxel attribution, especially at borders, given the overlapping shown on the grey level histogram (see Figure 6.8b), in order to optimally distinguish the solid skeleton of the rock from the pore space as illustrated in Figure 6.8. Due to the high connectivity of the pores, the marginal occluded porosities representing less than 1% of the total porosity allow building a model by removing them. Indeed, their removal will not have any significant impact on the mechanical and fluid simulations. This avoids excessive mesh refinement and significantly reduces the cost of the FEM simulations. Occluded pores are therefore eliminated by using a geodesic reconstruction (Beucher, 2001), thus keeping only the pore voxels having a connectivity with the boundary edges of the subset, thereby representing the conductive pores only. The roughness of the pore walls is slightly reduced by the application of a Gaussian filter generating an isotropic smoothing with $\sigma = 1$ voxel-length. Indeed, a fully detailed representation of roughness would induce important local curvatures, requiring a more important refinement of the mesh for a more accurate representation of the geometrical model. This would lead to a very costly mechanical computation. Indirectly, this will lead on the one hand to a reduction in the number of poor quality mesh elements, and on the other hand in an increase of the value of the computed permeability. An assessment of the impact of pre-processing steps is given in Table 6.1.

Representativity

In order to make the process manageable within realistic computational times, a subset that is statistically representative at the fine scale of the macroscopic transfer properties of the complete sample must be selected. As explained in literature, permeability tends to converge towards its macroscopic value when the subset is about 10 times larger than the diameter of the largest pore (Gniewek and Hallatschek, 2019; De Boever et al., 2016; Arns et al., 2005a), or when the sample size is in the order of 1 mm (Guibert et al., 2015; Mostaghimi et al., 2012). The pore size distribution of the complete segmented sample indicates a maximum pore radius of approximately 70 microns as illustrated in Figure 6.9. Therefore, a minimum sample size of 1.4 mm should be considered. In order to avoid excessive computation times, the choice is made to limit the sample size to 1.5 mm. The voxel size of the samples studied is $5 \times 5 \times 5\,\mu m$ leading to a sample size of $300 \times 300 \times 300$ voxels. The selected subset among the extracted ones at this size is the one with

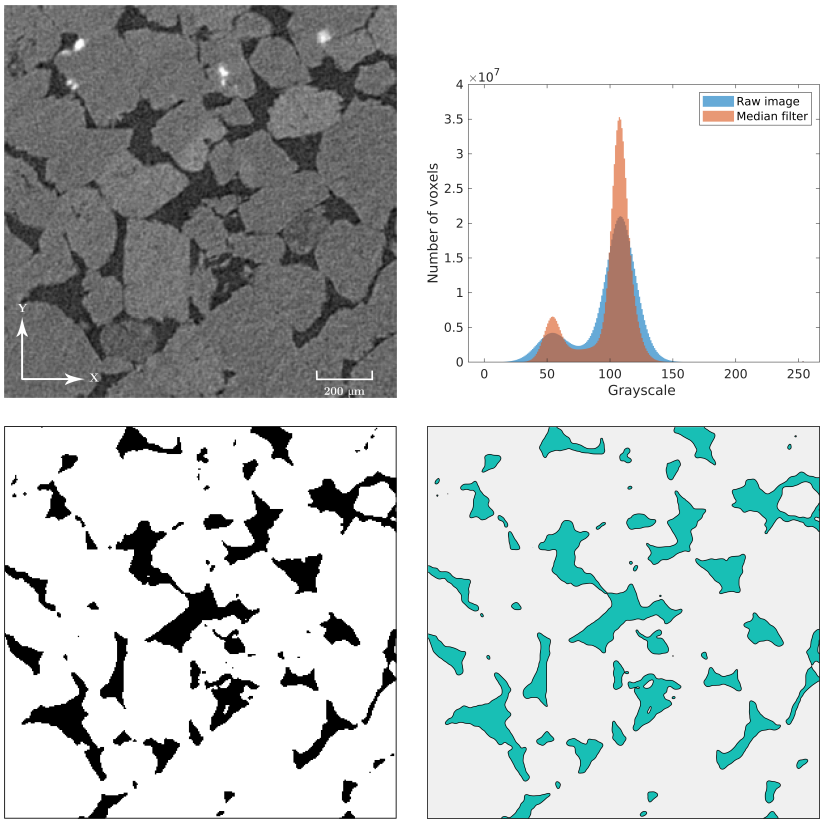

Figure 6.8: Image processing of a 2D slice of a subset of Vosges Sandstone sample : (a) 2D slice, (b) Gray level histogram, (c) Segmented image with hysteresis thresholding after applying a median filter, (d) Smoothed contours of the segmented image

porosity and permeability values that are the closest to those computed numerically for the complete segmented sample. The obtained porosity, connected porosity and mean permeability of the complete sample are respectively 16.08 %, 15.97 % and $7.98 \times 10^{-13}\, m^2$. The selected subset, for its part, has resulted in 16.18 %, 16.06 % and $7.99 \times 10^{-13}\, m^2$. The computed porosity is the Eulerian one, and is obtained as the current pore volume divided by the current subset volume. The estimate of porosity and permeability is in the right order of magnitude. Their computationally evaluated values are respectively slightly lower and higher than that the experimentally measured on a similar sample, mainly because of the resolution limited to 5 μm. Indeed, from one segmentation method to the other, or from one thresholding value to another, the values computed for porosity and permeability may vary. This sensitivity is logically amplified when resolutions are not fine enough to accurately identify the solid skeleton from the pores (Cox and Budhu, 2008). However, the applications will focus on relative changes in permeability before and after deformation. A future contribution could base the study on experimental results directly carried out on the sample (which is not the case here), thus enabling the model to be calibrated as early as the segmentation phase.

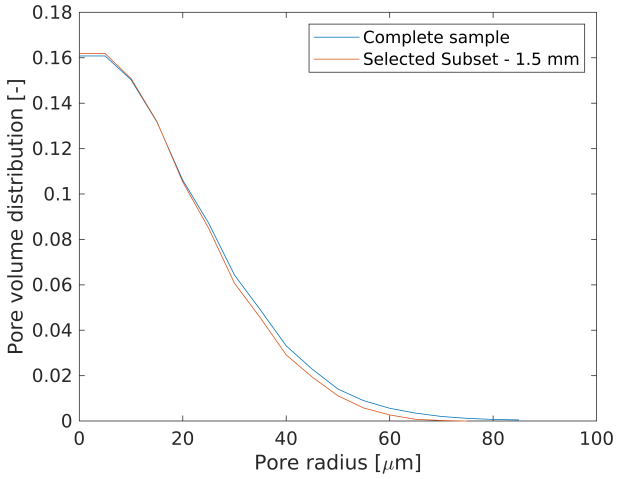

Figure 6.9: Pore size distribution of the complete sample and the selected subset of 1.5 mm of edge showing a good match in term of pore sizes and porosity

Mesh generation of the representative subset

After the extraction of a representative subset of the Vosges sandstone microCT scans and its image processing (segmentation, smoothing), a signed distance field is generated in order to mesh the geometry using the methodology outlined in Section 3. Figure 6.10 illustrates the treated subset and its corresponding signed distance field. The result of the discretisation is shown in Figure 6.11(a). Due to the purely mechanical process modelled by FEM simulations, only the solid phase is meshed. The mesh used as an input for the elastoplastic simulations is composed of $1,111,398$ nodes and $5,473,446$ elements. The voxellisation of the deformed mesh will be applied for each confining level extracted. The initial voxellisation from the undeformed mesh is illustrated in Figure 6.11(b)

Influence of pre-processing on evaluated porosity and permeability

After image processing, meshing and mechanical simulation, a revoxellization is performed to extract permeabilities. Thus a revoxellization is also performed on the undeformed subset to estimate the effect of the image processing and meshing on the computationally obtained permeability. The initial porosity and permeability values are obtained, respectively as 15.54% and $9.12 \times 10^{-13} m^2$, varied slightly throughout the process as shown in Table 6.1. These cumulative errors are the result of the resolutions being used. A higher resolution when generating the distance field or a finer mesh before revoxing on a finer grid will significantly reduce this variation at the expense of computing time. Also, the gaussian smoothing phase tends to reduce the roughness at the pore walls and to slightly inflate the solid skeleton, potentially leading to an influence on the assessment of the permeability and the porosity.

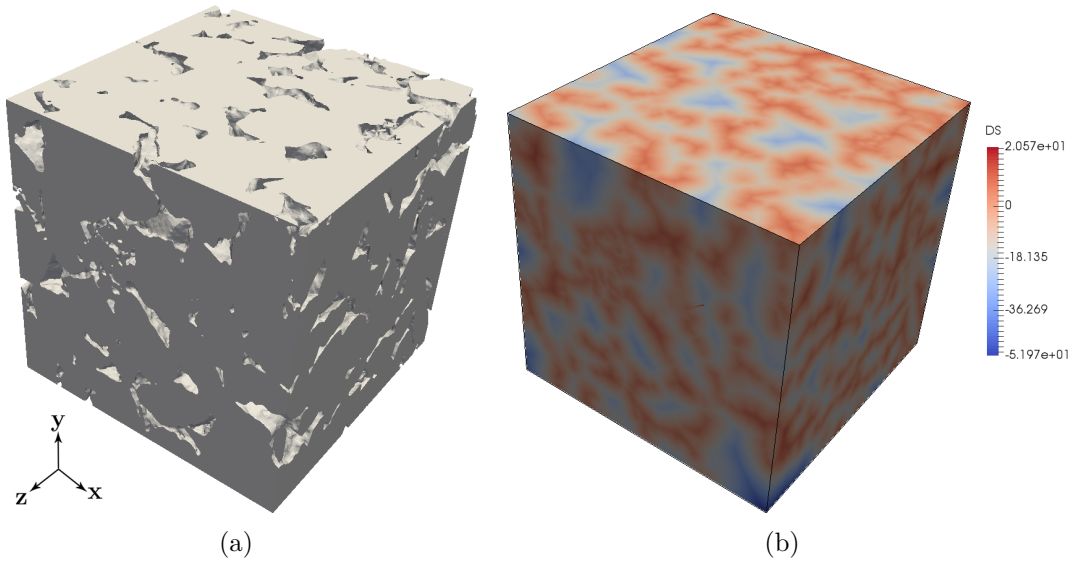

(a) (b)

Figure 6.10: Vosges sandstone subset model : (a) Treated 3D image after applying the segmentation, removing occluded porosities and smoothing the contours, (b) Signed distance field

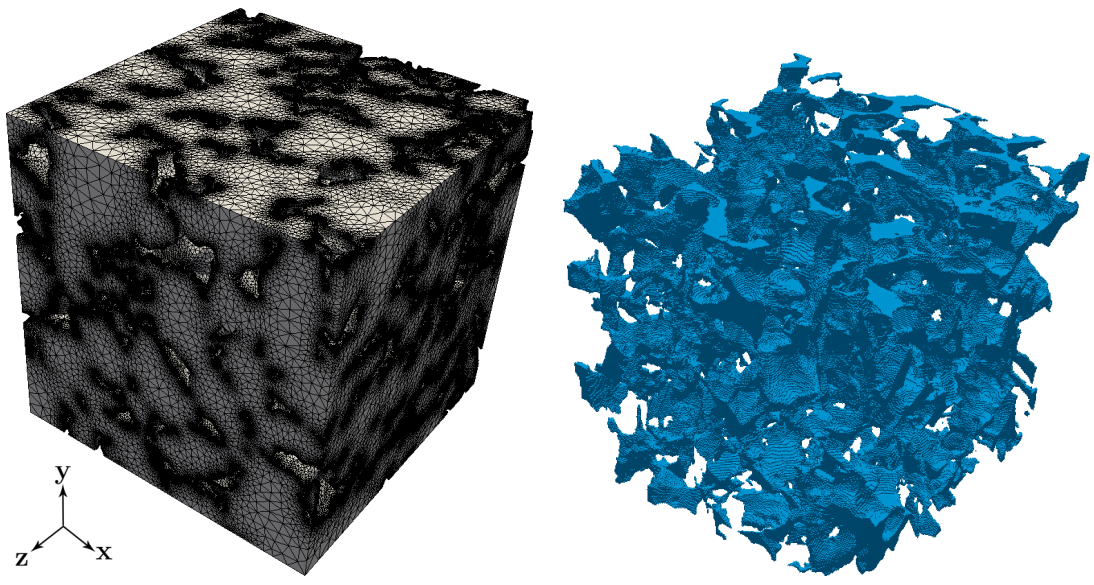

(a) (b)

Figure 6.11: Vosges sandstone subset model : (a) Conforming mesh generated by the extended Persson Truss analogy method (Ehab Moustafa Kamel et al., 2019) (# Nodes : $1,111,398$ /# Tetrahedra : $5,473,446$), (b) Initial voxellisation done from the undeformed mesh

	ϕ [%]	k_{xx} $[m^2]$	k_{yy} $[m^2]$	k_{zz} $[m^2]$	k $[m^2]$
Hyst. thres. segmentation	16.06	5.37×10^{-13}	9.52×10^{-13}	1×10^{-12}	7.99×10^{-13}
Gaussian smoothing	15.88	5.67×10^{-13}	9.93×10^{-13}	1.05×10^{-12}	8.39×10^{-13}
Signed dist. field	15.80	5.79×10^{-13}	1.01×10^{-12}	1.08×10^{-12}	8.66×10^{-13}
Volume mesh voxellisation	15.54	5.95×10^{-13}	1.1×10^{-12}	1.16×10^{-12}	9.12×10^{-13}
Error [%]	3.23	10.8	15.55	16	14.41

Table 6.1: Initial values of permeability and connected porosity values obtained for each step of the process for the selected subset of 1.5 mm of edge length. The reference ones for the evaluation of the permeability alterations under stress state variations are the ones obtained after the voxellisation of the volume mesh.

In order to overcome the fluctuations in permeability and porosity, this contribution chooses to consider as a reference for further simulations the permeability and porosity obtained at the end of the pre-process, i.e. that obtained after revoxellisation of the initial mesh. This is justified by the fact that the main objective of the developments presented is to illustrate an integrated process for investigating the link between the permeability alterations induced by deformation under stress state variations and the morphology of the pore space. This approach, due to its numerical and flexible nature, offers the possibility of testing a large number of fine scale assumptions and of establishing trends in terms of the behaviour of the material under deformation and its link with its transfer properties.

6.4.4 Results

In order to investigate the assumptions mentioned in the Materials sub-section, a set of 9 simulations with varying properties have been carried out. The parameters used for the different simulations are given in Table 6.2. The interest is focused on the effect of the three following parameters: cohesion, angle of friction and the consideration of a thin cement layer. The resulting deformation response of the microstructure subjected to isotropic macroscopic compression is computed in order to study its influence on the evolving permeability, porosity and pore size distributions. The Young's modulus is chosen on average at 20 GPa except for the last simulation. The Poisson coefficient ν is chosen to be identical for all the simulations. The values of the angle of dilation ψ were chosen according to the respective values of the angles of friction by being 3° lower. This answers

							CEM 10% - E = 1GPa - ν = 0.2			
	E [GPa]	c_0 [MPa]	c_f [MPa]	ϕ [°]	ψ [°]	ν [-]	c_0 [MPa]	c_f [MPa]	ϕ [°]	ψ [°]
1	20	-	-	-	-	0.2	-	-	-	-
2	20	9	10.5	35	32	0.2	-	-	-	-
3	20	6	8.5	35	32	0.2	-	-	-	-
4	20	9	10.5	30	27	0.2	-	-	-	-
5	22.11	9	10.5	35	32	0.2	9	10.5	30	27
6	22.11	9	10.5	35	32	0.2	9	10.5	20	17
7	22.11	9	10.5	35	32	0.2	0.5	2	20	17
8	22.11	9	10.5	30	27	0.2	0.5	2	20	17
9	40	10	15	35	32	0.2	0.5	2	20	17

Table 6.2: Finite element simulations are conducted with a set of nine different material properties configurations of the subset sample of Vosges sandstone with an added coating cement (CEM - 10% of the volume fraction of solid skeleton) with weaker properties for configurations 5 to 9 to analyse the effect of the three following parameters : cohesion, angle of friction, cement layer. Poisson coefficient ν is kept constant and the angle of dilation ψ is 3° lower than the corresponding angle of friction ϕ to avoid unstable material behaviour at high confining stress states

computational stability requirements related to the Mohr-Coulomb criterion as implemented in the Finite Elements Method ABAQUS software (Simulia, 2014), in order to avoid unstable material behaviour at high confining stress states. A slight isotropic strain-hardening of the cohesion is also considered where c_0 represents the initial cohesion while c_f represents the final value of hardening at an equivalent plastic strain of 1. It is noted that the values used remain consistent with those reported by Hu (Hu et al., 2018). However, it is obvious that these parameters are to some extent arbitrary since they are inspired from macroscopic data, while being used in a fine scale context. Fine scale parameters are however difficult to obtain and require advanced characterization methods such as micro-indentation tests (Randall et al., 2009; Mahabadi et al., 2012) or micro-scratch tests (Akono et al., 2011). Microstructural simulations are therefore useful to build a link between the macroscopic response of the system and the parameters of the fine scale constituents. The studies conducted in this contribution thus also aim at varying these parameters to quantify their respective influence in the context of a complex microstructural rock geometry, to be able to test hypotheses, and to interpret trends.

Considering the relatively low anisotropic behaviour of the studied sandstone, the stress states corresponding to the imposed macroscopic deformation (the simulations are macroscopic strain-driven) are almost isotropic, the variations being more

pronounced as the loading increases as shown in Figure 6.12(a). However, at about 100 MPa of average confining pressure, the difference between the values obtained for each direction is only about 4%, a variation considered negligible. Thus, the subsequent figures will illustrate the evolution of quantities such as porosity, permeability or pore size distribution as a function of the arithmetic mean of the equivalent macroscopic stress in the 3 principal directions as illustrated in Figure 6.12(b). The permeability values obtained in the 3 directions show that the permeability evaluated in the X direction is lower than the permeability obtained in the Y and Z directions by a factor of 2. It remains however in the same order of magnitude, and the difference tends to decrease as the sample considered is larger, the constraint of the size of the subset being chosen to keep affordable computing cost. Permeability is presented in a normalized form, where the permeabilities obtained after deformation are divided by the permeability of the undeformed subset, on the basis of its geometric mean, an estimate considered more appropriate for sandstones (Selvadurai and Selvadurai, 2014) in order to simplify interpretations. Figure 6.13 depicts the normalized permeability as a function of the porosity, showing a strong correlation between changes in porosity and permeability as experimentally observed in literature. Indeed, for all the sets of parameters used during the simulations, the different permeability-porosity curves obtained fit each other almost perfectly. Generally speaking, the porosity is deduced from a volume of pores while the permeability is mainly controlled by the throat pores (Zheng et al., 2015).

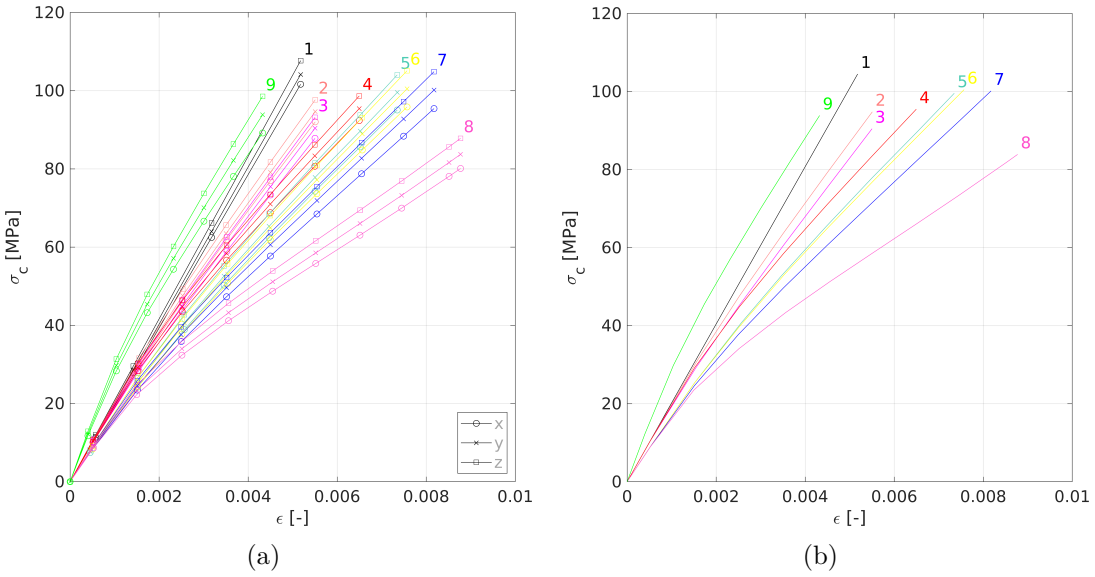

Figure 6.12: Confining pressure as a function of the applied macroscopic deformation for the nine simulations with properties shown in Table 6.2: (a) in $x - y - z$ principal direction separately, (b) as a geometric mean value of the three principal stresses values

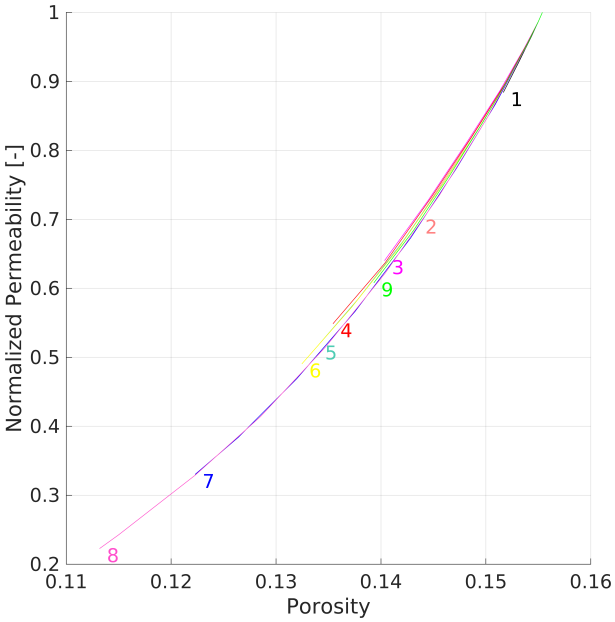

Figure 6.13: Normalized permeability as a function of porosity for the nine simulations of Vosges sandstone subset

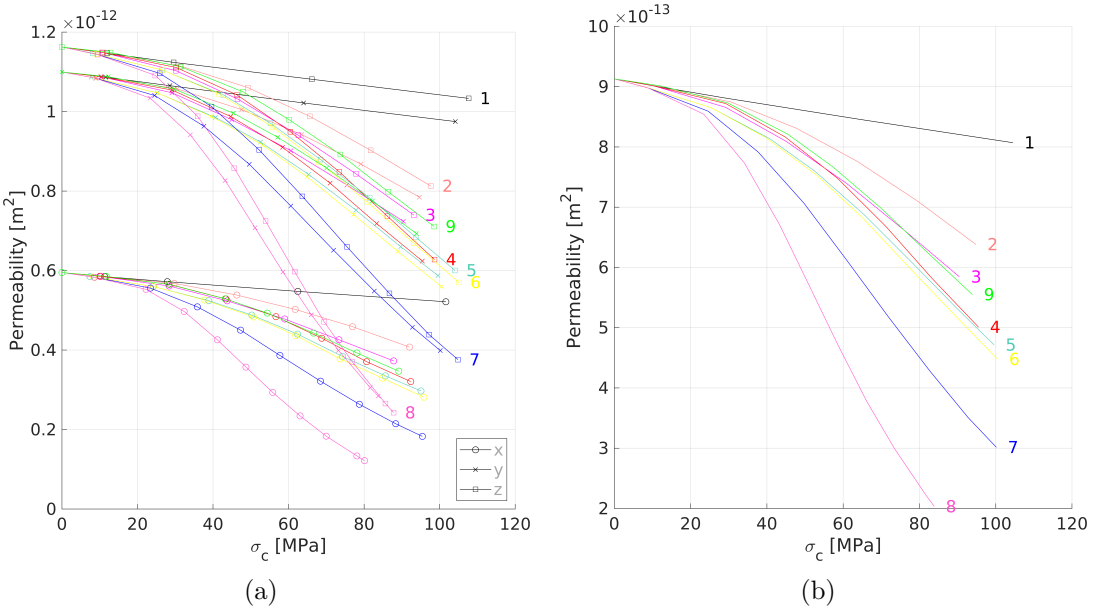

(a) (b)

Figure 6.14: Permeability as a function of stresses for the nine simulations with properties shown in Table 6.2 : (a) in $x - y - z$ principal direction separately, (b) as a geometrical mean value of the three values of permeability in the three principal directions

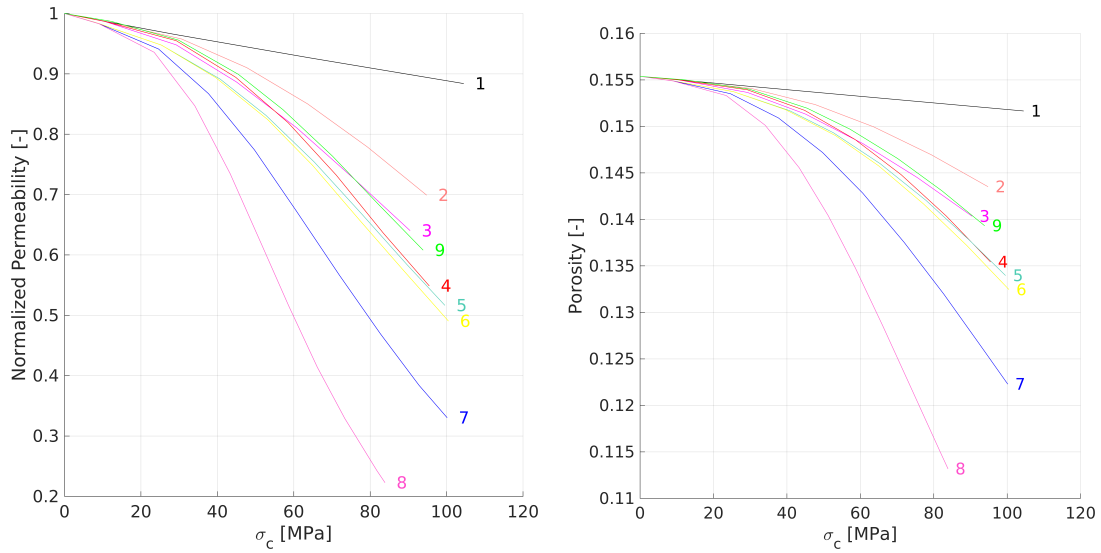

(a) (b)

Figure 6.15: (a) Normalized permeability as a function of confining pressure, (b) Porosity as a function of confining pressure

Influence of local plastic properties

The linear elastic simulation (Simulation 1) shows a very limited decrease in permeability and porosity under an isotropic variation of stress states as shown in Figure 6.14 and 6.15. At 40 MPa, the permeability decrease is only about 5% and reaches 10% when the confining pressure reaches 100 MPa. The behaviour is linear, implying relatively homogeneous and small reductions in pore throat cross-sections as shown in Figure 6.17 with the MIP curve. It can be seen that the average pore throats radius is around 15 microns. Moreover, this almost negligible reduction indicates the need to consider other physical phenomena occurring at the fine scale when the rock is subjected to a variation of stress state. In the present contribution, the consideration of plastification shows significant effect on permeability decrease from 40 MPa as shown in Figure 6.14 already in Simulation 2. The influence of the plastification at high confinement on a sandstone, and the permanent nature of this decrease by local plastification inducing progressive pore closures can be seen in Figures 6.17 and 6.16 with a decrease of pore throats size as the load increases or the mechanical properties become weaker. However, the concavity of the curves obtained seems to act differently from experimental results in (Hu et al., 2018). Indeed, before reaching such a level of confining pressure, sandstone essentially has a brittle behaviour, the transition to a more ductile behaviour taking place when it approaches an isotropic applied stress of 40 MPa as mentioned in (Hu et al., 2018). This implies that other phenomena not captured by the single consideration of non-associated elastoplasticity are likely

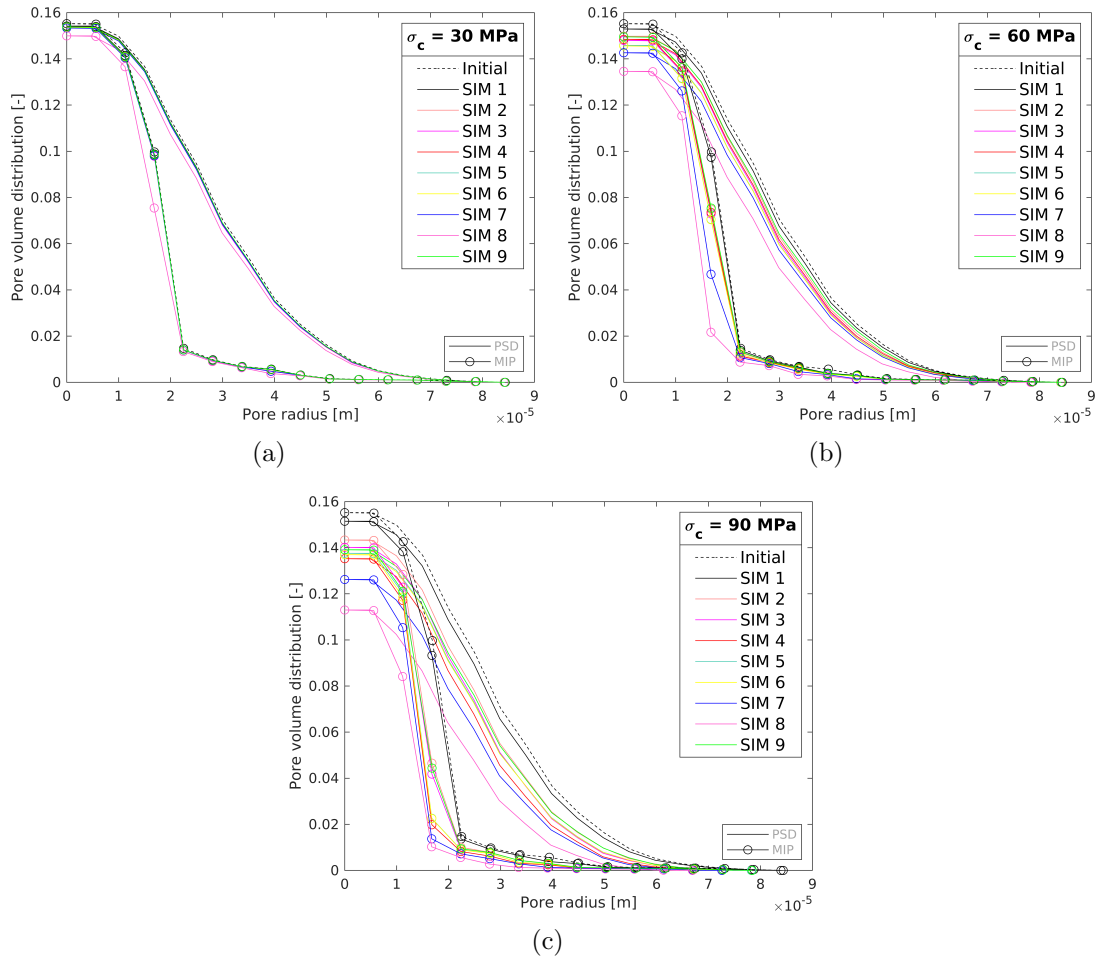

Figure 6.16: Effect of the confining pressure on the pore-size distribution (continuous line) and MIP simulation (circled line) at (a) 30 MPa, (b) 60 MPa, (c) 90 MPa for the nine simulations

to have a more significant effect on permeability when the confining pressure is below 40 MPa. As an example, consideration of damage would allow the simulation of material degradation leading to the detachment of surface sandstone particles that could potentially clog critical pores. This would have the consequence of modifying the concavity of the permeability decrease curves according to the trends obtained experimentally in the literature (Selvadurai and Głowacki, 2008; Hu et al., 2018). Figure 6.12 shows that the stress-strain curve yields from 30 MPa for the simulations showing the progressively larger impact of plastification on the macroscopic response of the material. It also marks the level of confinement at which the permeability decrease becomes more significant as a function of the selected parameters of cohesion and angle of friction.

The elasto-plastic simulations 3 and 4 with homogeneous properties of the solid skeleton show respectively the effect of the variation of the cohesion and the angle

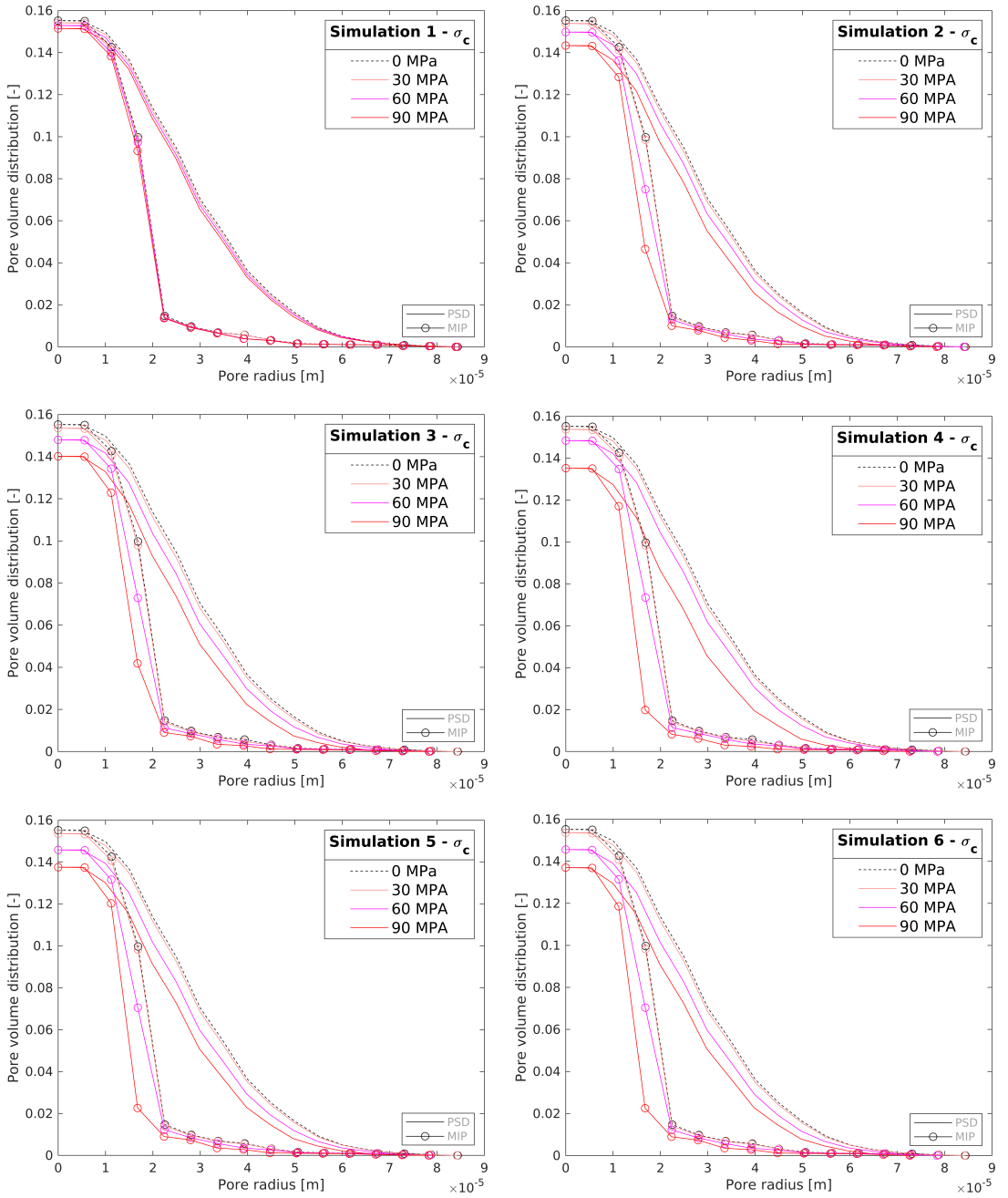

See the next page for complete description...

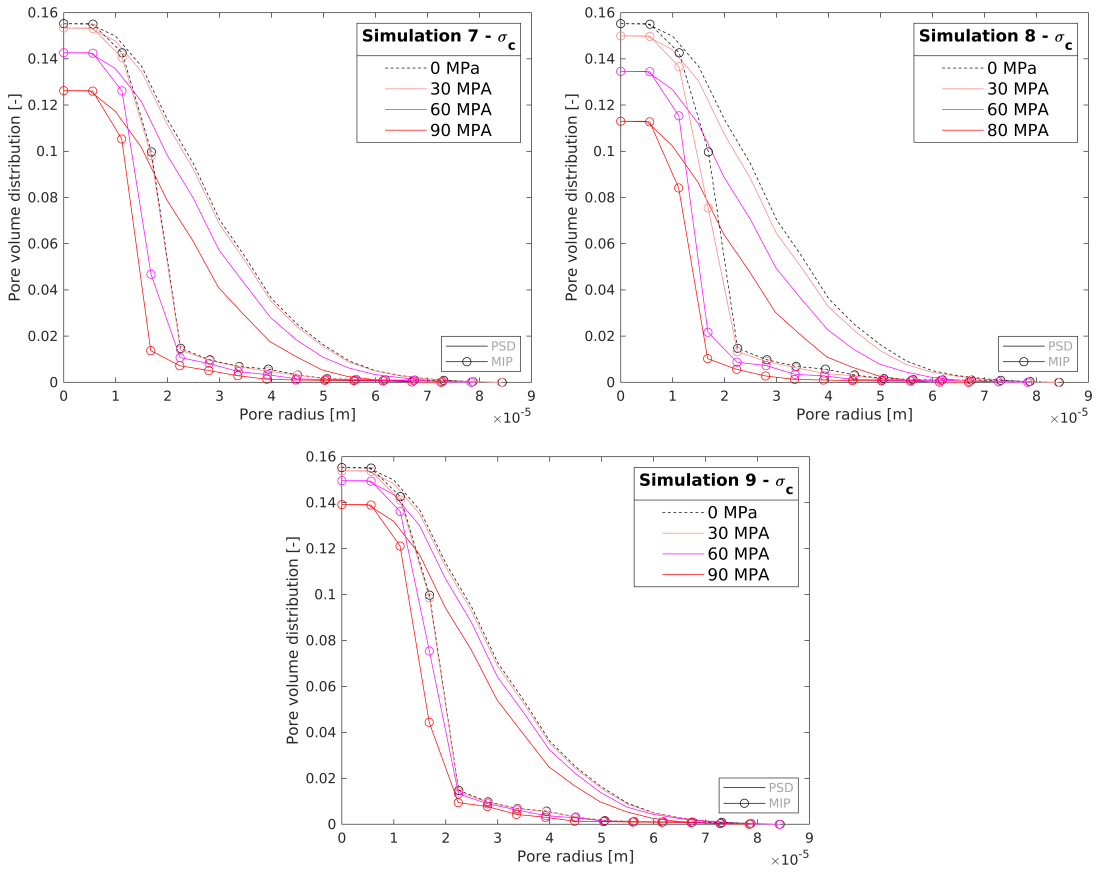

Figure 6.17: Effect of the confining pressure on the pore-size distribution (continuous line) and MIP simulation (circled line) at (a) 30 MPa, (b) 60 MPa, (c) 90 MPa for each simulation separately

of friction on the permeability compared to simulation 2. A decrease in the value of the cohesion (Simulation 3) shows a more significant impact on the plastification at low confining pressures, whereas a decrease in the angle of friction (Simulation 4) will have a larger effect at higher confining pressures. This is associated with the fact that a lower value of cohesion will trigger plastification in areas of high stress gradient at lower confining levels. In addition, the decrease in permeability and porosity is slightly lower for simulation 3 compared to simulation 4 up to 50 MPa. From this value, the trend is reversed and the difference becomes progressively more significant, reaching a permeability decrease of 55% and 65% respectively at about 90 MPa of confinement. This can be explained by the fact that in a Mohr-Coulomb type law, a modification of the cohesion will cause the ordinate at the origin of the failure curve to vary. It would therefore be necessary to reduce it considerably to see significant variations.

Figures 6.16 and 6.17 obtained by the method explained in Section 6.3.5 illustrate the modifications of the total pore size distributions, indicating that

as simulations progress, reductions in pore cross-sections are being observed. The MIP curves represent in some way the reduction of the pore size distribution at throat pores radii along the percolation paths. They show that the microstructure undergoes deformations which also affect them and explain the significant decreases in permeability as the elasto-plastic parameters decrease. The increasingly important evolution of the plastification of the elements as the confining pressure increases (30 MPa, 60 MPa and 90 MPa) is illustrated for Simulation 4 in Figure 6.18 where red regions have plastified. The intensity of the plastic strain is illustrated in Figure 6.19 by the equivalent plastic strain distribution. It shows that the plastic strain is relatively uniformly distributed within the microstructure. It should be noted that for a confining pressure of 60 MPa, local equivalent plastic strains equal to or larger than 10% can be observed, even though the macroscopic strain applied is approximately 0.5%. These large deformations explain the significant decrease in permeability, porosity and pore size distributions observed in Figures 6.14, 6.15, 6.16 and 6.17. Also, the a priori uniform distribution of plastic strains is strongly related to the isotropic compression applied to the subset during the FEM simulations. It should be noted that simulations are conducted for isotropic loading conditions. Potentially, deviatoric loading conditions would emphasize the non-uniform character of the deformations.

Influence of adding a cement layer

Rocks, by nature, are heterogeneous. Sandstone is made of an assembly of grains cemented together. This cement phase binding the grains together has weaker properties than the grains themselves composed mainly of quartz. Similarly, due to physical phenomena such as wheathering, the cement properties may also be weaker. This layer is potentially a preferential site of cracking or plastification phenomena which can play a significant role in the modification of the porous network. The effect of the presence of a thin cement layer with weaker material properties is studied in this sub-section through simulations 5 to 9. This cement layer is identified starting from the pore walls that can readily be identified thanks to the distance field (see Section 6.3.2). The thickness of the layer is applied as an offset to the implicit description of the solid phase (Sonon et al., 2012), so as to reach 10% of the volume fraction of the solid skeleton. This value is purely arbitrary and its purpose is mainly to determine the impact of the presence of this type of heterogeneities on the macroscopic mechanical behaviour of the material and its effect on the transfer properties. The signed distance field generated provides the Euclidean distance to the nearest internal surface of the centroids of the tetrahedra of the mesh. An offset representing the thickness of the cement layer gradually evolves, gradually surrounding the tetrahedra starting from the internal surfaces

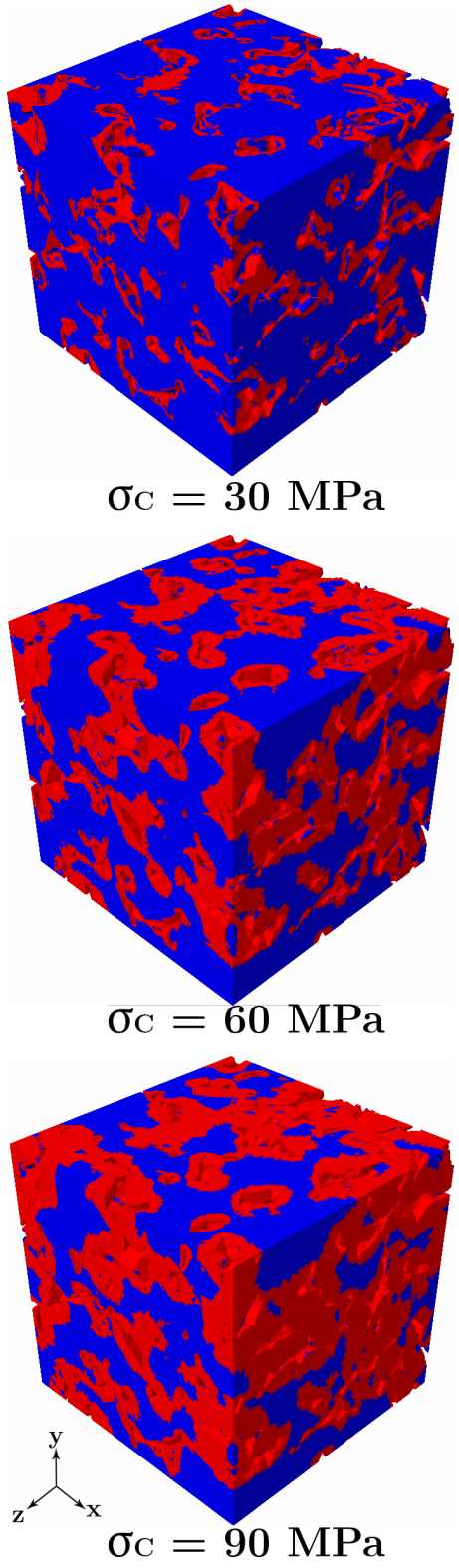

Figure 6.18: Evolution of regions in which the yield is reached (in red even with very limited plastic strains, distributions of plastic strains are plotted in Figure 6.19) of the solid skeleton for simulation 4 at three levels of confining pressure : 30 MPa, 60 MPa, 90 MPa.

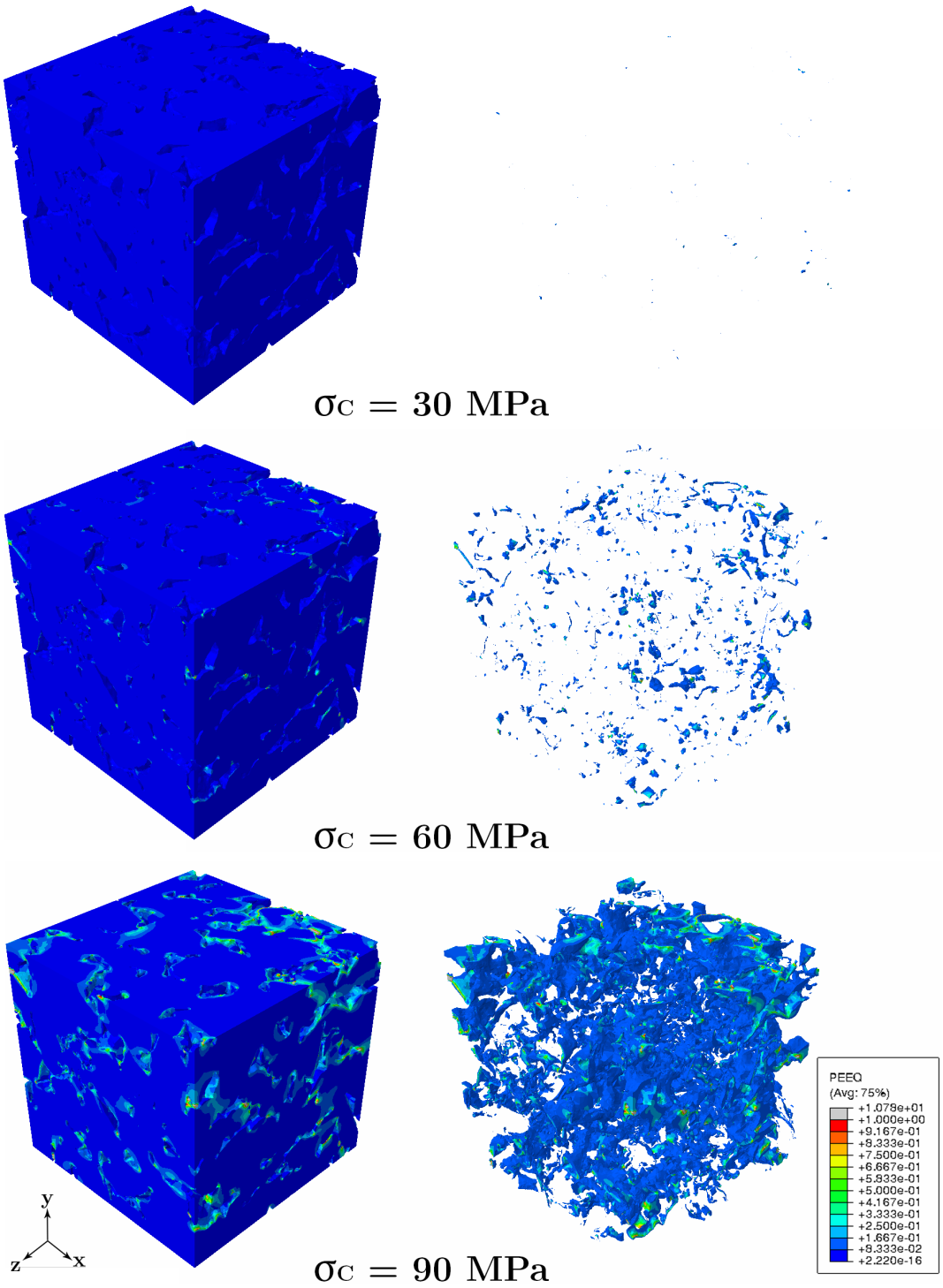

Figure 6.19: (Left) Equivalent plastic strain (PEEQ) and (Right) Elements with a PEEQ equal or higher than 10% of deformation for simulation 4 at three levels of confining pressure : 30 MPa, 60 MPa, 90 MPa.

of the pores until the desired volume fraction is reached as shown in Figure 6.20. The value of the corresponding thickness obtained is approximately 8 microns. Experimental measurements are obviously necessary to obtain more information on the precise composition of the different constituents of a Vosges sandstone.

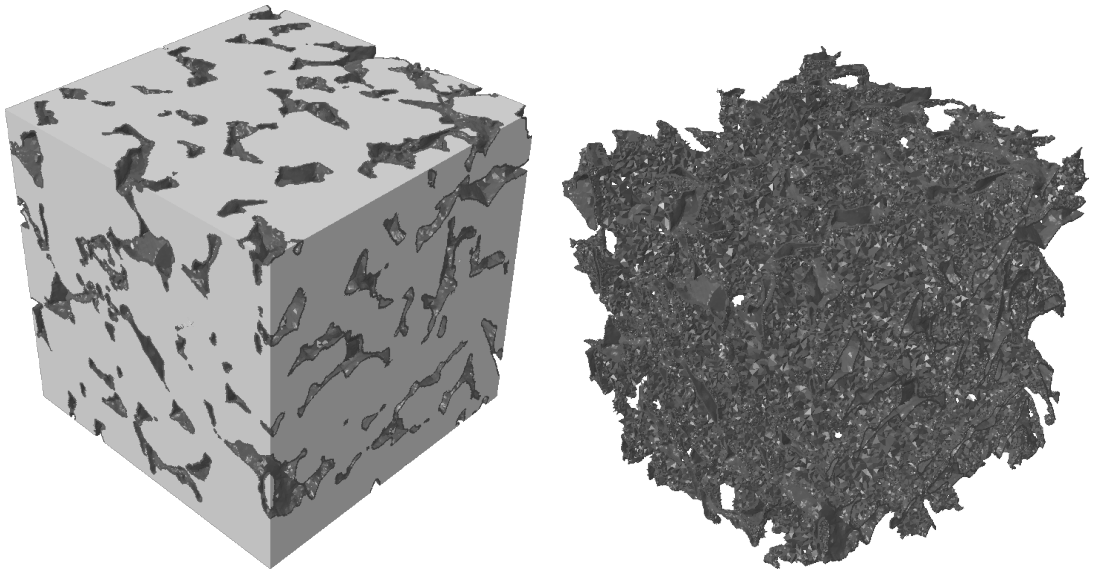

(a) (b)

Figure 6.20: (a) 3D representation of Vosges sandstone subset with the cement layer in dark grey and (b) Extracted cement layer from the whole 3D geometry with a thickness of 8 microns

To investigate the influence of the Mohr Coulomb parameters on the mechanical and hydraulic behaviour of the subset, simulations 5 to 9 progressively vary the plastic parameters in the cement layer one by one. Except for simulation 9, a classical mixing law is used to determine the Young modulus of the cement in order to keep the same global Young modulus of the sandstone as the first 4 simulations (i.e. $E_{skel} = 20$ GPa). By imposing a value of 1 GPa for the cement, a Young modulus of the grains of 22.11 GPa yields a macroscopic Young modulus of 20 GPa. From simulation 5, the overall mechanical behaviour is slightly weaker in the elastic phase as a consequence of the Young's modulus of the cement being 20 times lower (see Figure 6.14). This becomes more pronounced as soon as the plastification is initiated. Between simulations 4 and 8, the plastic properties of the grains are kept similar. The cohesion of the cement is 18 times smaller while the angle of friction is lower than in the grains by 15°. The addition of a thin layer of cement with the above-mentioned properties reduces the permeability by almost a factor of 2: for a confining pressure of 80 MPa the permeability decreases from 33% to 77% of its initial value. Between simulations 7 and 9, the increase in Young modulus of grains by a factor 2 and a slight increase in cohesion for

stability reasons will have the effect of limiting the decrease in permeability going respectively from 50% to 30% of its initial value. Simulation 9, with a higher stress-strain curve than the elastic simulation due to a higher grain modulus, will lead to a much more significant decrease in permeability and porosity due to the local plastifications induced during deformation.

The concavity transition of curves 7 and 8 (see Figure 6.15(a)) indicates that some critical paths are most probably completely occluded. The significant respective decreases in porosity (see Figure 6.15(b)) can potentially indicate that, due to the lack of consideration of contact in the mechanical simulations, grain interpenetration is starting to take place. Taking the contact into account, will probably change the concavity of the porosity decrease curve for the weakest cases, but the local re-arrangements caused by it might still significantly decrease the porosity and the permeability.

Comparing to Figures 6.18 and 6.19, considering a weaker cement layer will increase significantly the intensity of plastic strains as illustrated in Figures 6.21 and 6.22. The plasticity appears noticeably and denser for the same confining pressures compared to Simulation 4. The right side of Figure 6.21 shows the closed pore voxels for these same confining pressures obtained by the difference between the pore space binary voxellisation of the deformed configurations with the undeformed one. They provide an indication of which regions are the most strongly deformed as the confining pressure increases. This suggests that at high levels of confinement specific regions will be preferential sites for more or less important modifications of the pore network structure. A large deformation of pore chambers will have a significant impact on the decrease in porosity, while a large deformation of a critical pore will affect the fluid flow and consequently the permeability as will be illustrated in the sequel in Fig.6.27). Also, equivalent plastic strains equal to or larger than 10% observed are significantly more present from 30 MPa, in contrast to simulation 4 which only considers a homogeneous solid skeleton.

Permeability hysteresis

Given the simulated impact of an isotropic loading on the subset, there is interest in investigating in which way the emergence of local plastifications will affect the mechanical response during unloading, and in assessing the permanent nature of the permeability decrease. This effect is illustrated using the parameters of simulation 7 for three levels of unloading: 30 MPa, 60 MPa, 100 MPa. The macroscopic mechanical response of the microstructure as shown in Figure 6.23(a) left shows a strain-hardening phenomenon and the related irreversible plastic deformation of the material. This irreversible deformation increases with the confining level at the moment of unloading. The unloading path acts differently from the loading path.

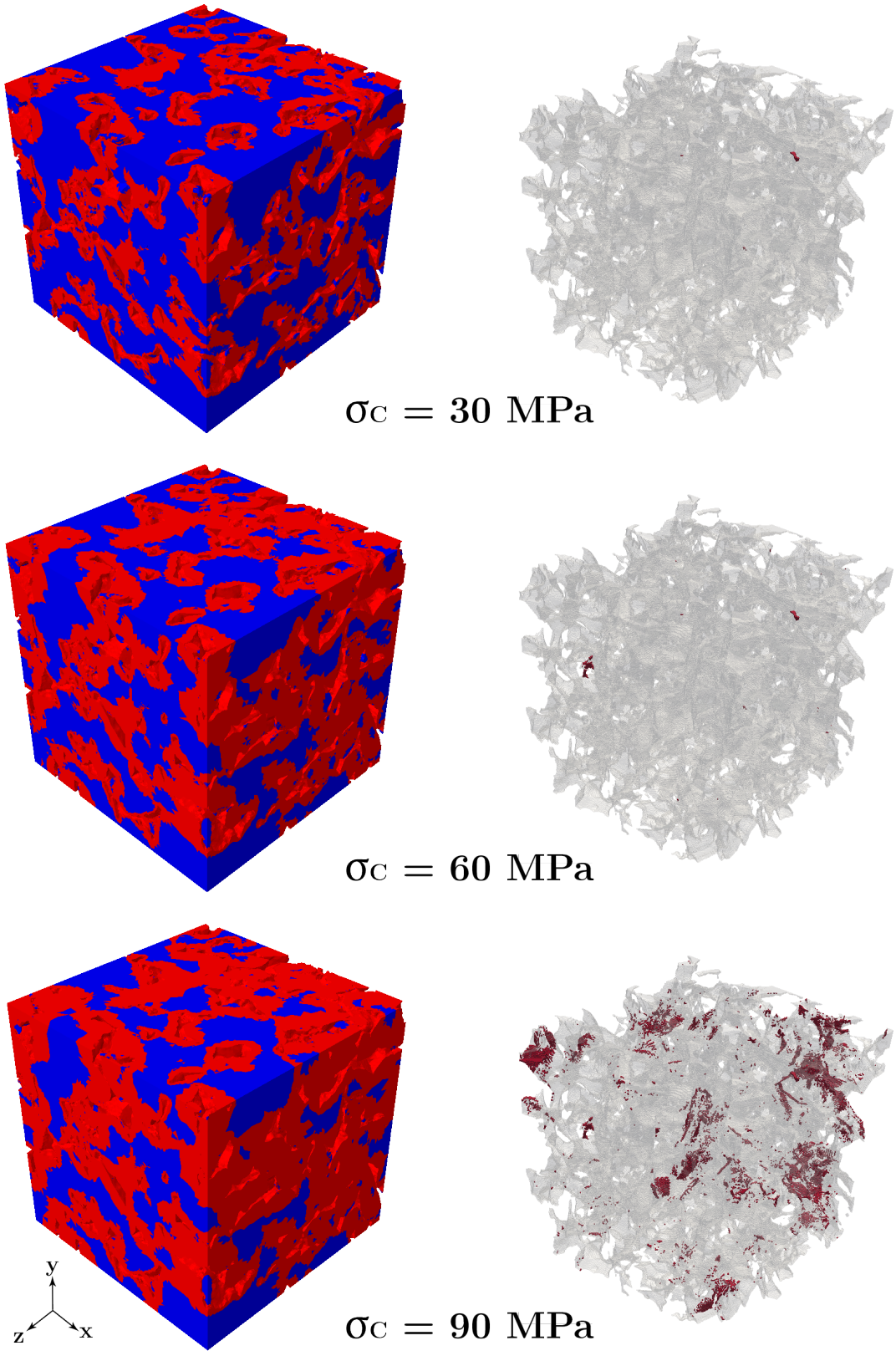

Figure 6.21: (Left) Evolution of regions in which the yield is reached (in red even with very limited plastic strains, distributions of plastic strains are plotted in Figure 6.22 of the solid skeleton and (Right) Voxels closed in relation to the undeformed space of the 3D pore space showing the most reduced pores section induced by the localization of the plastification for simulation 7 at three levels of confining pressure : 30 MPa, 60 MPa, 90 MPa.

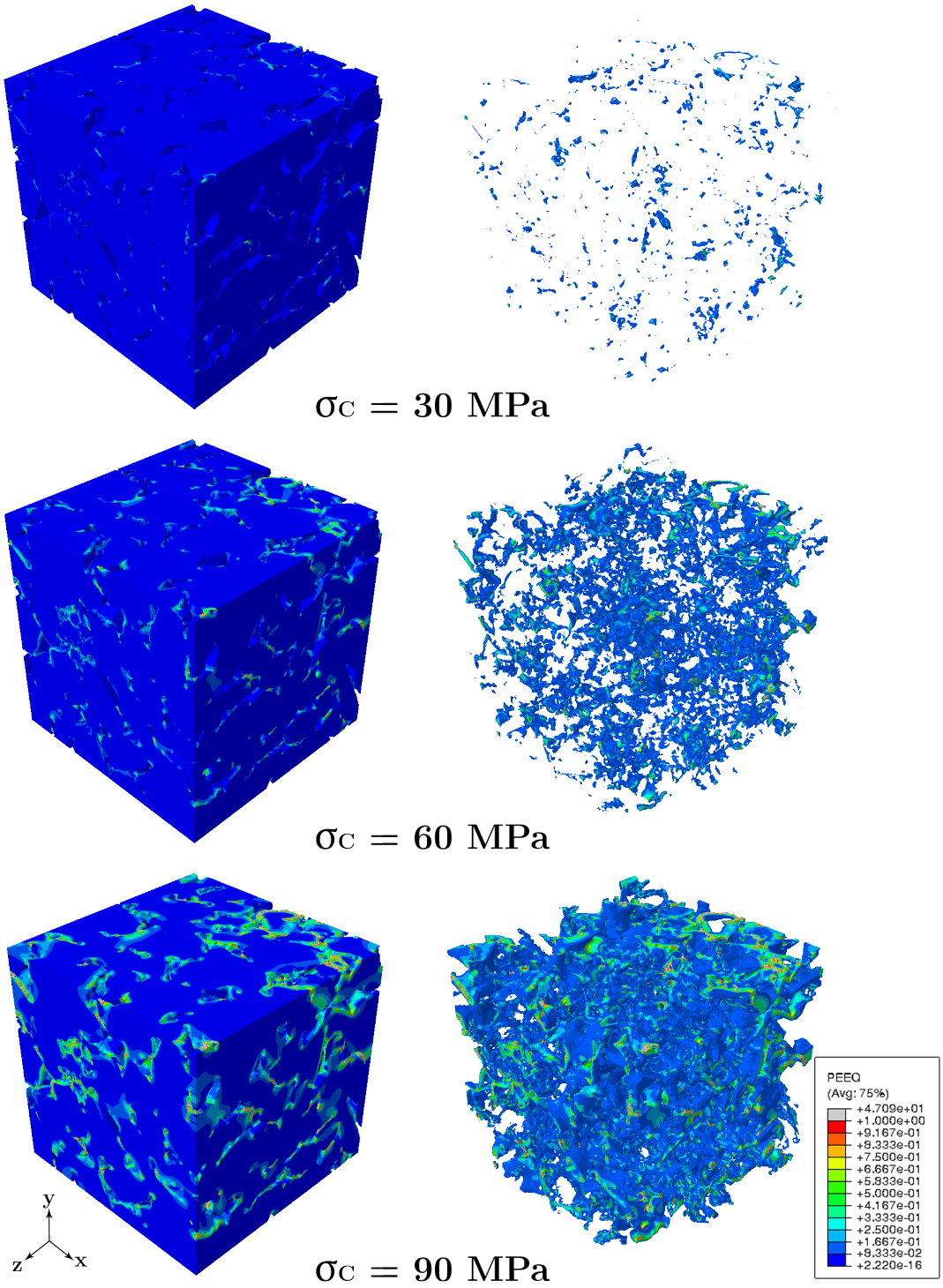

Figure 6.22: (Left) Equivalent plastic strain (PEEQ) and (Right) Elements with a PEEQ equal or higher than 10% of deformation for simulation 7 at three levels of confining pressure : 30 MPa, 60 MPa, 90 MPa.

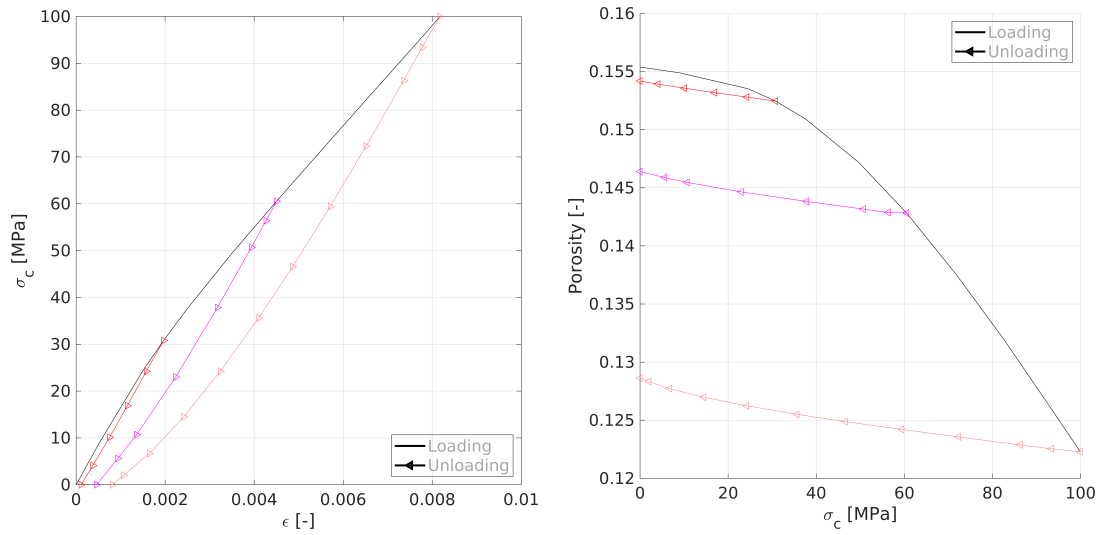

Figure 6.23: (a) Confining pressure as a function of the deformation and (b) Porosity as a function of the confining pressure of the subset sample with properties number 7 in Table 6.2 showing the effet of local plastifications on the curves after unloading at 30 MPa, 60 MPa, 100 MPa

Figure 6.23(b) indicates the permanent densification of the subset by a significant reduction in the void volumes not recovered after unloading.

Figure 6.24, on the other hand, illustrates the irreversible decreases in permeability occurring for the 3 different unloading levels. The initial permeability is not recovered during unloading. As the plastic behaviour becomes more and more significant from 30 MPa onwards during loading, the local irreversible deformations generated during loading have an increasingly significant impact on the morphology of the porous network.

These irreversible deformations obtained after unloading are illustrated through a 2D section of the microstructure in Figure 6.26 subjected to a 100 MPa isotropic loading before being unloaded. Local changes in pore sizes and throats are depicted. Naturally, these 2D cuts are not related to percolation paths and cannot be interpreted for 3D percolation. Figure 6.27 illustrates the effect of irreversible mechanical deformations on the fluid flow obtained upon loading and after the unloading on the 3D subset. The flow computed by Lattice-Boltzmann simulations is illustrated on each of the three geometries, corresponding respectively to the subset before loading, loaded at 100 MPa and unloaded. The fluid flow through the subset is significantly affected after loading as a result of the reduction of the conducting pores cross sections as shown in the pore size distributions in Figure 6.25 for Simulation 7. The slope of the unloading-permeability curve (see Figure 6.24) indicates a relatively similar return behaviour for the 3 levels of unloading. Indeed, when unloading, only

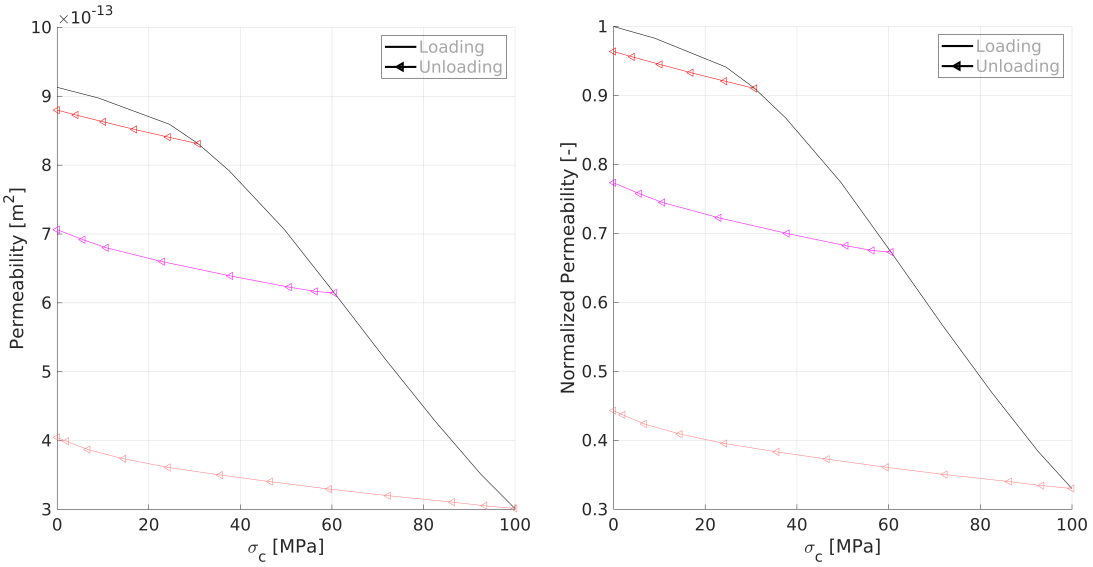

(a) (b)

Figure 6.24: (a) Absolute permeability and (b) normalized permeability as a function of confining pressure of the subset sample with properties number 7 in Table 6.2 showing the irreversible decrease of both porosity and permeability due to local plastifications after unloading at 30 MPa, 60 MPa, 100 MPa

the elastic deformation is recovered. It is characterised by a slight expansion of the compressed pores. This is confirmed by the pore size distribution curves reported in Figure 6.25 remaining however well below its pre-loading level.

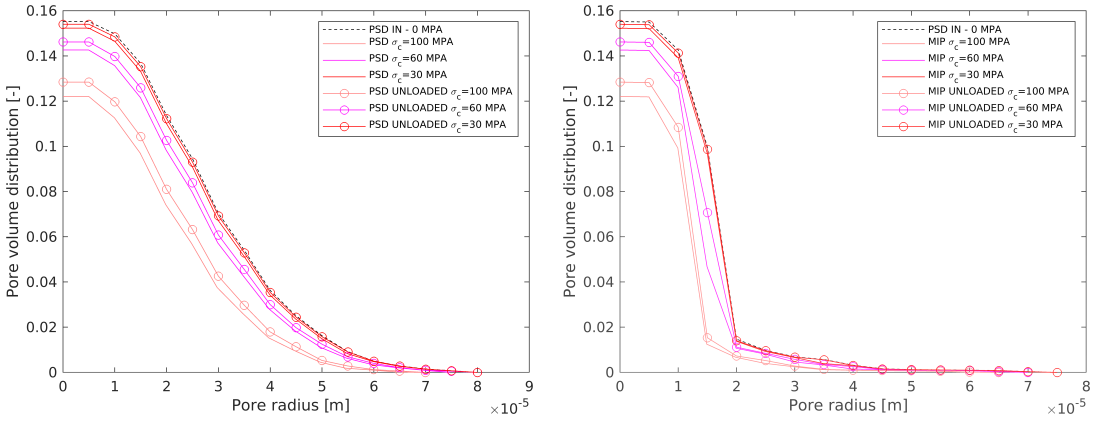

(a) (b)

Figure 6.25: (a) PSD and (b) MIP simulation of the subset sample with properties number 7 in Table 6.2 showing the effet of local plastifications on the curves after unloading at 30 MPa, 60 MPa, 100 MPa

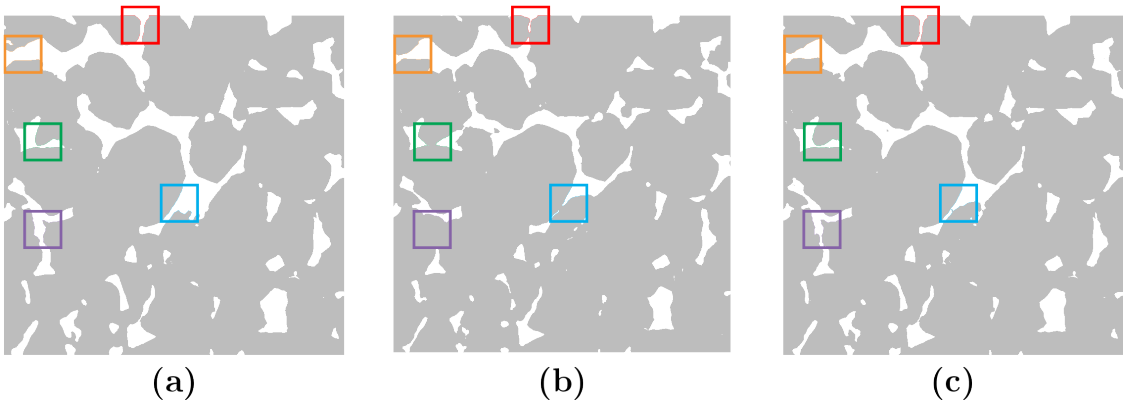

Figure 6.26: 2D cut view in $x-y$ plane at $z = 0.75\,mm$ of the deformed solid skeleton of the rock at 3 different states for simulation 7 in Table 6.2: (a) Initial state, (b) Loaded state at $\sigma_c = 100$ MPa, (c) Unloaded state highlighting the permanent deformations due to plasticity

6.5 Discussion

The integrated procedure developed in this contribution allows modelling the alteration of the permeability of a rock microstructure subjected to isotropic compression by local plastification. The uncoupled solid-fluid interaction by the combined use of FEM simulations using conformal meshing and LBM simulations based on the revoxellisation of the deformed mesh gives interesting results. Indeed, this integrated image-based procedure allows assessing a number of relevant and interesting assumptions in order to better understand the mechanical phenomena governing at the fine scale behaviour. This allows unravelling processes that can significantly affect the fluid flow within the microstructure and alter the macroscopic permeability based on realistic geometrical representations of the rock pore scale structure. The decision to develop the model from CT-Scan data was based on the desire to use realistic microstructures compared to the virtually generated geometries. The interest of developing virtually generated microstructural geometries resides in the possibility to parametrize the study from the geometrical part to the simulations, giving powerful analysis tools. It should be emphasized also that the use of CT-Scan data requires segmentation and image processing in order to make them suitable for FEM simulation. All these steps may potentially induce errors due to data acquisition, to the type of segmentation selected according to the type of geometry, the application of filters and smoothing, as well as the need to be correctly calibrated. These precautions are crucial to obtain a geometry as close as possible to the real morphology without compromising its use in a mechanical simulation. Moreover, the exploitation of the CT scans is made with a fixed, quite strong, resolution. In future investigations, a study of the impact of the scans resolution on the stress-permeability results could be useful in order determine the effects related to lower

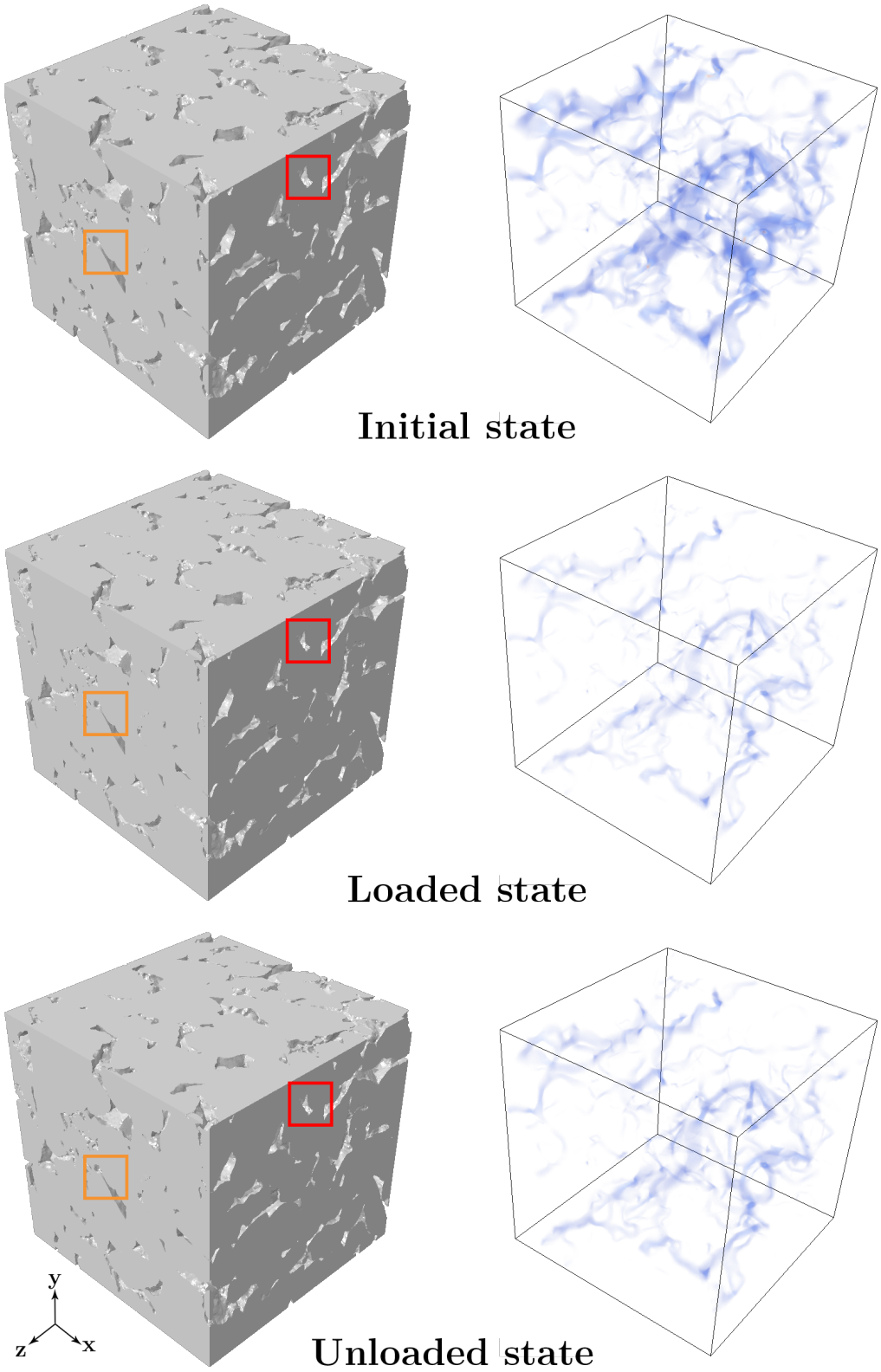

Figure 6.27: 3D representation of deformed configuration (Left) and fluid flow (Right) at 3 different states for simulation 7 in Table 6.2 : Initial state, Loaded state at $\sigma_c = 100MPa$, Unloaded state. Fluid is injected in the positive z-direction. The intensity of the color of the fluid flow is related to the flow magnitude while the denser flow is related to the diameter of throat pores

resolutions. It is noted that this could be done artificially by interpolating the CT scans datas on coarser grids. In the present contribution the choice was made to start the analysis after obtaining the segmented microstructure. This is justified by the fact that the main objective of the developments presented was to illustrate the process allowing the investigation of the link between variations of permeability due to mechanical deformation. A comparative study including experimental tests and their microtomographies obtained in-situ would make it possible to calibrate the model on the type of rock chosen and to establish a rigorous comparative grid between the experimental results and the numerical simulations.

Nevertheless, it is emphasized that the permeability values obtained by the Lattice-Boltzmann simulations are within the order of magnitude commonly obtained in experimental tests for sandstone, and especially the experimental values obtained on the Vosges sandstone (Hu et al., 2018). Their slightly higher values can be explained, among other things, by Gaussian smoothing, which tends to reduce the roughness of the geometry, making the solid-fluid surface much smoother. This step is here used in order to obtain a geometry leading to mechanical simulations performed within a reasonable time. Similarly, the porosity of 16.08% obtained after segmentation by hysteresis thesholding shows that a percentage of porosity is not resolved with the scan resolution of 5 microns.

Given the slightly initially anisotropic nature of the sandstone studied, the confining pressure corresponding to the macroscopic deformation is almost isotropic, with the deviation from a isotropic stress state becoming more pronounced as the confining pressure becomes important. However, at about 100 MPa of confining pressure on average, the difference between the values obtained for each axis does not exceed 4%, a variation considered negligible. This contribution focuses on the emergence of local plastifications causing permanent deformations of the porous network, inducing in turn a modification of the hydraulic conductivity through the use of a Mohr-Coulomb elasto-plastic law. The effect of these plastifications start being noticeable in results above 30 MPa, which corresponds to the confining pressure at which the sandstone behaviour starts being more ductile. Indeed, the failure mode of Vosges sandstone is typical of a brittle-ductile transition when the confining pressure varies from 0 to 40 MPa (Hu et al., 2018). The model developed therefore does not enable yet the simulation of other physical phenomena governing the modification of the micro-structural geometry for confining levels below 30 MPa. Indeed, the decrease in permeability are found much more significant through local plasticity than with a purely elastic law, it only allows the permeability reductions to be represented by a progressive reduction of the pores sizes. Phenomena such as sudden pore collapse or pore clogging may have a significant influence on the

permeability evolution at low confining pressures, which would have the effect of reversing the concavity of the permeability decrease curves obtained.

Yet, the use of a conforming finite element mesh makes the approach rather versatile as it allows the use of any other laws readily available in conventional FEM softwares such as Abaqus. Therefore, future contributions could include consideration of contact, damage or degradation in order to study their respective influence on the transfer properties. Of course, the addition of such constitutive laws, given the level of refinement required to obtain a sufficiently representative microstructure, is likely to increase considerably, the cost of the simulations and the complexity of the solution schemes motivating the use of an explicit approach.

The parametric study highlights the influence of the plastic parameters of the fine scale Mohr-Coulomb constitutive law, cohesion and angle of friction, as well as the addition of a cement layer on the geometrical representation of the porous network. The microscopic properties of the material were chosen on the basis of macroscopic values from (Hu et al., 2018) and may therefore be debatable. However, these are difficult to identify and require advanced characterisation methods. A decrease in cohesion will have a more significant effect at low confining pressures, while the impact of the angle of friction will be more significant at higher confining pressures. This can be explained by the fact that in a Mohr-Coulomb type criterion, a change in cohesion will cause the ordinate at the origin of the curve to vary. It would therefore be necessary to reduce it considerably to obtain significant variations. On the other hand, a decrease in the angle of friction by a few degrees will have a more pronounced influence on the plastification at high confining pressure since this affects the slope of the curve. The addition of a cement layer with weaker properties shows that intergranular stresses within the rock can have a considerable influence on permeability by significantly affecting the pore network through pore closures. The process also shows its ability to represent the irreversible decreases in permeability after unloading following the monotonic increase of the confining pressure, thus showing that the evolution of permeability is dependent on the stress state and is a stress-path dependent process.

6.6 Conclusion

This contribution presented a methodology for the numerical analysis of permeability alterations in natural rocks under varying stress states, taking explicitly into account the complexity of the rock microstructure. For this purpose, the modelling, in order to be geometrically realistic, relies on microtomographic scan data, and was illustrated here for a Vosges sandstone. The mechanical deformations under isotropic compression at the scale of the microstructure inducing pore closures by local

plastification were simulated using FEM simulations using a non-linear elastoplastic law allowing to take into account the redistribution of local stresses. Geometrical non linearities were also incorporated to account for pore closures. These simulations in a conventional FEM software were made possible by the use of a conformal mesh generator that allows the production of high quality meshes on complex geometries. The evolution of permeability was evaluated at different confining pressure levels using the Lattice-Bolzmann method. This unilateral solid-fluid coupling made it possible the study of the combined influence of pore space morphology and solid skeleton constitutive law parameters during loading and unloading. The proposed methodology is designed to be flexible thanks to the interfacing with 'classical' discretization approaches and a modular implementation plan. Future contributions are envisaged to better calibrate the model on experimental results in order to better understand the significant impact of irreversible permeability reductions by local plastification at high confining pressure levels. The integrated approach also makes it possible to test other microstructural features such as the effect on permeability of different initial pore size distributions. Similarly, as the sandstone composition is not homogeneous, it would be interesting to investigate in more detail the impact on permeability of an evolving distribution of the cement properties along the thickness of the layer or with a non-homogeneous distribution through the rock sample.

7 Conclusion & Perspectives

Contents

7.1 Conclusion

The objective of the thesis was to develop an integrated approach to model permeability alterations in natural rocks subjected to stress state variations by using a realistic image based representation of the microstructural morphology. The idea was to (i) explore the links between the properties of the porous network and the macroscopic transfer properties of the porous material considered, and (ii) incorporate modifications of the porous network induced by a deformation of the rock microstructure resulting from a variation in the state of stress.

For this purpose, an integrated and automated approach was developed to provide a robust tool allowing testing a series of assumptions on the fine scale behaviour linking the impact of the deformability of the solid skeleton of rock microstructures on the macroscopic permeability. The construction of this integrated approach is the result of ingredients put in place through the choices and developments of methods necessary to propose solutions to the identified research questions:

- The realistic description of the microstructural geometry was based on μCT scans of a Vosges sandstone provided by the University of Lille (Hu et al.,

2018). These images allow the analysis of data from a specific class of natural rock.

- Image processing tools were exploited in order to make the microstructural geometry of the Vosges sandstone usable in FEM simulations, requiring a high quality mesh at optimized affordable computational cost.
- The development of a robust conformal and periodic mesh generator for complex heterogeneous geometries obtained from virtually generated geometries or derived from CT-scans, based on implicit geometrical descriptions. The resulting optimized discretization makes it possible to conduct FEM simulations in conventional softwares that include the constitutive laws required to simulate the mechanical behaviour of rocks.
- An assessment of advanced discretization methods based on conforming meshes (FEM) and non conforming meshes (EFEM), able to handle complex microstructural geometries, has been set up to highlight the complementarity of the tools in the analysis of the mechanical behaviour of rocks.
- An interface with a FEM approach via the ABAQUS simulation software (Simulia, 2014) was set up, enabling to simulate the geometrical and material non-linear mechanical behaviour of rocks from an optimized conforming mesh.
- The efficient evaluation of the altered macroscopic permeability was obtained from simulated fluid flows within the porous network of the deformed microstructure at different levels of confining pressures by revoxellisation via Lattice-Boltzmann simulations.

The set of solutions presented above to address the research questions defined in this thesis has been presented through three distinct contributions in the framework of chapters 4, 5 and 6.
The contribution of this work to the state of the art can therefore be summarized along the identified research questions.

An integrated approach for the conformal discretization of complex inclusion-based microstructures

This contribution presented a new conforming mesh generation methodology for 2D and 3D periodic (or not) complex heterogeneous RVEs. The implementation is adapted and optimized for the RVEs generatorion tools developed by (Sonon et al., 2012) in order to propose an integrated approach. However, as demonstrated in this thesis, a natural extension can be built for general implicit geometries obtained from other geometry generation methods or from experimental techniques such as

CT scans. The newly developed approach is an iterative Delaunay mesh generator based on an extended Persson-Strang truss analogy optimization process. Such an approach, based on signed distance fields, carries the advantage that the level set information used during the generation of the geometry of the microstructure by (Sonon et al., 2012) can seamlessly be used in the subsequent discretization procedure.The meshing process is hierarchical and aims at generating a triangulation, optimizing and constraining progressively interfaces, boundary faces and the volume. It offers a specific control on the inherent specificities of each part and leads to the generation of high quality FEM meshes. On the internal surfaces, nodes are prevented from moving outside the interfaces by systematically constraining their normal movement acting like boundary reactions, while tension/compression forces act in the bars to reach the desired lengths defined by a size function. The latter allows optimizing the node distribution as a function of geometrical features such as curvature, nearness and narrowness between inclusions, or between pore walls. The distorsion of the elements is reduced by using a gradient limiting factor to better control the progressive spatial changes of elements sizes. Periodicity can be ensured by meshing independently non opposite master RVE faces before copying, translating and merging them to form the periodic enclosing box while conformity is ensured by using the Constrained Delaunay Tetrahedralization. The methodology is intended to be general and has been used successfully in various applications such as masonry (Massart et al., 2018, 2019) , woven composites (Wintiba et al., 2017, 2020) and metal foams (Ghazi et al., 2019; Kilingar et al., 2019).

Comparison of advanced discretization techniques for image-based modelling of heterogeneous porous rocks

This contribution presented the assessment of computational discretization strategies allowing to conduct automated simulations based on raw CT scan data for porous rocks with complex pore space morphologies. Both methods rely on pore and solid phase geometrical descriptions based on implicit functions and distance fields. Such a description can be obtained by level set-based segmentation techniques that were used here. Based on such implicitly described heterogeneous geometries, two discretization schemes were outlined. The first one makes use of the implicit description of the geometry to produce a conforming finite element discretization of the solid and pore phases. Based on the geometrical information, it allows generating selectively refined tetrahedral meshes to capture the complex geometry of the porous network and the corresponding solid boundaries. Complementarily, a second strategy based on a kinematic enrichment by incompatible modes is used to account for material boundaries based on a non-conforming mesh with uniform element sizes. Mechanical simulations conducted on the CT scan pre-processed geometry show that

the main feature of the behaviour can be captured by both methods. The conformal finite element procedure allows capturing the effect of more detailed geometrical features, while the incompatible mode-based framework is more flexible as it allows using the same (non conforming) mesh for potentially variable geometries. It is again emphasized that the simulations remain elastic in this contribution, and that stress redistributions have to be expected as from the first plastification.

Image based modelling of stress induced permeability alterations in sandstones

This contribution presented an image-based modelling methodology for the numerical analysis of permeability alterations in natural rocks under varying stress states, taking explicitly into account the complexity of the rock microstructure. The capacity of the approach is illustrated on a subset of the microCT scans of a Vosges sandstone. The mechanical deformations under isotropic compression at the scale of the microstructure inducing pore closures by local plastifications were simulated using FEM simulations with a non-linear elastoplastic law allowing to take into account the redistribution of local stresses. These simulations in conventional FEM software were made possible by the use of a conformal mesh generator that allows the production of high quality meshes on complex geometries. The evolution of permeability was evaluated at different confining pressure levels using the Lattice-Bolzmann method. This uncoupled solid-fluid interaction made it possible the study of the combined influence on the permeability, porosity and the pores size distribution of the pore space morphology and the solid skeleton constitutive law parameters during loading and unloading conditions.
The numerical results have shown that:

- The permeability of the unloaded Vosges sandstone is of the same order of magnitude as the experimental value, which demonstrates the relevance of the image processing and Lattice-Boltzmann methods.

- A significant modification of the permeability under isotropic compression (with a similar order of magnitude as observed experimentally on other rock materials), as well as irreversible changes in the permeability under isotropic loading-unloading cycles, can be obtained only when elastoplastic constitutive laws allowing local redistribution of stresses are considered, or when the heterogeneity of the solid phase (i.e. presence of an arbitrary cement layer with weaker mechanical properties around solid grains) is introduced.

This latter result highlights that local plasticity around critical pores can be a consistent assumption to explain the modification of the permeability observed experimentally under varying stress state. In addition, the proposed methodology is designed to be flexible thanks to the interfacing with 'classical' discretization approaches and can be easily readapted to other contexts given the block approach.

7.2 Perspectives

As a result of the developments made and the results obtained, some relevant insights could be addressed in future contributions:

- Improving the efficiency of the mesh generator by implementing the following functionalities:
  - A parallelization process in order to speed up computation times, especially for inclusion-based geometries where each inclusion can be processed independently.
  - The integration of meshing improvement tools by local operations such as Stellar (Klingner and Shewchuk, 2008) or the new developments proposed by (Marot et al., 2019) allowing generating the best tetrahedralization through an efficient parallelized serial implementation of the incremental Delaunay insertion algorithm.
- The development of a hybrid semi-conformal approach, proposed as 'oct-EFEM', exploiting the benefits of the conformal and non-conformal approaches discussed in Chapter 5. Indeed, some local geometrical information of the microstructure could be used to produce tailored non conforming meshes with selective refinement by octree meshing at a marginal pre-processing cost, thus improving the accuracy of the EFEM simulations, while reducing the cost involved in the generation of a conformal mesh.
- The implementation of an experimental study with in-situ microtomography performed on a sandstone under compression in order to allow a calibration of the model as early as in the segmentation phase. Based on this experimental study, it would potentially be interesting to use Digital Image Correlation (DIC) to identify the levels of the macroscopic strains to apply on the CT scan subset used in FEM simulations to improve the definition of the boundary conditions applied to this subset. This would provide a more relevant basis for comparison between experimental and numerical results.

- The use of the integrated methodology on virtually generated geometries via excursion sets (Roubin et al., 2015) or DN-RSA (Sonon et al., 2012) for which there is already a handle in view of comparison with the Vosges sandstone model obtained from μCT scans.
- The integrated and automated approach developed enables to test a series of hypotheses linking the deformability of the microstructure to the altered permeabilities that would be worth investigating in the short term:
  - The effect on permeability of a variation in the volume fraction of cement (non)homogeneously distributed along the surface under a variation in isotropic or deviatoric stress states (graded properties of the cement based on the distance to the pore walls).
  - The effect on the permeability of considering the evolving properties of the cement along the thickness of the layer.
  - The effect on permeability by the addition of contact, a damage law or clogging pore simulation, especially at the beginning of loading during the fragile-ductile transition.
  - The effect on permeability through the addition of cracking through the use of oct-EFEM, more adapted to simulations involving strong discontinuities with the potential of selective refinement in areas of interest.
  - The effect on permeability of a modification of the initial pore size distributions by targeted pore closures

Finally, the long-term goal of the tools developed in the scope of this thesis is to provide ingredients that would contribute in the future to engineering problems in the build-up of closed form stress-permeability relationships or in nested multiscale approaches to be used at the regional scale, such as FE^2 methods (Feyel, 2003).

Scientific communications

Peer-reviewed papers

1. Wintiba B, Sonon B, Ehab Moustafa Kamel K, Massart TJ (2017) An automated procedure for the generation and conformal discretization of 3d woven composites rves. Composite Structures 180(Supplement C):955 – 971

2. Massart T, Sonon B, Ehab Moustafa Kamel K, Poh L, Sun G (2018) Level set-based generation of representative volume elements for the damage analysis of irregular masonry. Meccanica 53(7):1737–1755

3. Massart T, Ehab Moustafa Kamel K, Hernandez H (2019) Chapter 11 - automated geometry extraction and discretization for cohesive zone-based modeling of irregular masonry. In: Ghiassi B, Milani G (eds) Numerical Modeling of Masonry and Historical Structures, Woodhead Publishing Series in Civil and Structural Engineering, Woodhead Publishing, pp 397 – 422

4. Ghazi A, Berke P, Ehab Moustafa Kamel K, Sonon B, Tiago C, Massart T (2019) Multiscale computational modelling of closed cell metallic foams with detailed microstructural morphological control. International Journal of Engineering Science 143:92–114

5. Ehab Moustafa Kamel K, Sonon B, Massart TJ (2019) An integrated approach for the conformal discretization of complex inclusion-based microstructures. Computational Mechanics 64(4):1049–1071

6. Kilingar N, Ehab Moustafa Kamel K, Sonon B, Massart T, Noels L (2019) Computational generation of open-foam representative volume elements with morphological control using distance fields. European Journal of Mechanics - A/Solids 78:103847

7. Ehab Moustafa Kamel K, Colliat JB, Gerard P, Massart T (2020) Comparison of advanced discretization techniques for image-based modelling of heterogeneous porous rocks. Acta Geotechnica 15(1):57–77

8. Wintiba B, Vasiukov D, Panier S, Lomov SV, Ehab Moustafa Kamel K, Massart TJ (2020) Automated reconstruction and conformal discretization of 3d woven composite ct scans with local fiber volume fraction control. Composite Structures 248:112438

9. Sonon B, Ehab Moustafa Kamel K, Massart TJ (2021) Advanced geometry representations and tools for microstructural and multiscale modelling, Advances in Applied Mechanics 53, In Press

10. Ehab Moustafa Kamel K, Colliat JB, Gerard P, Massart TJ, Image based modelling of stress induced permeability alterations in sandstones, International Journal of Rock Mechanics and Mining Sciences, In Preparation

Conferences

1. Ehab Moustafa Kamel K, Massart T J, Sonon B. Integrated level set methodology for the generation and discretization of inclusion-based RVEs, in European Mechanics of Materials Conference (EMMC15), (Brussels, Belgium), September 2016

2. Ehab Moustafa Kamel K, Massart T J, Sonon B. Integrated level set methodology for the generation and discretization of heterogeneous geomaterial RVEs, in 14th U.S. National Congress on Computational Mechanics (USNCCM14), (Montreal, Canada), July 2017

3. Ehab Moustafa Kamel K, Massart T J, Sonon B, Conformal discretization of hetereogeneous geomaterial RVEs generated by excursion sets of random fields, in the 4th International Symposium on Computational Geomechanics (ComGeoIV), (Assisi, Italy), May 2018

Bibliography

Adam A (2020) Mesh voxelisation. MATLAB Central File Exchange `https://nl.mathworks.com/matlabcentral/fileexchange/27390-mesh-voxelisation`

Adler RJ (2008) Some new random field tools for spatial analysis. Stochastic Environmental Research and Risk Assessment 22(6):809

Ahrenholz B, Tölke J, Krafczyk M (2006) Lattice-boltzmann simulations in reconstructed parametrized porous media. International Journal of Computational Fluid Dynamics 20(6):369–377

Akono AT, Miguel Reis P, Ulm FJ (2011) Scratching as a fracture process: From butter to steel. Physical review letters 106:204302

Andó E, Cailletaud R, Roubin E, Stamati O, Wiebicke M, Couture CB, Matsushima T, Okubadejo O, Bertoni F, Sun Y, Colliat J (2019) Spam: Software for Practical Analysis of Materials A Python toolkit built on Numpy and Scipy. In preparation

Andrew M, Bijeljic B, Blunt MJ (2013) Pore-scale imaging of geological carbon dioxide storage under in situ conditions. Geophysical Research Letters 40(15):3915–3918

Andrä H, Combaret N, Dvorkin J, Glatt E, Han J, Kabel M, Keehm Y, Krzikalla F, Lee M, Madonna C, Marsh M, Mukerji T, Saenger EH, Sain R, Saxena N, Ricker S, Wiegmann A, Zhan X (2013a) Digital rock physics benchmarks—Part I: Imaging and segmentation. Computers & Geosciences 50:25–32

Andrä H, Combaret N, Dvorkin J, Glatt E, Han J, Kabel M, Keehm Y, Krzikalla F, Lee M, Madonna C, Marsh M, Mukerji T, Saenger EH, Sain R, Saxena N, Ricker S, Wiegmann A, Zhan X (2013b) Digital rock physics benchmarks—part II: Computing effective properties. Computers & Geosciences 50:33–43

Andò E, Viggiani G, Hall SA, Desrues J (2013) Experimental micro-mechanics of granular media studied by x-ray tomography: recent results and challenges. Géotechnique Letters 3(3):142–146

Arns C, Knackstedt M, Martys N (2005a) Cross-property correlations and permeability estimation in sandstone. Physical Review E 72(4):046304

Arns CH, Bauget F, Limaye A, Sakellariou A, Senden T, Sheppard A, Sok RM, Pinczewski V, Bakke S, Berge LI, Oren PE, Knackstedt MA (2005b) Pore Scale Characterization of Carbonates Using X-Ray Microtomography. SPE Journal 10(04):475–484

Attene M (2014) Direct repair of self-intersecting meshes. Graphical Models 76(6):658 – 668

Baker T (2005) Automatic mesh generation for complex three-dimensional regions using a constrained delaunay triangulation. Engineering with Computers 5:161–175

Benkemoun N, Hautefeuille M, Colliat JB, Ibrahimbegovic A (2010) Failure of heterogeneous materials: 3D meso-scale FE models with embedded discontinuities. International Journal for Numerical Methods in Engineering 82(13):1671–1688

Bérend I, Cases JM, François M, Uriot JP, Michot L, Masion A, Thomas F (1995) Mechanism of adsorption and desorption of water vapor by homoionic montmorillonites: 2. the li+ na+, k+, rb+ and cs+-exchanged forms. Clays and Clay Minerals 43(3):324–336

Bernabé Y, Mok U, Evans B (2003) Permeability-porosity relationships in rocks subjected to various evolution processes. Pure and applied geophysics 160(5):937–960

Bernabé Y, Li M, Maineult A (2010) Permeability and pore connectivity: A new model based on network simulations. Journal of Geophysical Research: Solid Earth 115(B10):n/a–n/a, b10203

Bernard O, Friboulet D, Thevenaz P, Unser M (2009) Variational b-spline level-set: A linear filtering approach for fast deformable model evolution. IEEE Transactions on Image Processing 18(6):1179–1191

Besuelle P, Desrues J, Raynaud S (2000) Experimental characterisation of the localisation phenomenon inside a vosges sandstone in a triaxial cell. International Journal of Rock Mechanics and Mining Sciences 37(8):1223 – 1237

Beucher S (2001) Geodesic reconstruction, saddle zones & hierarchical segmentation. Image Analysis & Stereology 20(3):137–141

Bhatnagar PL, Gross EP, Krook M (1954) A model for collision processes in gases. i. small amplitude processes in charged and neutral one-component systems. Phys Rev 94:511–525

Biot MA (1941) General theory of three-dimensional consolidation. Journal of Applied Physics 12(2):155–164

Blunt MJ, Bijeljic B, Dong H, Gharbi O, Iglauer S, Mostaghimi P, Paluszny A, Pentland C (2013) Pore-scale imaging and modelling. Advances in Water Resources 51:197 – 216, 35th Year Anniversary Issue

Boek ES, Venturoli M (2010) Lattice-boltzmann studies of fluid flow in porous media with realistic rock geometries. Computers & Mathematics with Applications 59(7):2305 – 2314, mesoscopic Methods in Engineering and Science

Borujeni AT, Lane N, Thompson K, Tyagi M (2013) Effects of image resolution and numerical resolution on computed permeability of consolidated packing using lb and fem pore-scale simulations. Computers & Fluids 88:753 – 763

Bottasso CL, Detomi D, Serra R (2005) The ball-vertex method: a new simple spring analogy method for unstructured dynamic meshes. Computer Methods in Applied Mechanics and Engineering 194(39):4244 – 4264

Boyd SK, Müller R (2006) Smooth surface meshing for automated finite element model generation from 3d image data. Journal of Biomechanics 39(7):1287 – 1295

Bultreys T, Van Hoorebeke L, Cnudde V (2015) Multi-scale, micro-computed tomography-based pore network models to simulate drainage in heterogeneous rocks. Advances in Water Resources 78:36 – 49

Bultreys T, De Boever W, Cnudde V (2016) Imaging and image-based fluid transport modeling at the pore scale in geological materials: A practical introduction to the current state-of-the-art. Earth-Science Reviews 155:93 – 128

Béchet E, Minnebo H, Moës N, Burgardt B (2005) Improved implementation and robustness study of the x-fem for stress analysis around cracks. International Journal for Numerical Methods in Engineering 64(8):1033–1056

Cai M (2010) Practical estimates of tensile strength and hoek–brown strength parameter mi of brittle rocks. Rock Mechanics and Rock Engineering 43(2):167–184

Cancelliere A, Chang C, Foti E, Rothman DH, Succi S (1990) The permeability of a random medium: Comparison of simulation with theory. Physics of Fluids A: Fluid Dynamics 2(12):2085–2088

Canny J (1987) A computational approach to edge detection. In: Fischler MA, Firschein O (eds) Readings in Computer Vision, Morgan Kaufmann, San Francisco (CA), pp 184 – 203

Carman PC (1937) Fluid flow through granular beds. Trans Inst Chem Eng 15:150–166

Caselles V, Kimmel R, Sapiro G (1997) Geodesic active contours. Int J Comput Vision 22(1):61–79

Chalmers GR, Ross DJ, Bustin RM (2012) Geological controls on matrix permeability of devonian gas shales in the horn river and liard basins, northeastern british columbia, canada. International Journal of Coal Geology 103:120 – 131, shale Gas and Shale Oil Petrology and Petrophysics

Chan TF, Vese LA (2001) Active contours without edges. Trans Img Proc 10(2):266–277

Chang YL, Li X (1995) Fast image region growing. Image and Vision Computing 13(7):559 – 571

Chen S, Yue ZQ, Tham LG (2006) Digital image based approach for three-dimensional mechanical analysis of heterogeneous rocks. Rock Mechanics and Rock Engineering 40(2):145

Choo J, Sun W (2018) Coupled phase-field and plasticity modeling of geological materials: From brittle fracture to ductile flow. Computer Methods in Applied Mechanics and Engineering 330:1 – 32

Cline HE, Lorensen WE, Ludke S, Crawford CR, Teeter BC (1988) Two algorithms for the three-dimensional reconstruction of tomograms. Medical Physics 15(3):320–327, https://aapm.onlinelibrary.wiley.com/doi/pdf/10.1118/1.596225

Cnudde V, Boone M (2013) High-resolution x-ray computed tomography in geosciences: A review of the current technology and applications. Earth-Science Reviews 123:1 – 17

Collin F (2003) Couplages thermo-hydro-mécaniques dans les sols et les roches tendres partiellement saturés. PhD thesis, Université de Liège, Liège, Belgique

Cooper DW (1988) Random-sequential-packing simulations in three dimensions for spheres. Phys Rev A 38:522–524

Cox MR, Budhu M (2008) A practical approach to grain shape quantification. Engineering Geology 96(1):1 – 16

Csati Z, Moës N, Massart TJ (2020) A stable extended/generalized finite element method with lagrange multipliers and explicit damage update for distributed cracking in cohesive materials. Computer Methods in Applied Mechanics and Engineering 369:113173

Cundall P (1988) Formulation of a three-dimensional distinct element model—part i. a scheme to detect and represent contacts in a system composed of many polyhedral blocks. International Journal of Rock Mechanics and Mining Sciences & Geomechanics Abstracts 25(3):107 – 116

Cundall PA, Strack ODL (1979) A discrete numerical model for granular assemblies. Géotechnique 29(1):47–65, https://doi.org/10.1680/geot.1979.29.1.47

Darcy H (1857) Recherches expérimentales relatives au mouvement de l'eau dans les tuyaux, vol 1. Mallet-Bachelier

De Boever W, Bultreys T, Derluyn H, Van Hoorebeke L, Cnudde V (2016) Comparison between traditional laboratory tests, permeability measurements and ct-based fluid flow modelling for cultural heritage applications. Science of The Total Environment 554-555:102 – 112

de Jong C (2015) Gas storage valuation and optimization. Journal of Natural Gas Science and Engineering 24:365 – 378

Delshad M, Kong X, Tavakoli R, Hosseini SA, Wheeler MF (2013) Modeling and simulation of carbon sequestration at cranfield incorporating new physical models. International Journal of Greenhouse Gas Control 18:463 – 473

Desrues J, Viggiani G, Besuelle P (2010) Advances in X-ray Tomography for Geomaterials, vol 118. John Wiley & Sons

Dolbow J, Moës N, Belytschko T (2000) Discontinuous enrichment in finite elements with a partition of unity method. Finite Elements in Analysis and Design 36(3):235 – 260, robert J. Melosh Medal Competition, Duke University, Durham NC, USA, March 1999

Dolbow J, Moës N, Belytschko T (2001) An extended finite element method for modeling crack growth with frictional contact. Computer Methods in Applied Mechanics and Engineering 190(51):6825 – 6846

Dong H, Blunt MJ (2009) Pore-network extraction from micro-computerized-tomography images. Phys Rev E 80:036307

Drach A, Drach B, Tsukrov I (2014) Processing of fiber architecture data for finite element modeling of 3d woven composites. Advances in Engineering Software 72:18 – 27, special Issue dedicated to Professor Zdeněk Bittnar on the occasion of his Seventieth Birthday: Part 2

Ehab Moustafa Kamel K, Sonon B, Massart TJ (2019) An integrated approach for the conformal discretization of complex inclusion-based microstructures. Computational Mechanics 64(4):1049–1071

Ehab Moustafa Kamel K, Colliat JB, Gerard P, Massart T (2020) Comparison of advanced discretization techniques for image-based modelling of heterogeneous porous rocks. Acta Geotechnica 15(1):57–77

van den Eijnden A, Bésuelle P, Chambon R, Collin F (2016) A fe2 modelling approach to hydromechanical coupling in cracking-induced localization problems. International Journal of Solids and Structures 97:475 – 488

Eshghinejadfard A, Daróczy L, Janiga G, Thévenin D (2016) Calculation of the permeability in porous media using the lattice boltzmann method. International Journal of Heat and Fluid Flow 62:93 – 103

Farquhar R, Smart B, Todd A, Tompkins D, Tweedie A (1993) Stress Sensitivity of Low-Permeability Sandstones From the Rotliegendes Sandstone. In: SPE Annual Technical Conference and Exhibition, Society of Petroleum Engineers, Houston, Texas

Fatt I, Davis D (1952) Reduction in Permeability With Overburden Pressure. Journal of Petroleum Technology 4(12):16–16

Feng XT, Chen S, Zhou H (2004) Real-time computerized tomography (ct) experiments on sandstone damage evolution during triaxial compression with chemical corrosion. International Journal of Rock Mechanics and Mining Sciences 41(2):181 – 192

Feyel F (2003) A multilevel finite element method (fe2) to describe the response of highly non-linear structures using generalized continua. Computer Methods in Applied Mechanics and Engineering 192(28):3233–3244, multiscale Computational Mechanics for Materials and Structures

Field DA (1988) Laplacian smoothing and delaunay triangulations. Communications in Applied Numerical Methods 4(6):709–712

Field DA (2000) Qualitative measures for initial meshes. International Journal for Numerical Methods in Engineering 47(4):887–906

Freitag LA, Ollivier-Gooch C (1997) Tetrahedral mesh improvement using swapping and smoothing. International Journal for Numerical Methods in Engineering 40(21):3979–4002

Frey P, George PL (2000) Mesh Generation: Application to Finite Elements. Hermes Science

Fritzen F, Böhlke T (2011) Periodic three-dimensional mesh generation for particle reinforced composites with application to metal matrix composites. International Journal of Solids and Structures 48(5):706 – 718

Furrer R, Sain SR (2010) Spam: A sparse matrix R package with emphasis on MCMC methods for Gaussian Markov random fields. Journal of Statistical Software 36(10):1–25

Fusseis F, Xiao X, Schrank C, De Carlo F (2014) A brief guide to synchrotron radiation-based microtomography in (structural) geology and rock mechanics. Journal of Structural Geology 65:1 – 16

Gargallo-Peiró A, Roca X, Peraire J, Sarrate J (2015) Distortion and quality measures for validating and generating high-order tetrahedral meshes. Engineering with Computers 31(3):423–437

Gensterblum Y, Ghanizadeh A, Cuss RJ, Amann-Hildenbrand A, Krooss BM, Clarkson CR, Harrington JF, Zoback MD (2015) Gas transport and storage capacity in shale gas reservoirs – a review. part a: Transport processes. Journal of Unconventional Oil and Gas Resources 12:87 – 122

George PL (1997) Improvements on delaunay-based three-dimensional automatic mesh generator. Finite Elements in Analysis and Design 25(3):297 – 317, adaptive Meshing, Part 2

George PL, Borouchaki H (1998) Delaunay Triangulation and Meshing. Hermès, Paris

Gerber F, Furrer R (2015) Pitfalls in the implementation of Bayesian hierarchical modeling of areal count data: An illustration using BYM and Leroux models. Journal of Statistical Software, Code Snippets 63(1):1–32

Gerber F, Moesinger K, Furrer R (2017) Extending R packages to support 64-bit compiled code: An illustration with spam64 and GIMMS NDVI3g data. Computer & Geoscience 104:109–119

Geuzaine C, Remacle JF (2009) Gmsh: A 3-d finite element mesh generator with built-in pre- and post-processing facilities. International Journal for Numerical Methods in Engineering 79(11):1309–1331

Ghanizadeh A, Gasparik M, Amann-Hildenbrand A, Gensterblum Y, Krooss BM (2014) Experimental study of fluid transport processes in the matrix system of the european organic-rich shales: I. scandinavian alum shale. Marine and Petroleum Geology 51:79 – 99

Ghazi A, Berke P, Ehab Moustafa Kamel K, Sonon B, Tiago C, Massart T (2019) Multiscale computational modelling of closed cell metallic foams with detailed microstructural morphological control. International Journal of Engineering Science 143:92–114

Ghossein E, Lévesque M (2012) A fully automated numerical tool for a comprehensive validation of homogenization models and its application to spherical particles reinforced composites. International Journal of Solids and Structures 49(11):1387 – 1398

Ghossein E, Lévesque M (2013) Random generation of periodic hard ellipsoids based on molecular dynamics: A computationally-efficient algorithm. Journal of Computational Physics 253:471 – 490

Ghossein E, Lévesque M (2014) A comprehensive validation of analytical homogenization models: The case of ellipsoidal particles reinforced composites. Mechanics of Materials 75:135 – 150

Glasbey CA, Horgan GW (1995) Image Analysis for the Biological Sciences. John Wiley & Sons, Inc., USA

Gniewek P, Hallatschek O (2019) Fluid flow through packings of elastic shells. Phys Rev E 99:023103

Goldman R (2005) Curvature formulas for implicit curves and surfaces. Computer Aided Geometric Design 22(7):632 – 658, geometric Modelling and Differential Geometry

Grail G, Hirsekorn M, Wendling A, Hivet G, Hambli R (2013) Consistent finite element mesh generation for meso-scale modeling of textile composites with preformed and compacted reinforcements. Composites Part A: Applied Science and Manufacturing 55:143 – 151

Guibert R, Nazarova M, Horgue P, Hamon G, Creux P, Debenest G (2015) Computational Permeability Determination from Pore-Scale Imaging: Sample Size, Mesh and Method Sensitivities. Transport in Porous Media 107(3):641–656

Haddad R, Akansu A (1991) A class of fast gaussian binomial filters for speech and image processing. Signal Processing, IEEE Transactions on 39:723 – 727

Hashemi M, Massart T, Salager S, Herrier G, François B (2015) Pore scale characterization of lime-treated sand–bentonite mixtures. Applied Clay Science 111:50 – 60

Hashemi MA, Khaddour G, François B, Massart TJ, Salager S (2014) A tomographic imagery segmentation methodology for three-phase geomaterials based on simultaneous region growing. Acta Geotechnica 9(5):831–846

Hemes S, Desbois G, Urai JL, Schröppel B, Schwarz JO (2015) Multi-scale characterization of porosity in boom clay (hades-level, mol, belgium) using a combination of x-ray µ-ct, 2d bib-sem and fib-sem tomography. Microporous and Mesoporous Materials 208:1 – 20

Hormann K (2003) From scattered samples to smooth surfaces. In: Proceedings of Geometric Modeling and Computer Graphics

Hoshino K, Koide H, Inami K, Iwamura S, Mitsui S (1972) Mechanical Properties of Japanese Tertiary Sedimentary Rocks under High Confining Pressure, Geological Survey of Japan Report No.244

Hu C, Agostini F, Skoczylas F, Jeannin L, Potier L (2018) Poromechanical properties of a sandstone under different stress states. Rock Mechanics and Rock Engineering

Hu C, Agostini F, Skoczylas F, Jeannin L, Egermann P, Jia Y (2020a) Transport property evolution during hydrostatic and triaxial compression of a high porosity sandstone. European Journal of Environmental and Civil Engineering pp 1–14

Hu LB, Savidge C, Rizzo D, Hayden N, Dewoolkar M, Meador L, Hagadorn JW (2013) Characterization of Porous Media in Agent Transport Simulation, John Wiley & Sons, Inc., pp 172–179

Hu Z, Klaver J, Schmatz J, Dewanckele J, Littke R, Krooss BM, Amann-Hildenbrand A (2020b) Stress sensitivity of porosity and permeability of cobourg limestone. Engineering Geology 273:105632

Hyväluoma J, Thapaliya M, Alaraudanjoki J, Sirén T, Mattila K, Timonen J, Turtola E (2012) Using microtomography, image analysis and flow simulations to characterize soil surface seals. Computers & Geosciences 48:93 – 101

Iassonov P, Gebrenegus T, Tuller M (2009) Segmentation of x-ray computed tomography images of porous materials: A crucial step for characterization and quantitative analysis of pore structures. Water Resources Research 45

Ibrahimbegovic A, Wilson E (1991) Modified method of incompatible modes. Communications in Applied Numerical Methods 7(3):187–194

Icardi M, Boccardo G, Marchisio DL, Tosco T, Sethi R (2014) Pore-scale simulation of fluid flow and solute dispersion in three-dimensional porous media. Phys Rev E 90:013032

J Bossen F, Heckbert P (1996) A pliant method for anisotropic mesh generation. In: Proceedings of the 5th International Meshing Roundtable, pp 63–74

Jiang T, Shao J, Xu W, Zhou C (2010) Experimental investigation and micromechanical analysis of damage and permeability variation in brittle rocks. International Journal of Rock Mechanics and Mining Sciences 47(5):703 – 713

Ju T, Losasso F, Schaefer S, Warren J (2002) Dual contouring of hermite data. ACM Trans Graph 21(3):339–346

Kaestner A, Lehmann E, Stampanoni M (2008) Imaging and image processing in porous media research. Advances in Water Resources 31(9):1174 – 1187, quantitative links between porous media structures and flow behavior across scales

Kandhai D, Vidal DJE, Hoekstra AG, Hoefsloot H, Iedema P, Sloot PMA (1998) A Comparison Between Lattice-Boltzmann and Finite-Element Simulations of Fluid Flow in Static Mixer Reactors. International Journal of Modern Physics C 09(08):1123–1128

Katsube TJ, Mudford BS, Best ME (1991) Petrophysical characteristics of shales from the Scotian shelf. Geophysics 56(10):1681–1689

Katz D, Tek M (1981) Overview on underground storage of natural gas. Journal of Petroleum Technology 33:943–951

Kawamoto R, Andò E, Viggiani G, Andrade JE (2018) All you need is shape: Predicting shear banding in sand with ls-dem. Journal of the Mechanics and Physics of Solids 111:375 – 392

Keehm Y (2004) Permeability prediction from thin sections: 3D reconstruction and Lattice-Boltzmann flow simulation. Geophysical Research Letters 31(4):L04606

Keller LM, Holzer L, Schuetz P, Gasser P (2013) Pore space relevant for gas permeability in Opalinus clay: Statistical analysis of homogeneity, percolation, and representative volume element. Journal of Geophysical Research: Solid Earth 118(6):2799–2812

Kilingar N, Ehab Moustafa Kamel K, Sonon B, Massart T, Noels L (2019) Computational generation of open-foam representative volume elements with morphological control using distance fields. European Journal of Mechanics - A/Solids 78:103847

Kilmer N, Morrow N, Pitman J (1987) Pressure sensitivity of low permeability sandstones. Journal of Petroleum Science and Engineering 1(1):65 – 81

Kim KY, Zhuang L, Yang H, Kim H, Min KB (2016) Strength anisotropy of berea sandstone: Results of x-ray computed tomography, compression tests, and discrete modeling. Rock Mechanics and Rock Engineering 49(4):1201–1210

Klaas O, Beall MW, Shephard MS (2013) Construction of Models and Meshes of Heterogeneous Material Microstructures from Image Data, Springer Netherlands, Dordrecht, pp 171–193

Klingner BM, Shewchuk JR (2008) Aggressive Tetrahedral Mesh Improvement, Springer Berlin Heidelberg, Berlin, Heidelberg, pp 3–23

Kobbelt LP, Botsch M, Schwanecke U, Seidel HP (2001) Feature sensitive surface extraction from volume data. In: Proceedings of the 28th Annual Conference on Computer Graphics and Interactive Techniques, Association for Computing Machinery, New York, NY, USA, SIGGRAPH '01, p 57–66

Koko J (2015) A matlab mesh generator for the two-dimensional finite element method. Applied Mathematics and Computation 250:650 – 664

Kouznetsova V, Brekelmans WAM, Baaijens FPT (2001) An approach to micro-macro modeling of heterogeneous materials. Computational Mechanics 27(1):37–48

Kouznetsova V, Geers MGD, Brekelmans WAM (2002) Multi-scale constitutive modelling of heterogeneous materials with a gradient-enhanced computational homogenization scheme. International Journal for Numerical Methods in Engineering 54(8):1235–1260

Kozeny J (1927) Uber kapillare leitung der wasser in boden. Royal Academy of Science, Vienna, Proc Class I 136:271–306

Kwon O, Kronenberg AK, Gangi AF, Johnson B, Herbert BE (2004) Permeability of illite-bearing shale: 1. Anisotropy and effects of clay content and loading. Journal of Geophysical Research: Solid Earth 109(B10)

Ladd AJC (1994) Numerical simulations of particulate suspensions via a discretized boltzmann equation. part 1. theoretical foundation. Journal of Fluid Mechanics 271:285–309

Larsson F, Runesson K, Su F (2010) Computational homogenization of uncoupled consolidation in micro-heterogeneous porous media. International Journal for Numerical and Analytical Methods in Geomechanics 34(14):1431–1458, `https://onlinelibrary.wiley.com/doi/pdf/10.1002/nag.862`

Latt J (2008) Choice of units in lattice boltzmann simulations

Latt J, Malaspinas O, Kontaxakis D, Parmigiani A, Lagrava D, Brogi F, Belgacem MB, Thorimbert Y, Leclaire S, Li S, Marson F, Lemus J, Kotsalos C, Conradin R, Coreixas C, Petkantchin R, Raynaud F, Beny J, Chopard B (2020) Palabos: Parallel lattice boltzmann solver. Computers & Mathematics with Applications

Legrain G, Allais R, Cartraud P (2011a) On the use of the extended finite element method with quadtree/octree meshes. International Journal for Numerical Methods in Engineering 86(6):717–743

Legrain G, Cartraud P, Perreard I, Moës N (2011b) An x-fem and level set computational approach for image-based modelling: Application to homogenization. International Journal for Numerical Methods in Engineering 86(7):915–934

Levasseur S, Collin F, Charlier R, Kondo D (2013) A micro–macro approach of permeability evolution in rocks excavation damaged zones. Computers and Geotechnics 49:245 – 252

Li CS, Zhang D, Du SS, Shi B (2016) Computed tomography based numerical simulation for triaxial test of soil–rock mixture. Computers and Geotechnics 73:179 – 188

Li G, Liang ZZ, Tang CA (2015) Morphologic interpretation of rock failure mechanisms under uniaxial compression based on 3d multiscale high-resolution numerical modeling. Rock Mechanics and Rock Engineering 48(6):2235–2262

Li J, Konietzky H, Frühwirt T (2017) Voronoi-based dem simulation approach for sandstone considering grain structure and pore size. Rock Mechanics and Rock Engineering 50(10):2749–2761

Lian WD, Legrain G, Cartraud P (2013) Image-based computational homogenization and localization: comparison between x-fem/levelset and voxel-based approaches. Computational Mechanics 51:279–293

Liang Z, Ioannidis M, Chatzis I (2000) Permeability and electrical conductivity of porous media from 3d stochastic replicas of the microstructure. Chemical Engineering Science 55(22):5247 – 5262

Lin TJ, Guan ZQ, Chang JH, Lo SH (2014) Vertex-ball spring smoothing: An efficient method for unstructured dynamic hybrid meshes. Computers & Structures 136:24 – 33

Liu Y, Straumit I, Vasiukov D, Lomov SV, Panier S (2017) Prediction of linear and non-linear behavior of 3d woven composite using mesoscopic voxel models reconstructed from x-ray micro-tomography. Composite Structures 179:568 – 579

Llewellin E (2010) Lbflow: An extensible lattice boltzmann framework for the simulation of geophysical flows. part i: theory and implementation. Computers and Geosciences 36(2):115–122, cited By 27

Lo D (2015) Finite Element Mesh Generation. Taylor & Francis

Lo S (1991) Volume discretization into tetrahedra—ii. 3d triangulation by advancing front approach. Computers & Structures 39(5):501 – 511

Lorensen WE, Cline HE (1987) Marching cubes: A high resolution 3d surface construction algorithm. SIGGRAPH Comput Graph 21(4):163–169

Macri M, De S (2008) An octree partition of unity method (octpum) with enrichments for multiscale modeling of heterogeneous media. Computers & Structures 86(7):780 – 795

Mahabadi O, Randall N, Zong Z, Grasselli G (2012) A novel approach for micro-scale characterization and modeling of geomaterials incorporating actual material heterogeneity. Geophysical Research Letters 39:1303–

Manwart C, Aaltosalmi U, Koponen A, Hilfer R, Timonen J (2002) Lattice-boltzmann and finite-difference simulations for the permeability for three-dimensional porous media. Phys Rev E 66:016702

Marot C, Pellerin J, Remacle JF (2019) One machine, one minute, three billion tetrahedra. International Journal for Numerical Methods in Engineering 117(9):967–990, https://onlinelibrary.wiley.com/doi/pdf/10.1002/nme.5987

Martys NS, Chen H (1996) Simulation of multicomponent fluids in complex three-dimensional geometries by the lattice Boltzmann method. Physical Review E 53(1):743–750

Massart T, Sonon B, Ehab Moustafa Kamel K, Poh L, Sun G (2018) Level set-based generation of representative volume elements for the damage analysis of irregular masonry. Meccanica 53(7):1737–1755

Massart T, Ehab Moustafa Kamel K, Hernandez H (2019) Chapter 11 - automated geometry extraction and discretization for cohesive zone-based modeling of irregular masonry. In: Ghiassi B, Milani G (eds) Numerical Modeling of Masonry and Historical Structures, Woodhead Publishing Series in Civil and Structural Engineering, Woodhead Publishing, pp 397 – 422

Massart TJ, Selvadurai APS (2012) Stress-induced permeability evolution in a quasi-brittle geomaterial. Journal of Geophysical Research: Solid Earth 117(B7)

Massart TJ, Selvadurai APS (2014) Computational modelling of crack-induced permeability evolution in granite with dilatant cracks. International Journal of Rock Mechanics and Mining Sciences 70:593 – 604

Masson R, Bornert M, Suquet P, Zaoui A (2000) An affine formulation for the prediction of the effective properties of nonlinear composites and polycrystals. Journal of the Mechanics and Physics of Solids 48(6):1203 – 1227

McClure J, Prins J, Miller C (2014) A novel heterogeneous algorithm to simulate multiphase flow in porous media on multicore CPU–GPU systems. Computer Physics Communications 185(7):1865–1874

Meakin P, Tartakovsky AM (2009) Modeling and simulation of pore-scale multiphase fluid flow and reactive transport in fractured and porous media. Reviews of Geophysics 47(3)

Mees F, Swennen R, Geet MV, Jacobs P (2003) Applications of X-ray computed tomography in the geosciences. Geological Society, London, Special Publications 215(1):1–6

Menétrey P, Willam K (1995) Triaxial failure criterion for concrete and its generalization. ACI Structural Journal 92:311 – 318

Meng Z, Li G (2013) Experimental research on the permeability of high-rank coal under a varying stress and its influencing factors. Engineering Geology 162:108 – 117

Moës N, Dolbow J, Belytschko T (1999) A finite element method for crack growth without remeshing. International Journal for Numerical Methods in Engineering 46(1):131–150

Moes N, Cloirec M, Cartraud P, Remacle JF (2003) A computational approach to handle complex microstructure geometries. Computer Methods in Applied Mechanics and Engineering 192(28-30):3163–3177

Morrow CA, Shi LQ, Byerlee JD (1984) Permeability of fault gouge under confining pressure and shear stress. Journal of Geophysical Research: Solid Earth 89(B5):3193–3200

Mostaghimi P, Bijeljic B, Blunt M (2012) Simulation of Flow and Dispersion on Pore-Space Images. SPE Journal 17(04):1131–1141

Moës N, Belytschko T (2002) Extended finite element method for cohesive crack growth. Engineering Fracture Mechanics 69(7):813 – 833

Münch B, Holzer L (2008) Contradicting geometrical concepts in pore size analysis attained with electron microscopy and mercury intrusion. Journal of the American Ceramic Society 91(12):4059–4067

Narsilio GA, Buzzi O, Fityus S, Yun TS, Smith DW (2009) Upscaling of navier–stokes equations in porous media: Theoretical, numerical and experimental approach. Computers and Geotechnics 36(7):1200 – 1206

Narváez A, Yazdchi K, Luding S, Harting J (2013) From creeping to inertial flow in porous media: a lattice boltzmann–finite element study. Journal of Statistical Mechanics: Theory and Experiment 2013(02):P02038

Nikolić M, Roje-Bonacci T, Ibrahimbegović A (2016) Overview of the numerical methods for the modelling of rock mechanics problems. Tehnički vjesnik 23(2):627–637

Nixon MS (2012) Feature extraction & image processing for computer vision, 3rd edn. Academic Press, Oxford

Osher S, Fedkiw R (2003) Signed Distance Functions, Springer New York, New York, NY, pp 17–22

Osher S, Fedkiw R (2006) Level Set Methods and Dynamic Implicit Surfaces. Applied Mathematical Sciences, Springer New York

Otsu N (1979) A threshold selection method from gray-level histograms. IEEE transactions on systems, man, and cybernetics 9(1):62–66

Paiva A, Lopes H, Lewiner T, Figueiredo LHD (2006) Robust adaptive meshes for implicit surfaces. In: 2006 19th Brazilian Symposium on Computer Graphics and Image Processing, pp 205–212

Pande GN, Beer GG, Williams J R (John R) (1990) Numerical methods in rock mechanics. Chichester ; New York : Wiley, includes bibliographical references and index

Park JJ, Florence P, Straub J, Newcombe R, Lovegrove S (2019) Deepsdf: Learning continuous signed distance functions for shape representation. In: Proceedings of the IEEE/CVF Conference on Computer Vision and Pattern Recognition (CVPR)

Patil S, Ravi B (2005) Voxel-based representation, display and thickness analysis of intricate shapes. In: Ninth International Conference on Computer Aided Design and Computer Graphics (CAD-CG'05), pp 6 pp.–

Perras MA, Diederichs MS (2014) A review of the tensile strength of rock: Concepts and testing. Geotechnical and Geological Engineering 32(2):525–546

Persson PO (2005) Mesh generation for implicit geometries. PhD thesis, Massachusetts Institute of Technology, Cambridge, MA, USA

Persson PO, Strang G (2004) A simple mesh generator in matlab. SIAM Review 46:2004

Petrasch J, Meier F, Friess H, Steinfeld A (2008) Tomography based determination of permeability, dupuit–forchheimer coefficient, and interfacial heat transfer coefficient in reticulate porous ceramics. International Journal of Heat and Fluid Flow 29(1):315 – 326

Potter E, Pinho S, Robinson P, Iannucci L, McMillan A (2012) Mesh generation and geometrical modelling of 3d woven composites with variable tow cross-sections. Computational Materials Science 51(1):103 – 111

Rabbani A, Jamshidi S (2014) Specific surface and porosity relationship for sandstones for prediction of permeability. International Journal of Rock Mechanics and Mining Sciences 71:25 – 32

Ramstad T, Øren P, Bakke S (2010) Simulation of two-phase flow in reservoir rocks using a lattice boltzmann method. Spe Journal 15:917–927

Randall NX, Vandamme M, Ulm FJ (2009) Nanoindentation analysis as a two-dimensional tool for mapping the mechanical properties of complex surfaces. Journal of Materials Research 24(3):679–690

Raynaud S, Vasseur G, Soliva R (2012) In vivo ct x-ray observations of porosity evolution during triaxial deformation of a calcarenite. International Journal of Rock Mechanics and Mining Sciences 56:161 – 170

Robinet JC, Sardini P, Coelho D, Parneix JC, Prêt D, Sammartino S, Boller E, Altmann S (2012) Effects of mineral distribution at mesoscopic scale on solute diffusion in a clay-rich rock: Example of the Callovo-Oxfordian mudstone (Bure, France). Water Resources Research 48(5)

Ronse C (2008) Reconstructing masks from markers in non-distributive lattices. Applicable Algebra in Engineering Communication and Computing 19(1):51–85

Rothman DH, Zaleski S, Powell AC (1998) Lattice-gas cellular automata: Simple models of complex hydrodynamics. Computers in Physics 12(6):576–576, `https://aip.scitation.org/doi/pdf/10.1063/1.168762`

Roubin E, Colliat JB, Benkemoun N (2015) Meso-scale modeling of concrete: A morphological description based on excursion sets of random fields. Computational Materials Science 102:183 – 195

Ruppert J (1995) A delaunay refinement algorithm for quality 2-dimensional mesh generation. Journal of Algorithms 18(3):548 – 585

Rusinkiewicz S (2004) Estimating curvatures and their derivatives on triangle meshes. In: Proceedings of the 3D Data Processing, Visualization, and Transmission, 2Nd International Symposium, IEEE Computer Society, Washington, DC, USA, 3DPVT '04, pp 486–493

Rutqvist J, Börgesson L, Chijimatsu M, Hernelind J, Jing L, Kobayashi A, Nguyen S (2009) Modeling of damage, permeability changes and pressure responses during excavation of the tsx tunnel in granitic rock at url, canada. Environmental Geology 57(6):1263–1274

Sanchez-Palencia E (1980) Non-Homogeneous Media and Vibration Theory. Lecture Notes in Physics, Springer, Berlin

Schindelin J, Arganda-Carreras I, Frise E, Kaynig V, Longair M, Pietzsch T, Preibisch S, Rueden C, Saalfeld S, Schmid B, Tinevez JY, White DJ, Hartenstein V, Eliceiri K, Tomancak P, Cardona A (2012) Fiji: an open-source platform for biological-image analysis. Nat Meth 9(7):676–682

Schöberl J (1997) Netgen an advancing front 2d/3d-mesh generator based on abstract rules. Computing and Visualization in Science 1(1):41–52

Selvadurai A, Głowacki A (2008) Permeability Hysterisis of Limestone During Isotropic Compression. Groundwater 46(1):113–119

Selvadurai APS (2015) Normal stress-induced permeability hysteresis of a fracture in a granite cylinder. Geofluids 15(1-2):37–47

Selvadurai APS, Głowacki A (2017) Stress-Induced Permeability Alterations in an Argillaceous Limestone. Rock Mechanics and Rock Engineering 50(5):1079–1096

Selvadurai P, Selvadurai A (2014) On the effective permeability of a heterogeneous porous medium: the role of the geometric mean. Philosophical Magazine 94(20):2318–2338

Sethian J (1999) Level Set Methods and Fast Marching Methods: Evolving Interfaces in Computational Geometry, Fluid Mechanics, Computer Vision, and Materials Science, Cambridge Monographs on Applied and Computational Mathematics, vol 3. Cambridge University Press

Sezgin M, Sankur B (2004) Survey over image thresholding techniques and quantitative performance evaluation. Journal of Electronic Imaging 13(1):146 – 165

Shao J, Hoxha D, Bart M, Homand F, Duveau G, Souley M, Hoteit N (1999) Modelling of induced anisotropic damage in granites. International Journal of Rock Mechanics and Mining Sciences 36(8):1001 – 1012

Shapiro L, Stockman G (2001) Computer vision. New Jersey, Prentice-Hall pp 137–150

Sheppard A, Sok R, Averdunk H (2005) Improved pore network extraction methods. International Symposium of the Society of Core Analysts

Shewchuk JR (2002) Constrained delaunay tetrahedralizations and provably good boundary recovery. In: Proceedings of the 11th International Meshing Roundtable, IMR 2002, Ithaca, New York, USA, September 15-18, 2002, pp 193–204

Shewchuk JR (2012) Lecture notes on delaunay mesh generation. University of California, Department of Electrical Engineering and Computer Sciences

Shi Y, Karl WC (2008) A real-time algorithm for the approximation of level-set-based curve evolution. IEEE Transactions on Image Processing 17(5):645–656

Shi Y, Wang CY (1986) Pore pressure generation in sedimentary basins: Overloading versus aquathermal. Journal of Geophysical Research 91(B2):2153

Si H (2010) Constrained delaunay tetrahedral mesh generation and refinement. Finite Elem Anal Des 46(1-2):33–46

Si H (2015) Tetgen, a delaunay-based quality tetrahedral mesh generator. ACM Trans Math Softw 41(2):11:1–11:36

Si H, Gärtner K (2010) 3D Boundary Recovery by Constrained Delaunay Tetrahedralization. Preprint, WIAS

Simo J, Rifai M (1990) A class of mixed assumed strain methods and the method of incompatible modes. International Journal for Numerical Methods in Engineering 29(8):1595–1638

Simo J, Oliver J, Armero F (1993) An analysis of strong discontinuities induced by strain-softening in rate-independent inelastic solids. Computational Mechanics 12(5):277–296

Simulia (2014) ABAQUS/Standard User's Manual, Version 6.14. Dassault Systèmes Simulia Corp, United States

der Sluis O, Vosbeek P, Schreurs P, jer H (1999) Homogenization of heterogeneous polymers. International Journal of Solids and Structures 36(21):3193 – 3214

Soille P (2003) Morphological Image Analysis: Principles and Applications, 2nd edn. Springer-Verlag, Berlin, Heidelberg

Song Y, Davy C, Troadec D, Blanchenet AM, Skoczylas F, Talandier J, Robinet J (2015) Multi-scale pore structure of cox claystone: Towards the prediction of fluid transport. Marine and Petroleum Geology 65:63 – 82

Sonka M, Hlavac V, Boyle R (2007) Image Processing, Analysis, and Machine Vision. Thomson-Engineering

Sonon B, Massart TJ (2013) A level-set based representative volume element generator and xfem simulations for textile and 3d-reinforced composites. Materials 6(12):5568–5592

Sonon B, François B, Massart TJ (2012) A unified level set based methodology for fast generation of complex microstructural multi-phase rves. Computer Methods in Applied Mechanics and Engineering 223:103 – 122

Sonon B, François B, Massart TJ (2015) An advanced approach for the generation of complex cellular material representative volume elements using distance fields and level sets. Computational Mechanics 56(2):221–242

Souley M, Homand F, Pepa S, Hoxha D (2001) Damage-induced permeability changes in granite: a case example at the url in canada. International Journal of Rock Mechanics and Mining Sciences 38(2):297 – 310

Stone DC (1995) Application of median filtering to noisy data. Canadian Journal of Chemistry 73(10):1573–1581

Stroeven M, Askes H, Sluys L (2004) Numerical determination of representative volumes for granular materials. Computer Methods in Applied Mechanics and Engineering 193(30):3221 – 3238, computational Failure Mechanics

Succi S (2001) The Lattice Boltzmann Equation for Fluid Dynamics and Beyond. Clarendon Press, Oxford

Sufian A, Russell AR (2013) Microstructural pore changes and energy dissipation in gosford sandstone during pre-failure loading using x-ray ct. International Journal of Rock Mechanics and Mining Sciences 57:119 – 131

Sukop MC, Thorne DTJ (2007) Lattice Boltzmann Modeling: An Introduction for Geoscientists and Engineers, 1st edn. Springer Publishing Company, Incorporated

Sukumar N, Chopp D, Moës N, BelytschkoT̈ (2001) Modeling holes and inclusions by level sets in the extended finite-element method. Computer Methods in Applied Mechanics and Engineering 190(46-47):6183–6200

Sun W, fong Wong T (2018) Prediction of permeability and formation factor of sandstone with hybrid lattice boltzmann/finite element simulation on microtomographic images. International Journal of Rock Mechanics and Mining Sciences 106:269 – 277

Sun WC, Andrade JE, Rudnicki JW (2011) Multiscale method for characterization of porous microstructures and their impact on macroscopic effective permeability. International Journal for Numerical Methods in Engineering 88(12):1260–1279

Teatini P, Castelletto N, Ferronato M, Gambolati G, Janna C, Cairo E, Marzorati D, Colombo D, Ferretti A, Bagliani A, Bottazzi F (2011) Geomechanical response to seasonal gas storage in depleted reservoirs: A case study in the po river basin, italy. Journal of Geophysical Research: Earth Surface 116(F2)

Terada K, Hori M, Kyoya T, Kikuchi N (2000) Simulation of the multi-scale convergence in computational homogenization approaches. International Journal of Solids and Structures 37(16):2285 – 2311

TetMesh-GHS3D (2010) A powerful isotropic tet-mesher, version 4.2

Thijssen J (2007) Computational Physics. Cambridge University Press

Viggiani G, Lenoir N, Bésuelle P, Di Michiel M, Marello S, Desrues J, Kretzschmer M (2004) X-ray microtomography for studying localized deformation in fine-grained geomaterials under triaxial compression. Comptes Rendus Mécanique 332(10):819 – 826

Walsh J (1981) Effect of pore pressure and confining pressure on fracture permeability. International Journal of Rock Mechanics and Mining Sciences & Geomechanics Abstracts 18(5):429 – 435

Wang W, Kravchenko A, Smucker A, Rivers M (2011a) Comparison of image segmentation methods in simulated 2d and 3d microtomographic images of soil aggregates. Geoderma 162(3):231 – 241

Wang Y, Lesher C, Fiquet G, Rivers M, Nishiyama N, Siebert J, Roberts J, Morard G, Gaudio S, Clark A, Watson H, Menguy N, Guyot F (2011b) In situ high-pressure and high-temperature x-ray microtomographic imaging during large deformation: A new technique for studying mechanical behavior of multiphase composites. Geosphere 7:40–53

Washizu K (1982) Variational methods in elasticity and plasticity. Pergamon Press New York

White JA, Borja RI, Fredrich JT (2006) Calculating the effective permeability of sandstone with multiscale lattice boltzmann/finite element simulations. Acta Geotechnica 1(4):195–209

Wiktor C, Turner S, Zacher D, Fischer RA, Tendeloo GV (2012) Imaging of intact mof-5 nanocrystals by advanced tem at liquid nitrogen temperature. Microporous and Mesoporous Materials 162:131 – 135

Wilson E (1974) The static condensation algorithm. International Journal for Numerical Methods in Engineering 8(1):198–203

Wintiba B, Sonon B, Ehab Moustafa Kamel K, Massart TJ (2017) An automated procedure for the generation and conformal discretization of 3d woven composites rves. Composite Structures 180(Supplement C):955 – 971

Wintiba B, Vasiukov D, Panier S, Lomov SV, Ehab Moustafa Kamel K, Massart TJ (2020) Automated reconstruction and conformal discretization of 3d woven composite ct scans with local fiber volume fraction control. Composite Structures 248:112438

Yang ZJ, Li BB, Wu JY (2019) X-ray computed tomography images based phase-field modeling of mesoscopic failure in concrete. Engineering Fracture Mechanics 208:151 – 170

Yu Q, Yang S, Ranjith PG, Zhu W, Yang T (2016) Numerical modeling of jointed rock under compressive loading using x-ray computerized tomography. Rock Mechanics and Rock Engineering 49(3):877–891

Yuan R, Singh SS, Chawla N, Oswald J (2014) Efficient methods for implicit geometrical representation of complex material microstructures. International Journal for Numerical Methods in Engineering 98(2):79–91

Zhang Y, Bajaj C, Sohn B (2005) 3d finite element meshing from imaging data. Computer Methods in Applied Mechanics and Engineering 194(48-49):5083–5106

Zhang Y, Hughes TJ, Bajaj CL (2010) An automatic 3d mesh generation method for domains with multiple materials. Computer Methods in Applied Mechanics and Engineering 199(5):405 – 415, computational Geometry and Analysis

Zheng J, Zheng L, Liu HH, Ju Y (2015) Relationships between permeability, porosity and effective stress for low-permeability sedimentary rock. International Journal of Rock Mechanics and Mining Sciences 78:304 – 318

Zhou XP, Xiao N (2017) A novel 3d geometrical reconstruction model for porous rocks. Engineering Geology 228:371 – 384

Zhou XP, Xiao N (2018a) 3d numerical reconstruction of porous sandstone using improved simulated annealing algorithms. Rock Mechanics and Rock Engineering 51(7):2135–2151

Zhou XP, Xiao N (2018b) A hierarchical-fractal approach for the rock reconstruction and numerical analysis. International Journal of Rock Mechanics and Mining Sciences 109:68 – 83

Zienkiewicz OC, Taylor RL, Zhu JZ (2005) The Finite Element Method: Its Basis and Fundamentals, Sixth Edition, 6th edn. Butterworth-Heinemann

Zoback MD, Byerlee JD (1975) The effect of microcrack dilatancy on the permeability of westerly granite. Journal of Geophysical Research 80(5):752–755